Observations et Modélisation des systèmes planétaires autour des étoiles proches

Jérémy Lebreton

Jérémy Lebreton. Observations et Modélisation des systèmes planétaires autour des étoiles proches. Astrophysique stellaire et solaire [astro-ph.SR]. Université de Grenoble, 2013. Français. NNT : . tel-00876169

HAL Id: tel-00876169
https://theses.hal.science/tel-00876169

Submitted on 23 Oct 2013

UNIVERSITÉ DE GRENOBLE

THÈSE

Pour obtenir le grade de

DOCTEUR DE L'UNIVERSITÉ DE GRENOBLE

Spécialité : **Astrophysique & milieux dilués**

Arrêté ministérial : du 7 aout 2006

Présentée par

Jérémy Lebreton

Thèse dirigée par **Jean-Charles Augereau**

préparée au sein **de l'Institut de Planétologie et d'Astrophysique de Grenoble**
et de **l'École Doctorale de Physique**

Observations et Modélisation des systèmes planétaires autour des étoiles proches

Thèse soutenue publiquement le **6 mars 2013**,
devant le jury composé de :

Jean-Charles AUGEREAU
IPAG / OSUG, Directeur de thèse
Charles A. BEICHMAN
NExScI / California Institute of Technology, Rapporteur
Joachim KÖPPEN
Observatoire de Strasbourg, Examinateur
Jean-François LESTRADE
Observatoire de Paris / LERMA, Examinateur
Anne-Marie LAGRANGE
IPAG / CNRS, Examinatrice
Jean-Louis MONIN
IPAG / UJF, Président
Philippe THÉBAULT
Observatoire de Paris, LESIA, Rapporteur

Remerciements

Et voilà : trois années de recherche, des mois consacrés à l'écriture de la thèse que vous tenez en main, et déjà ce dur labeur paraît un lointain souvenir. Quelques menues corrections et c'est enfin l'heure de mettre un point final à mon mémoire de thèse. Les nuits blanches et le travail obsessionnel oublié, c'est surtout un grand sentiment de gratitude qui demeure, envers les nombreuses personnes qui m'ont aidé à mener ce travail à bien. J'espère n'oublier personne tant la liste est longue !

Cela ne surprendra personne mais c'est avec la plus grande sincérité que mes remerciements seront adressés tout d'abord à Jean-Charles. Directeur de thèse remarquable, Jean-Charles m'a dès le début donné les moyens d'embrasser le métier de chercheur. Grâce à son enthousiasme, son expertise et ses grandes qualités humaines, il m'a mis en position de rejoindre de grandes collaborations internationales et de prendre une part active à la recherche en Astrophysique.

Mes sentiments chaleureux sont adressés aux membres de mon jury : Philippe, Anne-Marie, avec qui j'ai eu la chance et le plaisir d'interagir tout au long de ma thèse. Je remercie tout particulièrement Joachim, Jean-François et bien sûr Chas qui m'ont tous trois fait l'honneur de voyager jusqu'à Grenoble pour assister à ma soutenance. Leurs conseils et leur bienveillance auront été essentiels à la bonne conclusion de mon doctorat. Je remercie également Jean-Louis, d'avoir assumé la présidence de mon jury et d'entretenir à l'IPAG d'excellentes conditions de travail pour les doctorants.

Je suis par ailleurs particulièrement reconnaissant envers Hervé qui a lui aussi été très présent tout au long de ma thèse et m'a fait bénéficier de son expérience précieuse. Au rang des collaborateurs qui auront joué un rôle déterminant dans mon travail, je remercie vivement Olivier, Denis et Bertrand avec qui j'ai eu grand plaisir à travailler. Un grand merci également à tous les membres de l'équipe Exozodi que je n'ai pas encore cités : Steve, Virginie, Julien(s), Quentin, Amy, pour les nombreux échanges que nous avons eus depuis le début du projet.

Cette thèse est rédigée partiellement en anglais et partiellement en français. Les parties introductives et les conclusions sont présentées dans la langue de Jules Verne tandis que mes projets de recherche le sont dans la langue d'Isaac Asimov. Il me paraît en effet important que la Science continue à s'écrire en français, mais tout à la fois que les travaux de recherche soient accessibles à travers le monde. J'espère que les lecteurs s'accommoderont de ce choix !

Cette digression me donne l'occasion d'une transition : *I sincerely acknowledge Carsten, Rik and Mihkel for the warm welcome they offered me during my visits at the University of Amsterdam.*

À cette étape, mes remerciements prennent fatalement la forme d'un austère listing. J'adresse pourtant individuellement mes remerciements à Wing-Fai, François, Christophe, Aki, Jessica, Carlos, Sasha, Jonty et à tous les membres des équipes DUNES et GASPS. Je remercie Jean-Baptiste, Jean-Philippe et Guillaume pour leur soutien lors de mes missions à Paranal. Merci également à Isabelle, Xavier, Fabien, et à tous les membres de l'équipe FOST et de l'IPAG qui auront contribué à rendre mon expérience agréable et enrichissante.

Une thèse c'est beaucoup de travail, et aussi beaucoup de bons moments. Je remercie les collègues et amis fidèles rencontrés à l'IPAG. Tout d'abord mes camarades de galère depuis le début : Vianney, pour nos interminables discussions sur la physico-chimie des grains (!) Rémi, qui a couru le marathon avec moi du début à la fin, et Fabrice qui incarne la définition de la personne sur qui l'on peut compter ! Je remercie chaleureusement Illya, Alexandre, Nicolas, Florian, Samuel, Julien(s), et tous les thésards, trop nombreux pour être cités individuellement, sans oublier Axel pour nos nombreux débats sur la vie, l'univers et le reste !

Enfin je tiens à adresser mes sentiments chaleureux à mes parents et à ma famille. C'est bien sûr grâce à leur soutien que j'ai eu la chance de poursuivre les études qui m'ont mené jusqu'ici.

Le mot de la fin sera pour mon épouse, Dimitra : merci infiniment de m'avoir supporté (dans tous les sens du terme) pour mon plus grand bonheur pendant toutes ces années somme toute assez éprouvantes, de partager ma vie et d'avoir bien voulu poursuivre l'aventure en Californie !

Résumé

Les disques de débris orbitant dans l'environnement des étoiles proches constituent un indicateur très important des propriétés des systèmes planétaires extra-solaires. Depuis l'espace et au sol, les moyens observationnels actuels permettent de déterminer dans divers domaines de longueurs d'ondes les propriétés spatiales de ces disques et celles des grains de poussières circumstellaires. Cette thèse aborde le sujet de la modélisation des disques de débris, à partir de données fournies par de multiples instruments, en premier lieu les télescopes spatiaux Hubble et Herschel, et les interféromètres infrarouges du VLTI, CHARA, et KIN.

Mes premiers projets ont pris place dans le cadre de deux programmes-clés de l'Observatoire Spatial Herschel dédiés à l'étude des disques circumstellaires autour des étoiles proches. Au sein du projet GASPS, j'ai obtenu des observations spectro-photométriques de HD 181327, une jeune étoile (12^{+8}_{-4} millions d'années, Ma) de type solaire entourée d'un anneau de débris massif de 90 unités astronomique (UA) de rayon vu aussi en lumière diffusée par le télescope spatial Hubble. La bonne détermination de la géométrie de l'anneau permet de se concentrer sur la modélisation de la distribution spectrale d'énergie, afin de mieux caractériser les propriétés des poussières. J'ai utilisé le code de transfert radiatif GRaTer et démontré que le système héberge une population de planétésimaux glacés, qui pourrait représenter une source d'eau et de volatils susceptible d'être libérée sur des planètes telluriques encore en formation. Je discute quelques résultats additionnels obtenus avec Herschel à propos de disques de débris jeunes, notamment HD 32297, et d'analogues faibles de la Ceinture de Kuiper.

Les disques exo-zodiacaux (exozodis), analogues du nuage Zodiacal du Système Solaire, représentent une contrepartie chaude (ou tiède) aux disques de débris, résidant proche de la zone habitable (moins de quelques unités astronomiques) et encore mal connue. Ils sont révélés par leur émission proche et moyen infrarouge et peuvent être étudiés avec la précision et la résolution requises grace à l'interférométrie optique. Dans le cas de l'étoile β Pictoris (12^{+8}_{-4} Ma), dont le disque est vu par la tranche, une fraction significative du disque externe diffuse de la lumière vers le champ de vue des interféromètres ; une composante interne chaude doit tout de même être invoquée pour justifier de l'excès mesuré dans l'infrarouge proche. En m'appuyant sur l'exemple de l'étoile Véga (440 ± 40 Ma), je présente la méthodologie employée et démontre que les exozodis chauds se caractérisent par une abondance de poussières sub-microniques, près de la distance de sublimation de l'étoile. D'un point de vue théorique, le mécanisme de production de ces petits grains non-liés est encore incompris. J'aborde plus en détails le cas du disque exozodiacal à deux composantes (chaude et tiède) de Fomalhaut (440 ± 40 Ma). Je développe une nouvelle méthode de calcul des distances de sublimation et recense les processus variés qui peuvent affecter un grain de poussière afin de fournir un cadre pour l'interprétation : l'exozodi chaud à $\sim 0.1 - 0.2$ UA serait la signature indirecte d'une ceinture d'astéroïdes située à ~ 2 UA à l'activité dynamique particulièrement intense.

Finalement, je dresse un bilan des propriétés des disques de débris et de ce qu'ils peuvent nous apprendre quand on les compare au Système Solaire, et propose de futures directions de recherche pour explorer davantage les systèmes planétaires et leur dynamique.

Abstract

Observations and Modelling of planetary systems around nearby stars

Debris disks orbiting in the environment of nearby stars are a very important indicator of extrasolar planetary system properties. From space and from the ground, current observational facilities enable a multi-wavelength determination of the disk structures and of the dust properties. This thesis addresses the topic of debris disk modelling, based on data from multiple instruments including first of all the Herschel and Hubble space telescopes, and the VLTI, CHARA and KIN infrared interferometers.

My first research projects took place in the framework of two key programs from the Herschel Space Observatory dedicated to the study of circumstellar disks around nearby stars. As part of the GASPS project, I obtained Herschel far-infrared spectro-photometric observations of HD 181327, a young (12^{+8}_{-4} Myr) Sun-like star surrounded by a massive, 90 AU-wide debris belt, also imaged in scattered light by the Hubble Space Telescope. Proper determination of the belt geometry allows one to focus on modelling the dust properties. I used the GRaTer radiative transfer code to demonstrate that the system hosts a population of icy planetesimals that may be a source for the future delivery of water and volatiles onto forming terrestrial planets. I discuss additional results obtained with Herschel related to young debris disks, in particular HD 32297, and to faint Kuiper-Belt analogues.

Exo-zodiacal disks (exozodis), those analogues to the Solar System Zodiacal cloud, represent a little known hot (or warm) counterpart of debris disks located close the habitable zone (inside of a few AUs). They are revealed by their near- to mid-infrared emission and can be assessed with the required accuracy and resolution with optical interferometers. In the case of the near edge-on star β Pictoris (12^{+8}_{-4} Myr), I show that a significant fraction of the outer disk scatters light towards the small field-of-view of the interferometers; an inner hot component must nonetheless be invoked to explain the measured near-infrared excess. Based on the example of the star Vega (440 ± 40 Myr), I introduce a methodology to study inner dust disks and I show that hot exozodis are characterized by an abundance of submicron-sized grains, close to the star's sublimation distance. From a theoretical point-of-view, the production mechanism for these small, unbound grains is not understood. I go into more details on the case of the Fomalhaut (440 ± 40 Myr) double-component (warm and hot) exozodiacal disk. I develop a new model for the calculation of the dust sublimation distances, and I address the various processes that can affect a dust grain in order to provide a framework for interpreting the exozodi: the hot exozodiacal disk may be the indirect signature of an asteroid belt with a particularly high dynamical activity.

Lastly I draw up a summary of the properties of dusty debris disks and of what they can teach us when compared to the Solar System. I propose possible future research directions for further investigations of planetary systems and their dynamics.

Table des matières

1 Introduction 9
1.1 L'ère des exoplanètes 10
1.2 Les débris du Système Solaire 12
1.3 Des systèmes planétaires poussiéreux 15
1.4 Apport du travail de thèse 21

2 Théorie des disques de débris 23
2.1 Introduction 24
2.2 Dynamique d'un grain de poussière 24
2.3 Equilibre d'un disque de poussière 28
2.4 Optique des grains 31
2.5 Le code GRaTer 35

3 Herschel's view of debris disks 41
3.1 An icy Kuiper belt around the young solar-type star HD 181327 42
3.2 More results from Herschel on cold debris disks 75
3.3 Conclusion 81

4 The Origin of Exozodiacal dust 83
4.1 The inner regions of nearby debris disks 84
4.2 Observing exozodiacal disks with long-baseline interferometry 86
4.3 Warm and hot dust around Fomalhaut: nulling interferometry and modelling 94
4.4 The peculiar case of the edge-on star β Pictoris 120

5 Toward a better understanding of inner debris disks 131
5.1 Introduction 131
5.2 A schematic exozodiacal disk model 133
5.3 Dust sublimation model 136
5.4 Application and results 143
5.5 Origin of the dust 153
5.6 Discussion 162
5.7 Conclusion 164

6 Conclusions et perspectives futures 167
6.1 De la nature de la matière planétaire extrasolaire 168
6.2 Vers des études dynamiques et collisionnelles 172
6.3 Vers des systèmes planétaires semblables au Système Solaire 177

A Deep near-infrared interferometric search for low-mass companions around β Pictoris 179

B Complements to Chapter 5 185
B.1 Maximum mass flux under PR drag and collisions 185
B.2 The blowout timescale 186
B.3 Bayesian probability curves 187

C Dynamical simulations of β Pictoris 191

Chapitre 1

Introduction

The stars, like dust, encircle me
In the living mists of light
And all of space I seem to see
In one vast burst of sight.

Isaac Asimov, *The Stars, Like Dust*, 1951

L'Astrophysique est souvent subdivisée en deux branches : l'Astrophysique Galactique et l'Astrophysique Extra-Galactique. Mon travail s'inscrit dans le contexte de l'Astrophysique Galactique et de ce fait appartient à un champ d'étude où l'axe temporel n'est que rarement évoqué. A quelques millénaires près, quelques décennies quand on parle des *étoiles du voisinage du Soleil* comme je le ferai au long de ce manuscript, c'est bien l'état présent des systèmes planétaires que nous pouvons observer. En sondant des étoiles d'âges et de types spectraux variés, nous assistons en direct à la formation et à l'évolution des systèmes planétaires. Je me suis intéressé au cours de ma thèse à un élément particulier des systèmes planétaires : les disques de débris, ces analogues des ceintures d'astéroïdes et d'objets glacés du Système Solaire révélés autour d'un grand nombre d'étoiles proches. Dans ce premier chapitre, je mets en évidence l'importance des disques de débris au sein des systèmes planétaires. Je présenterai en chapitre 2 les notions théoriques élémentaires nécessaires à l'étude de ces objets. Les chapitres 3 à 5, rédigés en langue anglaise, présentent les projets de recherche que j'ai conduits au cours de ma thèse, autour des disques froids observés par l'Observatoire Spatial Herschel (Chapitre 3), puis des disques chauds (exo-zodiacaux) révélés par l'interférométrie optique (Chapitres 4 et 5). Enfin au Chapitre 6 je présenterai quelques conclusions et les futures perspectives de recherches qui semblent déjà se dessiner.

1.1 L'ère des exoplanètes

S'il est un problème astrophysique qui mobilise les opinions, c'est bien l'existence de planètes extrasolaires. La volonté ancestrale de déterminer l'existence d'autres mondes que la Terre doit faire face à de profondes indéterminations. L'infinité apparente d'étoiles qui peuplent l'Univers offre autant de réalisations possibles de la formation planétaire, mais combien ont mené à des conditions propices à l'apparition de la vie ? L'histoire de la Terre et du Système Solaire est-elle à ce point unique que la Terre serait le seul endroit dans l'Univers où une vie complexe à pu se développer ? Ce n'est que depuis un petit nombre d'années que la recherche en astrophysique peut se targuer d'apporter des éclairages sur cette problématique.

C'est ainsi par l'angle de l'*Exoplanétologie* que j'ai l'habitude d'introduire mon travail de thèse. 925, c'est le nombre de planètes extrasolaires confirmées à l'heure du dépôt de ce manuscript [1]. Les premières exoplanètes détectées depuis la découverte historique de 51 Pegase b par Mayor & Queloz (1995) ont donné aux systèmes extrasolaires la réputation d'être très différents du Système Solaire. Les découvertes de Jupiters chauds, de planètes en orbites très excentriques, ou d'autres à des distances se comptant en centaines d'unités astronomiques (UA), ont entrainé de conséquentes révisions des modèles de formation planétaire préexistants. Les développements réçents convergent peu à peu vers une représentation plus familière de l'environnement des étoiles proches.

La précision atteinte par la méthode des vitesses radiales permet d'accéder à des planètes atteignant quelques masses terrestres seulement, de les suivre sur plusieurs périodes orbitales et de s'affranchir des biais de détection. On accéde ainsi déjà à une information statistique sur les exoplanètes de la Voie Lactée (Figure 1.1 à gauche). Les derniers résultats obtenus grâce au spectromètre HARPS montrent que 50% des étoiles de type solaire arborent au moins une planète de période orbitale inférieure à 100 jours (Mayor

---

[1] The Extrasolar Planets Encyclopaedia, Jean Schneider, `http://exoplanet.eu/`

et al. 2011). Plus remarquable encore, une étude portant sur les exoplanètes orbitant des étoiles de type M (Bonfils et al. 2011), les plus "faciles" à détecter, rapporte que $41^{+54}_{-23}\%$ possèdent une Super-Terre dans la *Zone Habitable* (ou "HZ", notion définie en détails par Selsis et al. 2007).

Ces tendances statistiques se retrouvent aussi dans les populations d'exoplanètes observées jusqu'à des rayons de 0.5 $R_\oplus$ par le télescope spatial Kepler qui a mis au jour pas moins de 2740 candidats exoplanètes (Batalha & Kepler Team 2012). La majorité de ces candidats sont plus petits que Neptune, et plus d'un tiers appartiennent à des systèmes de planètes multiples (Lissauer et al. 2011b, Figure 1.1 à droite), le record étant détenu par Kepler 11 et son système de 6 planètes (Lissauer et al. 2011a). Une extrapolation de la statistique aux périodes longues suggère que la fréquence des planètes telluriques dans la zone habitable des étoiles de type solaire (FGK) serait de $2 \pm 1\%$ à $34 \pm 14\%$ selon les auteurs (Catanzarite & Shao 2011; Traub 2012, respectivement) et on mesure également que les planètes internes sont le plus souvent moins massives que les planètes externes (Ciardi et al. 2012).

Ces systèmes multiples ont par ailleurs la particularité d'être dynamiquement stables, comme le suggèrent les faibles excentricités et inclinaisons orbitales mesurées pour la majorité des planètes à transits observées (Lissauer et al. 2011b), ou encore des simulations dynamiques conduites sur des objets individuels (par exemple Beust et al. 2008). Ainsi on découvre des systèmes planétaires de plus en plus similaires au Système Solaire.

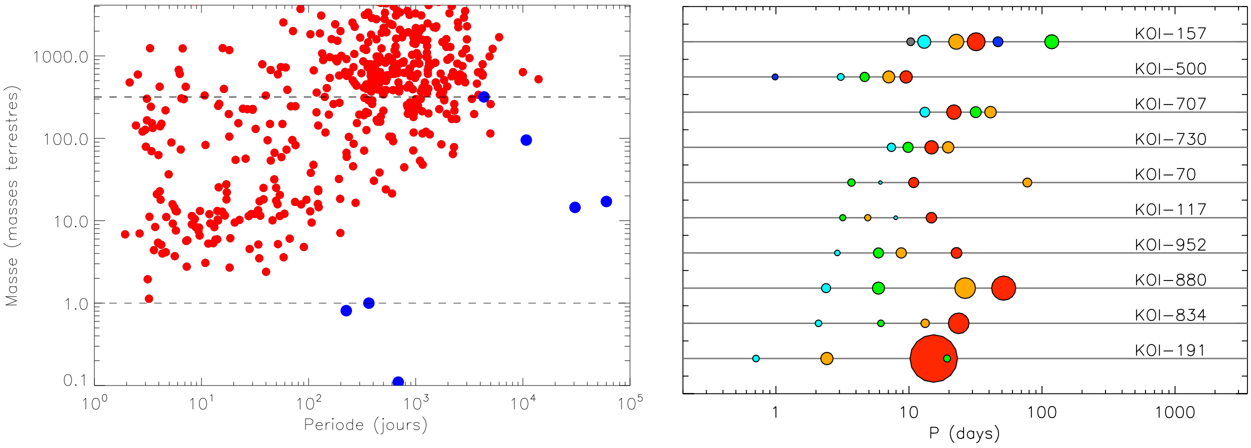

FIGURE 1.1: **À gauche** : Diagramme masse-période comprenant l'ensemble des planètes détectées par vélocimétrie toutes étoiles confondues (point rouge) : la majorité sont des étoiles de type solaire (données NASA Exoplanet Archive). Les points bleus indiquent les planètes du Système Solaire (à l'exception de Mercure). Les traits horizontaux marquent la masse de la Terre et de Jupiter. **A droite** : Systèmes de 4 à 6 planètes détectés par Kepler. La taille de chaque point est proportionnelle à la taille de la planète. Il existe 115 étoiles cibles comprenant deux candidats planètes, 45 en comprenant trois, 8 en comprenant quatre, 1 en comprenant cinq et 1 en comprenant six (Lissauer et al. 2011b).

1.2 Les débris du Système Solaire

Les systèmes planétaires ne sauraient se réduire à leurs seules planètes. Ainsi, le Système Solaire est caractérisé par plusieurs populations de planétésimaux : astéroïdes, comètes (Fig. 1.3) et planètes naines, qui peuplent le plan de l'écliptique conjointement à ses huit planètes (Figure 1.2).

La Ceinture Principale d'Astéroïdes, située entre les orbites de Mars et de Jupiter essentiellement entre 2,2 et 3,2 UA, comprend plusieurs millions de planétésimaux d'une taille supérieure au kilomètre (Tedesco & Desert 2002), pour une masse totale estimée à $6 \times 10^{-4}\, M_{\oplus}$. Elle contient des objets embrassant une large gamme de tailles, depuis la dimension de la planète naine Cérès (qui représente un tiers de la masse de la ceinture) jusqu'aux particules de poussières de dimensions microscopiques. On retrouve ces dernières dans l'environnement de la Terre sous forme de poussière zodiacale — sujet que l'on présentera plus en détail dans le chapitre 4. Les astéroïdes sont pour la majorité composés de matériaux carbonés dans les régions externes de la ceinture, de silicates dans les régions plus internes, tandis qu'une minorité est enrichie en métaux (DeMeo et al. 2009). Ayant cessé leur différentiation et leur évolution très tôt après leur formation, ils nous renseignent sur les conditions physiques qui prévalaient dans les premiers instants du Système Solaire quelques millions à dizaines de millions d'années après sa naissance. Tandis que l'accrétion des planètes se déroulait, les perturbations dynamiques infligées par les résonances de moyen-mouvement avec Jupiter ont freiné la croissance des embryons planétaires, on les retrouve aujourd'hui sous la forme de planétésimaux qui constituent ainsi des reliques de la formation planétaire. Au delà, partageant l'orbite de la planète Jupiter, se trouvent les astéroïdes troyens. Capturés aux points de Lagrange L4 et L5 de la planète, ils sont quelques milliers à être catalogués. On dénombre également quelques troyens dans le sillage des orbites de la Terre, de Mars et de Neptune. Entre Jupiter et Neptune, c'est le domaine des Centaures : des astéroïdes glacés évoluant sur des orbites chaotiques.

Au delà de l'orbite de Neptune, dans les régions plus froides du Système Solaire où la densité du disque protoplanétaire était trop faible pour accréter la matière efficacement, s'étend la ceinture de Kuiper (ou d'Edgeworth-Kuiper, "EKB"). Elle comprend plusieurs planètes naines : le système Pluton-Charon, Eris, Make-Make et Haumea ; un nombre estimé à au moins 70 000 objets d'un diamètre supérieur à 100 kilomètres, et jusqu'à 10^{10} objets de type cométaire, pour une masse totale de l'ordre de $0,1\, M_{\oplus}$. On distingue tout d'abord la famille des objets classiques de la Ceinture de Kuiper ("classical KBOs") entre 40 et 47 UA, cerclés par les résonances de premier ordre avec Neptune où s'accumulent les KBO résonnants. Cette population est dite dynamiquement froide et se caractérise par des excentricités faibles ($e \lesssim 0,2$), des inclinaisons inférieures à 10 degrés et des orbites stables sur des échelles de temps de l'ordre du milliard d'années. Les objets épars de la ceinture de Kuiper se définissent en revanche par des excentrités élevées ($e = 0,2 - 0,8$) et des inclinaisons orbitales atteignant 30 degrés. Leur périhélie s'étend de 30 à 40 UA ce qui les distingue des objets de Kuiper détachés dont le périhélie dépasse 40 UA. Ces deux familles d'objets constituent une population peu dense et dynamiquement chaude qui peut atteindre des distances de plus de mille UA. Enfin, aux confins du Système Solaire entre quelques dizaines et quelques centaines de milliers d'UA, on prédit de l'analyse des orbites des comètes à longues périodes l'existence du nuage d'Oort qui pourrait inclure quelques 10^{11} à 10^{12} corps kilométriques glacés et avoisinerait près d'une masse terrestre (Stern 2003).

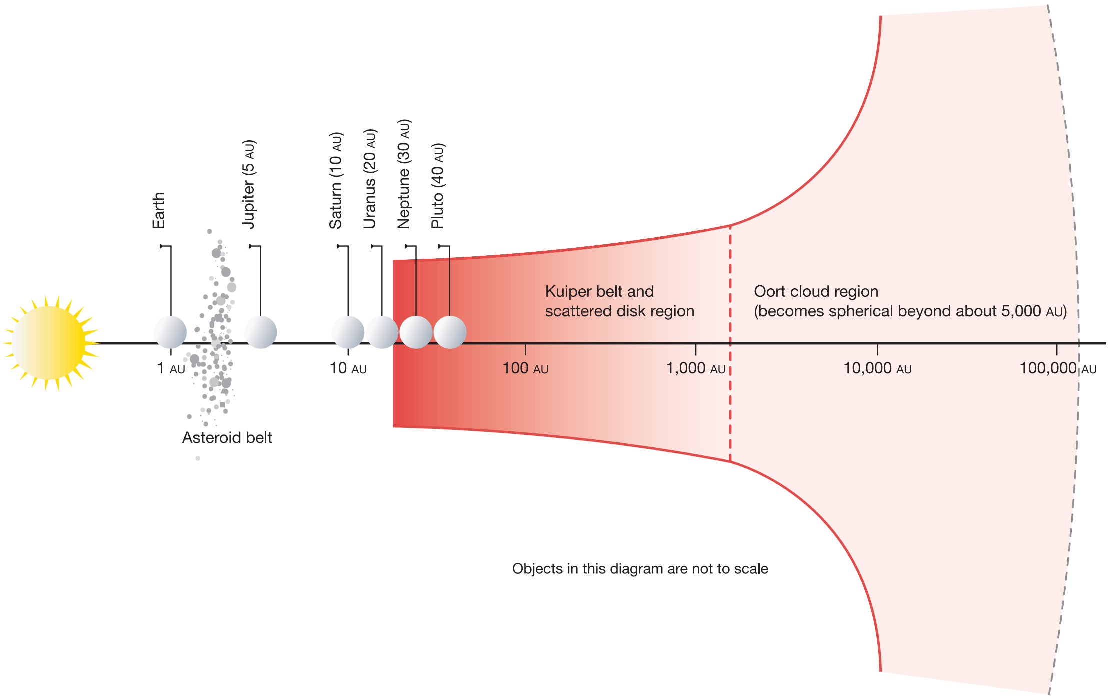

Figure 1.2: Diagramme montrant les différentes populations de débris du Système Solaire : Ceinture Principale d'Astéroïdes, Ceinture de Kuiper, et Nuage d'Oort, en représentation logarithmique (Stern 2003).

Longtemps demeurée une prédiction théorique découlant de l'observation des comètes à courte période lors de leur passage dans le voisinage de la Terre, la ceinture de Kuiper est aujourd'hui accessible à des observations directes et constitue un riche champ de recherche (voir par exemple l'article de revue de Jewitt 2010). Elle est le principal réservoir des comètes à courte période qui peuvent faire l'objet d'observations rapprochées et de collectes d'échantillons par des sondes spatiales. Ce fut le cas par exemple des comètes de Halley, Tempel 1 et Wild 2 qui ont été visitées notamment par les sondes Giotto, Deep Impact et Stardust. Avec des températures de l'ordre de 30 à 60 kelvins, les KBO sont riches en matériaux volatils : glace d'eau, de méthane, d'ammoniac (Jewitt 2010). Le télescope spatial Herschel a par exemple récemment révélé la présence de glaces d'eau à la surface d'Orcus : elles représenteraient 23% de la masse du Plutino, qui s'avère par ailleurs être doté d'une structure à 10% poreuse (Delsanti et al. 2010) : une composition analogue à celle trouvée pour plusieurs ceintures de Kuiper extrasolaires (notamment HD 181327, voir chapitre 3).

Les planétésimaux ont une contrepartie poussièreuse qui peut être détectée *in situ* par les sondes interplanétaires visitant les régions transneptuniennes. Aini la sonde américaine New Horizons fournit des mesures de la densité de poussières dans la ceinture de Kuiper interne (Poppe et al. 2010; Vitense et al. 2012). Après sa visite du système Charon-Pluton la sonde prendra la direction d'un ou plusieurs objets de la ceinture de Kuiper. L'ensemble, dont une représentation d'artiste est donnée en Figure 1.4 est de fait désigné sous le terme de *disque de débris*. Lorsque les comètes s'évaporent, ou par suite de l'érosion infligée aux planétésimaux lors de collisions occasionnelles, des fragments de plus petites tailles sont produits et entretiennent à leur tour la production de particules atteignant le domaine des *poussières interplanétaires*. Celles-ci sont directement accessibles aux expérimentateurs terrestres. La Lumière Zodiacale, que l'on peut observer à l'oeil nu par une nuit suffisamment profonde, fournit une observation directe du nuage de poussières dans lequel la Terre est littéralement plongée. Ainsi chaque jour, pas moins de 100 tonnes de particules de moins de quelques millimètres traversent l'atmosphère de notre planète. Récoltées dans la haute asmosphère ou sur les glaces de l'Antarctique, ces poussières procurent une mesure directe de la composition des planétésimaux qui en sont à l'origine.

Les grains de poussière diffusent et rayonnent efficacement le flux solaire incident. La quantité de poussière mesurée par les sondes spatiales voyageant dans le Système Solaire externe se traduit par une profondeur optique verticale estimée à environ 10^{-7} (Jewitt & Luu 2000; Vitense et al. 2012) qui, rapportée à la surface de la ceinture, en fait l'objet le plus brillant du Système Solaire dans l'infrarouge lointain, après le Soleil. Observé depuis une étoile proche, notre disque de débris tomberait néanmoins sous les limites de détection des instruments actuels. Cependant, l'astrophysique observationnelle récente a révélé l'existence d'objets analogues à la Ceinture de Kuiper évoluant autour d'étoiles proches du Soleil, si massifs que leur profondeur optique peut atteindre 10^{-4} à 10^{-3} les rendant accessibles aux télescopes modernes. Les disques de débris, préservés dans les régions froides des systèmes extrasolaires, représentent des fossiles des phases précoces de leur histoire et peuvent fournir des informations cruciales sur les systèmes planètaires sous-jaçents.

Figure 1.3: **A gauche** : L'astéroïde Itokawa, avec sa dimension de quelques centaines de mètres, photographié en 2005 par la sonde Hayabusa (JAXA) révélant une structure morcelée plutôt que de roche solide (ou "rubble-pile", Fujiwara et al. 2006). **A droite** : noyau glacé de la comète P/Tempel 1 (quelques dizaines de kilomètres) vu par la sonde Deep Impact (NASA) en 2005 et dont la surface s'avère recouverte de poussières très fines (Richardson et al. 2007, par exemple).

1.3 Des systèmes planétaires poussiéreux

1.3.1 Naissance des disques de débris

Il est bien établi que les systèmes planétaires prennent naissance dans les *disques protoplanétaires*, des disques de gaz et de poussières massifs ($\sim 10^{-2}\, M_{\odot}$) faisant suite à la phase d'effondrement de la nébuleuse protostellaire, où le rapport massique gaz sur poussière est d'environ 100. Rapidement des processus de dissipation : accrétion visqueuse, photo-évaporation, vents et pression de radiation, érodent le disque en un temps caractéristique de moins de 10 millions d'années. Dans le même temps, les poussières du disque circumstellaire, initialement de taille inférieure au micromètre, s'agglomèrent pour former des corps solides de tailles croissantes, transférant ainsi la masse vers les futurs planétésimaux. Le gaz s'accumule pour former les planètes géantes, soit par accrétion sur les protoplanètes solides ("core accretion model"), soit par la fragmentation du disque de gaz par instabilité gravitationnelle (Armitage 2009). Ces processus sont l'objet d'étude du programme clé GASPS de l'observatoire spatial Herschel que j'introduirai dans le chapitre 3. Lorsqu'une étoile rejoint la Séquence Principale, le disque de poussières a cédé la place à des planètes et des planétésimaux au sein desquels la formation des planètes rocheuses peut se poursuivre jusqu'à 10^8 années.

L'observation de l'environnement des étoiles jeunes dans l'infrarouge thermique était l'un des objectifs du télescope spatial IRAS (InfraRed Astronomical Satellite), lancé dans le début des années 1980. La découverte de disques de poussières entourant des étoiles de la Séquence Principale était en revanche totalement inattendue.

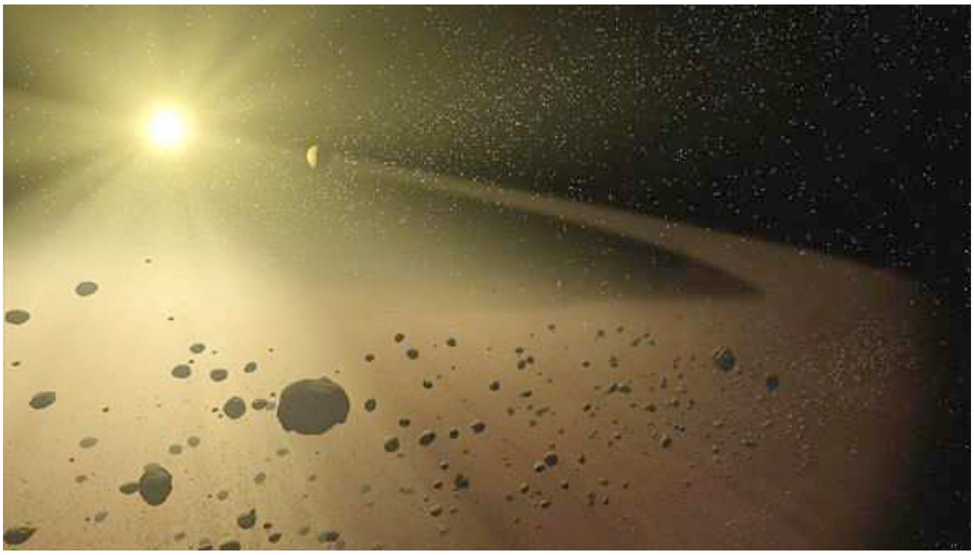

FIGURE 1.4: Représentation d'artiste d'un disque de débris orbitant une étoile similaire au soleil. NASA/JPL-Caltech/T. Pyle (SSC)

1.3.2 Le phénomène Vega

La première découverte est emblématique puisque c'est autour de Vega — qui servait jusqu'alors de calibrateur photométrique — que la présence d'un disque de poussière a pour la première fois été inférée. Ainsi le satellite IRAS a mesuré un excès de flux infrarouge dans le spectre de l'étoile qui a très vite été interprété comme la signature thermique de poussières circumstellaires — on parle alors d'une coquille de poussières (Aumann et al. 1984). Les grains de poussières étant éliminés par l'interaction avec le rayonnement solaire et les collisions destructrices sur des échelles de temps courtes en comparaison de l'âge des étoiles ($10^6 - 10^{10}$ années), les poussières ne peuvent être que de seconde génération (Backman & Paresce 1993). Elles sont le produit d'une cascade collisionnelle prenant départ au sein de populations de planétésimaux analogues à ceux de la Ceinture de Kuiper et qui constituent en ce sens les vestiges de la formation planétaire. Je reviendrai sur la physique qui gouverne les disques de débris dans le chapitre 2 et me concentrerai dans cette section sur les propriétés que l'on retire de leur observation.

Par la suite le "phénomène Véga" s'est révélé être un fait commun dans l'environnement des étoiles proches. 15% des étoiles de type solaire (AFGK) se sont révélées harborer un excès infrarouge (dans les limites de sensibilité d'IRAS) caractéristique de poussières froides dont l'émission thermique domine dans l'infrarouge lointain. De multiples instruments ont été mis à profit pour mieux caractériser ces disques de poussières, notamment depuis l'espace dans l'infrarouge lointain avec l'Infrared Space Observatory (de Muizon 2005), le télescope spatial Spitzer (Beichman et al. 2005b; Tanner et al. 2009) et aujourd'hui l'observatoire spatial Herschel sur lequel je reviendrai au chapitre 3. La figure 1.7 montre les limites de sensibilités de quelques instruments récents et futurs. La grande sensibilité du télescope Herschel porte à $\sim$30% la fréquence des disques autour des étoiles proches (voir chapitre 3). Pour étudier les disques de débris, il est crucial de disposer d'intruments opérant à de multiples longueurs d'onde qui permettent d'observer des populations de poussières embrassant une large gamme de températures. L'information fondamentale fournie par ces instruments est une mesure de la photométrie à différentes longueurs d'onde, qui permet de tracer la distribution spectrale d'énergie (SED) du système, dont un exemple est représenté en Figure 1.5. Une fois soustraite la contribution de l'étoile centrale à partir de modèles de photosphères stellaires aujourd'hui très précis (l'erreur est généralement $\lesssim$ 1% c'est-à-dire inférieure aux incertitudes de calibration photométrique des instruments), on constate que la SED est dominée par *l'émission thermique des poussières*, généralement à partir de 10-20 μm — longueurs d'onde accessibles à Spitzer. Le maximum d'émission se présente généralement autour de 70 - 100 μm — longueurs d'onde accessibles à Herschel — traçant des poussières typiquement $<$ 100 kelvins. Dans le proche infrarouge, il est nécessaire de recourir à des techniques de coronagraphie pour révèler la faible *émission en lumière diffusée des poussières.*

La plupart des disques sont non résolus spatialement, mais la modélisation des SED suggère des ceintures de poussières optiquement fines, constituées majoritairement de grains de l'ordre du micromètre, et qui contiennent typiquement 10^{-3}– 10^{-1} $M_\oplus$ en poussières. Le développement de l'imagerie à haut contraste et haute résolution spatiale fournit aujourd'hui des clichés de ces systèmes planétaires poussièreux depuis les longueurs d'onde visibles en lumière diffusée jusqu'à l'infrarouge proche et lointain puis le domaine millimétrique en émission thermique. Pour ne citer que les plus fameux, les disques de débris de Vega, de Fomalhaut (toutes deux âgées de 440 millions d'années), d'ϵ Eridani (entre 0.1 à 1 milliard d'années), de β Pictoris ou encore de AU Microscopii (toutes deux âgées de seulement 12 millions d'années) figurent parmis les plus étudiés. La figure 1.6 montre une sélection de clichés de disques de débris illustrant quelques propriétés communes mais surtout une grande diversité. Les instruments visibles et proche-infrarouges — déployés au

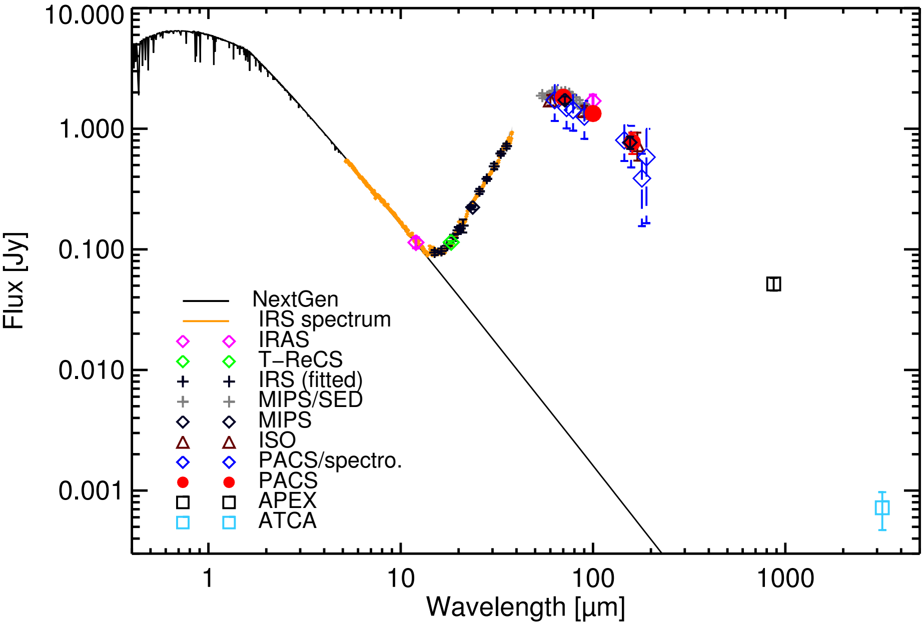

FIGURE 1.5: Exemple de distribution spectrale d'énergie (SED) telle que mesurée par de multiples instruments, ici pour le cas de l'étoile HD 181327 (Lebreton et al. 2012). Le trait plein représente un spectre de photosphère synthétique (NextGen, Hauschildt et al. 1999a). Dans l'infrarouge moyen et lointain, la SED est dominée par l'émission thermique de la poussière. En dessous de 12μm, la SED est dominée par l'émission de l'étoile et la contribution de la poussière en lumière diffusée qui pique dans le visible / proche infrarouge et ne peut être distinguée ($\ll$ 1% du flux stellaire) sans avoir recours à des techniques particulières pour masquer l'étoile centrale.

sol, par exemple avec les systèmes d'optique adaptative du Very Large Telescope (VLT) ou du Keck, ou depuis l'espace avec le Hubble Space Telescope (HST) — offrent l'avantage de la résolution spatiale et peuvent révéler les structures fines des disques observés.

Moyennant une résolution suffisante, l'infrarouge thermique permet d'imager les grains les plus gros (de l'ordre de $\lambda/2\pi$) tout en s'affranchissant de possibles artefacts de soustraction de l'étoile. Des observations complémentaires peuvent être menées dans le millimétrique où les interféromètres — au premier rang desquels ALMA — permettent aujourd'hui d'accéder à des résolutions spatiales comparables au domaine visible. Je reviendrai en outre sur les techniques d'interférométrie optique qui permettent de sonder les régions les plus internes des disques au Chapitre 4.

L'érosion des disques avec le temps entraine une perte de masse — les plus petits corps étant finalement éliminés par différents mécanismes que je détaillerai en section 2. Ceci se traduit par une décroissance (grossièrement linéaire) de la luminosité des disques pour des âges croissants, un phénomème attesté sur des bases aussi bien observationnelles que théoriques (Gaspar et al. 2012; Wyatt 2008; Rieke et al. 2005). Un grand nombre de disques agés de plusieurs centaines de millions d'années sont à l'origine d'un excès infrarouge qui semble incompatible avec une évolution collisionnelle qui aurait perduré pendant tout l'âge des systèmes. Cela amène à introduire la notion de stochasticité : nombre de disques de poussières observés seraient le produit de déséquilibres dynamiques majeurs survenant au sein des planétésimaux, voire de collisions catastrophiques récentes, et représenteraient de fait des phénomènes transitoires détectables pendant seulement quelques millions d'années. Ces objets offrent un sujet d'étude intéressant notamment parce qu'ils favorisent la détectabilité de signatures spectroscopiques émises par les grains sub-microniques produits en abondances lors de collisions. On accède ainsi à la minéralogie des poussières qui fournit une contrainte forte sur leurs tailles et leurs compositions, et par suite une information sur les corps parents et sur la nature des collisions qu'ils ont subies. On citera les exemples d'η Corvi et d'HD 69830 où c'est de la poussière chaude, plus semblable à notre ceinture d'astéroïdes, qui a pu être analysée grace au spectromètre de Spitzer (Lisse et al. 2012; Beichman et al. 2005a, respectivement, voir Chapitre 4).

1.3.3 La trace des planètes dans un disque

La structure spatiale des planétésimaux et par suite des poussières peut être fortement influencée par une possible interaction avec des planètes. L'hypothèse privilégiée pour expliquer les fines structures annulaires fréquemment observées — par exemple pour HR 4796 (Schneider et al. 1999; Lagrange et al. 2012c), HD 181327 (Lebreton et al. 2012, Chapitre 2) ou Fomalhaut (Figure 1.6) — est l'existence de planètes cachées qui creusent l'intérieur des disques en y engendrant une zone d'orbites chaotiques (Wisdom 1980). Les résonances de moyen mouvement entre des planétésimaux et des planètes peuvent créer des motifs assymétriques tels que des "grumeaux" ("clumps") visibles dans le disque de poussières et qui pourraient expliquer certaines structures observées, comme celle de ϵ Eri (Greaves et al. 2005), tandis que des effets séculaires peuvent engendrer une excentricité forcée du disque (Wyatt et al. 1999) ou des structures spirales (Eiroa et al. 2010; Wyatt 2005a), potentiellement détectables dans un disque de poussière collisionnel (Thebault et al. 2012). Dans le cas de Fomalhaut, dont l'anneau de poussière s'avère décentré par rapport à l'étoile, la planète a — par suite de sa prédiction — été détectée à la position prédite dans les images du télescope spatial Hubble (Quillen 2006; Kalas et al. 2005).

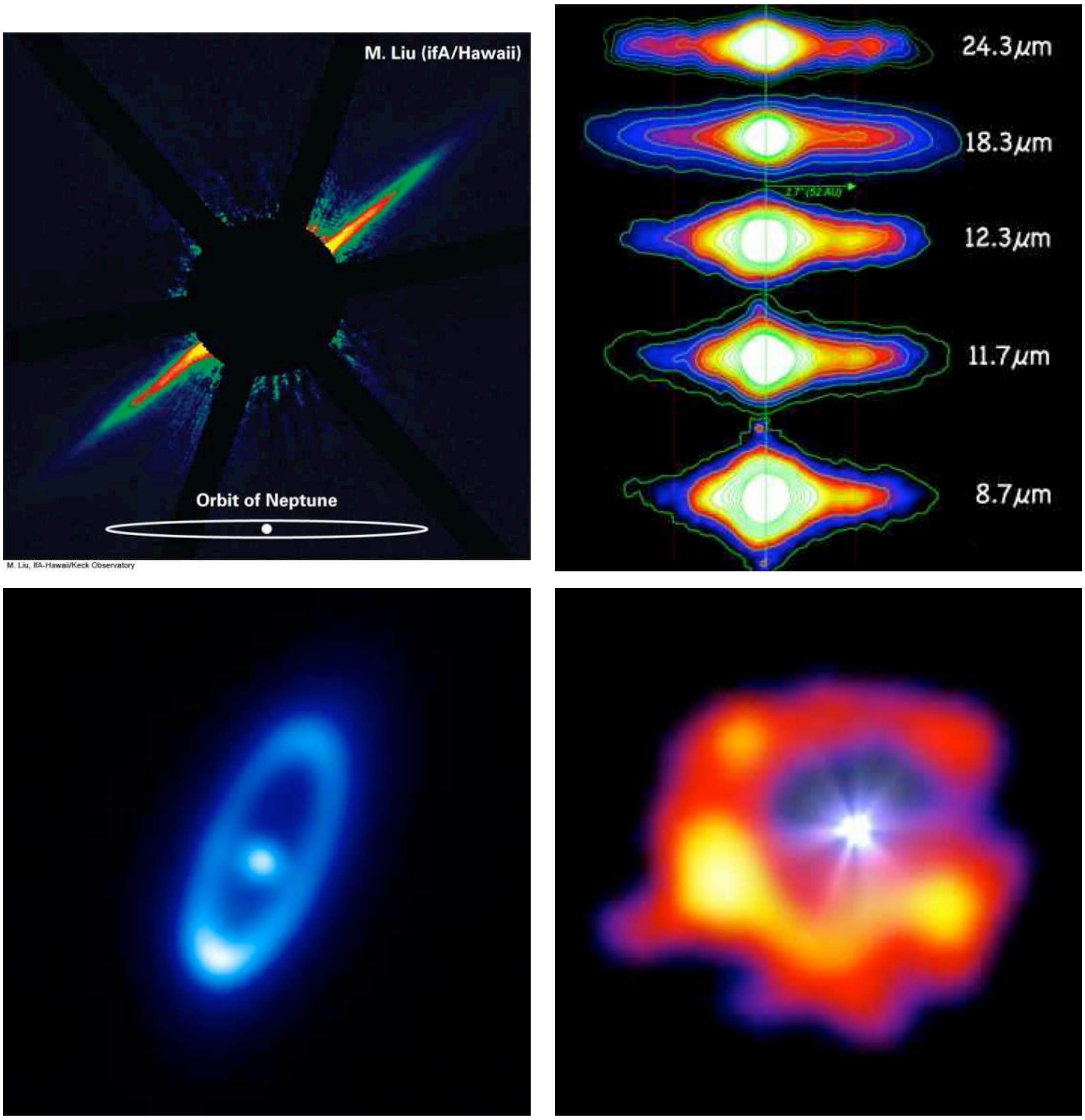

Figure 1.6: Panorama de quelques disques de débris observés à des longueurs d'onde croissantes. **En haut à gauche** : AU Mic vue dans le proche infrarouge (2μm) en optique adaptative au télescope de 10 mètres du Keck (Liu 2004) ; **en haut à droite** : β Pictoris dans le moyen infrarouge (8-24 μm) avec le télescope Gemini South ; **en bas à gauche** : Fomalhaut dans l'infrarouge lointain (70 μm) imagée par l'observatoire spatial Herschel (Acke et al. 2012) et, **en bas à droite** : Espilon Eridani dans le (sub-)millimétrique (850μm) avec le JCMT/SCUBA (Greaves et al. 1998). Les deux premiers ont la particularité d'être vus par la tranche révèlant leur structure verticale, tandis que les deux seconds exhibent leur structure annulaire et des asymétries azimuthales.

Une exoplanète responsable de la déformation du disque de β Pictoris dans ses régions internes (gauchissement, ou ”warp”) a récemment été découverte par imagerie directe avec le Very Large Telescope (VLT Lagrange et al. 2010). Les propriétés de cette planète sont en accord avec les prédictions des modèles basées sur les images résolues du disque de poussière (Mouillet et al. 1997; Augereau et al. 2001). Une structure similaire est observée dans le disque de HD 32297 (Boccaletti et al. 2012) et pourrait être liée à la présence d'une planète.

Par ailleurs, les disques de débris tiennent le rôle de traçeurs de la dynamique planétaire et de l'histoire des systèmes observés. Ainsi les comètes chutant vers β Pictoris (”falling evaporating bodies” Beust & Morbidelli 2000; Thébault & Beust 2001), révélées par des raies d'absorption décalées préférentiellement vers le rouge, permettent de contraindre les paramètres orbitaux de l'exoplanète.

Récemment l'idenfication d'un disque de débris entourant une célèbre étoile à planètes a été annoncée. Gliese 581, naine M déjà bien connue pour son système planétaire de quatre Super-Terres, devra maintenant compter avec une ceinture de Kuiper à 25UA (Lestrade et al. 2012). Celle-ci présente un bord interne net, qui ne peut s'expliquer par l'influence gravitationnelle des planètes connues et laisse présager la détection future d'une planète supplémentaire. On perçoit ainsi que la recherche future devra composer avec des systèmes planétaires de plus en plus similaires au Système Solaire.

1.3.4 Impact des planétésimaux

Si l'on revient un instant sur le cas du Système Solaire, l'histoire des planètes a été fortement marquée par leur interaction avec les ceintures de comètes et d'astéroïdes, en premier lieu pendant la période du Grand Bombardement Tardif (”Late Heavy Bombardment”, LHB). Le LHB est un fait observationnel attesté en premier lieu par la datation des cratères d'impact lunaire. Le modèle de Nice (Gomes et al. 2005) est son pendant théorique, il propose un scénario dynamique complet compatible avec de nombreux indices mesurables. Les éléments-clés du scénario peuvent se résumer comme suit. A une période relativement avancée de l'évolution du système solaire (700 millions d'années), surviennent des perturbations entre Jupiter et Saturne, leurs orbites entrent en résonance. L'orbite de Saturne est déstabilisée et s'approche de celles d'Uranus et Neptune qui à leur tour s'éloignent du Soleil et viennent perturber la jeune ceinture de Kuiper. Les perturbations dynamiques engendrées dispersent la Ceinture de Kuiper primordiale, éjectant la plupart des corps à l'extérieur du Système Solaire — où une partie reste conservée dans le nuage d'Oort —, certains vers les planètes internes qui connaissent alors une multiplication des impacts d'astéroïdes et de comètes. A l'issue de ce processus, la ceinture de Kuiper a perdu 99% de sa masse — limitant plus tard la fréquence des impacts catastrophiques avec la Terre, la configuration orbitale des planètes a été bouleversée, et d'importantes quantités de matériaux volatils ont été transférées jusqu'aux planètes rocheuses.

L'apport tardif de composés volatils vers les planètes internes constitue une piste sérieuse pour expliquer l'abondance de l'eau sur notre planète, malgré qu'elle se soit formée dans des conditions hostiles à son existence. La question est intensément débattue, et des résultats récents semblent désigner les comètes comme la principale source des océans terrestres (Hartogh et al. 2011) ; une solution alternative est que des glaces aient pu être piégées directement dans les grains pendant l'accrétion des planètes internes (Drake 2005).

De même l'apport tardif de molécules organiques sur Terre pourrait avoir eu un impact important sur l'histoire particulière de notre planète.

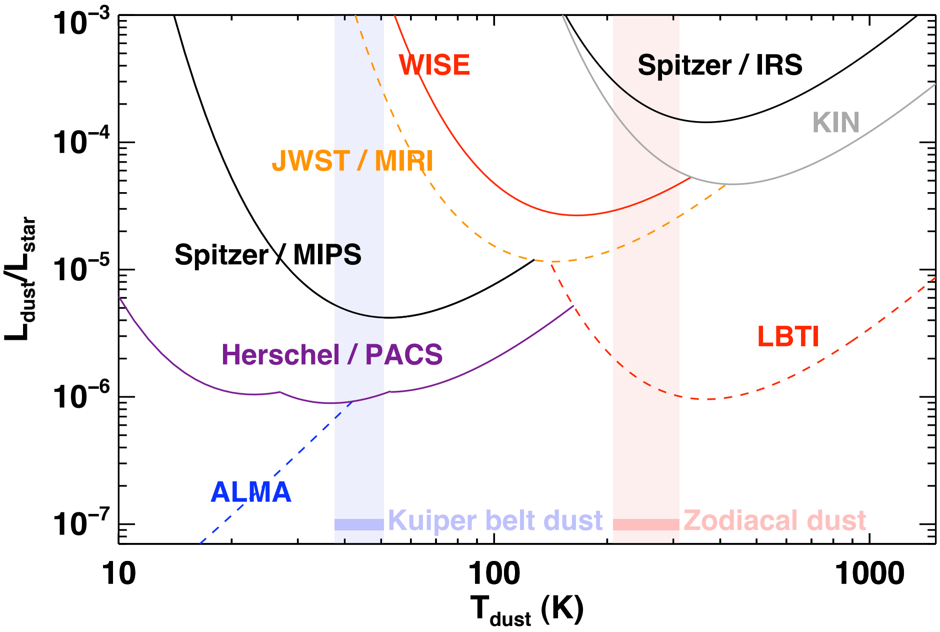

Figure 1.7: Limites de sensibilité de plusieurs instruments récents (Spitzer, WISE, KIN), actuels (Herschel, ALMA) et futurs (LBTI, JWST) à des disques de débris entourant des étoiles proches. La luminosité fractionnaire de la poussière ($L_{\rm dust}/L_\star$) accessible aux instruments est donnée en fonction de la température (à 3σ). Les barres verticales montrent les températures (de corps noir) de la ceinture de Kuiper et de la poussière zodiacale et les traits horizontaux donnent les valeurs de ($L_{\rm dust}/L_\star$) associées.

1.4 Apport du travail de thèse

Durant ma thèse, j'ai été amené à m'intéresser à l'observation, et surtout à la modélisation des disques de débris, à la physique des grains de poussière de manière générale, et plus largement à la formation et à la physique des systèmes planétaires.

Mon projet de thèse traite de la modélisation des disques de débris, qui peut être abordée de différentes manières. Je me suis dans un premier temps intéressé au transfert radiatif et au calcul des propriétés d'émission thermique et de diffusion de grains de poussière. Ces notions seront présentées dans le chapitre 2. J'ai pris en main les outils de modélisation dont nous disposons à l'IPAG, en particulier le code GRaTer destiné à modéliser le transfert radiatif au sein d'un disque de poussière optiquement fin. J'ai travaillé à l'optimisation de ce code, ce qui a permis de le rendre notablement plus performant. J'ai mis en place une méthode d'analyse statistique des résultats facilitant leur interprétation.

Je me suis plus particulièrement investi dans l'étude des disques froids, analogues massifs de la Ceinture de Kuiper, qui font l'objet du Chapitre 3. J'ai pris part à plusieurs projets au sein de deux consortia destinés à l'exploitation des données du télescope spatial Herschel, et ai dirigé une étude détaillée présentée en Sec.3.1. J'y présente des observations Herschel et ATCA du disque entourant l'étoile HD 181327 (β Pictoris Moving Group), qui a la particularité d'être résolue en lumière diffusée (notamment par Hubble) et en émission thermique. Cette information est un atout majeur qui permet de calculer des ajustements de la densité spectrale d'énergie en se concentrant sur les propriétés des grains de poussière, qui constituent la problématique majeure de ce travail.

Le calcul du transfert de rayonnement dans un disque de poussière permet également d'aborder le sujet des disques exozodiacaux qui constitue la deuxième thématique de ma thèse. Ces objets, analogues à la poussière zodiacale ou à la Ceinture Principale d'astéroïdes, sont la contrepartie chaude des disques de débris. Dans le Chapitre 4, je résume l'état de l'art sur les disques chauds et présente les techniques d'interférométrie optique qui permettent d'accéder aux régions les plus internes des disques. J'ai pris en charge la modélisation de 3 objets parmis les plus célèbres : Vega, β Pictoris et Fomalhaut, pour lesquels les interféromètres à longues bases révèlent l'existence de poussières chaudes dans leur proche environnement. Une étude plus approfondie du disque interne de Fomalhaut est enfin présentée en Chapitre 5, où j'entreprends une délicate réconciliation entre les contraintes observationnelles et théoriques.

Je présente enfin les conclusions de cette thèse au chapitre 6, et propose ma vision des sujets et des grandes orientations vers lesquels pourraient se diriger la recherche sur les disques de débris dans le futur proche, tant du point de vue observationnel que de la modélisation.

Chapitre 2

Théorie des disques de débris

2.1 Introduction

Comme nous l'avons vu dans le chapitre précédent, les grains de poussière détectés dans les disques circumstellaires peuvent apporter des informations majeures sur les systèmes planétaires dont ils font partie. Malgré des observations d'une sensibilité et d'une précision toujours croissante, l'interprétation des données requiert une compréhension fine des processus en jeu dans un disque.

A l'échelle individuelle, un grain de poussière subit les contraintes dynamiques imposées par l'étoile centrale. Le cas échéant, s'ajoute l'influence gravitationnelle des planètes qu'il rencontre ; dans ce chapitre, nous nous concentrerons sur les propriétés d'un disque non-perturbé par la présence de planètes. Du fait de leurs faibles dimensions, les grains de poussières ne sont pas uniquement affectés par la dynamique Képlerienne imposée par le corps central, mais subissent les effets de l'impact des photons stellaires (pression de radiation et force de freinage), possiblement ceux des vents stellaires, et une force de friction en présence de gaz éventuel. J'introduirai ces mécanismes en Section. 2.2.

A l'échelle d'un disque, la dynamique globale des grains et leur équilibre collisionnel peuvent se traduire en termes statistiques. On calcule alors des profils de densité théoriques (Sec. 2.3) que l'on peut par suite confronter aux observations.

Le lien entre théorie et observations passe par une étape cruciale : traduire les propriétés du disque en observables astrophysiques. Il est pour cela nécessaire de connaitre avec précision les propriétés optiques d'un grain, puis d'une population de grains, en fonction de la taille, de la composition, et de la configuration géométrique du disque. Si elle est une étape nécessaire à l'interprétation des données, l'étude de la composition des poussières nous renseigne plus profondément sur la nature du matériau à l'origine des planètes, à l'instar des poussières météoritiques dans l'environnement terrestre. Je présenterai en Sec. 2.4 le modèle que j'ai utilisé et perfectionné pour simuler l'absorption et la diffusion de la lumière par un ensemble de particules. Ce chapître s'appuie notamment sur les excellents articles de revue de Krivov (2010); Moro-Martin (2012) et Wyatt (2008).

2.2 Dynamique d'un grain de poussière

2.2.1 Loi de Kepler modifiée

Considérons une particule en orbite à une distance r autour d'une étoile de masse $M_\star$. Supposant sa masse m négligeable devant la masse du corps central, la particule est soumise en premier lieu à une interaction gravitationnelle, dont la norme s'exprime :

$$F_{\mathcal{G}} = -\frac{\mathcal{G}\, M_\star\, m}{r^2} \tag{2.1}$$

où $\mathcal{G}$ désigne la constante gravitationnelle. Cette force est dirigée vers l'étoile.

Dans le cas de particules suffisamment massives, cette seule force suffit à dériver l'équation du mouvement et les lois de Kepler.

Pour des particules tels que des grains de poussière, il devient nécessaire de prendre en compte la force radiale induite par la pression de radiation ("radiation pressure", RP), soit :

$$F_{\mathcal{RP}} = \frac{L_\star \, \langle Q_{\rm pr} \rangle \, \pi a^2}{4\pi \, r^2 \, c} \tag{2.2}$$

où l'on a introduit la luminosité de l'étoile $L_\star$, et la section efficace de pression de radiation moyenne $\pi a^2 \, \langle Q_{\rm pr} \rangle$ pondérée par le flux stellaire [1]. L'effet conjugué de ces deux forces peut se traduire par une force "photogravitationnelle" (Krivov 2010), faisant intervenir le rapport $\beta = \frac{F_{\mathcal{RP}}}{F_{\mathcal{G}}}$, indépendant de la distance à l'étoile, soit :

$$F_{\mathcal{G},\mathcal{RP}} = -\frac{\mathcal{G} M_\star \, (1-\beta) \, m}{r^2} \tag{2.3}$$

En supposant les grains sphériques et homogènes de densité ρ, le rapport $\beta_{\rm pr}$ s'écrit :

$$\beta_{\rm pr}(a) = \frac{3 L_\star}{16 \, \pi \mathcal{G} M_\star \, c} \, \frac{\langle Q_{\rm pr}(a) \rangle}{\rho \, a} \tag{2.4}$$

Du point de vue du grain, tout se passe comme si la masse de l'étoile avait été diminuée d'un facteur $(1-\beta)$. Quelques exemples de rapports β calculés pour plusieurs compositions de poussières représentatives sont présentés en figure 2.1. Par suite chaque grain, caractérisé généralement de manière unique par son rapport β, adopte une dynamique spécifique.

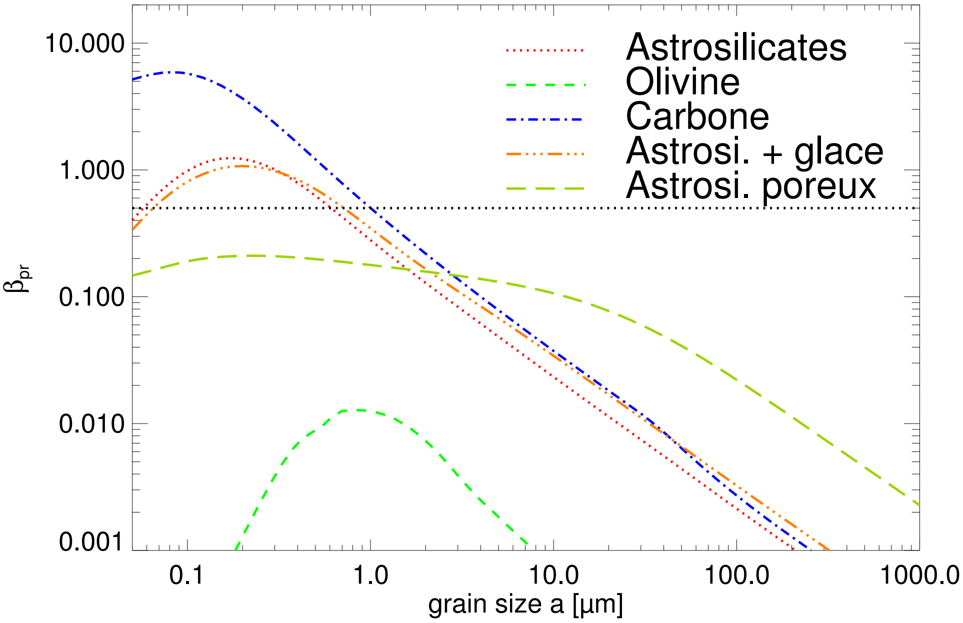

FIGURE 2.1: Correspondance entre la grandeur $\beta = F_{\mathcal{RP}}/F_{\mathcal{G}}$ et la taille de grain pour des particules supposées sphériques et homogènes. On a considéré ici une étoile de masse $M_\star = 1.2 \, M_\odot$, de luminosité $L_\star = 1.6 \, L_\odot$, et plusieurs exemples de compositions représentatifs (voir Sec 2.4). Le trait horizontal marque la limite $\beta = 0.5$ entre grains liés et non-liés pour des orbites initialement circulaires.

---

[1] $Q_{\rm pr} = \int Q_{\rm pr} F_\lambda {\rm d}\lambda / \int F_\lambda {\rm d}\lambda$ avec $Q_{\rm pr}$ l'efficacité de la pression de radiation et F_λ le flux stellaire à la longueur d'onde λ

Ainsi, les éléments orbitaux d'une particule produite à partir d'un corps parent à la position r en orbite Képlerienne, de demi-grand axe A et d'excentricité e s'écrivent :

$$A' = A\,\frac{1-\beta}{1-2A\,\beta/r} \tag{2.5}$$

$$e' = \sqrt{1 - \frac{(1-2A\beta/r)(1-e^2)}{1-\beta^2}} \tag{2.6}$$

Pour évoluer sur une orbite liée, une particule devra satisfaire : $\beta(a) \leq \frac{1-e}{2}$ si elle est produit au périhélie, $\beta(a) \leq \frac{1+e}{2}$ si elle est produite à l'aphélie. On définit alors la taille (rayon) d'éjection $a_{\text{blow}} = a(\beta_{\text{pr}} = 1/2)$ au delà duquel les grains produits sur des orbites initialement circulaires demeurent liés à l'étoile. Les grains plus petits que cette taille critique sont éjectés sur des orbites hyperboliques, à moins d'avoir été produits sur des orbites initialement excentriques et proches de l'aphélie. Au delà de $\beta_{\text{pr}} = 1$, aucune particule ne demeure liée. Des exemples de la fonction $\beta_{\text{pr}}(a)$ sont représentés en figure 2.1 où les propriétés optiques ont été calculées grâce à la théorie de Mie (Sec. 2.4). En fonction du matériau composant le grain et de la masse de l'étoile, il peut exister une population de particules sub-microniques en orbites liées du fait de leur faible efficacité de pression de radiation. La figure 2.2 extraite de Krivov (2010) illustre les différents types d'orbites possibles en fonction du rapport β_{pr}. On voit que la dépendence des orbites avec la taille de grains a pour effet de conserver les plus gros dans l'anneau où ils ont été produits, tandis que seuls les plus petits peuvent peupler les régions plus externes d'un disque de débris.

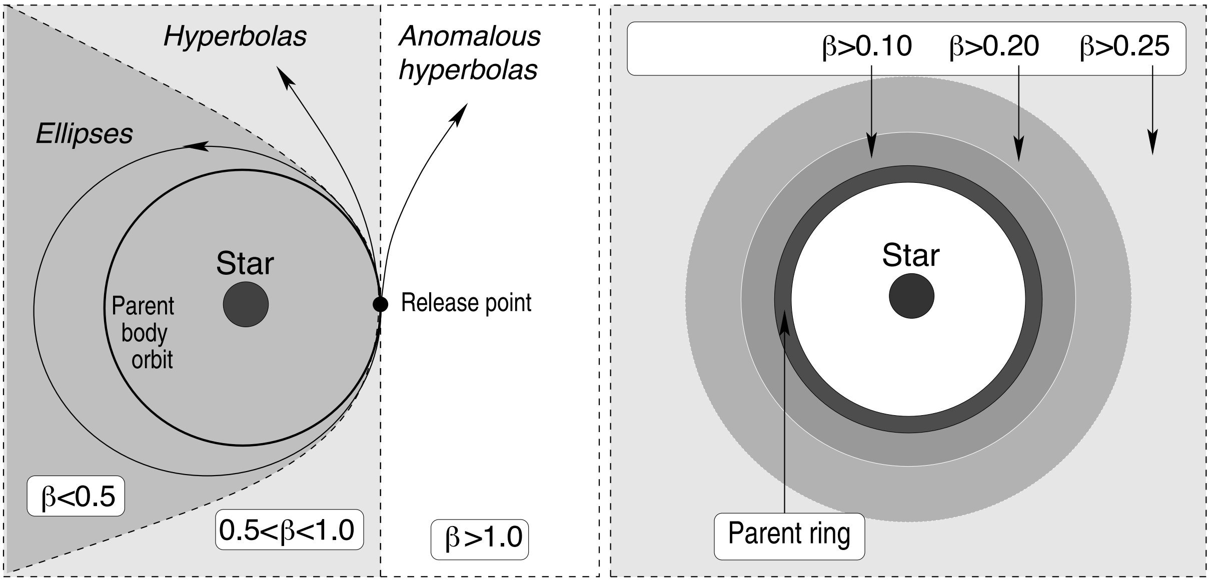

Figure 2.2: A gauche : différents types d'orbites possibles sous l'effet de la force "photo-gravitationnelle", où les particules sont supposées produites sur des orbites initialement circulaires. A droite : représentation schématique de la distribution spatiale des grains produits au sein d'une ceinture de corps parents (d'après Krivov 2010)

2.2.2 Forces de freinage

Effet Poynting-Robertson : En plus de la force radiale exercée par le rayonnement de l'étoile, un grain en mouvement subit une force tangentielle sous l'effet de l'impact des photons, qui engendre une perte progressive de moment cinétique pour le grain et la modification de ses éléments orbitaux avec le temps :

$$\frac{dA}{dt} = -\frac{\beta\mathcal{G}M_\star}{c}\,\frac{2+3e^2}{A(1-e^2)^{3/2}} \tag{2.7}$$

$$\frac{de}{dt} = -\frac{-5\,\beta\mathcal{G}M_\star}{2c}\,\frac{e}{A^2(1-e^2)^{1/2}} \tag{2.8}$$

Ce phénomène, appelé effet Poynting-Robertson (PR), découle de la relavité restreinte et peut s'interpréter comme suit : les photons stellaires se déplacant à une vitesse finie (c), leur angle d'incidence dans le référentiel d'un grain n'est pas orthogonal au vecteur vitesse du grain, mais semblent provenir légèrement de l'avant. Par conséquent, une force de freinage s'exerce sur le grain, qui a pour effet de faire spiraler les particules depuis leur orbite de demi-grand axe r_0 jusqu'à une distance r après un temps dit *temps de Poynting-Robertson* :

$$t_{\mathcal{PR}}(r) = \frac{(r_0 - r)^2\,c}{4\mathcal{G}\,M_\star\beta} \tag{2.9}$$

Vent stellaire : De la même manière que les photons stellaires transfèrent de l'énergie aux grains en orbites, la poussière peut interagir avec un flux de particules. Le vent stellaire est porteur d'une densité de flux d'énergie souvent négligeable en comparaison au flux radiatif : dans le Système Solaire, l'énergie portée par les photons est supérieure à l'énergie portée par les protons de près de 4 ordres de grandeur. En revanche, la faible vitesse des particules chargées comparée aux photons stellaires se traduit par un angle d'incidence important dans leur trajectoire de collision avec un grain, accentuant ainsi la force de freinage exercée dans le sens opposé au mouvement. Ainsi, la force de freinage due au vent stellaire atteint 35% de la force de Poynting-Robertson dans le Système Solaire (Gustafson 1994). Dans le cas d'étoiles de faible masse, cette composante peut devenir dominante du fait des vents stellaires intenses et de la luminosité faible.

Effet du gaz : Par ailleurs, autour des étoiles les plus jeunes les disques peuvent contenir une quantité non-négligeable de gaz ; dans les régions internes de systèmes de tout âge, du gaz peut être produit par la sublimation de la matière sous l'effet de collisions à haute énergie ou de la sublimation — on pensera par exemple au dégazage des comètes à l'approche du périhélie. La théorie prévoit que certaines espèces chimiques peuvent s'accumuler sur de grandes échelles de temps étant peu sensibles aux mécanismes de déplétion par freinage ou pression de radiation. Dès lors, le profil de densité du gaz sera déterminant, conduisant à une pression dirigée soit vers l'extérieur, soit vers l'intérieur du système en fonction du gradient de pression du disque. L'étude du gaz dans les disques de débris demeure à l'heure actuelle peu contrainte par les observations et les modélisations se limitent à quelques étoiles brillantes, notamment β Pictoris (Thébault & Augereau 2005; Krivov et al. 2009) ou HR 4796 (Lyra & Kuchner 2012) ; quelques contraintes sur la présence éventuelle de gaz autour de HD 181327, β Pictoris et Fomalhaut sont discutées dans la suite de ce manuscript.

2.3 Equilibre d'un disque de poussière

2.3.1 Cascade collisionnelle et distribution de tailles

Le bilan des interactions s'exercant sur les poussières permet de calculer les échelles de temps caractéristiques après lesquelles un grain est éliminé de l'environnement de l'étoile. L'action de la pression de radiation a pour conséquence d'éjecter les grains non liés après un temps comparable au temps dynamique $t_{\mathrm{dyn}} = 2\pi\ [A^3/(\mathcal{G}M_{\mathrm{star}}|1-\beta|)]$, soit typiquement $10^2 - 10^4$ années si les grains sont produits à quelques dizaines d'unités astronomiques. De fait, aucun grain inférieur à la taille d'éjection a_{blow} ne peut subsister de manière durable. L'effet Poynting-Robertson quant à lui fait migrer un grain isolé vers l'étoile avec un taux inversement proportionnel à la taille, jusqu'à les élimininer par sublimation. Ce mécanisme s'exerce sur des échelles de temps typiques $t_{\mathrm{PR}} \simeq 1$ Myr.

Ainsi, l'observation de disques de poussières autour d'étoile de la Séquence Principale ($\sim 10^7 - 10^{10}$ ans) conduit à invoquer l'existence d'un mécanisme de production. Les poussières sont produites à partir d'objets plus massifs, qui peuvent atteindre les dimensions des astéroïdes et des comètes formés à la naissance des systèmes considérés. Ces objets ont une durée de vie bien supérieure à l'âge des étoiles, suffisante pour entretenir une *cascade collisionnelle* au cours de laquelle les collisions destructrices occasionnelles produisent des fragments de plus en plus petits qui engendrent à leur tour de nouvelles collisions. Dans le cas idéal, ce processus conduit à une distribution de tailles suivant une loi de puissance (Dohnanyi 1969) :

$$\mathrm{d}n(a) \propto a^{2-3\mathrm{q}}\mathrm{d}a, \tag{2.10}$$

où $q = 11/6$ pour une cascade collisionnelle règnant au sein d'une distribution infinie de tailles de particules. Cette loi en $a^{-3.5}$ est largement indépendante du matériau considéré et montre un très bon accord avec les propriétés des disques de débris couramment déduites des observations comme, nous le verrons tout au long de ce manuscript. Elle s'étend jusqu'aux corps les plus gros comme les planètes naines, bien qu'une déviation significative soit prévue par les simulations collisionnelles — et observée dans le Système Solaire notamment dans les KBO éparses (Shankman et al. 2012) — au délà du kilomètre pour lesquels l'autogravité n'est plus négligeable (Löhne et al. 2008) et l'équilibre collisionnel n'est pas nécessairement atteint (le temps de collision des plus gros corps dépassant l'âge des systèmes considérés). En outre, l'absence de grains plus petits que la taille d'éjection perturbe également l'équilibre collisionnel : l'absence de ces impacteurs entraine une surabondance de grains légèrement plus grand que a_{blow} se traduisant par un motif "en vague" dans la distribution qui se répercute jusqu'aux plus grandes tailles (Thébault & Augereau 2007; Durda & Dermott 1997). La Figure 2.3 illustre la distribution de taille de grains (ici exprimée en masse totale par intervalle de taille de grain) résultant de l'évolution collisionnelle d'une population massive de poussières en orbites autour d'étoiles de différentes masses.

Il est à noter que la force de pression de radiation transporte préférentiellement les plus petits grains vers l'extérieur (voir Fig. 2.2), l'anneau de corps parents pouvant quant à lui être peuplé d'un éventail de tailles de grains. La distribution de tailles devient ainsi plus pentue à l'extérieur de l'anneau-parent. Dans la suite de cette thèse, nous décrirons

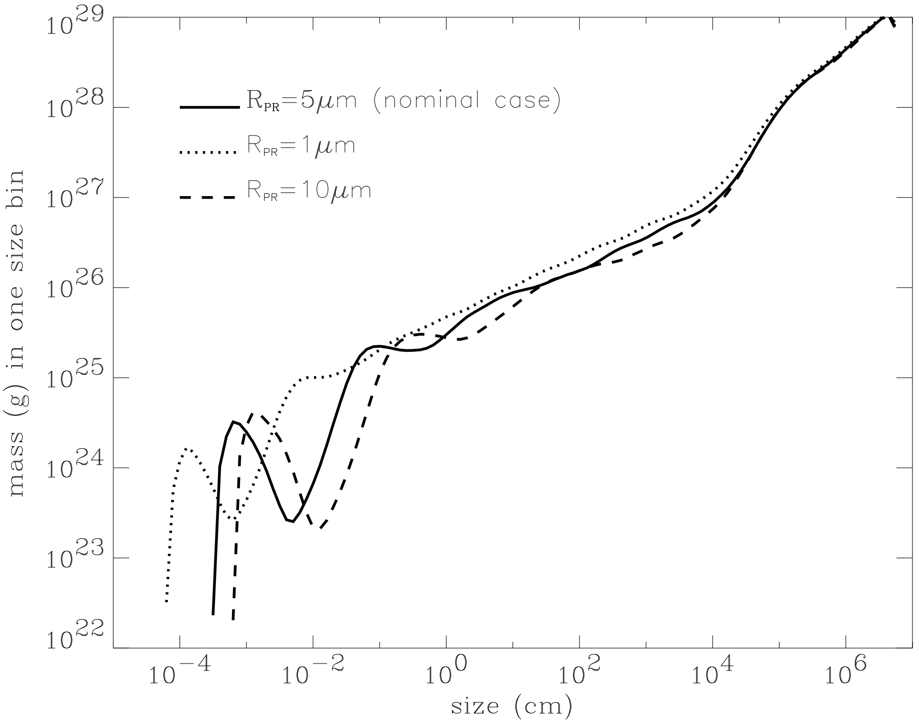

Figure 2.3: Exemples de distributions de la masse totale des grains résultant de l'évolution dynamique et collisionnelle d'un disque de débris massif ($M = 0.1 M_\oplus$ pour $a < 1$ cm) après 10^7 années (Thébault & Augereau 2007). Plusieurs masses stellaires sont testées correspondant à autant de tailles d'éjection, notées ici $R_{\rm PR}$ ($M_\star = 1.7$, 2.1, 2.5 $M_\odot$)

la distribution de tailles de grain par une loi de puissance de pente $\kappa < 0$:

$$\mathrm{d}n(a) \propto a^{\kappa}\,\mathrm{d}a \tag{2.11}$$

Pour $\kappa = -3.5$, la masse du disque est contenue dans les plus corps, mais ce sont les petits grains qui dominent la section efficace du disque. On remarquera que pour $\kappa < -4$, la masse du disque devient dominée par les petits grains, tandis que pour $\kappa > -3$, les grains les plus gros dominent la section efficace.

De cette distribution de tailles découle que les destructions collisionnelles surviennent de manière privilégiée entre grains de même taille ou de taille proche. On montre que l'échelle de temps caractéristique des collisions mutuelles peut s'écrire :

$$t_{\mathrm{col}} = \frac{t_{\mathrm{orb}}}{2\pi\tau_{\perp}}, \tag{2.12}$$

où t_{orb} est la période orbitale et $\tau_{\perp}$ la profondeur optique géométrique verticale à cet endroit. Cette relation définit le *temps de collision* et est valable pour des grains dominant la profondeur optique verticale $\tau_{\perp}$, c'est-à-dire les plus petits grains liés. A cette étape, il est utile de rappeler que la profondeur optique verticale d'un disque optiquement fin est proportionnelle à sa densité de surface et peut être grossièrement approximée par la luminosité fractionnaire $\tau_{\perp} \sim L_{\mathrm{disk}}/L_{\star}$.

2.3.2 Production et pertes, profils de densité

À l'état stationnaire, les propriétés d'un disque de débris sont déterminées par un équilibre entre mécanismes de production et de dépletion. Selon les propriétés de l'étoile centrale et la masse des poussières, un disque peut-être alternativement dominé par les collisions où par les mécanismes de transport (soufflage par pression de radiation et forces de freinage). La plupart des disques détectés jusqu'aujourd'hui sont suffisamment denses pour être dominés par les collisions, mais pour des disques aussi ténus que la ceinture de Kuiper du Système Solaire, les mécanismes de transport deviennent prédominants. Je présente ici les profils de densité radiale attendus pour un disque de poussière en fonction des mécanismes dominants.

Considérons une population de poussière produite à partir d'un anneau de planétésimaux. La migration par PR s'exercant avec un taux constant en masse, elle produit, en l'absence de collisions et compte tenu de la dépendence en β de la vitesse de chute des grains (Eq. 2.9), une densité de surface constante vers l'intérieur de l'anneau (Annexe A de Acke et al. 2012).

A l'inverse, la vitesse des grains éjectés par la pression de radiation étant constante au premier ordre, leur densité de surface décroit lentement avec la distance : $\Sigma(r) \propto r^{-2}$; néanmoins, ces grains ne contribuent que peu à la profondeur optique à l'exception des régions très externes du disque où seuls des grains non liés sont présents (Moro-Martin 2012).

Si l'on considère maintenant un disque dominé par les collisions, et dont la distribution de taille de grains suit la loi en $a^{-3.5}$ à l'endroit de leur production, la dispersion des vitesses induite par la pression de radiation crée naturellement un profil de densité en $r^{-1.5}$ à l'extérieur de l'anneau-parent (voir par exemple Strubbe & Chiang 2006; Thébault

& Augereau 2007; Thébault & Wu 2008).

La densité de surface d'un disque dépend ainsi de l'effet conjugué de ces différents mécanismes. Par la suite, on verra qu'il est commode de paramétriser la densité de surface d'un disque par une double-loi de puissance qui tiendra compte de la dispersion des grains vers l'extérieur et l'intérieur de la population-parent. Notons que l'influence gravitationnelle de potentielles planètes, ou encore des mécanismes hydrodynamiques peuvent avoir un impact crucial sur le profil de densité d'un disque (voir respectivement Thebault et al. (2012); Lyra & Kuchner (2013) et Chapitre 1). En particulier, les perturbations séculaires imposées par une planète (intérieure ou extérieure aux corps parents) peuvent engendrer des disques de forme annulaire et excentriques ; des développements récents indiquent toutefois que l'interaction avec un disque de gaz de masse comparable au disque de poussière pourrait produire des structure similaires.

2.4 Optique des grains

Les différents processus à l'oeuvre au sein d'un disque de débris à l'équilibre déterminent donc ses propriétés géométriques (profils de densité, masse) et les propriétés des grains de poussières (distributions de tailles, compositions), et par suite les temps caractéristiques en jeu. De manière observationnelle, il n'est pas possible de mesurer directement ces quantités : l'interprétation des mesures (SED, images) nécessite la connaissance préalable des propriétés optiques des poussières en présence et la résolution du transfert radiatif au sein du disque.

Les disques de débris sont considérés comme optiquement fins selon toutes les directions (profondeur optique $\ll 1$) et la seule source d'irradiation est supposée être l'étoile centrale. Nous pouvons ainsi négliger les réflexions multiples et le couplage thermique qu'imposerait un disque optiquement épais. En particulier, l'observateur voit à travers toute l'épaisseur du disque, l'ensemble des grains en présence. La problématique est alors de calculer l'équilibre thermique d'une population de poussière et ses efficacités de diffusion et d'absorption/réemission en fonction de la taille et des indices optiques des grains individuels, ce que je présente dans les paragraphes suivants.

2.4.1 Flux diffusé et émis par une poussière

Nous nous intéressons ici à l'interaction d'un grain de poussière avec un rayonnemment incident de longueur d'onde λ. Les grains sont supposés sphériques, homogènes et caractérisés entièrement par leur paramètre de taille $x = \frac{2\pi a}{\lambda}$ (avec a le rayon du grain et λ la longueur d'onde) et leur indice optique complexe $n = n' - i\,n''$ (qui dépend de λ).

Dans la limite des grands paramètres de tailles ($a \gg \lambda$), la section efficace d'interaction d'un grain avec le rayonnement se ramène à sa section efficace géométrique. Pour des grains dont la dimension est comparable à la longueur du rayonnement incident, les propriétés optiques des poussières sont transcrites en termes d'efficacités d'absorption $Q^{\lambda}_{\text{abs}}(x)$, et de diffusion $Q^{\lambda}_{\text{sca}}(x)$ pout tout indice de taille x et indice optique n, ou encore de section efficace d'absorption et de diffusion $\sigma_{\text{abs}} = Q^{\lambda}_{\text{abs}}\pi a^2$ et $\sigma_{\text{sca}} = Q^{\lambda}_{\text{sca}}\pi a^2$.

Soumis au flux stellaire monochromatique $F_\star(\lambda)$ du point de vue de l'observateur situé à une distance $d_\star$ de l'étoile, un grain de poussière de rayon a orbitant à la distance r

émet un flux thermiquement :

$$\Phi_{\mathrm{th}}^{\lambda}(a) = \mathcal{B}_{\lambda}(\mathcal{T}_{\mathrm{g}}) \frac{Q_{\lambda}^{\mathrm{abs}}(a)\, 4\pi a^2}{4\, d_{\star}^2} \tag{2.13}$$

où $\mathcal{B}_{\lambda}(T_{\mathrm{g}})$ est la fonction de Planck à la température $T_{\mathrm{g}}(a, r)$ d'équilibre du grain. Cette dernière est calculée en fonction de la distance en résolvant l'équilibre thermique du grain avec l'étoile, ce qui nécessite d'inverser la fonction :

$$r(a, T_{\mathrm{g}}) = \sqrt{\frac{\int_{\lambda} Q_{\mathrm{abs}} F_{\star}(\lambda) \mathrm{d}\lambda}{\int_{\lambda} Q_{\mathrm{abs}}\, \pi B_{\lambda}(T_{\mathrm{d}}) \mathrm{d}\lambda}} \frac{d_{\star}}{2} \tag{2.14}$$

où d est la distance de l'étoile à l'observateur, ce qui traduit l'équilibre énergétique entre absorption du flux stellaire et ré-émission. Par ailleurs, le grain diffuse dans la direction de l'observateur un flux total :

$$\Phi_{\mathrm{sc}}^{\lambda}(a) = F_{\star}^{\lambda}\, f(\varphi)\, \frac{Q_{\mathrm{sca}}^{\lambda}(a)\, \pi a^2}{r^2}, \tag{2.15}$$

qui englobe les processus de réflexion et de diffraction et met en évidence la diffusion en r^2 du flux incident. Cette expression fait intervenir la fonction de phase $f(\varphi)$ qui mesure l'anisotropie de diffusion et est définie telle que $\int\int_{4\pi} f \mathrm{d}\varphi = 1$, φ désignant l'angle solide entre les directions incidente et diffusée des photons. Dans le cas isotrope, $f(\varphi) = 1/4\pi$.

2.4.2 Calcul des propriétés optiques

Finalement, le rayonnement diffusé et émis thermiquement par un disque de débris est entièrement déterminé par les efficacités d'absorption, de diffusion et la fonction de phase de la population de grains, connaissant la distribution spatiale des poussières.

Ces quantités peuvent être calculées à l'aide de la théorie de Mie (Mie 1908; Bohren & Huffman 1983) qui fournit une solution exacte aux équations de Maxwell. Ce modèle s'applique formellement à des grains sphériques et homogènes. Dans la limite des grand paramètres de tailles, les grains se comportent comme des corps noirs et la théorie de Mie peut-être avantageusement remplacée par les lois de l'optique géométrique ($Q_{\mathrm{abs}}^{\lambda} = 1$, $Q_{\mathrm{sca}}^{\lambda} = 1$). A l'inverse, pour les petits paramètres de taille, la théorie de Rayleigh-Gans fournit une bonne approximation.

Dans la réalité les poussières, aussi bien interstellaires, interplanétaires que circumstellaires, dévient évidemment de la simple hypothèse de grains sphériques et homogènes. Un exemple de grain récolté dans la haute atmosphère terrestre est présenté en figure 2.4, on constate qu'en plus de revêtir la forme d'un aggrégat, il comporte des inclusions de matériaux divers, ce qui complexifie considérablement le calcul de ses propriétés optiques. La théorie de Mie reste une bonne approximation pour des poussières revêtant la forme d'aggrégats de forme proche d'ellipsoïdes, la fonction de phase, de même que la polarisation, étant les plus affectées par une déviation à la symétrie sphérique. En revanche, pour tenir compte de l'hétérogénéité des indices optiques au sein d'un grain, il est nécessaire de recourir à une *théorie des milieux effectifs.*

La théorie de Bruggeman fournit un cadre utile puisqu'elle permet d'obtenir les *indices effectifs* d'un assemblage de matériaux quel que soit leur agencement. Il suffira pour cela de calculer les racines de la permittivité diélectrique $\epsilon_{\mathrm{eff}} = n^2$ pour chaque longueur d'onde considérée, elle-même étant solution de l'équation :

$$f_{\mathrm{v}}\,\frac{\epsilon_1-\epsilon_{\mathrm{eff}}}{\epsilon_1+2\epsilon_{\mathrm{eff}}}+(1-f_{\mathrm{v}})\,\frac{\epsilon_2-\epsilon_{\mathrm{eff}}}{\epsilon_2+2\epsilon_{\mathrm{eff}}}=0 \tag{2.16}$$

où ϵ_1 et ϵ_2 sont les permittivités diéletriques des 2 matériaux, et f_{v} est la fraction volumique occupée par la premier matériau. Dans le cas où plusieurs matériaux sont présents, on pourra appliquer cette méthode de manière itérative pour obtenir l'indice effectif global. Par exemple, une théorie des milieux effectifs pourra servir à calculer l'indice effectif d'un grain composé d'un coeur de silicates et de carbone recouvert d'un manteau de glace. On pourra également calculer les propriétés d'un grain poreux en incluant du vide, c'est-à-dire un matériau d'indice optique nul (voir en particulier le Chapitre 3).

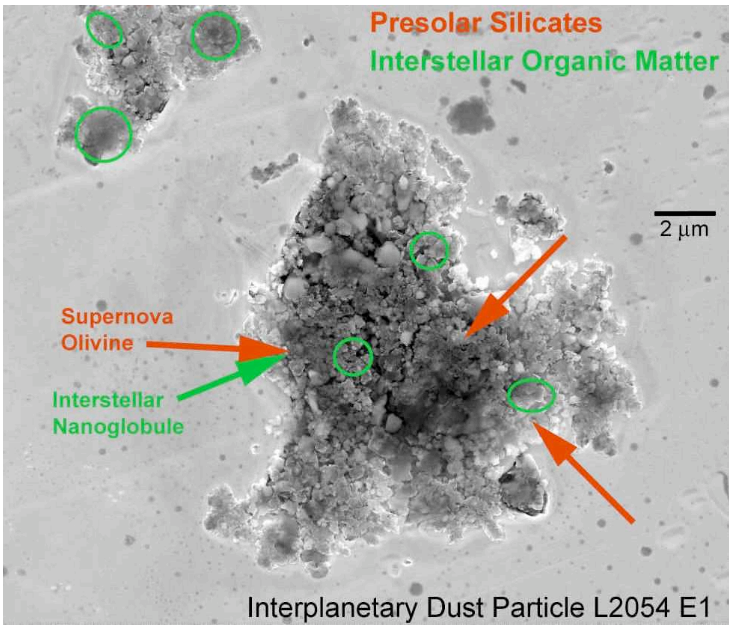

FIGURE 2.4: Grain de poussière planétaire d'origine cométaire collecté dans la haute atmosphère terrestre (Busemann et al. 2009)

2.4.3 Emission totale d'un disque

Une fois connus les flux élémentaires — thermiques et en lumière diffusée — d'un grain individuel composé de plusieurs matériaux, il reste à déterminer le flux total émis par le disque, c'est-à-dire prendre en compte sa *densité de surface* et opérer une intégration sur les distances, et sur les tailles. Les détails de la procédure et la paramétrisation utilisés au cours de ma thèse seront exposés en détails dans le Chapitre 5. Je donne ici quelques relations utiles traduisant l'émission globale d'un disque de poussière.

La densité de surface Σ donne le nombre moyen de grains par unité de surface tel que la masse totale du disque soit égale à :

$$M_{\mathrm{disk}} \quad = \quad \int_{r=0}^{\infty}\left(\int_{a_{\mathrm{min}}}^{a_{\mathrm{max}}}\rho\frac{4\pi}{3}a^3\mathrm{d}n(a)\right)\Sigma(r)2\pi r\mathrm{d}r \tag{2.17}$$

où ρ est la densité d'un grain, a_{min} et a_{max} les tailles minimales et maximales considérées.

La *luminosité fractionnaire*

$$\frac{L_{\text{disk}}}{L_\star} = \frac{L_{\text{sc}} + L_{\text{th}}}{L_\star} \tag{2.18}$$

où L_{sc} et L_{th} s'écrivent :

$$L_{\text{sc/th}} = 4\pi d_\star^2 \int_\lambda \int_{r=0}^{\infty} \Phi_{\text{sc/th}}(\lambda, r)\Sigma(r) 2\pi r \mathrm{d}r \mathrm{d}\lambda\,, \tag{2.19}$$

et la *profondeur optique verticale* $\tau_\perp$

$$\tau_\perp^\lambda(r) = \left(\int_{a_{\text{min}}}^{a_{\text{max}}} \pi a^2 Q_{\text{ext}}(\lambda, r, s) \mathrm{d}n(r, a) \right) \Sigma(r) \tag{2.20}$$

avec $Q_{\text{ext}} = Q_{\text{sca}} + Q_{\text{abs}}$ l'efficacité d'extinction, sont deux observables fondamentales caractéristiques d'un disque. Elles peuvent être rapportées à la densité de surface du disque une fois connues les propriétés d'émission des grains :

$$\sigma_{\text{sca}}\,\Sigma(r) = \omega\,\tau_\perp(r) \tag{2.21}$$

où ω est l'*albedo* qui se calcule à partir des efficacités d'absorption :

$$\omega(r) = \frac{Q_{\text{sca}}(\lambda)}{Q_{\text{ext}}(\lambda)} \tag{2.22}$$

Les propriétés optiques d'une distribution de tailles de grains sont avantageusement exprimées en terme d'*opacité de masse*, c'est-à-dire une section efficace moyenne par unité de masse :

$$\kappa(\lambda) = \frac{\int 4\pi a^2\, Q_\lambda^{\text{abs}}(a) \mathrm{d}n(a)}{\int (4\pi/3)\, \rho a^3\, \mathrm{d}n(a)} \tag{2.23}$$

2.4.4 Quelques exemples

La figure 2.5 montre quelques exemples d'efficacités d'absorption et de diffusion calculées avec les théories de Mie et des milieux effectifs de Bruggeman pour plusieurs matériaux représentatifs :

- Des silicates astronomiques ("Smoothed UV Astronomical Silicate", matériau "théorique" issu de l'ajustement de modèle à de multiples observations, Draine 2003) de la classe des silicates amorphes

- Des minéraux d'Olivine Crystalline (Fabian et al. 2001) de la classe des silicates crystallins (formule : $Mg_{1.9}Fe_{0.1}SiO_4$)

- Des carbones amorphes (formule : C, Zubko et al. 1996)

- Mélange homogène de silicates astronomiques et de glaces amorphes ("glaces sales" dominées par de la glace d'eau, 50% en fraction volumique, Li & Greenberg 1997)

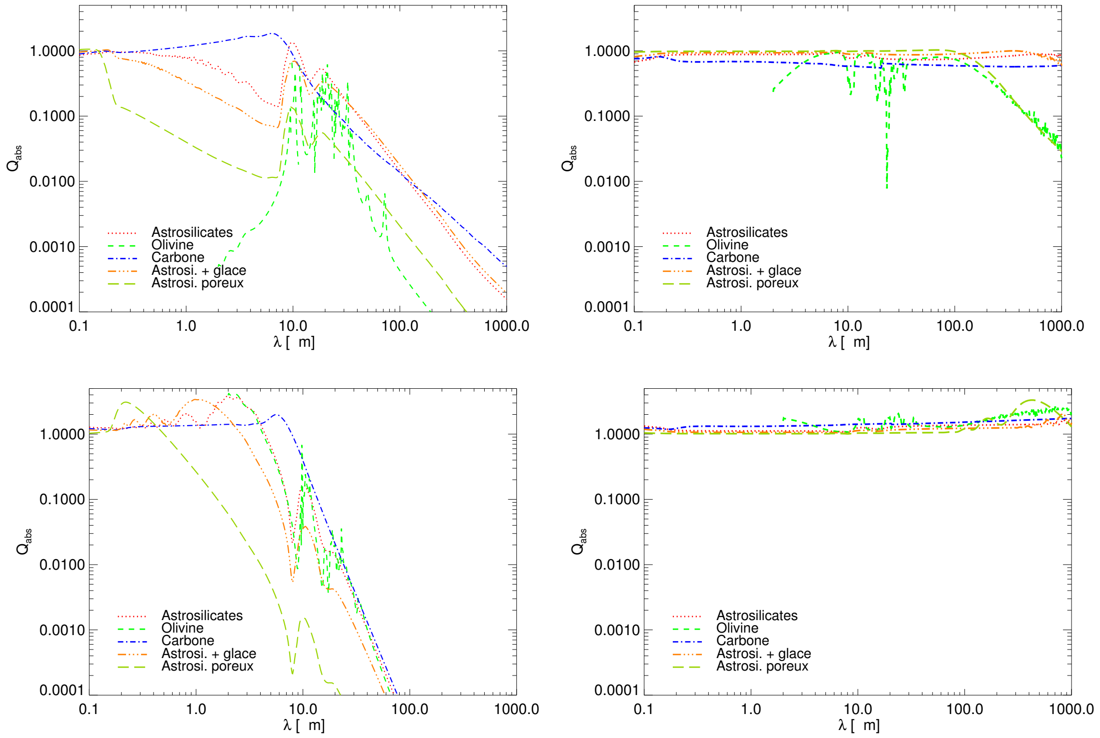

FIGURE 2.5: Efficacité d'absorption (en haut) et de diffusion (en bas) en fonction de la longueur d'onde. Deux tailles de grains sont représentées : $a = 1\mu$m (à gauche) et $a = 1$mm (à droite).

- Des silicates astronomiques poreux, contenant 90% de vide.

On remarquera en particulier l'existence des raies de silicates à 10 et 18 μm qui se traduisent par des bandes d'absorption larges lorsque la structure est amorphe, et plusieurs raies d'absorption dans la cas crystallin. L'ajout de porosité a pour effet de décaler le pic d'émision vers les plus grandes longueurs d'onde (Augereau & Papaloizou 2004).

Une fois intégrées sur la distribution de taille, ces efficacités permettent de calculer la fonction d'opacité du disque en fonction de la longueur d'onde. Celle-ci est représentée en Figure 2.6.

2.5 Le code GRaTer

2.5.1 Un modèle de disque de poussière

Durant ma thèse, j'ai pris en main le code GRaTer qui simule des observations de disques de débris optiquement fins en mettant en œuvre le modèle discuté précédemment de manière particulièrement efficace. Le code, d'abord écrit en FORTRAN mais maintenant implémenté sous IDL (Interactive Data Language), a été conçu à l'origine pour modéliser les observations du disque froid qui entoure l'étoile HR 4796A (Augereau et al. 1999) et a depuis bénéficié de constantes améliorations auxquelles j'ai moi-même pris part. Je résume ici les principales étapes de la modélisation, qui seront reprises en détails dans la suite de la thèse.

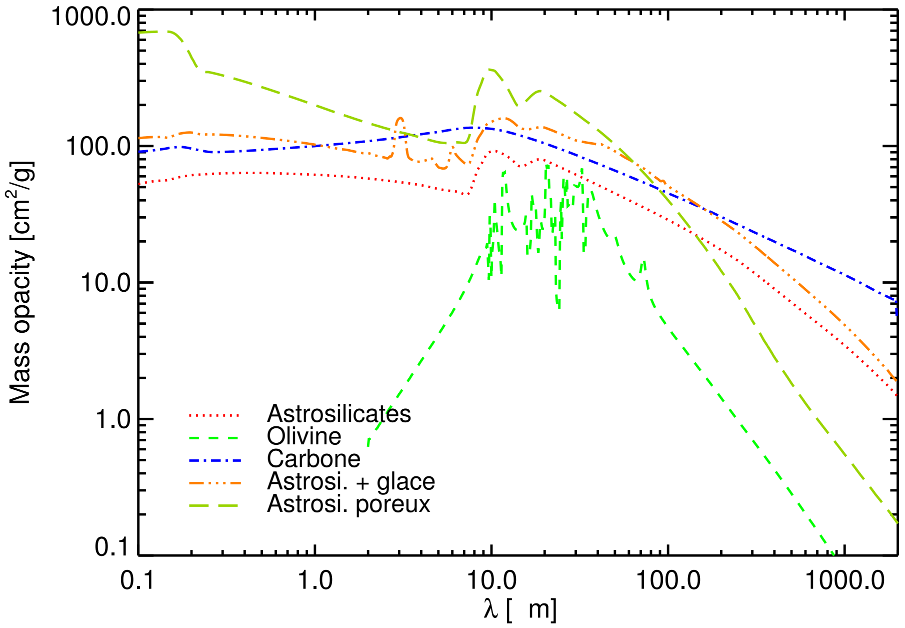

Figure 2.6: Fonction d'opacité de masse calculée pour une distribution standard de tailles de grains ($\kappa = -3.5$, $a_{\text{min}} = 1\,\mu$m, $a_{\text{max}} = 1$mm)

1. **Propriétés de l'étoile et spectres stellaires** : L'étape préliminaire à tout effort de modélisation est la détermination, à partir de données d'archive et de la littérature, des paramètres stellaires du système : magnitude visible, type spectral, masse de l'étoile, distance. Il est à noter que ces quantités sont déterminées avec des incertitudes très variables en fonction des étoiles cibles. Il convient ensuite de soustraire la contribution de l'étoile des données, étape que je réalise via un ajustement à 2 paramètres ($\log g$, T_{eff}) d'un modèle NextGen (Hauschildt et al. 1999a) de photosphère au flux en bande V. La marge d'erreur est typiquement $\leq$2%.
2. **Géométrie** : Les disques sont supposés avoir une géométrie à 2 dimensions, hypothèse suffisante pour un disque optiquement fin dès lors que les contraintes spatiales sont modestes. La connaissance ou l'exploration de l'inclinaison du disque permettent une comparaison avec des images résolues. Vus de face, les disques sont supposés axisymétriques. J'utiliserai par la suite des profils de densité paramétriques (Chapitres 4, 5), ou tirés de l'inversion d'images résolues (Chapitre 3). Le modèle 2D peut-être ramené à un modèle 3D pour générer des images synthétiques, comme détaillé en section 4.4.
3. **Tailles de grains** : Les grains sont supposés suivre une distribution de taille décrite par une loi de puissance indépendante de la distance. Autrement exprimé, la probabilité de présence des grains en fonction de la distance est supposée au premier ordre indépendante de la taille. Les paramètres de taille minimale (a_{min}) et de pente sont explorés et confrontés aux arguments dynamiques et collisionnels qui prescrivent $a_{\text{min}} \sim a_{\text{blow}}$ et $\kappa \sim -3.5$. Une implémentation astucieuse permet d'éviter les redondances dans les boucles sur les tailles de grains pour différentes valeurs de a_{min}. Les grains plus chauds que la température de sublimation sont éliminés du disque ; j'ai

mis en place à l'occasion de l'étude des exozodis (Chapitres 4, 5) un nouveau modèle de sublimation tenant compte des méchanismes de productions et d'élimination au sein du disque. Ce modèle fait l'objet d'une section détaillée au chapitre 4.

4. **Propriétés optiques** : Les propriétés d'émission et de diffusion sont calculées pour la distribution de taille sur la base de mesures d'indices optiques réalisées en laboratoire ou reconstruites à partir d'observations astronomiques : j'utiliserai par la suite des grains de silicates, des matériaux carbonés et des glaces — amorphes ou crystallins et possiblement poreux. Le calcul des propriétés optiques est un processus très gourmand en temps, spécialement dans la limite des grandes paramètres de taille. Un des tout premiers objectifs de ma thèse a été de mettre en place une méthode pour optimiser cette étape du calcul. J'ai comparé les performances des approximations de l'optique géométrique et de Rayleigh-Gans par rapport à la théorie de Mie. Cette dernière a l'avantage de fournir une solution exacte des équations de Maxwell et produit des efficacités sensiblement différentes pour les paramètres de tailles considérés. Pour palier au problème du temps de calcul, j'ai opté pour une méthode de stockage des propriétés optiques. Les efficacités $Q_{\rm abs}$, $Q_{\rm sca}$ et $Q_{\rm pr}$ sont pré-calculées pour une grille de compositions où varient les fractions volumiques des différents constituants, tabulées dans une base de données et stockées sous forme de binaires IDL. Par suite, ces propriétés optiques (indépendantes du modèle de disque) peuvent être ré-utilisées dans les études ultérieures, et ce de manière souple via une interpolation à 2 dimensions par la méthode des splines. Cet ajout au code a constitué une amélioration considérable des performances : environ un facteur 10 de gain de temps de calcul, et a favorisé l'utilisation systématique du code qui est aujourd'hui à l'oeuvre. Typiquement pour une seule SED, une grille de modèle standard ($>$ 1 million de modèles) est calculée en environ 6 heures, soit un modèle en quelques millisecondes.

5. **Ajustement de données :** GRaTer est prévu pour simuler des données de types variés. On peut ainsi interpréter les observations en terme de masse de poussières, de propriétés des grains et de géométrie du disque. En premier lieu, on ajuste des densités spectrales d'énergie : photométrie en bande large et spectres étroits. Pour ce faire, chaque modèle (déterminé par ses paramètres de géométrie, de taille et de composition) est ajusté séparément à la SED globale observée. De nouvelles méthodes ont récemment été mises en place pour ajuster les images résolues par Herschel conjointement à la SED (Augereau et al. in prep, voir Chapitre 3). Il est également possible de simuler des observations interférométriques comme je l'expliquerai en détails au chapitre 4.

   Les différentes données sont ajustées par une minimisation de χ^2 pour chaque modèle. L'interprétation de données non-résolues constitue un problème *dégénéré*, puisqu'on accède essentiellement à une information de température. Il est dès lors difficile de déterminer la distance caractéristique du disque, la température étant aussi une fonction de la taille de grain (en particulier $a_{\rm min}$, Figure 2.7, en haut). En revanche, les images résolues permettent de *lever les dégénerescences*, d'identifier des minimums globaux dans les cartes de χ^2, et d'explorer plus en détails les propriétés des grains (Figure 2.7, en bas). J'ai mis en place une méthode d'analyse statistique par inférences Bayésiennes qui autorise l'étude indépendente de chaque paramètre et le calcul d'incertitude sur la fiabilité des modèles proposés. Ces méthodes d'ajustement sont développées plus en détails dans la prochaine section, qui est adaptée de Lebreton et al. (2012) et est de ce fait rédigée en langue anglaise.

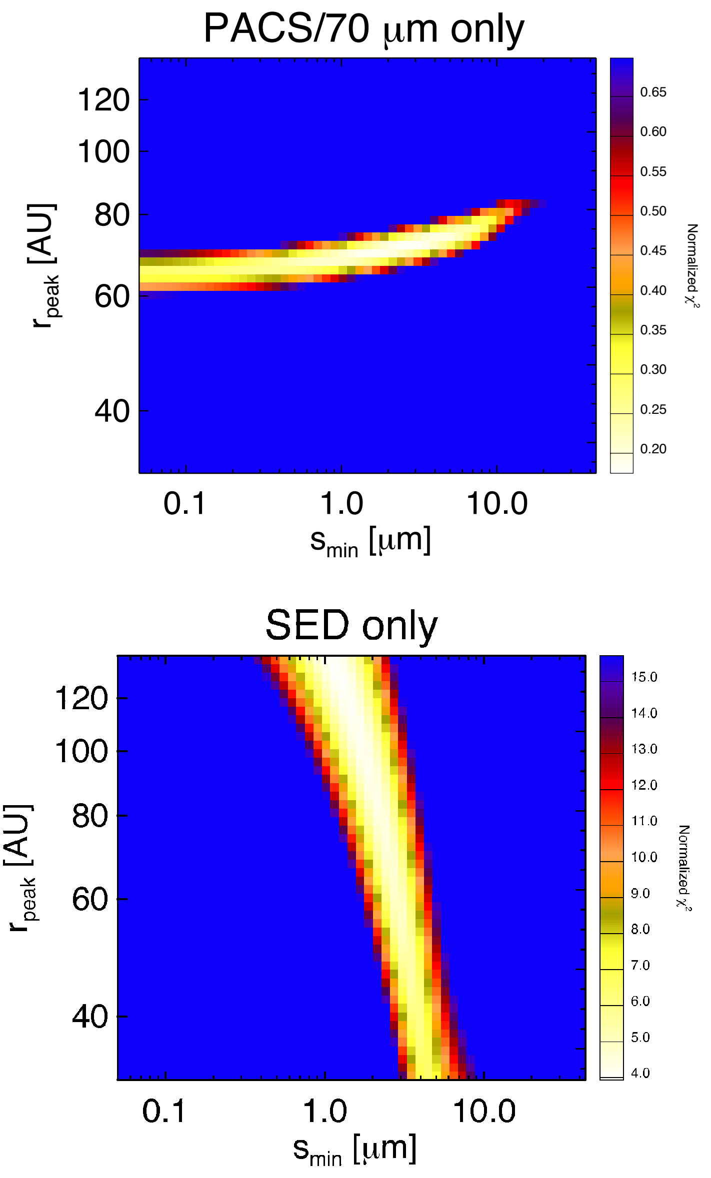

Figure 2.7: Ces cartes illustrent la dégénérescence rencontrée lors de l'ajustement d'un modèle de disque à des observables : en haut la SED, en bas une image résolue. Dans cet exemple nous explorons deux paramètres : la taille minimale de grain $s_{\min}$ et la distance du pic de la densité de surface $r_{\rm peak}$, pour reproduire des observations Herschel du disque de q^1 Eridani ; la qualité de l'ajustement est mesurée par la valeur du χ^2 réduit. On observe que les contraintes sur ces 2 paramètres sont orthogonales, ce qui permet de lever la dégénérescence.

2.5.2 Ajustement de χ^2 et analyse Bayésienne

The strength of the GRaTer code, in comparison with an optimization algorithm that would provide a unique best-fit solution and possibly miss local minima, is that all the models are stored enabling fast and easy post-processing of the results.

To find the best solution in the grid of models, we use a classical least-square minimization approach with $n_{\rm free}$ free parameters, which results in $N - n_{\rm free}$ degrees of freedom (dof) where N is the number of independent data points. The free parameters can be κ, $a_{\rm min}$ and $M_{\rm dust}$, and depending on the situation the grain composition $v_{\rm C}$, $v_{\rm ice}$ or $\mathcal{P}$[2] or the disk density profile parameters (density peak $\rm r_0$, power-law slope $\sigma_{\rm in}$ or $\sigma_{\rm out}$). $M_{\rm dust}$ is handled separately because it is automatically adjusted to reproduce the surface density profile in the code.

Let $\vec{a}$ be the vector of parameters. Here $\vec{a} = (\kappa, a_{\rm min}, v_{\rm ice}, \mathcal{P})$. For each set of parameters, we can define the quantity:

$$\chi^2(\vec{a}) = \sum_{i=1}^{N} \frac{(D_i - M_i)^2}{\sigma_i^2} \tag{2.24}$$

where D_i and M_i are the observed and modeled values, respectively, and σ_i is the measured uncertainty. For each χ^2 value, we can define the likelihood of the data, *i.e.* the probability of the data given the parameters of a model. This assumes the errors are distributed normally and are uncorrelated.

$$P(\vec{D}|\vec{a}) = \frac{1}{C} \exp\left(\frac{-\chi^2(\vec{a})}{2}\right) \tag{2.25}$$

where C is a normalization constant and $D = \{D(i)\}_{\rm i=1...N}$. In order to evaluate the effect of each individual parameter a_i on the quality of the fit, we implement a Bayesian inference method. We define the posterior probability of $\vec{a}$ as the probability distribution of the parameters $\vec{a}$ given the data $\vec{D}$. It has to be noted that this formulation implicitly assumes that the model is suited to describe the observation. Bayes' theorem says that this quantity can be written:

$$P(\vec{a}|\vec{D}) = \frac{P(\vec{a})P(\vec{D}|\vec{a})}{P(\vec{D})} \tag{2.26}$$

where $P(\vec{D})$ is the prior probability of the data under all possible hypothesis (a normalization constant in practice), and $P(\vec{a})$ is the prior probability distribution of the parameters $\vec{a}$. Here we use uniform priors for all the parameters, meaning that we do not favor any realization of the parameters prior to obtaining the data. That fundamental theorem provides a simple way to individually assess the parameters of a model. Indeed, the marginal probability of each parameter $a_{\rm i}$ can be computed regardless of the values of the other parameters $\vec{a_{\rm j\neq i}}$:

$$P(a_{\rm i}|\vec{D}) = \int\limits_{a_0} \dots \int\limits_{a_{i-1}} \int\limits_{a_{i+1}} \dots \int\limits_{a_{\rm i_{max}}} P(\vec{a}_{\rm j\neq i}|\vec{D}) da_0 \dots da_{\rm i_{max}} \tag{2.27}$$

---

[2] volume fractions of carbons and ice w.r.t. silicates, and porosity

Then we obtain a probability law as a function of the realization of each individual parameter. Finally, we estimate the parameters by calculating the mathematical expectation and variance. These are the values usually given with 3σ uncertainties in this paper.

$$
\begin{aligned}
E(a_{\mathrm{i}}) &= \int_{a_{i_{min}}}^{a_{i_{max}}} a_{\mathrm{i}} P(a_{\mathrm{i}}|\vec{D}) && (2.28)\\
\sigma^2(a_{\mathrm{i}}) &= E(a_{\mathrm{i}}^2) - E(a_{\mathrm{i}})^2 && (2.29)
\end{aligned}
$$

2.5.3 Utilisation

Le code GRaTer peut désormais être utilisé de manière systématique en un temps raisonnable et avec une interprétation facilitée. Il est exploité notamment pour le projet Herschel/DUNES (Sec. 3.2.3), pour l'interprétation d'images coronagraphiques NaCo (Boccaletti et al. 2012; Lagrange et al. 2012c; Buenzli et al. 2010) et pour le projet Exozodi (Chapitre 4). J'ai par ailleurs développé une version "stand-alone" du code qui peut-être utilisée par des usagers extérieurs sans connaissance approfondie du modèle (voir notamment Sec.3.2.2). Les prochains chapitres illustreront l'utilisation faite du modèle pour ajuster les observations de disques froids vus par Herschel (Chapitre 3), et de disques chauds détectés par l'interférométrie optique (Chapitre 4 et 5).

Chapter 3

Herschel's view of debris disks

"Maybe they didn't grow up in the Vega system. Maybe they're just visiting"
"That's no good either. The system is full of debris. It's a failed solar system or solar system still in its early stages of development. If they stay very long, their spacecraft'll be clobbered."

Carl Sagan, *Contact*, 1997

Throughout this chapter, I will focus on the modelling of cold debris disks that are best probed at long wavelengths most notably by the Herschel Space Observatory. Herschel is an ESA space observatory, with important participation from NASA. It operates from a Lissajous orbits close to the second Lagrange point of the Earth-Sun system. With its 3.5 meter effective diameter it is the largest astronomical telescope ever sent to space. Its impressive dimensions are well evidenced in Picture 3.1 that was taken shortly before its launch by an Ariane V rocket shortly before my thesis in May 2009. It provides far-infrared (IR) and sub-millimetre observations at an unprecedented spatial and spectral resolution and sensitivity. Observations of circumstellar disks are performed with the Herschel/PACS instrument (Photodetector Array Camera and Spectrometer; Poglitsch et al. 2010) at 70, 100 μm and 160 μm where the dust emission is the strongest, and Herschel/SPIRE instrument (Spectral and Photometric Image Receiver; Griffin et al. 2008) at 250 μm, 350 μm, and 500 μm. I have been involved in two Open Time Key Programmes that focus on the evolution of the dust grains and gas in circumstellar disks around young and Main Sequence stars: GASPS (GAS in Protoplanetary Systems) and DUNES (DUst around nearby stars).

©2009 ESA-CNES-ARIANESPACE / Optique Vidéo du CSG - P BAUDON

Figure 3.1: The Herschel Space Observatory photographed at ESA/ESTEC

3.1 An icy Kuiper belt around the young solar-type star HD 181327

The GASPS project is dedicated to the study of gas dissipation processes occurring in protoplanetary disks toward their path to evolved planetary systems. An unbiased survey of atomic and molecular gas and dust is carried out in more than 250 disks covering a wide range of ages (1–30 Myr), disks masses ($10^{-5} - 10^{-2} M_{\odot}$), and stellar types (A to M).

The majority of the targets lie in 6 of the closest (< 160 pc) young stellar clusters with well defined ages: Taurus, Upper Sco, TW Hya, Tuc Hor, Beta Pic and Eta Cha. Over the optically thin dusty disks of its sample, the young (∼12 Myr) Beta Pictoris Moving Group (BPMG) F5/6 star HD181327 rather corresponds to a very young debris disk and appeared an excellent case study. The following section (adapted from Lebreton et al. 2012) presents the first big project of my thesis that consisted in performing a detailed study of the HD 181327 debris disk based on new Herschel observations. The disk is well-resolved in the near-infrared alleviating any ambiguity on the location of the grains. Therefore I found appropriate to focus on the properties of the circumstellar dust in this young Kuiper Belt analogue.

"AN ICY KUIPER BELT AROUND THE YOUNG SOLAR-TYPE STAR HD 181327"

J. Lebreton, J.-C. Augereau, W.-F. Thi,A. Roberge, J. Donaldson,
G. Schneider, S. T. Maddison, F. Ménard, P. Riviere-Marichalar,
G.S. Mathews, I. Kamp, C. Pinte, W. R. F. Dent, D. Barrado, G. Duchêne,
J.-F. Gonzalez, C. A. Grady, G. Meeus, E. Pantin, J. P. Williams, P. Woitke

Published in A&A, Received July 15, 2011; accepted December 7, 2011

3.1.1 Introduction

The evolution of planets in the Solar System is intimately connected to the existence of a reservoir of planetesimals in its outer regions. The depletion of the Kuiper Belt and the main asteroid belt that occurred during the Late Heavy Bombardment not only delivered large amounts of water, volatiles and carbonaceous material onto the inner planets, but it also reduced the later rate of catastrophic impacts onto the Earth, opening the path to the emergence of life (Morbidelli et al. 2000; Greaves & Wyatt 2010; Hartogh et al. 2011). Although detecting Kuiper Belt-like objects around nearby planetary systems will remain an unachievable goal for the foreseeable future, their collisional erosion produces circumstellar disks of dust responsible for a characteristic excess emission detectable at infrared and sub-millimeter wavelengths. Recent studies using the Herschel Space Observatory reveal that as much as ∼30% of nearby Main-Sequence F, G, K stars are surrounded by cold debris rings analogous to the Kuiper Belt (latest Herschel/DUNES Open Time Key Program results, Eiroa et al. 2013). However, the cold temperature and the large grain sizes make it impossible to detect solid-state features in their spectrum, thus preventing unambiguous identification of the dust composition. We are thus left with model-dependent methods to constrain the dust composition from color and polarimetric measurements, and from the Spectral Energy Distribution (hereafter SED).

Another uncertainty in planet formation theories lies in the lack of detailed observational constraints for the mutual dust and gas dissipation timescales in circumstellar disks, or more precisely, on how the gas-to-dust mass ratio evolves with time and location in disks at the very early stages of planet formation. The study of stellar clusters of different ages shows that, statistically, a population of young stars loses its massive dust disks in only a few million years on route to the Main Sequence (Carpenter et al. 2005), although, for individual objects, the transition from an optically thick to an optically thin disk is expected to occur more quickly (a million years or less, Cieza et al. 2007; Currie & Sicilia-Aguilar 2011). However not much is known about the characteristic evolutionary timescales for the gas in these disks. Observing young stars at different evolutionary stages can help elucidate the extent to which gas and dust simultaneously dissipate in disks. This requires observations of both the dust and gas components and, at the same time, modeling of the continuum and line emission.

As part of the GASPS (Gas in Protoplanetary Systems) Herschel Open Time Key Programme, we observed HD 181327, a young (∼12 Myr) F5.5V star located at 51.8 pc (Holmberg et al. 2009, Tab. 3.1) belonging to the β Pictoris moving group (Zuckerman & Song 2004; Mamajek et al. 2004). HD 181327 was identified as a debris disk hosting main sequence star through its SED with a fractional infrared luminosity $L_{\rm IR}/L_\star = 0.2\%$ (Mannings & Barlow 1998). Schneider et al. (2006), from NICMOS coronagraphic observations in scattered light, discovered a ring-like disk of circumstellar dust located at radius ~ 89 AU from its star. The ring is inclined by 31.7±1.6° from face-on and shows an apparent brightness asymmetry with respect to the minor axis that is well explained by a strong directionally preferential scattering. No photocenter nor pericenter offset is seen in the ring relative to the position of the central star and the disk appears axisymmetric. Recent reprocessing of these data (Schneider et al., in prep.) confirms the annulus shape of the disk, and suggests a narrow radial distribution of the dust in the system (FWHM = 24.5 AU). A low surface brightness diffuse halo is seen in the NICMOS image and in complementary HST/ACS images at a distance of $\sim 4'' \leq r \leq 9''$ from the central star, which may correspond to a population of very weakly bound grains originating in the main ring. Mid-infrared images at 18.3 μm by Chen et al. (2008) suggest azimuthal asymmetries in the density profile of the ring with respect to the apparent minor axis. These 18.3 μm observations also show that little to no emission ($\lesssim$ 15%) comes from inside the ring resolved in scattered light. Therefore, the density profile of the HD 181327 dust disk should be well constrained by the scattered light and thermal emission images, allowing a detailed study of the dust properties. Interestingly, from IRS and MIPS-SED data, Chen et al. (2008) also inferred the presence of crystalline ice in the debris disk.

In this paper we perform SED and line fitting of new Herschel/PACS observations of HD 181327 (presented in Sec. 3.1.2), supplemented by data from the literature. We also present new ATCA imaging of the disk (Sec. 3.1.2). In Sec. 3.1.3, we derive surface density profiles from the newly reduced HST/NICMOS data, which well constrain the ring geometry. We describe our dust model and present the results of the SED fitting in Sec. 3.1.3 and 3.1.4. We assess the gas content in this young debris disk in Sec. 5.5.5. Finally we discuss the results in Sec. 5.6, 5.3.2 and 3.1.7 and present our conclusions in Sec. 5.7.

3.1.2 Observations and Data Reduction

Herschel/PACS continuum

We obtained new far-IR photometry and spectroscopy of HD 181327 using the PACS instrument onboard the Herschel Space Observatory (Pilbratt et al. 2010; Poglitsch et al. 2010). The observations were carried out in two modes: 1) 159 sec of point-source chop-nod mode imaging at 70 and 160 μm (obsid: 1342183658) and 2) two 276 sec scan map imaging observations at 100 and 160 μm (obsids: 1342209057-8). The scan maps were executed with the medium scan speed (20″/s), at scan angles of 70° and 110°. The two cross scan maps at different scan angles were combined to increase the signal-to-noise by cutting down on streaking in the image background along the scan direction.

We reduced the photometry with the Herschel Interactive Processing Environment

Table 3.1: Star and disk properties

Parameter	Value	Reference
Spectral Type	F5/F6V	Nordström et al. (2004)
Magnitude V	7.0	Bessell (2000)
Gravity ($\log(g)$)	4.510	Chen et al. (2006)
Distance ($d_\star$)	51.8 pc	Holmberg et al. (2009)
Age	12 Myr	Zuckerman & Song (2004) Mamajek et al. (2004)
Luminosity ($L_\star$)	$3.33\,L_\odot^{(a)}$	this study
Mass ($M_\star$)	$1.36\,M_\odot$	this study
Disk PA$^{(b)}$	107±2°	Schneider et al. (2006)
Disk inclination	31.7±1.6°	Schneider et al. (2006)
$L_{\rm IR}/L_\star$	$\sim 2\times10^{-3}$	this study

$^{(a)}$From integrating the synthetic stellar spectrum, $^{(b)}$Position Angle, East of North.

(HIPE, Ott 2010) version 4.2. The uncertainties in the absolute flux calibration for this version are 10% at 70 and 100 μm and 20% at 160 μm (see the PACS Scan Map Astronomical Observation Templates release note[1]). For the 70" and 160 μm chop-node images, we performed aperture photometry using apertures of 7″ and 11″, respectively. For the 100 and 160 μm scan map observations, we used apertures of radii 12″ and 24″, respectively. An annulus for sky background estimation was placed from 10″ − 20″ beyond the aperture in each case, and an aperture correction was applied to the measured fluxes. Both estimations at 160 μm are fully compatible within the error bars; the 160 μm scan-map flux is used in the rest of the study. Since the source is marginally resolved at 70 and 100 μm (see Section 3.1.2), we calculated our own aperture corrections following the procedure described in Poglitsch et al. (2010). The photometry results are presented in Table 3.2.

Table 3.2: Photometry results for HD 181327 from chop-nod$^{(1)}$ and scan map$^{(2)}$ observations.

Wavelength (μm)	$F_{\rm cont}^{\dagger}$ (Jy)	Absolute Flux Cal. Uncertainty
$70^{(1)}$	1.827 ± 0.0069	10%
$100^{(2)}$	1.337 ± 0.0082	10%
$160^{(1)}$	0.767 ± 0.015	20%
$160^{(2)}$	0.772 ± 0.011	20%

†The $\pm1\sigma$ error bars on the flux measurements include statistical uncertainty only.

HD 181327 is more extended than the Herschel point-spread function (PSF) in both the 70 μm and 100 μm images. The 70 μm image of HD 181327 appears in Figure 3.2, along with the 70 μm image of a PSF reference star (HD 148387) observed using the same chop-nod mode. The upper panel of Figure 3.3 shows the azimuthally-averaged radial brightness profiles for HD 181327 and HD 148387. In the case of the 100 μm scan map observation of HD 181327, we used a different PSF reference observation, i.e. a scan map

---

[1] available at http://herschel.esac.esa.int/AOTsReleaseStatus.shtml

of α Boo. The 100 μm α Boo radial profile appears in Figure 3.3, bottom panel. At both wavelengths, the azimuthally averaged radial profile of HD 181327 is clearly extended beyond that of the PSF reference. The FWHM of the HD 181327 70 μm profile is $6''44$, compared to a FWHM of $5''28$ for HD 148387. At 100 μm, the FWHM for HD 181327 is $7''58$, compared to $6''94$ for α Boo.

ATCA 3.2 mm observations

The Australia Telescope Compact Array (ATCA) was used to observe HD 181327 at 3.2 mm in May and September 2010. The observations were carried out in continuum double sideband mode, with 2046 × 1 MHz channels per sideband with an effective total bandwidth of just over 2 GHz. The ATCA has five antenna with 3-mm receivers, and our observations were carried out with the compact H75 array configuration with baselines of 31–98 m. The quasars PKS 1815-553 and PKS 1253-055 were used for the gain and bandpass calibrations respectively, and Uranus was used for the absolute flux calibration. The ATCA calibration uncertainty is estimated to be about 20% in the 3-mm band. The data were calibrated and reduced with the MIRIAD package (Sault et al. 1995). The frequency pair for the observations were centered at 93 and 95 GHz, and during the reduction process the data was averaged over 64 channels to improve the signal-to-noise, shifting the frequency pairs to 92.968 and 94.969 GHz. The final CLEANed map combined the two sidebands, resulting in an image at 93.969 GHz (3192.5 μm) presented in Fig. 3.4. Our total on-source integration time was 770 minutes. We determined an integrated flux of 7.2×10^{-4} Jy, with an RMS of $\sigma = 1.1 \times 10^{-4}$ Jy/beam. Including the 20% calibration uncertainty, this yields an uncertainty of 2.5×10^{-4}Jy. The disk is marginally resolved. Assuming a Gaussian profile, we find a PA of ~ 102°, consistent with that seen on the NICMOS image (107 ± 2°, Tab. 3.1), and along which the FWHM is $\sim 7.8''$ (beam:

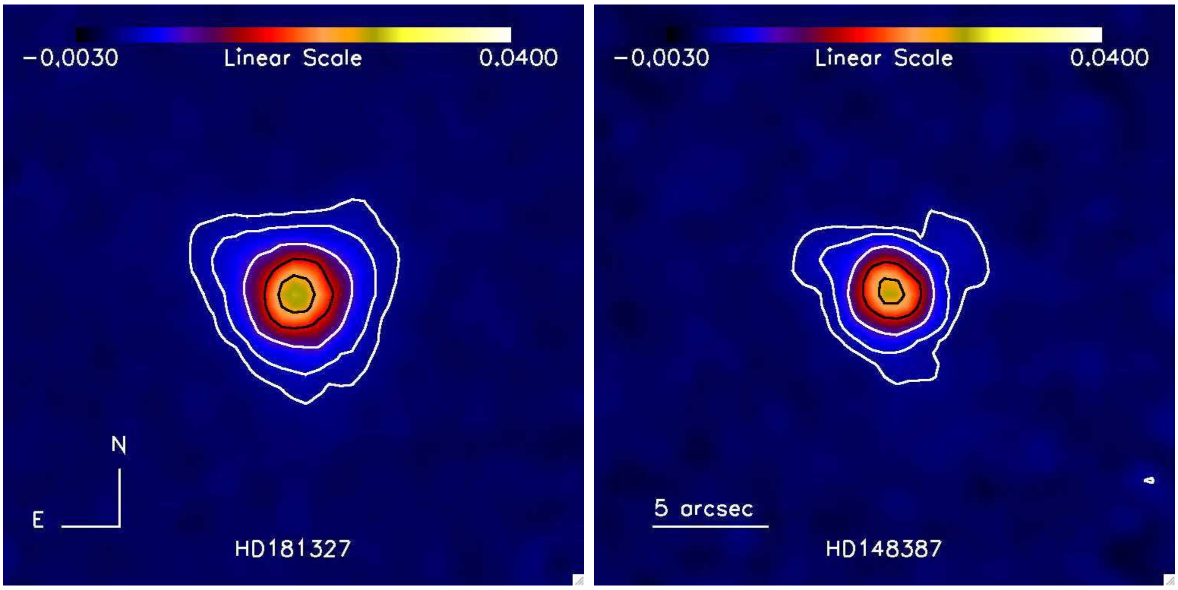

Figure 3.2: PACS 70 μm imaging of **(left)** HD 181327 and **(right)** a PSF reference star, HD 148387. Both images were acquired in chop-nod mode. The field of view of each image is $25'' \times 25''$. Brightness contours at 5, 10, 25, 50 and 75 times the background noise in the HD 181327 image are overlaid on both images.

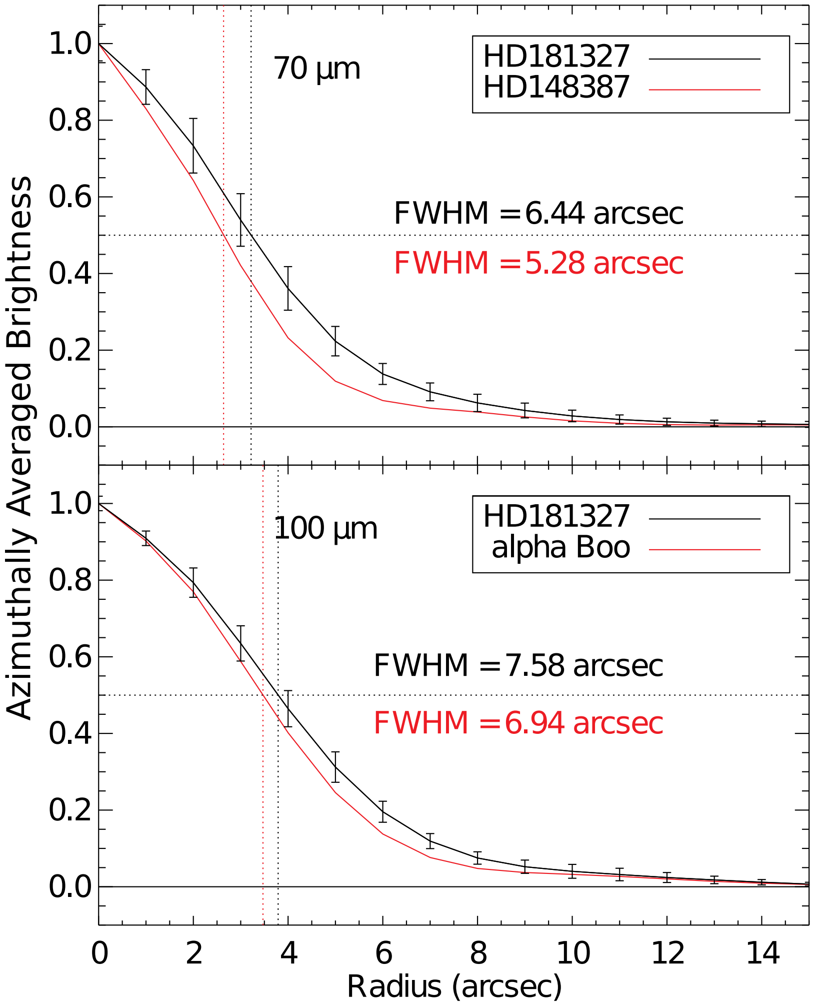

Figure 3.3: Radial profiles of HD 181327 at 70 μm (**top**), compared to HD 148387 as a PSF reference, and at 100 μm (**bottom**), compared to α Boo as a PSF reference. Both plots show the azimuthally averaged, normalized radial brightness profile vs. radius from the star. Each error bar is the standard deviation of the brightness values at that radius. The FWHM values for the profiles are given on the plot.

$3.5'' \times 2.8''$, PA = 85.4°). The center of the Gaussian fit is also shifted by $0.6''$[2] toward the West with respect to the star position. Structures consistent with a belt at ~100 AU are detected along the semi-minor axis with a peak flux of 4.01×10^{-4} Jy/beam on the NW side. We note a possible brightness asymmetry with respect to the SE side.

Herschel/PACS Spectroscopy

We obtained far-infrared spectroscopy using the PACS Integral Field Unit which provides a 5 × 5 array of $9''4 \times 9''4$ spaxels. The data were taken in chop-nod mode using the line scan and range scan modes. The spectra cover eight small wavelength ranges

---

[2] The pointing accuracy of ATCA is $\sim 1''$.

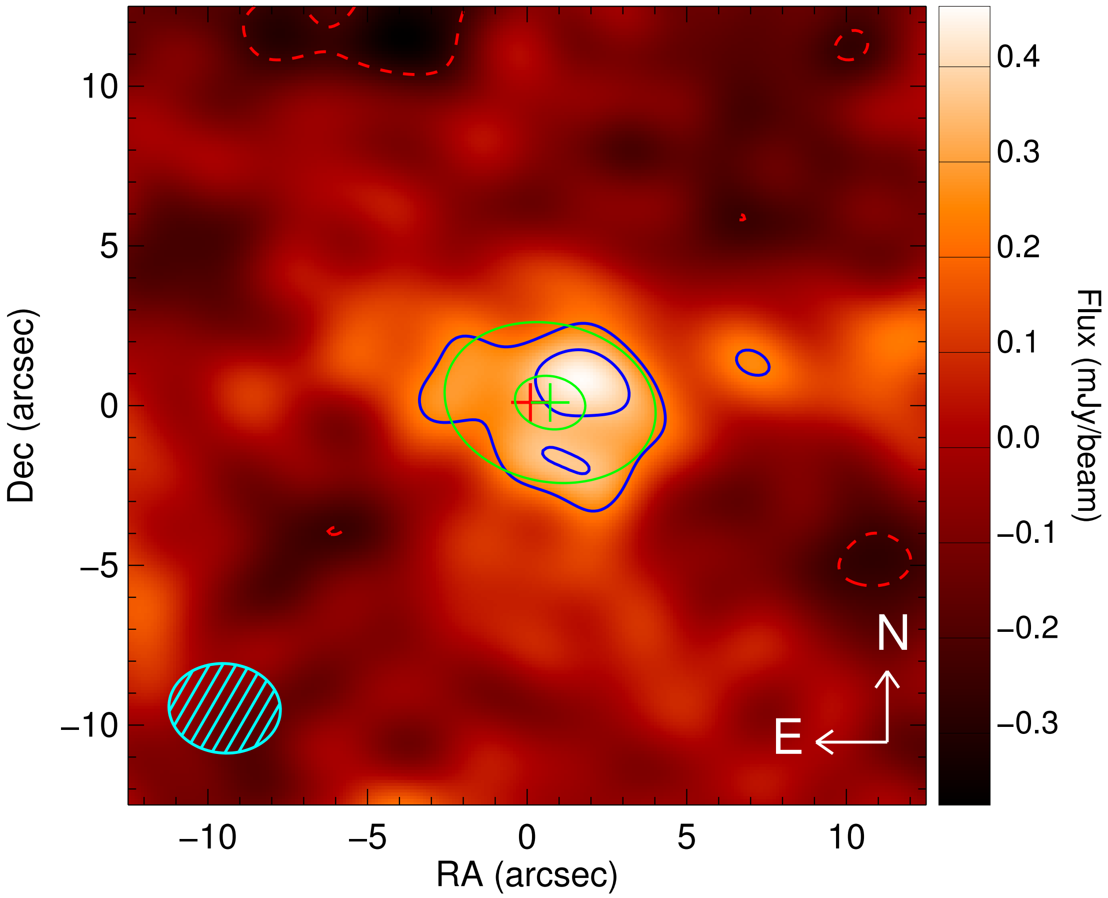

Figure 3.4: ATCA 93.969 GHz (3.192 mm) map of HD 181327 with contours at -2 (dashed red line), 2 and 3σ (solid blue lines), where σ is the image RMS given by 1.1×10^{-4} Jy/beam. The dashed blue area represents the beam. The Gaussian fit is overplot with contours at 2 and 3σ (solid green lines). The red and green crosses denote respectively the star position and the Gaussian fit center.

($\sim$ 1.8 μm wide) targeting particular emission lines, including [O I] at 63 μm and [CII] at 158 μm. The spectral resolution of the data varies between $R \approx 1100$ and 3400. Additional details on the observations appear in Mathews et al. (2010).

The data were calibrated with the Herschel Interactive Processing Environment (HIPE) version 4.2. The wavelength-dependent flux and aperture corrections provided by the PACS development team were applied, giving an uncertainty in the absolute flux calibration of 30% (see the PACS Spectroscopy Performance and Calibration Document[2]). Significant emission was detected only in the central spaxel. No emission lines are seen, only continuum flux. The central spaxel spectrum centered on the [O I] 63 μm line appears in Figure 3.5.

The continua were binned at half the instrumental FWHM and fitted with 1st degree polynomials, using the fluxes and errors produced by our HIPE reduction script. The

HIPE uncertainties appeared to be slightly too small, however. New flux random errors were calculated from the RMS of the data minus the continuum fits, over wavelength ranges spanning 6 to 14 times the instrumental FWHM, centered on the expected line rest wavelengths. The continuum fluxes at the rest wavelengths of the expected emission lines appear in Table 3.3. To determine the upper limit on the integrated line flux ($F_{\rm int}$) for each available emission line, we integrated the data over a small wavelength range, either ±1 or ±1.5 resolution elements, centered on the rest wavelength of the expected emission line. The flux errors were propagated to determine the 1σ upper limit on each integrated line flux. The 3σ integrated line flux upper limits appear in Table 3.3 as well.

Table 3.3: Spectroscopy Results for HD 181327

Line	Wavelength (μm)	$F^{\dagger}_{\rm cont}$ (Jy)	$F^{\ddagger}_{\rm int}$ ($\times10^{-18}$ W/m^2)
[O I]	63.1852	1.731 ± 0.236	< 9.82
CO 36-35	72.8429	1.491 ± 0.185	< 18.41
o-H_2O	78.7414	1.431 ± 0.187	< 10.51
CO 29-28	90.1630	1.264 ± 0.222	< 8.90
[O I]	145.5350	0.804 ± 0.107	< 8.48
[C II]	157.6790	0.767 ± 0.175	< 7.02
o-H_2O	179.5265	0.388 ± 0.201	< 6.87
DCO^+ 22-21	189.5700	0.581 ± 0.378	< 16.71

† The ±1σ error bars on the flux measurements include statistical uncertainty only. The absolute calibration uncertainty amounts to 30%. ‡ 3σ upper limit

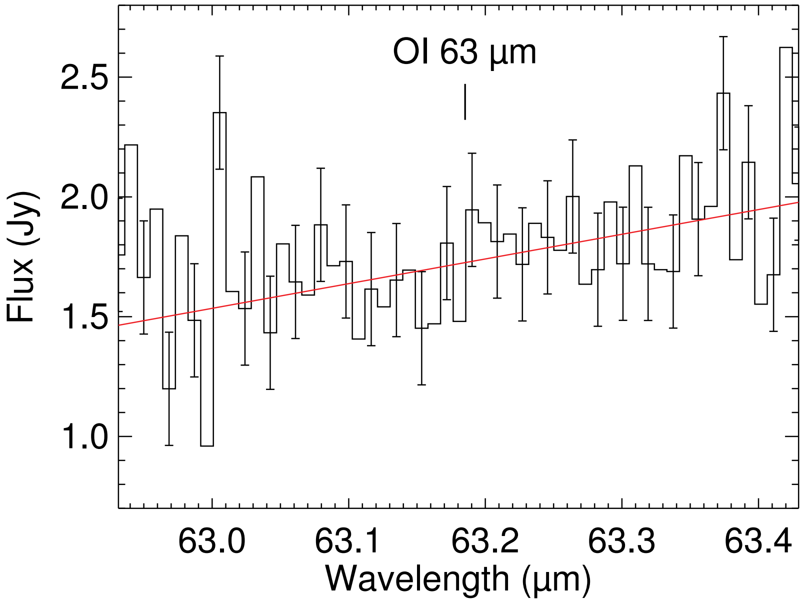

Figure 3.5: PACS spectrum of HD181327, centered on the wavelength of the [O I] 63 μm emission line. The linear fit to the continuum flux is overplotted with the red line. The [O I] 63 μm emission line was not detected.

3.1.3 Model Setup

The dust and gas models developed in Secs. 3.1.4 and 5.5.5 rely on some assumptions on the spatial distribution of the dust and the gas, as well as on the dust properties. These are detailed below in Secs. 3.1.3 and 3.1.3. Additional data collected from the literature and stellar properties are summarized in Sec. 3.1.3.

New Surface Density Profile for the HD 181327 Ring

Our spatially resolved imaging constrains the location of the dust. We advantageously impose this constraint in order to examine the dust properties in details and to get an upper limit on the gas mass from the Herschel non-detections of gaseous emission lines. The disk around HD 181327 was spatially resolved in scattered light with HST/NICMOS 1.1 μm imaging by Schneider et al. (2006), which alleviates many uncertainties on the disk structure. The NICMOS images revealed a ring-like disk with a peak density position $r_0 = 1.71$" ($\sim$ 88.6 AU, according to the new distance to the star, 51.8 pc, by Holmberg et al. 2009), with an azimuthally medianed photometric FWHM of $\sim$ 0.538" ($\sim$ 28 AU).

Recently, Schneider et al. (in prep.) improved the data reduction of the original HST/NICMOS observations of HD 181327 thanks to PSF subtraction template images better matched to the stellar PSF structure in the HD 181327 images. This results in an overall improvement of the signal-to-noise, especially inside the ring, and leads to a slight sharpening of the belt. The new profiles, displayed in the top panel of Fig. 3.6, show a peak at a distance of 88.6 AU and a surface brightness fainter by $\sim$ 21% (0.76 mJy.arcsec^{-2} at the peak position) compared to the original Schneider et al. (2006) study.

We derive the surface density profile $\Sigma(r)$ by inverting the new scattered light surface brightness profile. We employ the methodology described in Augereau & Beust (2006), assuming a disk inclination of $i = 31.7°$ from face-on. The inversion procedure yields the product $\sigma_{\rm sca}\Sigma(r)$, where $\sigma_{\rm sca}$ is the mean scattering cross section of the grains at 1.1 μm. This is equivalent to the product of the vertical optical depth $\tau_\perp(r)$, multiplied by the mean albedo ω at that wavelength ($\sigma_{\rm sca}\Sigma(r) = \omega\tau_\perp(r)$, see Eqs. 2–3 in Schneider et al. 2006). The inversion solution depends on both the anisotropic scattering phase function, and on the disk vertical profile. Nevertheless, Schneider et al. (2006) showed that the density profile is largely independent of the shape for the vertical dust distribution in the range of acceptable vertical scale heights H_0. We here assume a Gaussian vertical profile with a scale height $H_0 = 6$ AU at the observed peak radius of the ring $r_0 = 88.6$ AU ($H_0/r_0 \sim 0.068$, consistent with the theoretical lower limit of 0.04 from Thébault 2009). The observed phase function of the disk at 1.1 μm is well-represented by a Henyey-Greenstein scattering phase function with asymmetry parameter $|g_{\rm HG}| = 0.30 \pm 0.03$. This value was discussed by Chen et al. (2008) in light of asymmetries identified in T-ReCS thermal emission images in the Q_a-band. Chen et al. (2008) suggest that the asymmetries may have led to an overestimate of $|g_{\rm HG}|$, which may be as small as 0.16 ± 0.04. We thus perform the inversion for both $|g_{\rm HG}| = 0.16$ and $|g_{\rm HG}| = 0.30$.

The results are displayed in the bottom panel of Fig. 3.6, where we also show the impact of the surface brightness uncertainties on the inferred surface density profile. We find an actual surface density peak at 89.5 AU from the star. A higher $|g_{\rm HG}|$ leads to a globally higher surface density profile. The surface brightness measured interior to $\sim$ 1.5" ($\sim$ 78 AU) is not reliable because of PSF subtraction residuals. We fit the profiles from 79 to 83 AU obtained for both $|g_{\rm HG}|$ values by a very steep power-law function of the form

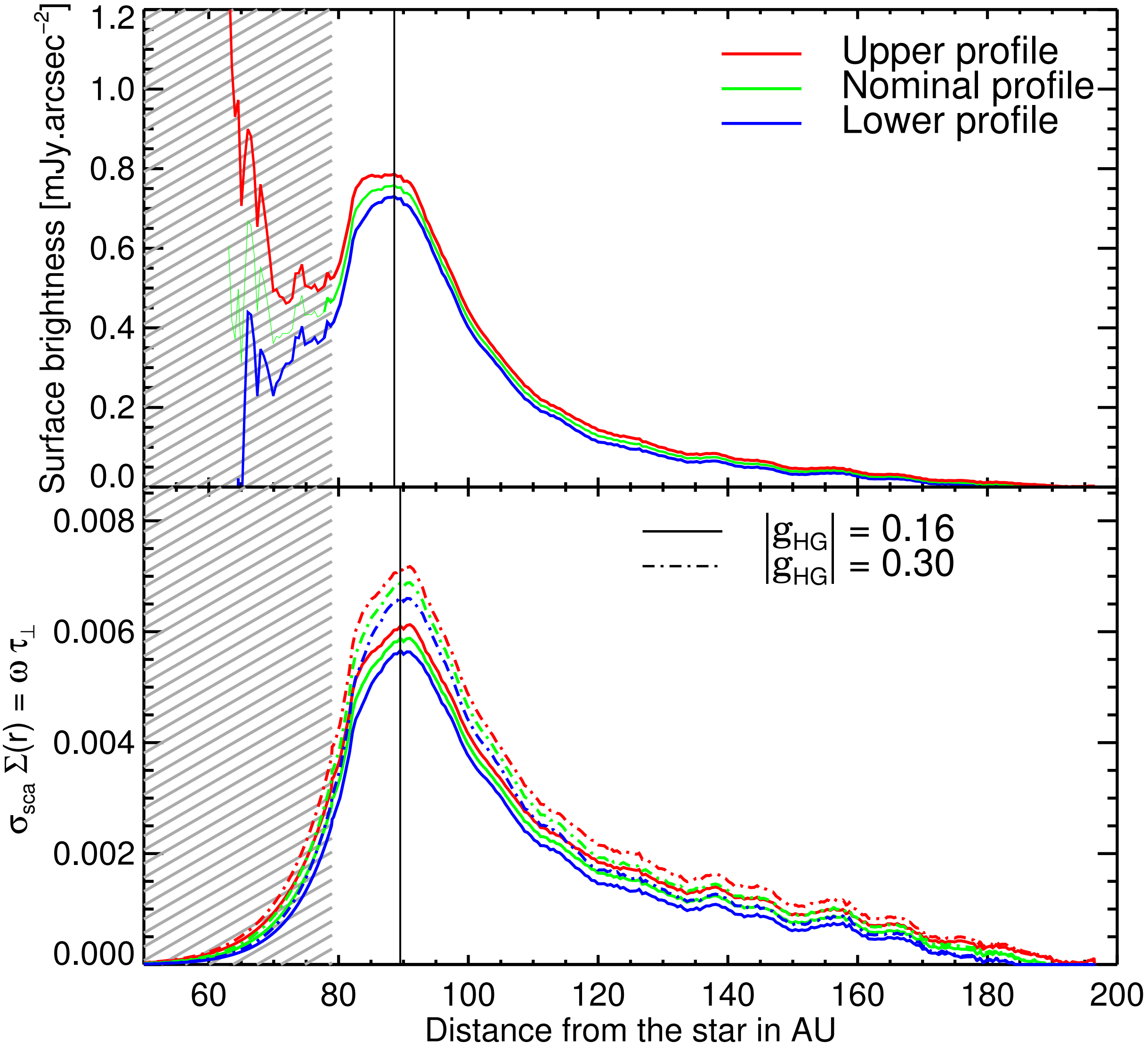

Figure 3.6: New HST/NICMOS 1.1 μm surface brightness profiles (**top**, nominal and $\pm 1\sigma$ profiles), and surface density profiles resulting from direct inversion of the brightness profiles (**bottom**), assuming two possible values for the asymmetry parameter. The color-coding is the same for both panels. The striped areas identify regions dominated by PSF-substraction residuals where the density has been extrapolated.

$\sim r^{+10\pm1}$. We extrapolate this profile interior to 78 AU as shown in Fig. 3.6 (striped area). This extrapolation is supported by the mid-IR results of Chen et al. (2008), who show that the inner part of the disk is largely cleared toward the center, containing little to no dust.

Outside of the belt peak position, the improved data reduction results in a profile that falls off as $\sim r^{-4.7\pm0.3}$ from ~92 to 162 AU, a steeper fall-off than the Schneider et al. (2006) original profiles ($\sim r^{-3}$). The dust is thus more tightly confined to the parent-belt than previously estimated, and the profile is also steeper than theoretical expectations. The exact value of the outer slope can only slightly impact the modelling results, as most of the emission arises from the inner part of the belt where the temperature is larger, except possibly for the longer-wavelengths.

Eventually, the differences between the several radial profiles in Fig. 3.6 essentially translate into a scaling factor that impacts the total disk mass estimate. We estimate that the uncertainty on the asymmetry parameter adds an additional ~4% to the uncertainty on our final mass values. The density profile obtained for $|g_{\mathrm{HG}}|$=0.30 is used in the rest of this study. We stress that, in order to focus on the other disk properties, we make the assumption that this profile is valid for any dust grain constrained by the SED, *i.e.* for grain sizes ranging from the micron to the millimetre scale. This assumption assumes no radial segregation in dust sizes and it remains reasonable as long as the flux at any wavelength arises predominantly from regions close to the density peak position (see Sec. 3.1.6).

Spectral Energy Distribution

The Herschel and ATCA data presented in this paper are complemented by IR and sub-mm data collected from the literature. These are listed in Table 3.4. The shortest wavelength flux we use is the 12 μm IRAS photometry for which the emission shows no excess from the stellar photosphere level. This observation is documented in Schneider et al. (2006) together with IR-excess from the IRAS Faint Source Catalogue and obtained with the Spitzer/MIPS instrument. These are complemented by ground-based mid-IR measurements performed with the T-ReCS imager on Gemini-S by Chen et al. (2008), and 13 points extracted from the 5–35 μm Spitzer/IRS spectrum that we reduced using the c2d Legacy team pipeline (Lahuis et al. 2006).

Additional MIPS observations were obtained in SED-mode by Chen et al. (2006) between 54.5 and 95.5 μm, well-constraining the shape of the disk SED around its maximum emission wavelength. Far-IR excess was reported by Moór et al. (2006) using the ISO database. The shape of the SED in the far-IR domain (100-200 μm) is well constrained by our new Herschel measurements.

Because the uncertainties on the dust optical constants at millimetre wavelengths are high, we chose not to use the ATCA flux to constrain the dust model (see Sec. 3.1.6 for a discussion on the compatibility of the model to these observations). Therefore, the sub-mm regime is only represented by a measurement with the LABOCA bolometer array at the 12-m telescope APEX (Nilsson et al. 2009, $\lambda \sim 870\,\mu$m), which thus represents a key piece of information. These archival data, together with our new observations, constitute the 49 measurements that are displayed in Fig. 3.7.

Star Properties and disk geometry

We derive excesses from a comparison of the SED with a synthetic stellar spectrum ex-

Table 3.4: HD 181327 photometric observations from the literature. The Herschel continuum values used for the dust modeling are in Tables 3.2 and 3.3.

Wavelength (μm)	Flux (Jy)	Uncertainty (Jy)	Instrument & Reference
12	0.114	0.011	IRAS [1]
15.0	0.094	0.004	Spitzer/IRS [2]
16.3	0.097	0.005	Spitzer/IRS [2]
17.4	0.107	0.005	Spitzer/IRS [2]
18.3	0.114	0.003	T-ReCS [3]
18.7	0.125	0.007	Spitzer/IRS [2]
19.8	0.144	0.009	Spitzer/IRS [2]
20.4	0.149	0.008	Spitzer/IRS [2]
21.1	0.157	0.020	Spitzer/IRS [2]
23.1	0.224	0.007	Spitzer/IRS [2]
23.7	0.223	0.009	Spitzer/MIPS [1]
25	0.306	0.024	IRAS [1]
25.7	0.303	0.014	Spitzer/IRS [2]
28.0	0.384	0.014	Spitzer/IRS [2]
30.6	0.488	0.026	Spitzer/IRS [2]
33.1	0.623	0.025	Spitzer/IRS [2]
35.5	0.718	0.034	Spitzer/IRS [2]
54.5	1.88	0.09	MIPS-SED [4]
58.0	1.83	0.07	MIPS-SED [4]
60	1.73	0.17	ISO [5]
61.4	1.98	0.08	MIPS-SED [4]
64.9	2.01	0.08	MIPS-SED [4]
68.4	1.98	0.08	MIPS-SED [4]
71.4	1.73	0.12	Spitzer/MIPS [1]
71.6	1.99	0.09	MIPS-SED [4]
75.1	1.93	0.10	MIPS-SED [4]
78.4	1.81	0.10	MIPS-SED [4]
81.8	1.72	0.11	MIPS-SED [4]
85.3	1.62	0.11	MIPS-SED [4]
88.8	1.47	0.11	MIPS-SED [4]
90	1.41	0.14	ISO [5]
92.0	1.46	0.13	MIPS-SED [4]
95.5	1.37	0.17	MIPS-SED [4]
100	1.7	0.2	IRAS [1]
155.9	0.77	0.09	Spitzer/MIPS[1]
170	0.736	0.192	ISO [5]
870	0.052	0.006	LABOCA [6]
3190	7.2×10^{-4}	2.5×10^{-4}	ATCA [7]

Notes and References – All uncertainties are 1σ and include absolute calibration error. [1] Schneider et al. (2006), [2] This study, data reduced with the Spitzer/c2d team pipeline (Lahuis et al. 2006), [3] Gemini, Chen et al. (2008), [4] Spitzer, Chen et al. (2006), [5] Moór et al. (2006), [6] APEX, Nilsson et al. (2009), [7] This study, Sec. 3.1.2.

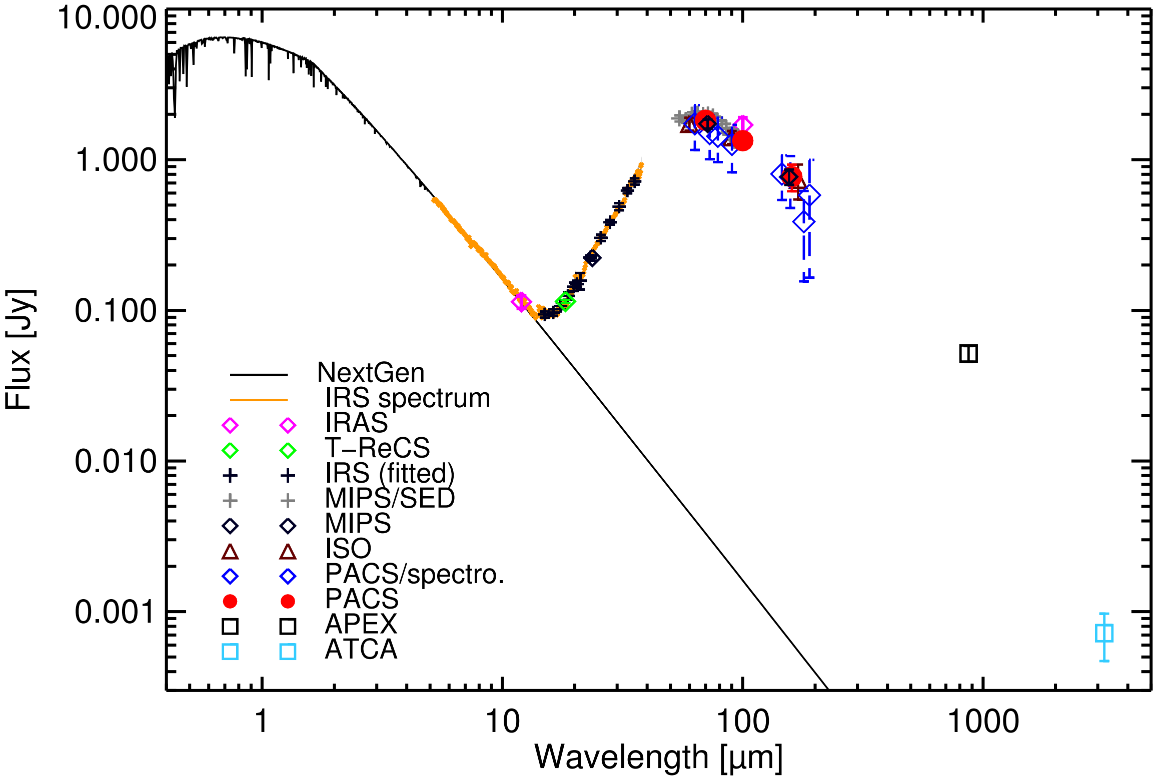

Figure 3.7: Observed Spectral Energy Distribution of HD 181327 (see Tables 3.2, 3.3 and 3.4)

tracted from the "NextGen" model atmosphere grid (Hauschildt et al. 1999b) and scaled to match the visible magnitude V = 7.0 mag (Bessell 2000), assuming $\log(g) = 4.5$, $T_{\text{eff}} = 6600$K, which leads to a stellar luminosity of $3.33\,L_\odot$ and a mass of $1.36\,M_\odot$. This stellar model shows good agreement with the Spitzer/IRS spectrum at wavelengths shorter than 10–15 μm, longward of which the excess starts dominating over the stellar photospheric emission. The star properties and disk geometry adopted in this study are summarized in Table 3.1.

Table 3.5: Parameter space explored with GRaTeR, corresponding to a total of about 1,150,000 models. The volume fractions $v_{\rm Si}$, $v_{\rm C}$, $v_{\rm ice}$ and the porosity $\mathcal{P}$ are defined in Sec. 3.1.3 (Eq. 3.1)

	Description	Parameter	Explored range	Values	Distribution
Sec. 3.1.3	minimum grain size	$a_{\rm min}$ [μm]	$0.01\ldots100$	77	log
	size power law index	κ	$-6.0\ldots-2.5$	50	linear
	maximum grain size	$a_{\rm max}$ [mm]	7.8	fixed	–
	Disk mass up to 1 mm	$M_{\rm dust}$ [$M_\oplus$]	> 0	fitted	–
	1 AND 2-MATERIAL MODELS				
Sec. 3.1.4	Si+Amorphous C	ACAR volume fraction $v_{\rm C}$	$0.00\ldots1.00$	21	linear
Sec. 3.1.4	Si+amorphous ice	ice volume fraction $v_{\rm ice}$	$0.00\ldots0.90$	19	linear
Sec. 3.1.4	Si+crystalline ice	ice volume fraction $v_{\rm ice}$	$0.00\ldots0.90$	19	linear
Sec. 3.1.4	Porous Si	Porosity $\mathcal{P}$	$0.00\ldots0.99375^{\rm (a)}$	24	linear
	3 AND 4-MATERIAL MODELS				
Sec. 3.1.4	Si	astrosi volume fraction $v_{\rm Si}$	$1/3\times$(1-$v_{\rm ice}$)	–	–
	+amorphous C	am. carbon volume fraction $v_{\rm C}$	$2/3\times$(1-$v_{\rm ice}$)	–	–
	+amorphous ice	ice volume fraction $v_{\rm ice}$	$0.00\ldots0.90^{\rm (b)}$	12	linear
	+vacuum	Porosity $\mathcal{P}$	$0.00\ldots0.95^{\rm (c)}$	18	linear

NOTES – (a) 19 linearly distributed points from 0.00 to 0.95 + additional high porosity points : 0.96875, 0.975, 0.9875, 0.99375. (b) 10 linearly distributed points from 0.00 to 0.90 + additional points at 0.65 and 0.75. (c) 10 linearly distributed points from 0.00 to 0.90 + additional points at 0.45, 0.55, 0.625, 0.65, 0.675, 0.75, 0.85, 0.95.

Dust Properties: Size Distribution and Composition
For both the dust and gas modeling, we make the assumption that the grain population has a single differential size distribution valid anywhere in the ring. This is a central hypothesis that necessarily limits the uniqueness of the solution. We discuss its impact in Sec. 5.6. The differential size distribution follows a classical power law $\mathrm{d}n(a) \propto a^{\kappa}\mathrm{d}a$, from a minimum size $a_{\rm min}$ to a maximum size $a_{\rm max}$. The minimum grain size $a_{\rm min}$ and the power law exponent κ are free parameters that are constrained by the SED fitting (Sec. 3.1.4). The maximum grain size $a_{\rm max}$ is a fixed parameter, sufficiently large so that it does not affect the light emission properties at the wavelengths considered (we chose $a_{\rm max} \sim 8\,\mathrm{mm}$). For standard κ values (close to -3.5 or smaller), the mass of solid material in a debris disk can be "arbitrarily" large depending on the assumed higher cut-off value of the size distribution (that can extend up to planetesimal sizes). In this article, we define the dust mass $M_{\rm dust}$ as the total mass of material contained in grains smaller than 1 mm. This definition has been followed within the GASPS consortium because it allows direct comparison between different studies independently from the model assumptions.

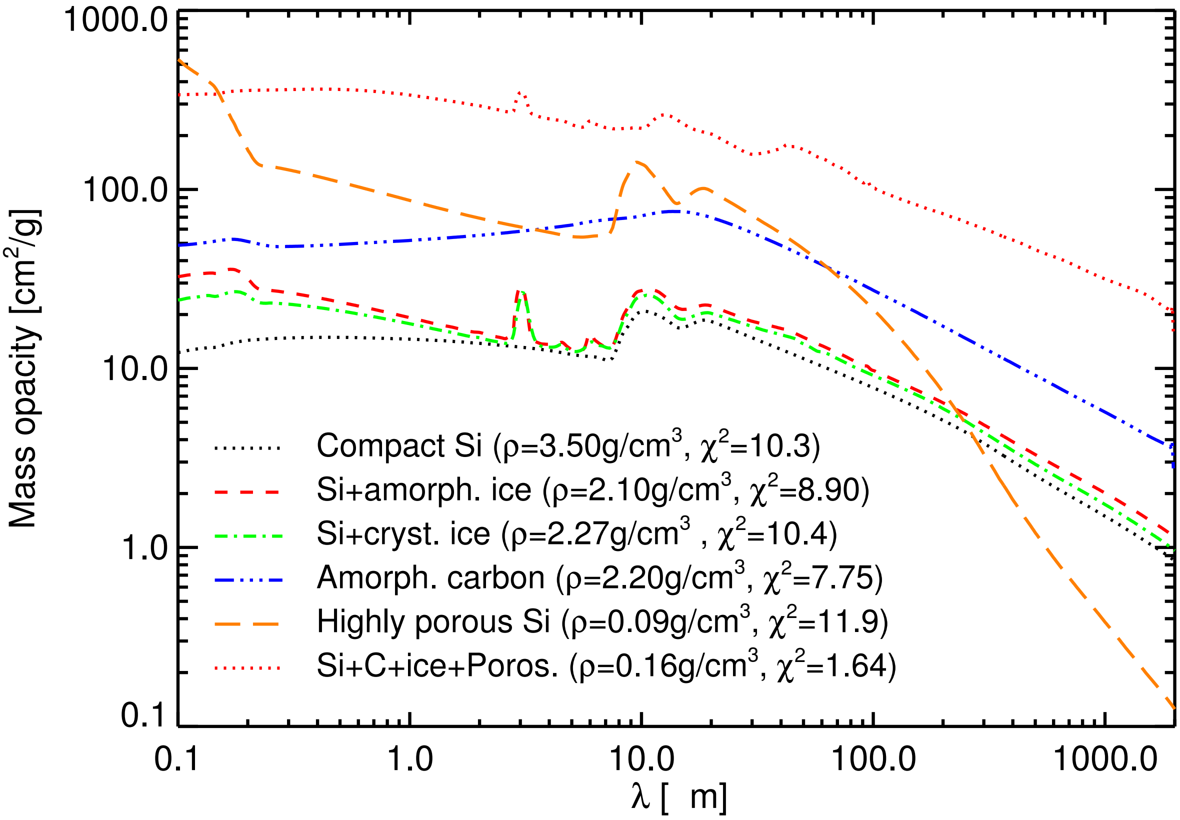

Figure 3.8: Mass opacity of spherical grains computed with the Mie theory and Bruggeman mixing rule for several prototypical compositions detailed in Tab. 3.6 and their associated best-fit size distributions.

We adopt a complex grain model that bears some similarities to those succesfully employed by several authors for fitting SEDs of young debris disks (Li & Greenberg 1998; Augereau et al. 1999; Li & Lunine 2003a,b), and for fitting scattered light disk colors (Köhler et al. 2008). We consider icy porous aggregates, with silicate cores and organic refractory mantles (or simplified versions of this model; see Sec. 3.1.4), to mimic fluffy particles made of essentially unalterred interstellar material (the so-called "cold-coagulation" dust model in Li & Lunine 2003a,b). Assuming cosmic abundances, the volume of the carbonaceous mantle $V_{\rm C}$ is estimated to be ~ 2.12 times that of the silicate core $V_{\rm Si}$ in the interstellar medium, a value similar to the one derived from the mass spectra of comet Halley in the Solar System ($V_{\rm C}/V_{\rm Si} \sim 2$, Greenberg 1998).

To calculate the optical properties, we use a number of representative materials with well established optical indexes. These are either derived from laboratory measurements or from observational and analytical arguments. The materials are: (1) the astronomical silicates (astroSi) from Draine (2003), a theoretical material consisting of amorphous silicates polluted by carbonaceous materials and other metals ($\rho = 3.5$ g.cm^{-3}); (2) the ACAR sample of amorphous carbon from Zubko et al. (1996) as organic refractories ($\rho = 1.95$ g.cm^{-3}); (3) the H_2O-dominated ice from Li & Greenberg (1998) (amorphous ice, $\rho = 1.2$ g.cm^{-3}); and (4) the crystalline water ice from Warren (1984) ($\rho = 0.92$ g.cm^{-3}).

The optical indexes of an aggregate are obtained using a standard effective medium theory (EMT), the Bruggeman mixing rule (Bohren & Huffman 1983), and following the methodology of Li & Greenberg (1998) and Augereau et al. (1999). The optical properties are computed with Mie theory valid for hard spheres. The EMT-Mie combination has been shown to be a good approximation for the absorption and scattering efficiencies, provided that grain shapes are close to ellipsoids such that the porosity can effectively be seen as the volume fraction of vacuum (Shen et al. 2009, and references therein). In fact, Shen et al. (2009) show that only the polarization and the phase functions are significantly sensitive to grain shapes. We define the composition of a grain through the volume fractions of its different components :

$$v_{\rm Si} = \frac{V_{\rm Si}}{V_{\rm mat}},\ v_{\rm C} = \frac{V_{\rm C}}{V_{\rm mat}},\ v_{\rm ice} = \frac{V_{\rm ice}}{V_{\rm mat}},\ \mathcal{P} = \frac{V_{\rm vac}}{V_{\rm mat} + V_{\rm vac}} \tag{3.1}$$

where $V_{\rm Si}$, $V_{\rm C}$, $V_{\rm ice}$ and $V_{\rm vac}$ are the total volume of astronomical silicates, carbonaceous material, ice and vacuum in the grain, respectively, and $V_{\rm mat} = V_{\rm Si} + V_{\rm C} + V_{\rm ice}$ is the total volume of solid material. $\mathcal{P}$ denotes the porosity. Should one of the materials within the grains reach its sublimation temperature, it is replaced by vacuum and the optical properties are adjusted accordingly in the model. In most cases however, the disk is too cold for any material to sublimate. Fig. 3.8 shows the mass opacity (absorption cross section per unit mass) calculated using Eq. 4 of Draine (2006) for several prototypical dust compositions, with the size distributions given in Tab. 3.6.

3.1.4 Modeling the Dust Continuum Emission

We use the GRaTer code (Augereau et al. 1999) to compute a grid of models with a goal of reproducing the HD 181327 Spectral Energy Distribution. GRaTer is a SED, image and interferometric data fitter, specially designed to efficiently model optically thin disks with parametric grain size and radial distributions, or distributions from dynamical simulations. The code accounts for both the scattered light and continuum emission of dust grains in thermal equilibrium with a star.

In the present case, the spatial dust distribution is constrained by the resolved HST

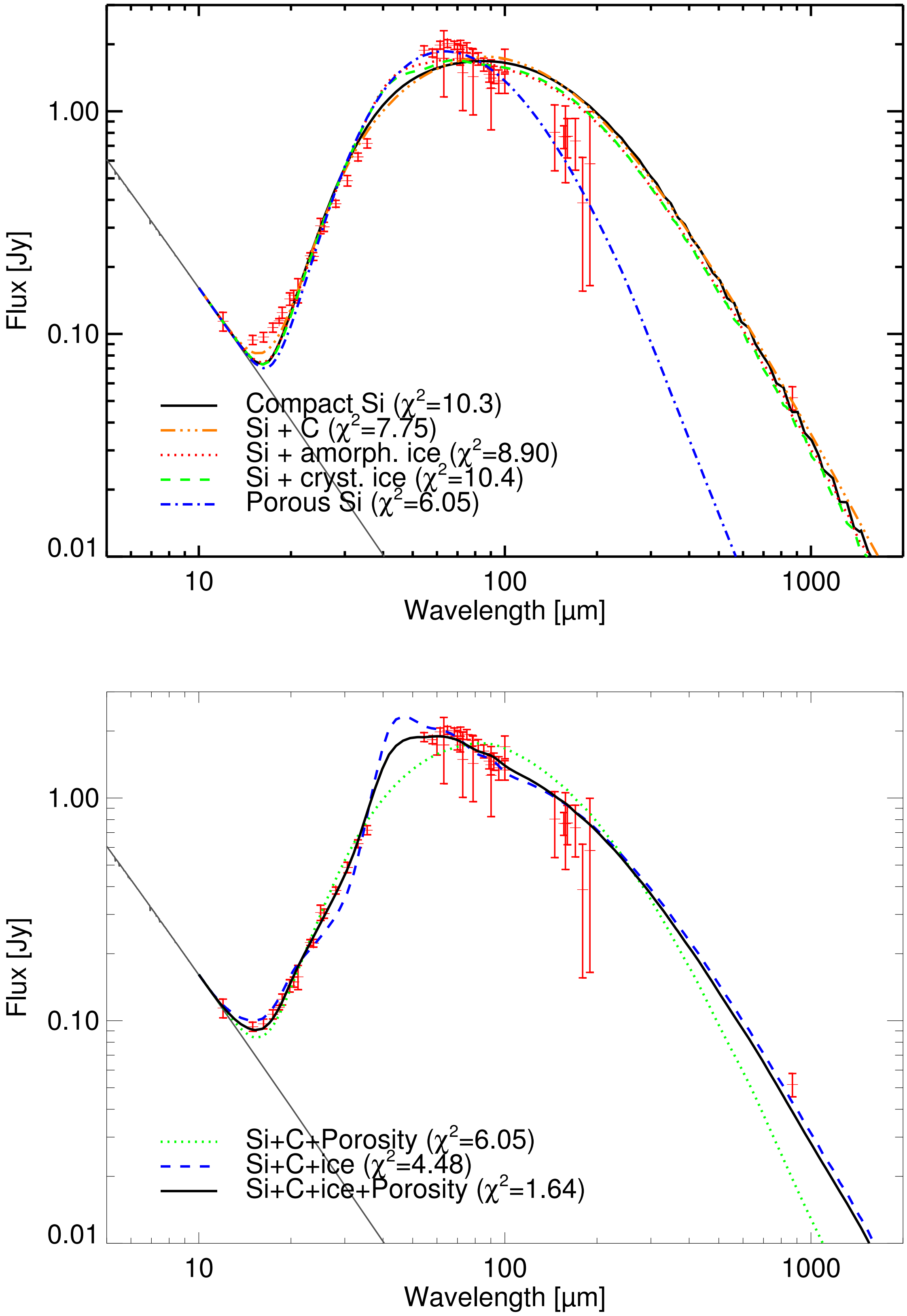

Figure 3.9: Best fit models (Table 3.6) for several 1- or 2-material mixtures (**top**) and 3- to 4-material mixtures (**bottom**). Red crosses: photometric data (Fig. 3.7). Solid grey line: synthetic stellar spectrum.

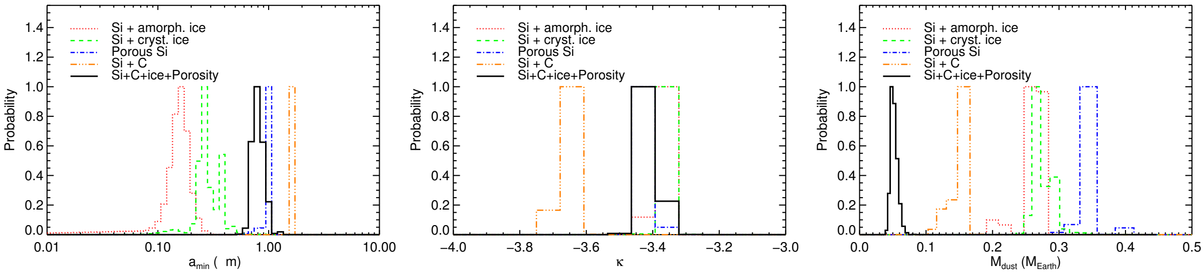

Figure 3.10: Bayesian probabilities for the models in Table 3.6: minimum grain size, size distribution power law index, and total dust mass.

images (Sec. 3.1.3, Fig. 3.6). The surface density profile derived from inverting the observed surface brightness was imposed in the model. Our study of the disk continuum emission focuses on the properties of the dust particles, namely their size distribution and composition. To that end, we computed large grids of models reflecting various possible dust properties, starting from the simplest composition (astronomical silicates) and progressively increasing the model complexity until obtaining a good match to the SED. For each model, the dust mass $M_{\rm dust}$ and the quality of the fitting are obtained from linear least-square fit between the observed and the synthetic SEDs. The χ^2 listed in this section are obtained using the 48 data points presented in Tables 3.2, 3.3 and 3.4, and with the numbers of degrees of freedom listed in Table 3.6. We subsequently use a statistical (Bayesian) inference method to derive the probability distribution of each parameter.

In total we consider ~ 300 compositions, with 77×50 grain size distributions for each, leading to $\sim 1,150,000$ models. All the parameters of the grain models are summarized in Table 3.5.

Table 3.6: Best-fitting (*Best*, i.e. lowest χ^2_r) and most probable (*Proba*, i.e. highest probability) parameters assuming different grain compositions (see text for the definition of the parameters). The most probable parameters are given with 3-σ uncertainties. The volume fractions marked with the † symbol are imposed knowing the other free volume fractions.

Composition		v_Si	v_C	v_ice	$\mathcal{P}$	$a_\mathrm{min}(\mu\mathrm{m})$	κ	$M_\mathrm{dust}(\mathrm{M}_\oplus)$	χ^2_r
1-MATERIAL (dof = 45)									
Si	*Proba* :	1.00	–	–	–	0.99±0.13	-3.43±0.04	0.35±0.03	
	Best :	1.00	–	–	–	1.00	-3.42	0.35	10.3
C	*Proba* :	–	1.00	–	–	1.62±0.03	-3.65±0.07	0.15±0.03	
	Best :	–	1.00	–	–	1.62	−3.64	0.15	7.75
2-MATERIAL (dof = 44)									
Si+C (1)	*Proba* :	0.007†	0.99±0.04	–	–	1.62±0.03	-3.65±0.07	0.15±0.03	
Si+am.ice	*Proba* :	0.59†	–	0.41±0.05	–	0.15±0.13	-3.36±0.07	0.26±0.05	
	Best :	0.60	–	0.40	–	0.16	-3.35	0.26	8.90
Si+cr.ice	*Proba* :	0.67†	–	0.33±0.12	–	0.29±0.24	-3.35±0.02	0.27±0.04	
	Best :	0.65	–	0.35	–	0.26	-3.35	0.27	10.4
Si+$\mathcal{P}$	*Proba* :	0.94†	–	–	0.057±0.062	0.98±0.20	-3.42±0.05	0.35±0.04	
	Best :	0.025	–	–	0.975	0.010	-3.28	0.039	11.9
3-MATERIAL (dof = 44)									
Si+C+$\mathcal{P}$	*Proba* :	0.33†	0.67†	–	$0.95\pm6\times10^{-5}$	9.45±3.20	-3.13±0.09	0.042±0.001	
	Best :	0.33†	0.67†	–	0.95	10.0	-3.14	0.042	6.05
Si+C+ice	*Proba* :	0.07†	0.13†	0.700±0.002	–	0.78±0.04	-3.50±0.03	0.11±0.01	
	Best :	0.07†	0.13†	0.80	–	0.55	-3.42	0.11	4.48
4-MATERIAL (dof = 43)									
Si+C+ice+$\mathcal{P}$	*Proba* :	0.11†	0.22†	0.67±0.07	0.63±0.21	0.81±0.31	-3.41±0.09	0.051±0.016	
	Best :	0.12†	0.23†	0.65	0.65	0.89	-3.42	0.048	1.64

NOTES

– "dof" means degrees of freedom. (1) The best fit for the Si+C mixture is obtained for silicate-free grains. The best-fitting parameters for that solution are given in the 1-MATERIAL part of the table.

First Steps Toward a Complex Dust Model

We start by fitting the HD 181327 SED with a single- or two-material grain model, which show the need for a more complex dust model. We consider several mixtures of the materials presented in Sec. 3.1.3 to assess the broad properties of the grains. The model then includes 3 or 4 free parameters: (1) the minimum grain size $a_{\rm min}$; (2) the slope of the size distribution κ; (3) the total mass of the disk $M_{\rm dust}$; and in the case of 2-component grains: (4) the volume fraction of either carbon ($v_{\rm C}$) or ice ($v_{\rm ice}$), or the porosity ($\mathcal{P}$). The detailed results of the investigation are summarized in Table 3.6, the best-fitting SEDs are displayed in Fig. 3.9 (top panel) and probability curves are shown in Fig. 3.11.

Silicates or Organic Refractories?

The most basic grain model to consider is the case of compact spheres made of pure astronomical silicates (astroSi), a configuration that is often used by default in many modeling approaches. We let $a_{\rm min}$, κ and $M_{\rm dust}$ vary and we compute a grid of χ^2 on which we apply a Bayesian analysis. We find that pure astronomical silicate grains would have $a_{\rm min} = 0.99 \pm 0.13\,\mu$m and $\kappa = -3.43 \pm 0.04$, leading to a total dust mass $M_{\rm dust} = 0.35 \pm 0.03 M_{\oplus}$ for grains smaller than 1 mm (Tab. 3.6). These values are consistent with the ones typically found for debris disks, but they actually lead to very poor fits, as illustrated in Figure 3.9 (top panel) where the model with the smallest χ^2 ($\chi^2_{\rm r} = 10.3$) is displayed. Although the model is in fairly good agreement with the data over the full spectral range and agrees well with the sub-mm measurement, it fails to reproduce the shape of the emission peak at $\sim 50 - 100\,\mu$m and the mid-IR fluxes, shifting the dominant part of the disk to colder temperatures. It overestimates by 30-40% the excess at far-IR wavelengths ($\lambda \sim 100 - 160\,\mu$m), in particular the Herschel/PACS measurements.

We take a further step and consider mixtures of amorphous silicates and carbonaceous materials. We ran a Bayesian analysis and find that the actual best composition corresponds to pure carbon. Qualitatively, the effect on the SED is not significant (see Fig. 3.9, top panel), even if it leads to a better minimum chi-square ($\chi^2_{\rm r} = 7.75$). This model gets closer to the measured fluxes at the peak emission ($\lambda \sim 50 - 100\ \mu$m), but does not provide an overall good fit. The addition of carbonaceous material slightly shifts the best fit parameters of the grain size distribution (Tab. 3.6), resulting in slightly larger $a_{\rm min}$ values and slightly steeper size distributions.

Icy Grains?

Chen et al. (2008) suggested that HD 181327 may contain a significant fraction of water in the form of crystalline ice, producing a broad peak in the combined Spitzer/IRS (5-35 μm) and MIPS-SED (60-77 μm) spectrum. To assess the presence of water ice in the debris disk of HD 181327, we model the disk with grains made of a mixture of astronomical silicates and water ice, either in the form of amorphous ice or crystalline ice.

The results of the statistical analysis are documented in Table 3.6. The quality of the fit is only slightly improved compared to the pure silicate model: the best models have $\chi^2_{\rm r} = 8.90$ for amorphous ice, $\chi^2_{\rm r} = 10.4$ for crystalline ice. In fact, the addition of water ice, crystalline or amorphous, does not modify the general shape of the synthetic SED (see Fig. 3.9, top panel). The smallest χ^2 calculated with amorphous ice is slightly smaller than the one of crystalline ice, but in both cases the values are too high to accept these models.

Porous Grains?

As a final step in our preliminary study of the dust composition, we consider a grid of models consisting of silicate grains with different porosities, from compact silicates to extremely fluffy silicate grains ($\mathcal{P}_{\rm max} = 99.375\%$). The marginal probability distribution for the porosity $\mathcal{P}$ reveals a bimodal probability distribution: the most probable models are the ones with either no porosity (discussed in Sec. 3.1.4), or very high porosity ($\mathcal{P} = 97.5\%$). Both solutions are presented in Tab. 3.6. A visual inspection of Figure 3.9 resolves the ambiguity. The compact grain model better reproduces the minimum and maximum wavelength ends of the SED, and in particular fits the sub-mm point, but it fails at reproducing the intermediate wavelength range around the emission peak. On the other hand, the highly porous grain model is orders of magnitude below the observed value at 870 μm, but it is within the error bars in the other regions of the SED, especially at Herschel wavelengths. In sum, none of these models lead to overall good fits to the whole SED.

Construction of an Advanced Grain Model

From what precedes, we conclude that none of the 2-component mixtures considered are sufficient to provide a satisfactory fit to the SED. This is essentially a consequence of the disk surface density being known *a priori* in this model; it cannot be adjusted to compensate for the emission properties of the dust grains. We note, however, that the addition of one component to silicates, should it be carbonaceous material, amorphous ice, or porosity, provides some slight improvements. This suggests that their combined effect could produce a more realistic model.

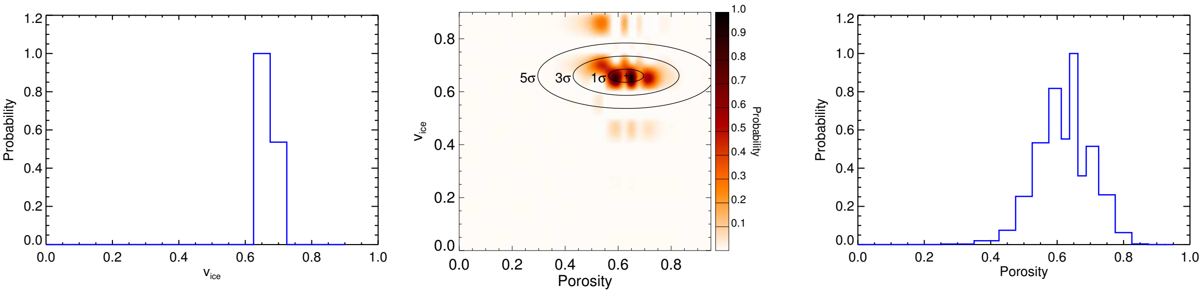

Figure 3.11: Bayesian probabilities for the grain composition in the case of 4-material dust mixtures.

We evaluate the improvement provided by a 3-component mixture on the fitting of the SED. We showed in Sec. 3.1.4 that it is not clear how to disentangle the respective contribution of silicates and organic materials by looking at the SED. Instead of including an additional free parameter, we consider grains (approximately) in fixed Si/C ratio described in Sec. 3.1.3 ($v_{\rm C}/v_{\rm Si} = 2$), and we restrict the discussion to the ice fraction and the porosity of the grains. We thus assume that grains are made of silicate and carbonaceous material, which are either icy ($v_{\rm ice}$ parameter) or porous ($\mathcal{P}$ parameter). The results are reported in Tab. 3.6. For porous ice-free grains, the best model is found for a porosity $\mathcal{P} = 95\%$ and leads to some improvement to the fit with $\chi^2_{\rm r} = 6.05$. If we now consider only compact icy grains, we can achieve a very reasonable $\chi^2_{\rm r} = 4.48$ with comparison to previous models, assuming an amorphous ice fraction $v_{\rm ice} = 0.7$. Overall, both the addition of either water ice or vacuum to silicate + carbonaceous grains do contribute to improving the fit to the SED of HD 181327. This can can be seen in Figure 3.9 (bottom panel). Nevertheless, the fits are still unsatisfactory ($\chi^2_{\rm r}$ much larger than 1), and justify an even more advanced dust model.

We next consider a 4-component grain model inspired by the "cold coagulation dust model" by Li & Lunine (2003a,b), which has been successfully employed for modeling debris disks (Li & Greenberg 1998; Augereau et al. 1999; Li & Lunine 2003a,b; Köhler et al. 2008). We keep the Si/C volume ratio fixed ($v_{\rm Si}$:$v_{\rm C}$=1:2) and let both the ice fraction and the porosity vary, in addition to the other usual free parameters in this study, namely the minimum grain size $a_{\rm min}$, the slope of the size distribution κ, and the total mass of the disk $M_{\rm dust}$. This leads to a five-free-parameter disk model to fit the 48 data points in the SED. We compute three grids of models corresponding to the three surface density profiles shown in Fig. 3.6 for $|g_{\rm HG}| = 0.30$ (i.e. the nominal and $\pm 1\sigma$ profiles). The Bayesian analysis is then applied to the 3 grids separately and the probabilities for each point of the parameter space are calculated as the sum of the probabilities for the 3 profiles. The detailed results are documented in Tab. 3.6.

Figure 3.11 presents the results of the Bayesian analysis on the composition of the dust grains, with a 2D-map showing the probability as a function of $\mathcal{P}$ and $v_{\rm ice}$ for the grid models, after projection of the probabilities over the other parameters. It clearly illustrates the need for a composition within a limited range of possible values. In particular, the fraction of H_2O-dominated ices is well defined: the probability peak is obtained for an ice fraction $v_{\rm ice} = 0.67 \pm 0.07$. The porosity is not so strongly constrained but we find a peak of probability for $\mathcal{P} = 0.63 \pm 0.21$. The best fit model in terms of χ^2 is found for grains made of 23% carbonaceous materials, 12% silicates, 65% ice, and with a porosity $\mathcal{P} = 65\%$. As can be seen in the bottom panel of Figure 3.9, for such grains, the synthetic SED very reliably describes the observed SED from the mid-IR to the sub-mm, with $\chi^2_{\rm r} = 1.64$, a value significantly better than those obtained for simpler grain models. The grain size distribution derived from the statistical analysis has $a_{\rm min} = 0.81 \pm 0.31$ μm and $\kappa = -3.41 \pm 0.09$, a power law index very consistent with that predicted for theoretical collisional cascades ($\kappa = -3.5$). The mass in grains smaller than 1 mm, $M_{\rm dust} = 0.051 \pm 0.016\, M_{\oplus}$, may look surprisingly small at first glance compared to the other models, but it results from the significant fractions of ice and vacuum in the grains, implying larger mass opacities (Fig. 3.8). The temperature of the grains at the surface density peak position (89.5 AU) ranges from 86 K for the smallest grains to 40 K for $\sim$ 8 mm-sized grains.

To summarize, our approach, based on a fixed surface density profile constrained by resolved imagery of the disk, clearly highlights the need to consider the presence of both ice and porosity to find an overall good fit to the SED. Icy grains are naturally expected at such a large distance from a solar-type star and the fluffiness of the grains is likely a by-product of their formation process. We applied a similar cold-coagulation dust model as Li & Lunine (2003a) did fitting the very young HD 141569A debris disk, except that we used no *a priori* assumption on the ice fraction, but with arguing the grain composition must reflect the primordial abundances of condensable elements, they chose $v_{\rm ice} \approx 30\%$ for cold regions and they find a best-fitting porosity $\mathcal{P} \approx 0.8$. Hence we propose a dust model that is especially ice-rich with a degree of porosity that is not unexpected. Further comparisons with the literature and implications on the nature of the dust are discussed in more details in Sec. 5.6.

3.1.5 Limits on the Gas Content

At 12 Myr-old, HD 181327 offers a chance to assess the amount of gas in a young debris disk, at a time when, according to planet formation theories, the accretion of gas by giant planets has already occurred while the formation of rocky planets might be ongoing.

We use the upper limits on the oxygen and ionized carbon fine-structure lines ([O I] at 63 and 145 μm, and [C II] at 158 μm, see Tab. 3.3) to constrain the amount of gas present in the disk. We solve the photochemistry and energy balance in the disk using the photochemical code ProDiMo [3]. The abundance of 71 species is computed in steady-state, under the influence of adsorption, desorption (thermal, photo and cosmic-ray induced), and molecular hydrogen formation on grain surfaces.

The gas density profile is supposed to match the one of the dust, as presented in Sec. 3.1.3. The total mass of *solid* (defined as the mass in grains from 0.81 μm to 8 mm) is constrained by the best dust model of Sec. 3.1.4 ($M_{\rm solid} = 4.9 \times 10^{-7}$ M$_\odot$ = 0.164 M$_\oplus$) and we let the total atomic+molecular gas mass $M_{\rm gas}$ vary from a gas-poor disk ($M_{\rm gas}/M_{\rm solid}$=$10^{-2}$) to a gas-rich disk ($M_{\rm gas}/M_{\rm solid}$=$10^3$). The parameters of the model are summarized in Tab. 3.7. One of the main parameters controlling the gas energy balance is the amount of PAHs ($f_{\rm PAH}$), which remains unconstrained in the disk of HD 181327 because their abundance is too small to produce detectable PAH emission features in the IR. We adopted two "extreme" values for $f_{\rm PAH}$: a low PAH abundance ($f_{\rm PAH}$=10^{-5}) and a high PAH abundance ($f_{\rm PAH}$=0.1) [4].

The non-LTE line fluxes for the [O I], [C II], CO J=3 → 2, and CO J=2 → 1 transitions are given in Fig. 3.12 and Table 3.8. Among all the lines, only the CO J=3 → 2 and J=2 → 1 line fluxes behave monotonically, increasing in flux with increasing disk mass. The reasons for the apparent erratic behaviour of the fine-structure lines come from the non-linear nature of several physico-chemical phenomena. For example, the [C II] flux depends on the abundance of C$^+$ and on the excitation of the first energy level. The C$^+$ abundance first increases with total gas mass until CO self-shielding against photodissociation is efficient enough such that a significant fraction of C$^+$ is converted into neutral C and CO. The presence of CO also changes the heating and cooling balance, since the CO absorption of IR stellar photons becomes the main source of heating. The change from a disk with no CO self-shielding to a CO self-shielded disk manifests itself as a jump in CO fluxes between a disk with gas-to-solid ratio of 1 to a disk with gas-to-solid ratio of 10. The abundance of PAHs has a weak influence on the gas temperature because the small UV flux from a F5/F6 star without excess accretion luminosity cannot ionize PAHs. On the other extreme, when the gas mass is very small (at gas-to-solid mass ratio below 1), the PAH and molecular absorption heating are nonexistent. Photoelectric heating by large grains dominates and explains why the line fluxes are similar for the high and low PAH abundance models.

Line fluxes from models with $f_{\rm PAH}$=10^{-5} are consistent with the PACS upper limits for all gas-to-solid mass ratios (upper part of Table 3.8). Only in the case $f_{\rm PAH}$=0.1, the disk gas mass is constrained by [OI] at 63 μm to be below ∼17 M$_\oplus$ ($M_{\rm gas}/M_{\rm solid} \lesssim 10^2$, lower part of Tab. 3.8).

---

[3] Woitke et al. (2009) provide a detailed description of the code, with subsequent improvements described in Kamp et al. (2010), Thi et al. (2011), and Woitke et al. (2011).

[4] The high PAH abundance is an upper-limit to the amount of PAHs in HerbigAe disks, where it is found to be of the order of 0.1-0.01 (e.g., Meeus et al. 2010, $f_{\rm PAH}$=0.03 for HD 169142).

Eventually, even if the integration of the [O I] 63 and 145 μm, and [C II] lines we performed was not sufficient to derive strong constraints on the gas-to-solid mass ratio in the disk, the combination of the GRaTeR and ProDiMo codes proved efficient to make predictions on the fluxes in the CO J=3 → 2 and J=2 → 1 lines. These lines will be detectable for instance by ALMA, finally allowing to assess the gas content of the debris disk.

Table 3.7: Setup of ProDiMo for the gas disk model

Parameter	Value
Elemental abundances	ISM-like
UV field	1 Habing field $^{(a)}$
Cosmic-ray ionization rate ζ	1.7×10^{-17} s^{-1} $^{(b)}$
Non-thermal line width dv	0.15 km.s^{-1}
$f_{\rm PAH}$ $^{(c)}$	10^{-5} - 10^{-1}

$^{(a)}$ Dalgarno (2006), $^{(b)}$ Standard interstellar UV field, $^{(c)}$ $f_{\rm PAH}$ scales with the gas mass and is defined with respect to an interstellar abundance of 3×10^{-7}.

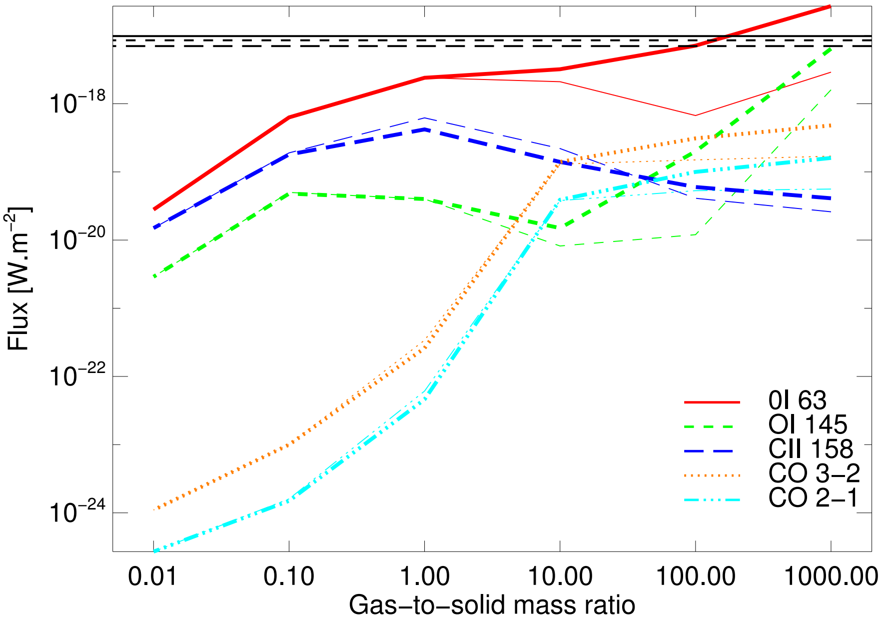

Figure 3.12: Expected gas line fluxes as a function of gas-to-solid mass ratio for either a low-PAH abundance (thin lines) or a high-PAH abundance (thick lines). The horizontal lines denote the PACS 3σ upper-limits and do not include the 30% flux calibration uncertainty. The gas-to-solid mass ratios assume a solid mass of 0.164 $M_\oplus$.

3.1.6 Additional constraints on the disk

Scattered light: evidence for irregular aggregates

The surface density profile used in this study comes from a new reduction of the scattered

Table 3.8: Gas line fluxes. The gas to solid mass ratios assume a solid mass of 0.164 $M_\oplus$. The PACS 3-σ upper limits do not include the 30% flux calibration uncertainty.

Gas-to-Solid mass ratio	[O I] 63μm (W m^{-2})	[O I] 145μm (W m^{-2})	[C II] 158μm (W m^{-2})	CO J=3 → 2 (W m^{-2})	CO J=2 → 1 (W m^{-2})
	Herschel-PACS (3σ)				
	9.8×10^{-18}	8.5×10^{-18}	7.0×10^{-18}	-	-
	ProDiMo predictions with $f_{\rm PAH}$=10^{-5}				
1000	2.9×10^{-18}	1.6×10^{-18}	2.6×10^{-20}	1.7×10^{-19}	5.6×10^{-20}
100	6.7×10^{-19}	1.2×10^{-20}	4.1×10^{-20}	1.5×10^{-19}	5.3×10^{-20}
10	2.1×10^{-18}	8.2×10^{-21}	2.2×10^{-19}	1.3×10^{-19}	3.8×10^{-20}
1	2.4×10^{-18}	4.0×10^{-20}	6.2×10^{-19}	3.4×10^{-22}	6.1×10^{-23}
0.1	6.4×10^{-19}	5.0×10^{-20}	1.9×10^{-19}	1.0×10^{-23}	1.6×10^{-24}
0.01	2.8×10^{-20}	2.9×10^{-21}	1.5×10^{-20}	1.1×10^{-24}	2.7×10^{-25}
	ProDiMo predictions with $f_{\rm PAH}$=0.1				
1000	2.7×10^{-17}	6.4×10^{-18}	4.1×10^{-20}	4.8×10^{-19}	1.6×10^{-19}
100	7.1×10^{-18}	2.0×10^{-19}	6.0×10^{-20}	3.1×10^{-19}	1.0×10^{-19}
10	3.2×10^{-18}	1.5×10^{-20}	1.4×10^{-19}	1.4×10^{-19}	3.9×10^{-20}
1	2.4×10^{-18}	4.0×10^{-20}	4.2×10^{-19}	2.6×10^{-22}	4.6×10^{-23}
0.1	6.3×10^{-19}	4.8×10^{-20}	1.8×10^{-19}	1.0×10^{-23}	1.5×10^{-24}
0.01	2.8×10^{-20}	2.9×10^{-21}	1.5×10^{-20}	1.1×10^{-24}	2.7×10^{-25}

light images of Schneider et al. (2006) obtained with HST/NICMOS (see Sec. 3.1.3). This ensures by definition that the shape of any synthetic scattered light surface brightness profile in this study perfectly agrees with the observed profile at $1.1\,\mu$m. However, the consistency is limited to the shape, and the agreement in terms of absolute flux is not guaranteed. This is because our fitting approach in Sec. 3.1.4 consists of adjusting the disk mass to get a best fit to the SED, which is equivalent to scaling up or down the surface density profile. A reason for adopting this strategy comes from the fact that the scattered light images do not directly provide the surface density $\Sigma(r)$, but its product by the mean scattering cross section $\sigma_{\rm sca}$ at the observing wavelength ($1.1\,\mu$m). The fitting process to the SED, on the other hand, yields an independent, absolute scaling of the surface density profile, thus allowing one to obtain an initial estimate of $\sigma_{\rm sca}$. We find $\sigma_{\rm sca} = 3.7\,\mu\rm m^2$ in the NICMOS $1.1\,\mu$m band.

A second estimate of $\sigma_{\rm sca}$ is obtained by calculating the theoretical scattering cross section for compact spherical grains given the grain properties (composition, size distribution) that were inferred in Sec. 3.1.4: $\sigma_{\rm sca}(\lambda) = \int_{a=a_{\rm min}}^{a_{\rm max}} \pi a^2 Q_{\rm sca}(a,\lambda) {\rm d}n(a)$ where $Q_{\rm sca}$ is the scattering efficiency at wavelength λ and for a grain radius a. For the best model (in the Bayesian sense, Tab. 3.6) we find $\sigma_{\rm sca} = 16.8\,\mu\rm m^2$ at $1.1\,\mu$m, a factor of about 4.5 higher than the first estimate. This implies a peak flux density of 3.14 mJy.arcsec^{-1} inconsistent with the 0.76 mJy.arcsec^{-1} measured in the NICMOS profile. In other words, this means that our model predicts an albedo ($\omega = 59\%$ at $1.1\,\mu$m) that is a factor of about 4.5 larger than the observed value. This suggests that smaller grains than those required to fit the SED dominate the scattering behavior of the disk. It is worth noting that such a conclusion is not specific to HD 181327, but is also observed in other debris disks. Recent examples include HD 207129 for which Krist et al. (2010) predict an albedo (based on dust properties also obtained from a fit to the SED) that is an order of magnitude larger than the value suggested by the scattered light image. A similar inconsistency is noticed for HD 92945 by Golimowski et al. (2011) who point out that different observing diagnostics suggest different minimum grain size.

It is important to keep in mind that although our model suggests the grains are very porous and hence likely to have an irregular, fractal structure, we used hard spheres (Mie theory) to calculate both the thermal emission and scattered light optical properties. Unlike the thermal behavior, light scattering will likely strongly depend on the exact shape of the dust aggregates, and on the size of their elemental constituents, two features that are not accounted for by the Mie theory (Voshchinnikov et al. 2007). Another piece of evidence that Mie theory might be a limiting factor for a self-consistent model of HD 181327 comes from the observed scattering asymmetry parameter $g_{\rm HG}$ that is a measure of the direction of the light scattered by a particle. For our best model (Sec. 3.1.4) the Mie theory yields a mean scattering asymmetry parameter $|g_{\rm HG}|= 0.95$ at $\lambda = 1.1\,\mu$m, much larger than the $|g_{\rm HG}|= 0.30$ measured on the NICMOS image. Only a population of much smaller particles could produce such a low scattering asymmetry parameter if we stick to the Mie formalism, as already noted by Schneider et al. (2006). An analogous problem arises from the modeling of the debris disk of HD 92945 (Golimowski et al. 2011). Our micron-sized grains are highly anisotropic, essentially due to their spherical shapes. Incorporating vacuum homogeneously inside the grains does not suffice to decrease $|g_{\rm HG}|$ and a more accurate description of the shape of fluffy aggregates is eventually needed. In fact, the scattering efficiencies and asymmetry parameters of fluffy aggregates are known to be correctly described by an EMT-Mie model (porous spheres) only in the Rayleigh regime, *i.e.* when the size of the inclusion (vacuum here) is small compared to the wavelength (see e.g. Voshchinnikov et al. 2007). This is not the case for the relatively large grain sizes and porosity when the wavelength becomes small.

A narrower parent belt?

Unlike scattering, we expect the continuum thermal emission to be largely independent of the exact shape of the grains. Our best model of HD 181327's disk produces a sub-mm flux of 39 mJy at 870 μm, consistent within 2σ with the LABOCA measurement (52 ± 6 mJy). The ATCA measurement at 3.2 mm was not model-fitted, because of large uncertainties on the optical constants at millimetre wavelengths. As a sanity check, we calculate the flux in the ATCA band using a power-law extrapolation of the SED. In the far-IR to mm regime, the model emission declines as $\lambda^{-2.51\pm0.16}$[5]. This results in a flux equal to $1.6^{+0.4}_{-0.3}$ mJy, which is within $\sim 3\,\sigma$ compatible with the measured flux of 0.72 ± 0.25 mJy. Thus, the model remains valid for the longest wavelength observations (coldest emitting particles), showing that the ring resolved in the near-IR with the HST is compatible with the spatial distribution of the largest grains, at least at first order.

A limit of our approach is the assumption that the grain size distribution is the same everywhere in the disk, while it is known that only the smallest grains can populate the outer disk due to radiation pressure. The maximum size and power law slope of the dust size distribution should vary with the distance from the star (e.g. Fig. 4 in Augereau et al. 2001), whereas the model keeps both large grains in the outer disk and a constant slope for the size distribution. Such a radial variation of the size distribution is suggested by a comparison of a synthetic image at 70μm with the PACS 70 μm map (Sec. 3.1.2). The synthetic image appears broader than the observed one with a FWHM of 7.68″, versus 6.44″ for the PACS image. Our interpretation is that the PACS band reveals larger grains that experience less the force due to the radiation pressure and thus are more bound to the parent belt. Assuming all grains are equally distributed results in putting too many large grains in the outer disk: a more complex model should account for the true dynamics of the particles.

Emission from inside the belt?

The region of the disk interior to 75 AU cannot be reliably assessed from the NICMOS data because of the coronagraph and artefacts from the PSF-substraction interior to 1.5″ (78 AU). Therefore we cannot exclude the existence of an additional dust component interior to the main belt, that would be invisible in the surface density profile we use. If micron-sized grains populate the inner disk, they would radiate mainly in the mid-IR, which might affect the results of our study. From the Gemini/T-ReCS images of Chen et al. (2008), we estimate that less than ∼15% of the light emitted by the disk at 18.3 μm originates from a region interior to 1″ (Fig. 2 in Chen et al. 2008).

We perform a simple test of the robustness of our results. Suppose that a belt of black body dust particles is orbiting the star at a distance $r < 1''$. We calculate a black body spectrum that peaks at 18.3 μm ($T = 150$ K) and we adjust it such that its maximum flux represents 15% of the 53 mJy attributed to the disk at that wavelength. Then we subtract the black body flux from the observed SED of Tab. 3.4 to simulate an observation of the system excluding the hypothetical inner component. We reproduce the approach of Sec. 3.1.4 with this new SED. Interestingly the results of the Bayesian analysis are not

---

[5] Note that, at longer wavelengths, the emission seems to falls-off faster than a simple power-law.

significantly impacted. To account for the deficit of flux at mid-IR wavelengths, only the minimum grain size needs to be slightly adjusted to eliminate the smallest grains: $a_{\rm min} = 1.0\,\mu$m and $\kappa = -3.43$, while we have $a_{\rm min} = 0.89\,\mu$m and $\kappa = -3.42$ for our best fit (Tab. 3.6). The composition remains unchanged for the best model ($\chi^2_{\rm r} = 1.52$) and no change is induced that would improve the consistency of the model with the scattered light flux (Sec. 3.1.6). Consequently we cannot reject the possible existence of an inner component to the disk, but none of our conclusions would suffer from its existence.

3.1.6.1 Grain dynamics and ice origin

Blowout size

Grains in the HD 181327 debris disk for which radiation pressure overcomes gravity are put on unbound orbits and eventually ejected from the system on a short time scale (see for instance Krivov 2010, and ref. therein). The balance between radiation pressure ($F_{\rm P}$) and stellar gravity ($F_{\rm G}$) forces is evaluated with the distance independent, but size-dependent, $\beta_{\rm pr}$ factor, given by

$$\beta_{\rm pr} = \frac{|F_{\rm P}|}{|F_{\rm G}|} = \frac{\sigma}{m}\frac{\langle Q_{\rm pr}\rangle L_\star}{4\pi c G M_\star} \qquad (3.2)$$

where $\langle Q_{\rm pr}\rangle$ is the pressure efficiency averaged over the stellar spectrum, m the grain

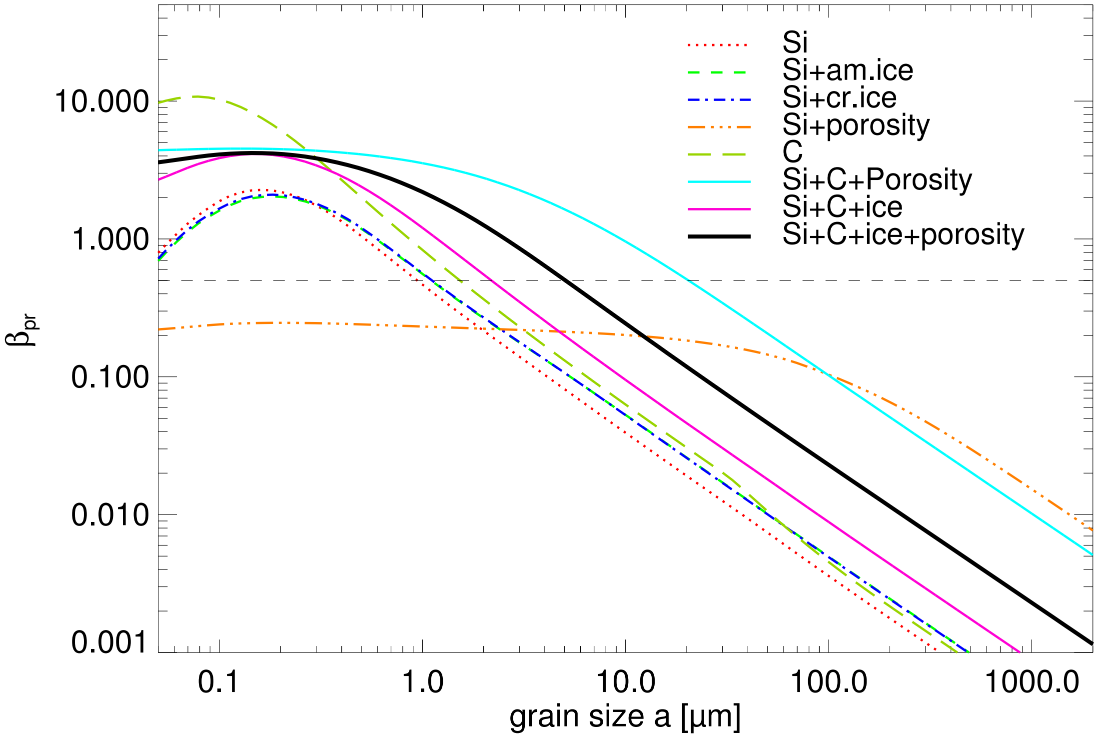

Figure 3.13: $\beta_{\rm pr} = |F_{\rm P}|/|F_{\rm G}|$ as a function of grain radius. The horizontal dashed line denotes the limit between bound ($\beta < 1/2$) and unbound ($\beta > 1/2$) grains.

mass, σ the grain geometrical cross section, c the speed of light, G the gravitational constant, and $L_\star$ and $M_\star$ documented in Tab. 3.1. Assuming that the grains are spherical, Eq. 3.2 yields a critical size below which the grains originating from the parent belt are ejected from the system: $a_{\rm blow} = a(\beta_{\rm pr} = 1/2)$ (assuming circular orbits for the parent bodies).

In Fig. 5.2, we represent the $\beta_{\rm pr}$ ratios as a function of grain radius for different compositions. Our best 4-component grain model has a blowout size $a_{\rm blow} = 4.83\,\mu$m, that is 5 times larger than the inferred minimum grain size in the system. Models implying no porosity nor carbon, on the other hand, have blowout sizes of the order of the inferred value of $a_{\rm min}$, more consistent with the theoretical argument that grains below the blowout size should be expelled from the system. The response of silicate grains to the stellar irradiation and gravity fields is only slightly affected by the presence of ice, leading to similar shape and moderated values for $\beta_{\rm pr}(a)$. Organic refractory grains on the other hand are highly sensitive to the radiation pressure and they can reach high $\beta_{\rm pr}$ values. Fig. 5.2 shows that porosity has the effect of flattening the $\beta_{\rm pr}(a)$ function, pushing the critical value $\beta_{\rm pr} = 1/2$ to larger grains. Hence the addition of porosity to a mixture of carbon and silicates produces a strong effect: $\beta_{\rm pr}$ not only reaches a high value at its maximum due to carbon, but the $\beta_{\rm pr}(a)$ function decreases slowly such that the critical value $\beta_{\rm pr} = 1/2$ is reached only for large grain sizes.

Decreasing the amount of carbon in the grains (it was imposed somehow arbitrarily, see Sec. 3.1.4) would mechanically decrease their blowout size. Pure silicate grains with the same porosity and ice content have $a_{\rm blow} = 0.89\,\mu$m, but they do not provide good fits to the SED. We computed additional grid of models with alternative $v_{\rm C}/v_{\rm Si}$ values. The results confirm the conclusion of Sec. 3.1.4: all Si+C+H_2O+porosity models lead to similarly good fits to the SED, as long as a sufficient fraction of carbon is considered. For instance, if silicates represent only 10% of the C+Si mixture, then $v_{\rm ice}$ remains at 0.65 and the porosity is reduced to 55%, with $M_{\rm dust} = 0.043\,M_\oplus$, $a_{\rm min} = 0.89\,\mu$m and $\chi^2_{\rm r} = 1.66$. All these values remain within the uncertainties of the original model. Models involving carbon-poor grains do not provide good fits to the SED, but as long as $v_{\rm C}/v_{\rm Si} \gtrsim 0.5$, the results remain unchanged. In summary, the discrepancy between $a_{\rm min}$ and $a_{\rm blow}$ does not lie on the hypothesis we made on the composition of the grains.

Our estimation of $a_{\rm blow}$ is based on the assumption that the grains are spherical and homogeneous, but the actual response of inhomogeneous aggregates to radiation pressure cannot be that simple. Saija et al. (2003) for instance show that the fluffiness of the grains tends to decrease their radiation pressure cross-section, as if aggregates behaved like their elemental constituents. This would make grains below the theoretical blowout size less sensitive to radiation pressure, and allow them to remain bound to the star. Thus the apparent inconsistency may be interpreted as another signpost of the complex structure of the grains. We emphasize that fixing $a_{\rm min}$ as equal to $a_{\rm blow}$ calculated with the (EMT-)Mie theory would not be a relevant approach when dealing with porous grains.

Another possibility is that grains are not in dynamical equilibrium (i.e. an imbalance between production and ejection), following for instance a major collisional event, such as an asteroid break-up. An excess of dust grains from all sizes would have been produced, including grains below the blowout size. These grains could have survived destructive collisions and radiation pressure blowing for long enough to be observed. Of course, observing such an event is unlikely, because dust typical lifetime is only of the order of 1,000 years, which is small with comparison to the age of the star (see Sec. 3.1.6.1). But this "rare event hypothesis" would be consistent the scenario proposed by Chen et al. (2008)

to justify the brightness asymmetry they claim to observe in thermal light.

Time scales and origin of the ice

Collisions occurring between grains in a debris disk are a key process as they generally result in the production of smaller dust particles, either by fragmentation of the target, or excavation. Any phenomenon longer than the characteristic collisional time scale will be considered negligible in the evolution of the dust population. Based on the principle that any particle will cross the disk midplane twice during one orbit, we use a simple estimate of the time scale for mutual collisions, valid for the smallest grains: $t_{\mathrm{col}} = t_{\mathrm{orbit}}/2\pi\tau_{\perp}^{\mathrm{geo}}$, with t_{orbit} the orbital period at the surface density peak, and $\tau_{\perp}^{\mathrm{geo}}$ the geometrical vertical optical depth (Thébault & Augereau 2007). Here the orbital period at 89.5 AU is $\sim$ 850 years, leading to $t_{\mathrm{col}} \sim 7600$ years for the best model. This is more than three orders of magnitude smaller than the age of the system and two orders of magnitude smaller than the characteristic time-scale for Poynting-Robertson drag: $t_{\mathrm{pr}} = 0.1$ Myr for $\beta_{\mathrm{pr}} = 1/2$ grains (Wyatt 2008). The evolution of the HD 181327 debris disk is clearly dominated by collisions requiring a mechanism to generate dust on a $10^3 - 10^4$ years characteristic time scale.

Attempts to model time-dependent chemistry with ProDiMo reveals that the grain water ice mantle would be photo-evaporated in a few hundred years (for $\sim 1\,\mu$m grains), to a few thousand years (for $\sim 10\,\mu$m grains), a similar (or shorter) time scale to the dust mutual collision, requiring as well an ice reprocessing mechanism. This provides a consistent view that the icy dust grains are maintained through collisions in a reservoir of icy planetesimals. We highlight that, while detecting the mid-infrared spectral features in the emission of a debris disk is very challenging – unambiguous detection have only been made in brighter circumstellar disks (see, e.g. Malfait et al. 1999) – the sole analysis of the continuum SED alone can provide clues on the amount of ice in dust disks, thus on the nature of the parent bodies, often referred to as the leftovers of planet formation.

In the Solar System Kuiper Belt, the study of icy planetesimals, Kuiper Belt Objects (KBOs) in particular, is a prolific topic (for a recent review see e.g. Jewitt 2010). The presence of ice, together with the porous nature of the objects, is inferred from estimates of their densities. Unambiguous detection of water ice has been made possible by the spectroscopic near-IR signature of crystalline ice, for instance by Delsanti et al. 2010 who completed their study of the plutino Orcus by radiative transfer considerations concluding that it contains a mixture dominated by amorphous and crystalline water ice. Confronted with space weathering, crystalline ice should be amorphidized in a short timescale. This implies that ice needs to be stored (and possibly produced) in the interior of the object before being brought to the surface, possibly through cryovolcanic events. The nature of water ice in KBOs remains unclear, but the vast majority of these objects are too small to experience such geological processes (Dumas et al. 2011, and references therein). Thus KBOs covered by crystalline ice can only constitute particular examples, and the water ice covering the collisionally produced dust in the Solar System is more likely amorphous. The young age of HD 181327 allows the possibility that primordial crystalline ice has survived in its debris disk. Our study tilts in favor of the amorphous nature of that ice, suggesting that either ice was predominantly incorporated in an amorphous form in HD 181327's Kuiper Belt objects, or that the amorphization timescale is shorter than $\sim$10 Myr in this distant belt.

3.1.7 Discussion

The properties of the HD 181327 debris disk can be compared to those of the disks surrounding two of its co-moving "sister" stars, β Pictoris (A3V, 1.7 $M_{\odot}$) and AU Microscopii (M1V, 0.5 $M_{\odot}$), which formed in the same molecular cloud from the same material and are coeval. Of course comparisons are limited by the specific models used to study each object. The relatively large porosity found here should be put in the context of the grain properties found for AU Mic (Graham et al. 2007; Fitzgerald et al. 2007). Assuming a Si+C+H_2O mixture, only highly porous grains ($\mathcal{P}$ = 80%), reproduces the scattered light profiles (exhibiting strong forward scattering), the high polarization and the thermal SED. In that model, the Mie theory remains valid to represent the scattering properties of porous grains, because the grains filling the outer disk are very small and stay in the Rayleigh regime. A total dust mass of $0.01 M_{\oplus}$ is found, that essentially reflects the contribution from the inner mm-sized grains, concentrated in a ∼40 AU belt. A similar porous grain model was used by Li & Greenberg (1998) to model β Pictoris yielding a dust mass ∼0.4 $M_{\oplus}$, contained in the ∼ 100 AU-wide outer disk. Overall, "cold coagulation-like" dust models prove effective at reproducing observations of these young debris disks. A trend appears for increasing dust mass with spectral type as could be intuitively expected, but despite this difference of scale, the three stars are orbited by a similar material.

Given the young age of these objects, we are investigating the conditions holding within disks just after the planetary embryos may have formed, the gas dispersed, and possible accretion onto outer giant planets happened. To explain the belt-like structure of the HD 181327 disk, the most straightforward explanation is to invoke the dynamical influence of a planet inside the belt. The Wisdom (1980) analytical criteria gives the width of the chaotic zone a planet mean-motion resonances would create. Assuming circular orbits for the planetesimals, as suggested by the sharpness of the belt, this yields a range of possible values for the planet semi-major axis depending on its mass. Assuming the inner edge of the disk is located at 78 AU from the star, the yet undiscovered planet would lie from 73 AU for a Neptune-mass planet, down to 59 AU for a 10 Jupiter-mass planet.

The material at that stage appears as very hydrated providing a considerable reservoir of water in the outer system. The existence of such a reservoir is hypothesized in scenarios of the Solar System formation to explain the unexpectedly large water content on Earth for instance (Morbidelli et al. 2000). Indeed, terrestrial planets at this age (12 Myr) are likely too hot to hold on to water and later impacts of icy comet-like bodies from the outer regions are a possible mechanism for delivering water and volatiles to planets in the habitable zone. Thus, not only HD 181327's debris disk reveals that the system has already grown planetary embryos – including maybe the bricks of rocky planets in the inner disk – but it likely holds the conditions that were prevailing before the Solar System Late Heavy Bombardment that depleted the Kuiper Belt and determined terrestrial planets history.

3.1.8 Summary and conclusions

We have presented new Herschel/PACS and ATCA imaging of the HD 181327 debris disk, a 12 Myr old star belonging to the β Pictoris moving group. The 70 and 100 μm images as well as the 3.2 millimetre observation reveal a marginally resolved extended emission. Fluxes in the three PACS photometric channels were derived and complemented by continuum fluxes obtained from PACS spectroscopic observations. Together, these data provide precise information on the continuum thermal emission of the debris disk, but detailed models such as the one developed in this study are required to interpret the precise nature of the emitting material. Degeneracies between the grain properties and disk's spatial structure are broken in our model by making use of a reprocessed HST/NICMOS coronagraphic image revealing that the dust is bound to a narrow belt peaking at 89.5 AU from the central star. We focus our study on the dust properties (composition, size distribution) using a radiative transfer code, and run a large grid of debris disk models for subsequent statistical (Bayesian) analysis. We conclude that the thermal light spectrum of the disk is well reproduced assuming a mixture of silicates, carbonaceous material and amorphous ice, as well as vacuum to mimic a significant porosity. The observed SED can be very reliably reproduced by a population of grains larger than $\sim 1\,\mu$m, which follows a power-law distribution matching the ideal collisional equilibrium case and represents $\sim$0.05 $M_\oplus$ ($1.5 \times 10^{-7} M_\odot$) in grains with sizes up to 1 mm. Extending the size distribution to the parent bodies of the observed dust grains leads to a mass of $\sim 50 M_\oplus$ for planetesimals up to 1 km. The composition we infer for the dust grains must be a good representation of a considerable reservoir of material hidden in unseen planetesimals.

In this study, we attempted to use Herschel/PACS spectroscopy to detect for the first time far-infrared emission lines in the debris disk. The non-detections we obtain were used to investigate the gas content of the debris disk with our photochemical disk model ProDiMo based on the dust model found with GRaTer. The main uncertainty lies in the amount of PAHs in the disk. The current non-detections of [OI] and [CII] lines alone do not provide unambiguous upper limits to the gas content. Only in the case of a high PAH abundance, we can set an upper limit to the gas mass of $\sim 17 M_\oplus$ (one Neptune mass). Coupling with other tracers, in particular with the CO lines accessible to ALMA, offers much better prospects to reach lower limits on the low gas content of debris disks. However, steady-state chemistry is likely not ideally suited to debris disk modeling, and in future studies more appropriate prescriptions, time-dependent chemistry in particular, will be explored.

We note that both the low albedo estimated from the scattered light images and the dust dynamics are not well modelled by spherical grains filled with vacuum, and that the grains are likely complex fluffy aggregates. Though their thermal behavior is correctly described by the EMT-Mie theory, the scattering of light at short wavelengths and their sensitivity to radiation pressure require a more accurate description of the exact shape of the aggregates. Our statistical analysis highlights that ignoring the porosity of the grains or setting the minimum grain size as equal to the blowout size would result in incorrect interpretation of the observations, in particular because the grain opacity is strongly dependent on the exact grain composition.

We stress some necessary limitations of the models. First, we use a grain size distribution that is independent of the distance to the star, whereas it is known that only the smallest grains can populate the outer parts of the disk under the effect of radiation pressure. In this paper we discussed clues that the observed scattered light profile may not be a perfect representation of that seen in thermal light, by Herschel or ATCA. The long wavelength emission emanating from the largest grains might originate from an even narrower belt. Further studies will need to account for the radial differentiation of grain sizes with the objective to fit altogether resolved images from the near-IR to the millimetre domain. Secondly, the Dohnanyi-like power-law size distribution is known to be an insufficient description; if the real distribution implies wavy patterns as proposed by Thébault & Augereau (2007), then adjusting a power-law likely puts too many/too few small grains in the disk. Dynamical models are required to understand better the general outcome of the collisional evolution of the disk.

3.2 More results from Herschel on cold debris disks

3.2.1 Recent news from HD 181327

Recent Herschel/SPIRE observations at 250, 350 and 500 μm obtained by the GASPS team confirmed remarkably the prediction of the SED model (Fig.3.14). The stronger constraints provided in the sub-millimeter clarify on the measurements from the millimetric antennas. The new data are adjusted by mean of increased ice fraction and porosity with respect to the previously discussed results — consistent within 2σ with the given statistical uncertainties. The (single-dish) LABOCA flux appears to be over-estimated, probably due to its wide field-of-view, while the ATCA flux is perfectly compatible with the SPIRE data.

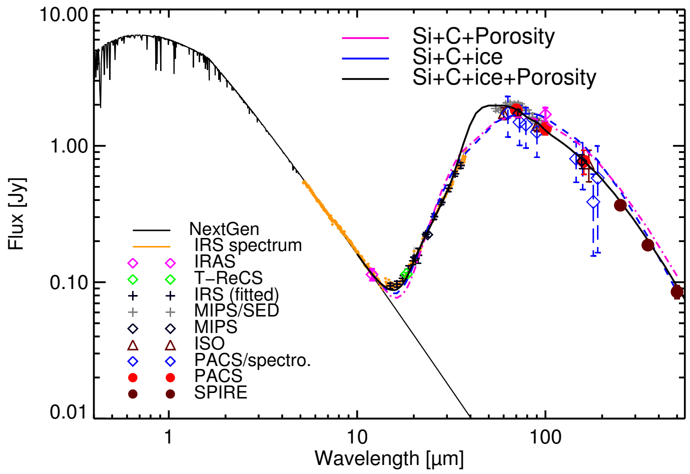

Figure 3.14: Newest Spectral Energy Distribution and models for the HD 181327 debris ring.

Lastly, impressive images presented in Figure 3.15 have recently been presented by Glenn Schneider and his collaborators, using STIS visible-light PSF-subtracted multi-roll coronagraphic imaging (Schneider et al. 2012). Previously unseen sub-structures and asymmetries are revealed that may implicate the presence of yet undetected planets. In particular the asymmetry measured along the semi-minor-axis cannot be explained by simple anisotropic scattering. The interpretation of the new images could benefit from the accurate dust model that I proposed (Stark et al., private comm.).

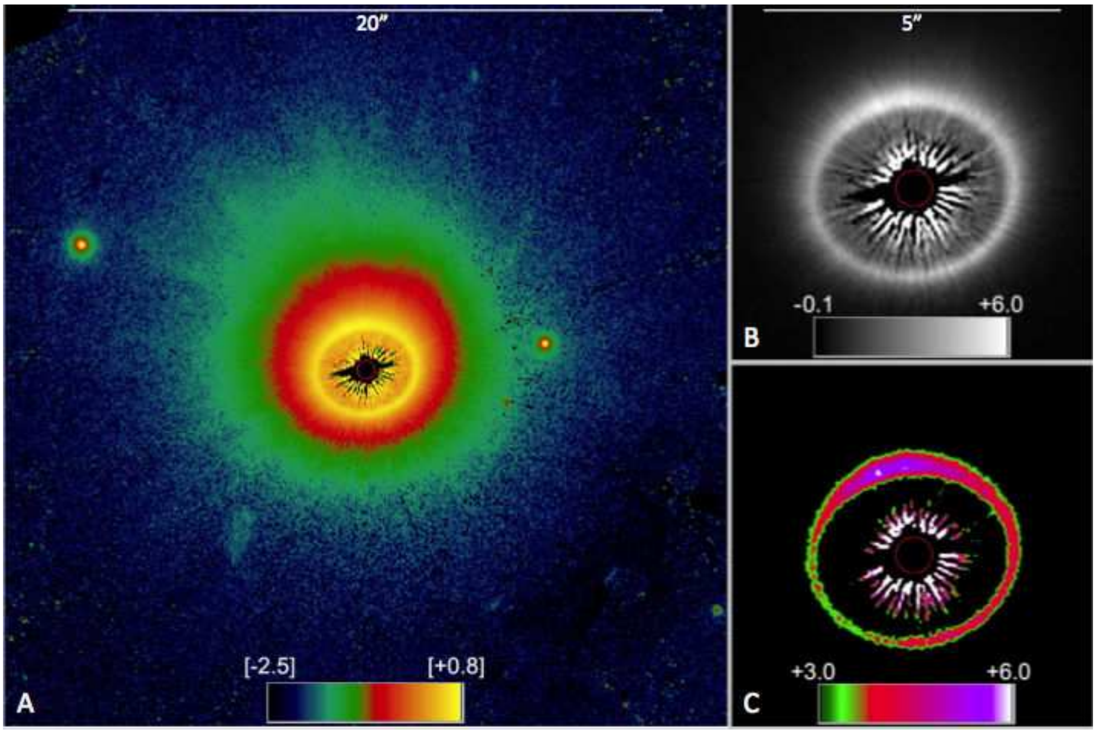

Figure 3.15: HST/STIS image of HD 181327 (Courtesy of G. Schneider and the GO 12228 team)

3.2.2 HD 32297 and other GASPS debris disks

Using the stand-alone version of the GRaTer code, a similar methodology has been applied by Donaldson et al. (2013) to the debris disk of HD 32297, a young A-star (~ 30 Myr) 112 pc away with a bright edge-on debris disk that has been resolved in scattered light (Boccaletti et al. 2012, Fig. 3.16). As part of the GASPS project, we observed the HD 32297 debris disk in the far-infrared and sub-millimeter with the PACS and SPIRE instruments, populating the SED from 63 to 500 μm. We aimed at determine the composition of dust grains in the HD 32297 disk through SED modeling, using geometrical constraints from the resolved imaging to break degeneracies. Unlike HD 181327, we find that fitting the SED requires a model (Fig. 3.16) with 2 components: an outer ring centred around 110 AU, seen in the scattered light images, and an inner disk near the habitable zone of the star. The outer disk appears to be composed of grains > 2 μm consisting of silicates, carbonaceous material, and water ice with an abundance ratio of 1:2:3 respectively and 90% porosity, a global composition very similar to that of HD 181327. These grains also appear consistent with cometary grains, implying the underlying planetesimal population is dominated by comet-like bodies. Gas is also detected at 3.7σ in the form of [C II] emission at 158 μm with the Herschel PACS Spectrometer, making HD 32297 one of only a handful of debris disks with circumstellar gas detected.

We have also detected neutral gas, namely [0I] at 63 μm, around the BPMG member HD 172555, most likely originating from second-generation production of gas from solid bodies (Riviere-Marichalar et al. 2012). The GASPS sample includes 17 other members of the BPMG that share common age with those three stars, $\geq 37\%$ of which have detected disks (Dent et al., submitted to PASP)

3.2.3 The faint debris disks of the DUNES project

The DUNES Open Time Key Programme is a deep, systematic survey for cold, faint debris disks. It aims at finding and characterizing faint extrasolar analogues to the Edgeworth-Kuiper Belt (EKB) down to a fractional luminosity equal to a few times that of the EKB ($L_{\rm disk}/L_\star = 10^{-7}$) at 70$\mu$m. Due to the unprecedented sensitivity of Herschel and the ability to observe at longer wavelengths (with reasonable sensitivity) compared to earlier missions, this survey is able to extend the sample of known debris disks towards disks of lower mass (lower fractional luminosity) and towards colder disks (emitting at longer wavelengths). It is based on PACS observations complemented by SPIRE for follow-up studies. The DUNES observing programme is now achieved and observational results are presented by Eiroa et al. (2013). Here I first describe some of the results I have been involved in for individual objets (q^1 Eri, HD 207129) and unusual SED properties discovered for several disks. Then in Sec. 3.2.4, I present first statistical results obtained by the team (as of October 2011).

Cold disks and steep SEDs: I participated to the identification of new classes of debris disks enabled by the high sensitivity of Herschel. The *cold disks* ($\sim 1/5$ of DUNES detections) are detected at 160μm but have no (or faint) emission at 100μm (Eiroa et al. 2011). They are faint and cold and their exact origin remain a puzzling issue; Krivov et al. (2013) conclude that the most likely explanation is a ring of unstirred primordial macroscopic grains larger than a millimeter, but smaller than a few kilometers in size,

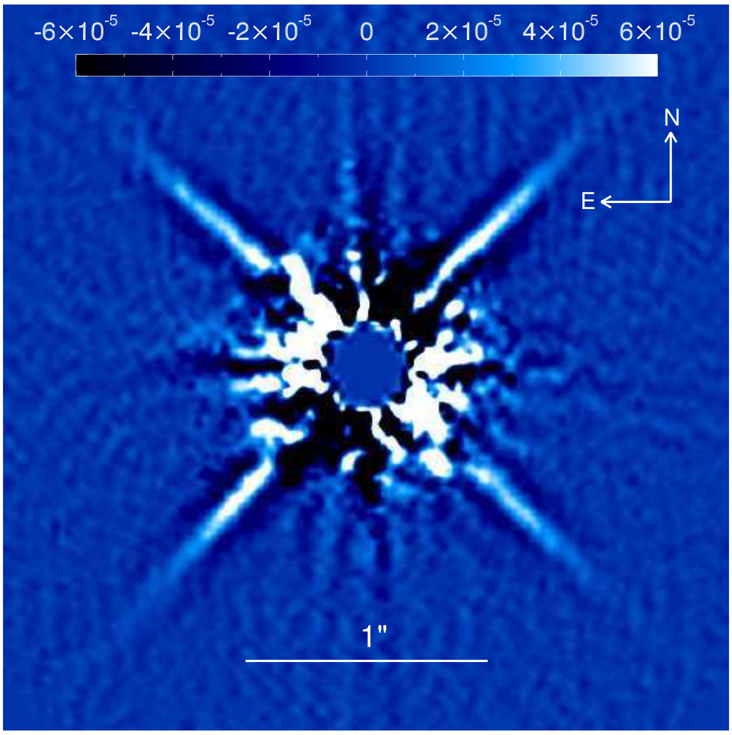
-6×10^{-5}
-4×10^{-5}
-2×10^{-5}
0
2×10^{-5}
4×10^{-5}
6×10^{-5}
N
E
1"

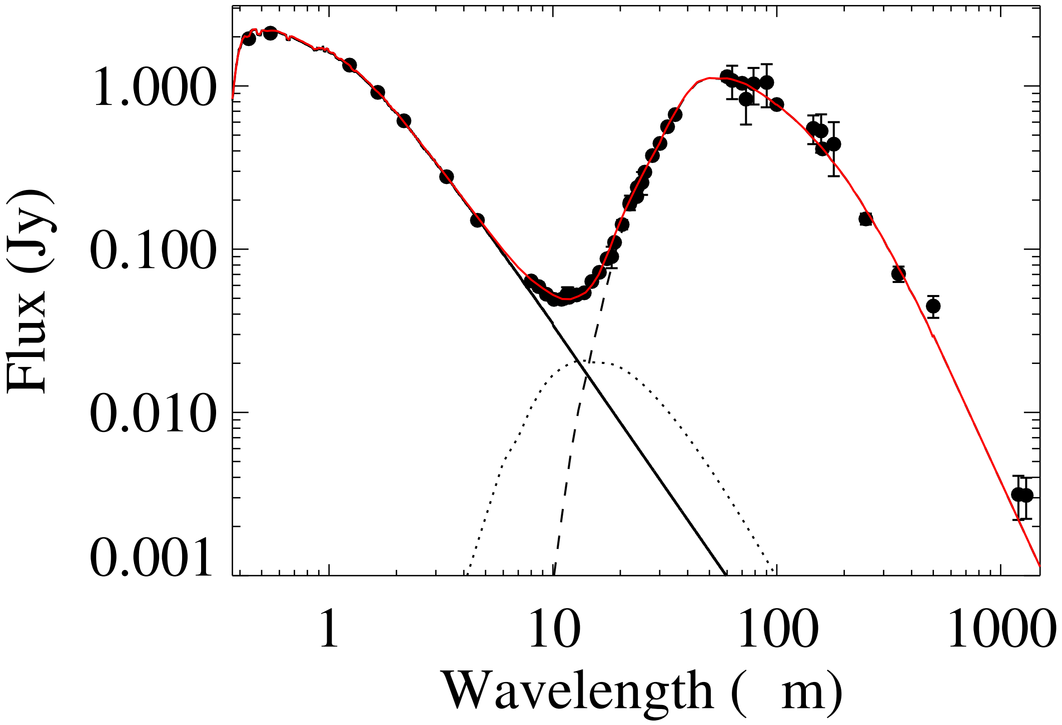
Flux (Jy)
1.000
0.100
0.010
0.001
1
10
100
1000
Wavelength (m)

that could have survived for gigayears, largely preserving the primordial size distribution. Another peculiar class of objets was identified by the unusually *steep far-infrared SED* of several sources, that suggests a deficit of large grains with respect to a standard debris disk (Ertel et al. 2012).

q^1 Eridani: Resolved, multi-wavelengths images of debris belts like q^1 Eri (Liseau et al. 2010) can be efficiently modelled with the GRaTer code, allowing to break the model degeneracy and identify disks properties with no ambiguity (Augereau et al., in prep.). The ~2 Gyr-old planet-host star (F8V) q^1 Eri, located at 17 pc is surrounded by a ~40 AU-wide belt at 85 AU that contains $0.04 M_\oplus$ (up to 1 mm grains) of ice-rich dust grains. It is resolved in scattered light and in thermal emission by Herschel at 70, 100 and 160μm (Figure 3.17). It has a fractional luminosity $L_{\rm IR}/L_\star = 3.8 \times 10^{-4}$ and is one of the debris disks the most similar to our Edgeworth-Kuiper Belt discovered so far. The initial disk mass inferred from collisional modelling is unrealistically high, suggestive of a recent dynamical event, such as delayed stirring by a yet undiscovered planet.

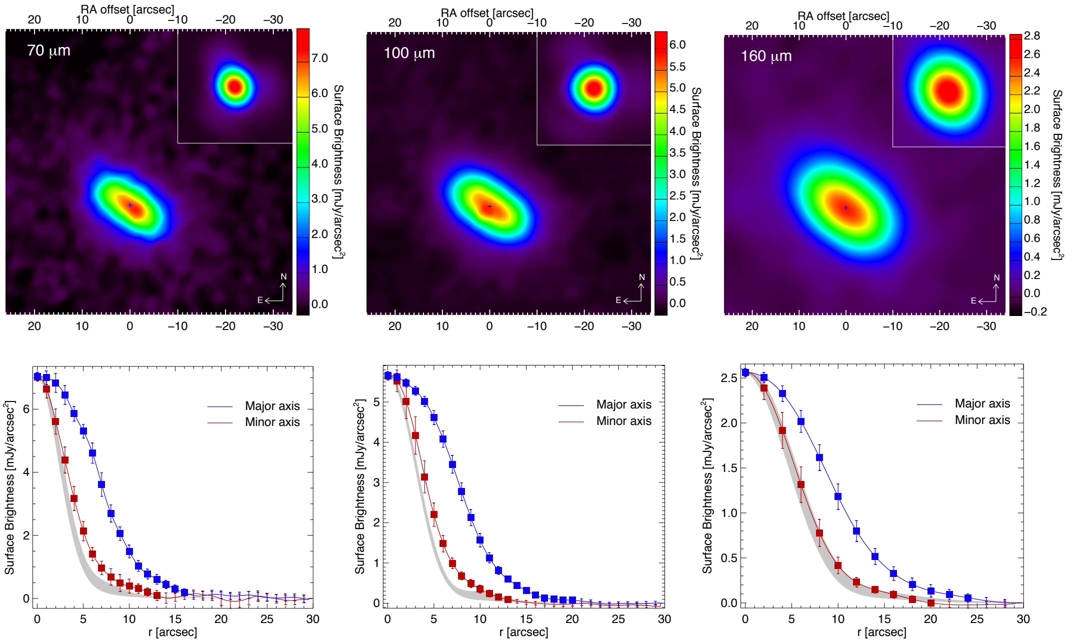

Figure 3.17: **top panels**: Herschel/PACS images of the q^1 Eri disk at 70, 100 and 160μm. The images are 30″ × 30″. Insets show the PSF images rotated to align the maps with the telescope pupil orientation (83° counter-clockwise). **Bottom panels**: left to right: Surface brightness radial profiles at 70, 100 and 160 μm along the major and minor axis, and compared to azimuthally averaged PSF profiles (grey area).

HD 207129: The huge belt surrounding the Sun-like star HD 207129 (Marshall et al. 2011) peaks at a distance of 140 AU and its annular structure is well-resolved by Herschel (Figure 3.18). The best-fit models contain nearly $10^{-2} M_\oplus$ in dust, with typical grain sizes in the planetesimal belt ranging from 4 to 7 μm. The counter-intuitive dust spatial distribution implies a low velocity dispersion in the parent-belt, which results in very long collisional lifetimes and a drag that notably fills the inner gap. Both slowly self-stirring and planetary perturbations could be at the origin of these peculiar properties (Löhne

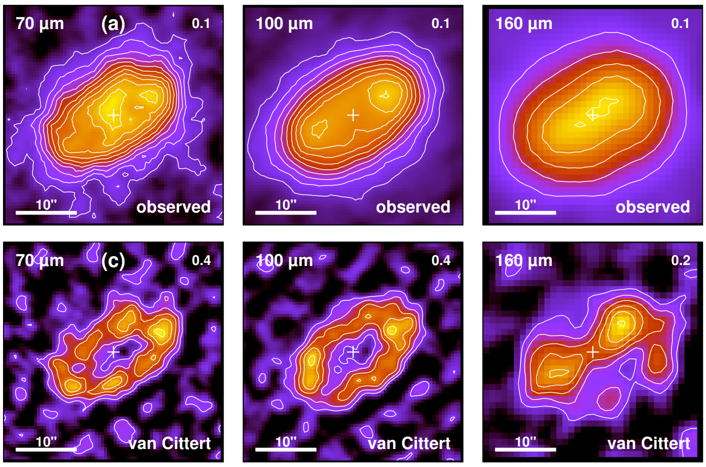

Figure 3.18: Herschel/PACS images of HD207129. Left to right: wavelengths of 70 μm, 100μm, and 160μm. Top: as observed. Bottom: star subtracted and deconvolved.

et al. 2012).

3.2.4 Debris disks statistics

The DUNES consortium is taking a census of extrasolar analogues to the Edgeworth-Kuiper Belt with unprecedented sensitivity and provides new statistics on the occurence rate of debris disks. This subsection is an extract from the conference proceeding of the EPSC-DPS joint meeting 2011 I prepared in collaboration with *J.P. Marshall, J.-C. Augereau, C. Eiroa and the DUNES consortium* (Lebreton et al. 2011).

We performed PACS (70, 100, 160 μm) and SPIRE (250, 350, 500 μm) photometric observations of cold disks around an unbiased, statistical sample of 133 nearby FGK Main Sequence (MS) stars (d < 25 pc), some known to host exoplanets. Results for the first 126 targets are presented in Tab. 3.9. The EKB sensitivity limit has been reached ($L_{\rm dust}/L_* \sim 10^{-7}$), revealing that ~30% of nearby MS stars host a debris disk, which doubles the previous statistics. Most of the new detections were obtained for late-type stars, which were too faint for previous surveys. No clear tendency was found regarding the occurrence of planets versus the detection of excess, but the structure of two disks imply the presence of an exoplanet shaping it.

Table 3.9: DUNES statistics

Sp. type	F	G	K	Total
Sample	28	53	52	133
Observed	26	51	49	126
Non-excess	17	37	38	92
Excess (New)	9 (2)	14 (6)	11 (5)	34 (13)
"Peculiar"	2	2	4	
Resolved	4 (3)	8 (4)	4 (2)	12 (9)
Excess+planet	2 (2)	7 (1)	2 (1)	11 (4)

3.3 Conclusion

The recent availability of resolved high resolution images from optical (HST, VLT/NaCo) and sub-millimeter (Herschel, ALMA) telescopes enables to constrain precisely the cold debris disks spatial density in order to focus on the grain properties. Despite the lack of unambiguous spectral features — because of the grain sizes and moderate fractional luminosity — I showed that is has become possible to characterize the composition of the grains providing insight on the dust-producing parent bodies and their dynamics. The level of accuracy offered by Herschel requires sophisticated grains mixtures including significant amounts of water ice and porosity as clearly evidenced by Bayesian analysis methods. In the case of HD 32297 we underline that despite the clear improvement provided after considering complex compositions, an additional inner disk component is required to be consistent with the mid-infrared observations. The study of such warm, or hot, counterparts to cold debris disks are the scope of the next two chapters.

Chapter 4

The Origin of Exozodiacal dust

> *Beaucoup de comètes sont invisibles, parce que les rayons du soleil les effacent. [...] Souvent, après le coucher du soleil, on voit près de son disque des feux épars : c'est que le corps de la comète, noyé dans la lumière du soleil, ne peut se distinguer; mais sa chevelure est en dehors des rayons.*
>
> SÉNÈQUE, *Questions Naturelles, Livre VII*, 65 ap. J.C.

Figure 4.1: The Zodiacal sky at the VLTI.

4.1 The inner regions of nearby debris disks

Cold extra-solar Kuiper Belt analogues probing the outer regions of nearby planetary systems can now be studied in great details by mean of complementary observations combining resolved imaging and precise spectrophotometry. On the other hand, little is known about the architecture of the very inner parts of debris disks, *i.e.* inside of a few AU. Nonetheless, if the Solar System habitable zone was imaged by an astronomer inhabiting an exoplanet in orbit around another star using ideal coronagraphic techniques, the most striking feature signing the presence of solid material would be the Zodiacal dust cloud. The zodiacal light is the extended, diffuse, triangular glow visible along the Solar System's ecliptic plane over dark nights, as revealed by Picture 4.1 taken from the Paranal Observatory. As a matter of fact, it is the most luminous object in the habitable zone as its total brightness surpasses the planets point-source luminosity. It is produced by sunlight scattered and thermally emitted by a torus of small (1 to $\geq 100\mu$m) dust grains that populates the neighbourhood of the inner planets (Grün 2007; May 2008). The transition from scattered light to thermal emission occurs at about 3.5 μm and the spectral energy distribution peaks in the mid-infrared ($\sim 24\mu$m) where the flux ratio with respect to the Sun is approximately $\sim 3 \times 10^{-4}$ (Backman et al. 1998). The present mass of the inner zodiacal cloud inside of 5 AU is estimated to a few $10^{-9}\,M_\oplus$ (Dermott et al. 2002). The exact origin of the zodiacal dust remains a debated issue: while Dermott et al. (2002) argue that the Zodiacal dust bands indicate interplanetary dust particles inside of 5 AU originate from catastrophic disruptions of small "rubble piles" asteroids of the Main Belt, Nesvorný et al. (2010) defend that the break-up of short-period comets is the main source for the zodiacal dust seen in the mid-infrared.

A few warm disks ($\simeq 300-500$K) comparable to the Zodiacal Cloud have been evidenced by space observatories around mature stars via their photometric excess emission at mid-infrared wavelengths. Lawler et al. (2009) find than less than 1% of nearby solar-type stars harbor a detectable excess in the short wavelength band of the IRS instrument onboard the Spitzer Space Telescope, corresponding to a brightness level higher than 1000 times the zodiacal emission. A rare counter example is the detection of large Spitzer 8 to 35 μm excess around HD 69830 (Beichman et al. 2007), just outside the orbits of 3 Neptune-mass planets (Lovis et al. 2006). In fact, nearly nothing is known about warmer dust in the inner, planetary forming region; their characterization suffers from insufficient spatial information and large photometric uncertainties.

Recent developments in high-angular resolution observational astrophysics have offered powerful tools to characterize *exo-Zodiacal disks* ("Exozodis"), free of any modelling assumptions on the stellar spectrum. In particular, the sensivity achieved by long-baseline interferometers (less than 1% with respect to the photospheric level) has yielded the intriguing discovery of hot (1000-2000K) exozodis in the close environment (typically less than 3 AU) of a large fraction of nearby stars. In Section 4.2.1 I will introduce the basic principles of stellar interferometry and the methodology used to derive some major disk properties from the observations, illustrated by the example of the Vega exozodiacal disk. The science of exozodis has been observationally driven, with a large effort invested by two leading teams in the US and in Europe to conduct surveys with near- and mid-IR interferometers worldwide. Long baseline interferometers such as the VLTI (Absil et al. 2009), IOTA (Defrère et al. 2011a) and the CHARA array at Mount-Wilson make it possible to detect dust within the first few AU of nearby stars at the 1% level.

I joined the team responsible for the first interferometric characterization of an exozodiacal disk around the star Vega (Absil et al. 2006), who is now conducting the first statistical (unbiased) K- and H- band survey of exozodiacal dust around nearby solar-type (A, F, G, K) stars in the Northern hemisphere with CHARA/FLUOR (Fiber Linked Unit for Optical Recombination) and in the Southern hemisphere with VLTI/PIONIER (Precision Integrated-Optics Near-infrared Imaging ExpeRiment, EXOZODI project, PI: J.C. Augereau, Ph. Thébault). The CHARA/FLUOR long baseline interferometric array offers the best K-band visibility amplitude accuracy demonstrated so far (about 0.2% rms for bright stars), and a large range of baseline lengths. Both features are unique to this instrument, and essential for the proper detection and characterization of exozodiacal disks carrying 1% or less of the stellar flux. PIONIER is a visitor instrument for the VLTI that relies on the integrated optics technology to combine four VLTI beams in the H-band from four Auxiliary Telescopes (or four UTs). It provides simultaneous measurements of 6 visibilities and 3 closure phases and should allow to reach visibilities precision of 0.5% (at 3σ) on individual measurements. A total of 200 stars ($K < 5$) from both hemispheres is being observed, half of them with a known cold debris disk, the other half without (known) cold dust. The ongoing, yet not-unbiased survey with the two long-baseline interferometers reveal that a large fraction of nearby Main-Sequence stars might harbor a visibility deficit at small spatial frequencies consistent with excess emission at the 1% level with respect to the photosphere. To date (January 2013), we have observed 74 stars and preliminary (not yet unbiased) statistics from FLUOR indicate a detection rate of typically $\sim$30% in K band (Defrère et al. 2011b; Absil et al. 2013), and probably less ($\lesssim$ 10%) in H-band from PIONIER. Preliminary results suggest, that the excess fraction in H band is significantly lower than in K band, probably constraining the temperature of typical exozodiacal dust (Ertel et al., in prep.).

In the mid-infrared, observations conducted with single telescopes or nulling interferometers until now have only yielded a handful of detections. One example of such detection is discussed in Sec. 4.3 for the case of the star Fomalhaut.

Throughout the chapter, I will show that radiative transfer analysis of the light emitted by exozodiacal disks often identify small refractory grains, thermally emitting at high temperatures. One crucial and puzzling fact is that, due to collisions, drag forces and radiation pressure, small grains cannot survive in exozodiacal disk more than a few years before being eliminated from the system (e.g. Krivov et al. 2006); yet they represent typical masses of 10^{-8} to 10^{-10} $M_\oplus$ — equivalent to the mass of a 70 km diameter asteroid — and that need to be delivered by equivalent masses of dust-producing parent bodies. Proper description of the mechanisms that produce and preserve the hot dust is missing. Being much hotter and more massive than the Zodiacal disk, these hot exozodis are difficult to reconcile with the steady-state collisional evolution of parent-bodies belts (Wyatt 2007). Rather, they are suspected to originate from stochastic and/or isolated catastrophic events such as planetesimals collisions or break-up, or major dynamical perturbations.

The connection with exoplanets and cold disks, remain open issues that I introduce in Sec. 5.7. Determination of the prevalence of the ”Exozodi phenomenon” around nearby stars, and its characterization, are critical issues to handle as they represent a source of noise for future direct imaging and spectroscopy of exo-Earths.

4.2 Observing exozodiacal disks with long-baseline interferometry

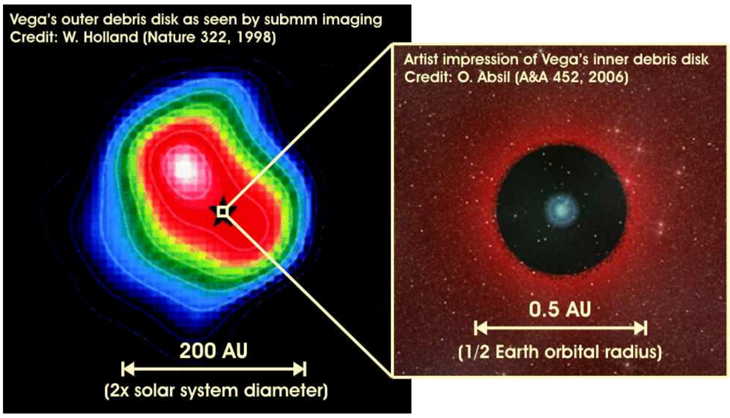

Figure 4.2: Representation of the Vega debris disk at different spatial scales. Sub-millimeter image **left panel** showing a $\sim$ 200 AU-wide dusty analogue to our Kuiper belt (Holland et al. 1998), that may be sculpted by a hidden planet and be the mass reservoir for the observed exozodiacal dust (**right panel**) lying inward of the first AU from the star (Absil et al. 2006; Defrère et al. 2011a).

The fundamental observable provided by optical interferometers is the visibility (or visibility amplitude), defined as the contrast between the fringes generated when the light beams from a pair of two telescopes interfere:

$$\mathcal{V} = \frac{I_{\max} - I_{\min}}{I_{\max} + I_{\min}} \tag{4.1}$$

where $I_{\max}$ and $I_{\min}$ are the mimimum and maximum intensities of the fringes. In fact, an interferometer samples the discrete components of the spatial frequency spectrum of the sky brightness distribution, which is formally proportional to the amplitude of the complex 2D Fourier transform of the observed object sampled at the spatial frequencies b/λ, with b the baseline and λ the wavelength. Three (or more) telescope interferometry is achieved by combining pair-wise the beams from individual telescopes, enabling to sample the Fourier space along various directions and spatial frequencies, which benefits from the availability of multi-wavelengths observations. The physical size of an astrophysical object can be derived from the visibilities. For instance, taking a uniform disk model as a first approximation for a star or a (single) circumstellar disk of angular diameter θ_{UD}, the squared visibility is given by:

$$\mathcal{V}^2(b_\perp, \lambda, \theta_{\mathrm{UD}}) = \left(\frac{2J_1(\pi\theta_{\mathrm{UD}}b_\perp/\lambda)}{\pi\theta_{\mathrm{UD}}b_\perp/\lambda}\right)^2 \tag{4.2}$$

where $b_\perp$ is the baseline vector projected onto the sky plane and J_1 is the 1^{st} order Bessel function. For $\theta_{\mathrm{UD}} \ll \lambda/b_\perp$ the object is unresolved and the visibility is close to 1. It decreases with increasing baselines and reaches 0 for $\theta_{\mathrm{UD}} = 1.22\lambda/b_\perp$, providing a direct measurement of the resolved disk diameter.

Due to their very different spatial scales, a star and a circumstellar disk have distinct signatures in the Fourier space. For nearby stars, the star is fully resolved with the long baselines ($\geq$ 80m) while the extended emission can be detected at the short baselines ($\sim$ 30m). A disk has a visibility $\mathcal{V}$ lower than that of a star (assuming a uniform disk model here for simplicity) and thus reduces the global visibility of the system, which can be expressed as:

$$\mathcal{V}^2(b_\perp, \lambda) = \left((1-f)\frac{2J_1(\pi\theta_{\mathrm{UD}}b_\perp/\lambda)}{\pi\theta_{\mathrm{UD}}b_\perp/\lambda} + f\mathcal{V}_{\mathrm{disk}}(b_\perp, \lambda)\right)^2 \tag{4.3}$$

where f is the fraction of flux attributed to the disk. At short baselines, the disk visibility $\mathcal{V}$ reaches 0 *i.e.* the disk is fully resolved, the star is considered unresolved ($\theta_{\mathrm{UD}} < \lambda/b$) and assuming small flux ratio ($f \ll 1$), the squared visibility reads:

$$\mathcal{V}^2(b_\perp, \lambda) = (1-2f)\left(\frac{2J_1(\pi\theta_{\mathrm{UD}}b_\perp/\lambda)}{\pi\theta_{\mathrm{UD}}b_\perp/\lambda}\right)^2 \tag{4.4}$$

Thus, the visibility deficit at short baseline provides a direct measurement of the disk flux, as it equals twice the flux ratio with respect to a single star. More thorough analysis of the geometry of the circumstellar emission can be achieved by a combination of short and long baselines, and precise adjustment of the visibilities as we will see in the next section. Its exact morphology could in principle be reconstructed from a very good coverage of the spatial frequency plane; however an even better precision would be required (a few 0.1%) which is not accessible to current facilities. The main outcomes of these observations are therefore a maximum radius where the dust must be confined, corresponding to the small field-of-view of the interferometer, and an accurate estimate of the near-IR flux ratio.

The Fourier phase can be equalled to the phase of the fringe pattern, but in practice this information is lost by various sources of contamination, most importantly by atmospheric turbulences. Random phase terms are added for each of the individual telescope (i), but their fluctuations are not independent. Therefore, with three-telescope interferometers a simple way is used to retrieve partial information on the phase of the source structure: the phase $\Phi(i-j)$ variation is measured between pairs of telescopes and the three phases are added in such a way to eliminate the phase error, defining the closure phase:

$$\Phi(i-j-k) = \Phi(i-j) - \Phi(j-k) + \Phi(k-i) \tag{4.5}$$

that depends only on the brightness distribution of the source. It offers a tool to constrain departures from central symmetry in the observed objects. An application of closure-phase measurements is presented in Sec. A (Absil et al. 2010) where it serves to constrain the presence of a binary companion in the environment of β Pictoris from VLTI/AMBER 3-unit telescope observations. It must be noted that for the faint debris disks discussed in this chapter, closure-phase measurements are found to be consistent with central symmetry and are therefore not used in the analysis.

4.2.1 Observations and modelling of Vega's exozodi using near-infrared interferometry

The nearby star Vega (Fig. 4.2) is emblematic of debris disks research. It can be considered the first planetary system candidate ever discovered (*cf* Chapitre 1) and the pioniering detection by Aumann et al. (1984) was already interpreted by mean of two dust populations : a cold outer component at $\sim$ 85K and a warm inner one at $\sim$ 500K. Optical interferometry offers the appropriate tool to study the innermost parts of the disk. As explained in the previous section, at near-infrared wavelengths, the detection principle of an exozodi is based on the small decrease of visibility produced by the resolved circumstellar structure with respect to the expected photospheric visibility. This departure from the stellar size can best be detected at short baselines, while the long baseline measurements determine the stellar parameters. In the following I will introduce the methodology I used based on the example of Vega. This section is adapted from Defrère et al. (2011a) who present new resolved observations of the Vega exozodi based on IOTA/IONIC observations. First, simple geometrical models are fitted to the visibilities to evaluate some fundamental disk properties. Sophisticated radiative transfer models are required to translate astronomical observables into physical quantities. I will focus on the results I obtained for this published paper with the GRaTer code on the properties of the dust and on its location.

4.2.1.1 A circumstellar disk in the close environment of Vega

Further to the pioneering K-band observations of Absil et al. (2006), we obtained new infrared interferometric observations of the hot inner part of the debris disk around Vega. Visibility and closure phase H-band measurements measured with the 3-telescope IOTA/IONIC instrument in June 2006 are presented in Fig. 4.3.

As shown by Absil et al. (2006) with CHARA/FLUOR, a realistic stellar photospheric model cannot reproduce K-band visibility measurements. This is also the case for our H-band IOTA/IONIC data with measured visibilities clearly below the expected level of the photospheric visibility. These observations cannot be reconciled with a purely photospheric model, because on the one hand short-baseline data are weakly sensitive to the model parameters (angular diameter and limb-darkening profile), and on the other, the model parameters are already known with good accuracy (Aufdenberg et al. 2006; Peterson et al. 2006). Furthermore, the visibility deficit is observed on the three different baselines with roughly the same magnitude so that it cannot be explained by the apparent oblateness of Vega's photosphere (which is not significant since Vega is seen almost pole-on). To explain this visibility deficit, Absil et al. (2006) proposed a model of a star surrounded by an exozodiacal disk accounting for 1.26 ± 0.28% of the K-band stellar flux within the FLUOR field-of-view (∼8 AU in radius). In particular, they addressed and ruled out a series of scenarios. For instance, a bound low-mass companion was also shown to be a viable explanation although much less probable. Other explanations, such as a bright background object within the FLUOR field-of-view (probability less than 10^{-6}) or stellar spots (appearing in the second and higher lobes of the visibility function), were ruled out with good confidence.

To constrain the near-infrared excess emission around Vega, three simple models of a circumstellar disk have been fitted to the data:

- A diffuse emission uniformly distributed across the field-of-view
- The zodiacal disk model of Kelsall et al. (1998), which is implemented in the *Zodipic* package
- A narrow ring of dust located at twice the sublimation radius ($r_{\text{sub}} = 0.1$ AU for a sublimation temperature $T_{\text{sub}} = 1700$ K).

All models are assumed to be centrally-symmetric, as suggested by the calibrated closure phases, and use an effective temperature of 8027 K for Vega as viewed by the dust in the equatorial plane. The photosphere model used to reconstruct the SED on the other hand is based on the polar temperature of 10150 K. All three models fit the data set ($\chi^2_{\text{r}} \simeq 0.5 - 0.7$) equally well with a best-fit flux ratio of $1.35 \pm 0.49\%, 1.26 \pm 0.45$ and $1.20 \pm 0.43\%$ respectively, for the uniform disk model, the zodiacal disk model, and the ring model. All the best-fit contrasts are compatible within 1σ, which indicates that the final flux ratio does not heavily depend on the distribution of the circumstellar emission. To confirm this conclusion, the squared visibilities from synthetic images of a geometrically and optically thin debris disk were computed and compared to the data set. The synthetic images are based on three parameters: the disk/star flux ratio, the inner disk radius r_{in} , and the exponent α of the power law describing the density decrease as a function of distance ($n_{\text{r}} \propto r^{\alpha}$). The synthetic images only include thermal emission, which is expected to be largely dominant for the dust temperatures explored here, and they assume pure blackbody emission (grain temperature proportional to $r^{-0.5}$, with $T = 1700$ K at 0.1 AU). For each couple of parameters (r_{in}, α) ranging between the sublimation radius and 2 AU and between 0 and -50, respectively, the best-fit flux ratio was computed by χ^2 optimization. The results show that all models fit the data equally well with a reduced χ^2 ranging between 0.48 and 0.84, confirming exozodiacal dust as a good scenario to explain the deficit of visibility. It is, however, impossible to conclude on the location of the dust based on the sole interferometric data. The best-fit disk/star flux ratios are all compatible within approximately 1-σ error bars and range from 1.04% to 1.42%. We therefore adopt a H-band flux ratio of $1.23 \pm 0.53\%$ in the following discussions. The error bar includes both the uncertainty due to the model (±0.19%) and the maximum error bar on an individual model (±0.49%). This inferred disk/star contrast is marginally compatible with the one predicted by Absil et al. (2006) based on the CHARA/FLUOR observations (about 0.6% with an inner rim located between 0.17 and 0.3 AU).

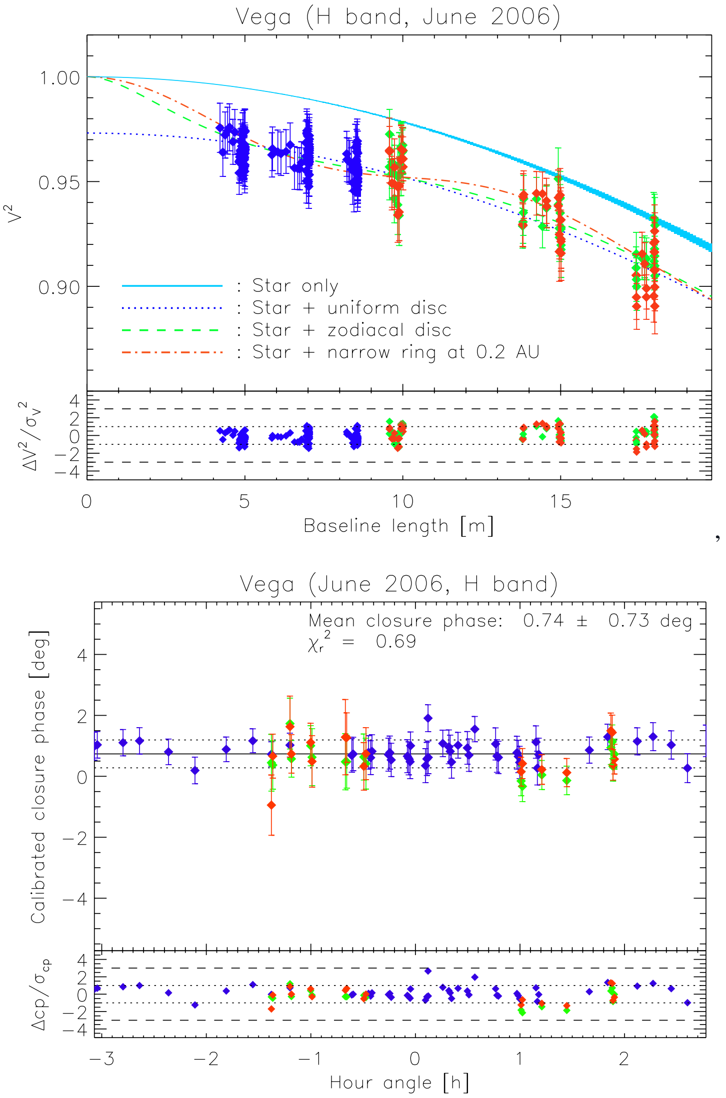

Figure 4.3: **Left:** Expected squared visibility as a function of baseline for Vega's photosphere (blue solid line), given with the measured squared visibilities. The best fitting models of a limb-darkened photosphere surrounded by a circumstellar emission of several geometries are also represented. Residuals of the fit are given in the bottom panel for the uniform disk model. **Right**: Calibrated closure phase measurements as a function of hour angle. The mean closure phase is represented by the black solid line, while the dotted lines represent the 1σ statistical uncertainty on its value. The bottom plot shows the residual between the data and the mean closure phase.

4.2.1.2 Model constraints on the exozodiacal disk

The analysis presented in the previous section confirms that the most straightforward scenario for explaining the visibility deficit is the presence of hot dust grains producing

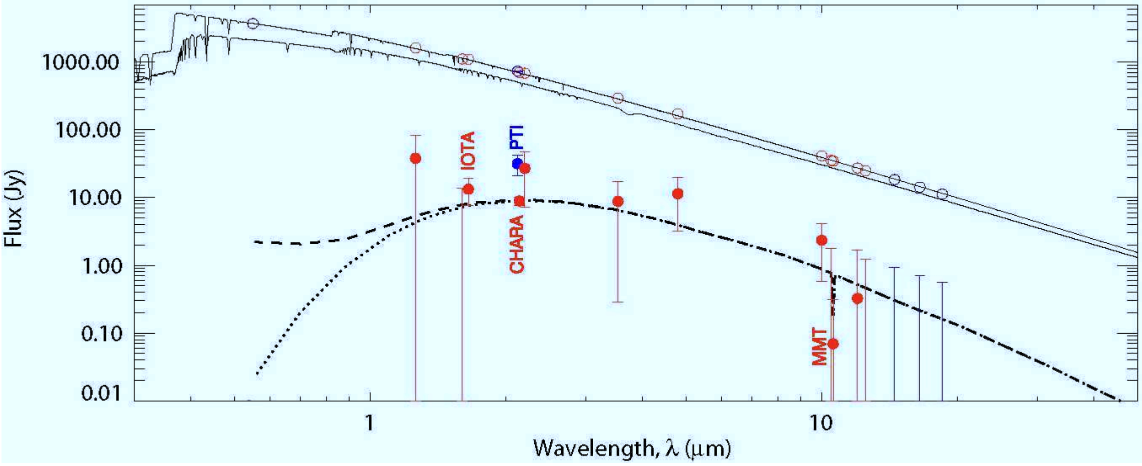

Figure 4.4: A possible good fit of our debris disk model to the photometric and interferometric constraints ($\chi_r^2 = 0.84$). The model used here has a size distribution exponent of -5 with limiting grain sizes of $a_{\min} = 0.2\mu$m and $a_{\max} = 1000\mu$m, a surface density power law of -3, and it assumes a disk composed of 50% silicates and 50% carbonaceous grains. The dashed and dotted lines represent the total emission from the disk on a 6 AU field-of-view, respectively with and without the scattered emission. The photospheric SED, simulated by a NextGen model atmosphere, is represented by the two solid lines as seen pole-on (upper curve) and from the equatorial plane (lower curve). Only measurements plotted in red have been taken into account in the fit.

thermal emission in the near-infrared. To constrain the disk parameters, several archival spectrophotometric and interferometric measurements at near- and mid-infrared wavelengths exist in the literature (See Defrère et al. 2011a). In addition to the measurements used by Absil et al. (2006), we add our direct measurement of the H-band excess flux (1.23 ± 0.53%) and the IRS spectrum found in the Spitzer archives. The Spitzer spectrum has been reduced with the c2d pipeline developed by Lahuis (2006), and binned into a few equivalent broad-band photometric measurements for the sake of spectral energy distribution (SED) modelling. The idea is then to check whether there is at least a disk model that is compatible with all the constraints and derive its properties. To reproduce the SED of the infrared excess, radiative transfer modelling was performed using the code developed by Augereau et al. (1999) for cold debris disks, and adapted to the case of exozodiacal disks (e.g., Absil et al. (2006); di Folco et al. 2007; Absil et al. 2008, 2009). The code considers a population of dust grains with a parametric surface density profile and size distribution, and computes the thermal equilibrium temperature of the grains exposed to the stellar radiation. It can handle various chemical compositions for the grains in order to investigate for instance the fraction of carbonaceous or silicate material contributing to the observed emission. Specific care is given in the model to the treatment of exozodiacal dust close to the sublimation radius, to account for the size-dependent position of this radius. On output, the code computes the thermal and scattered light emissions of debris disk models and produces both images and SEDs over a broad parameter space to combine observations from different instruments (IOTA/IONIC, CHARA/FLUOR, MMT/BLINC, Spitzer/IRS, broad-band fluxes), taking their specific response into account.

Using the code described above with an effective temperature for Vega of 8027 K as viewed by the dust in the equatorial plane, a grid of debris disk models was computed with the following parameters: the peak position r_0 of the surface density profile (possible values ranging from 0.05 to 1 AU, provided that the sublimation radius is not reached), the minimum size $a_{\rm min}$ of the size distribution (from 0.01 to 54.6 μm), the slope κ of the size distribution (from -2.7 to -9), the slope α of the surface density profile beyond r_0 (from 0 to -9.5), and the volume fraction $C_{\rm r}$ of carbon grains (from 0 to 100%). Each model assumes no azimuthal dependence and sublimation temperatures of 1200 K for silicate grains ("astrosilicates", Draine 2003) and 1900 K for carbonaceous grains ("amorphous carbon", Zubko et al. 1996). The size distribution (between $a_{\rm min}$ and $a_{\rm max}$) has been accordingly truncated at the sublimation size ($a_{\rm sub}$), which depends on the radial distance to the star since only grains large enough to survive the sublimation process can actually coexist (Fig. 4.5).

For each model on the grid, the SED has been computed and compared to the measurements. The first obvious result obtained from the $\chi^2_{\rm r}$ analysis is that pure silicate models ($C_{\rm r} = 0$) do not fit the SED well with a $\chi^2_{\rm r}$ always larger than 7. The goodness of the fit improves significantly by introducing carbonaceous grains, which can survive closer to Vega due to their higher sublimation temperature. This conclusion is supported by previous studies explaining the lack of significant silicate emission features around 10 μm by the presence of large amounts of highly refractive grains in the inner disk (Laor & Draine 1993; Zubko et al. 1996; Gaidos & Koresko 2004). The actual amount of carbonaceous grains can, however, not be constrained since the $\chi^2_{\rm r}$ typically varies from 1.3 for a carbonaceous-poor disk ($C_{\rm r} = 5\%$) to 0.8 for a pure carbonaceous disk ($C_{\rm r} = 100\%$) in the steep power law regime ($\alpha < -3$). For a flatter power law ($\alpha > -3$) like in our zodiacal disk ($\alpha \sim -0.34$, Kelsall et al. 1998), the disk models do not fit the various measurements well with a $\chi^2_{\rm r}$ always higher than 5 even for pure carbonaceous disks. In addition, relatively small grains ($a_{\rm min} < 1\mu$m) with a steep size distribution profile ($\kappa < -3$) are also required to obtain a good fit to the SED ($\chi^2_{\rm r} < 3$).

Two good-fit models are represented in Fig.4.5 by flux density maps given as a function of grain size and distance to the star. The upper figure corresponds to the best-fit model ($\chi^2_{\rm r} = 0.84$, total mass $= 1.9 \times 10^{-9} M\oplus$) obtained for $a_{\rm min} = 0.2$ μm and $\kappa = -5$, while the bottom figure corresponds to the same model with $a_{\rm min}$ equal to 0.01 μm ($\chi^2_{\rm r} = 1.01$, total mass $= 2.1 \times 10^{-9} M_\oplus$). The dependence of sublimation distance on the grain size is clearly visible in these figures, the larger grains surviving closer to Vega than the small ones. The figures also show that the largest grains located near 0.1 AU contribute relatively less to the total flux than the smaller grains located further away from the star and present in larger numbers. In both cases, the flux density decreases very quickly with the distance to Vega as shown by the various contours. This geometry is mostly constrained by the interferometric measurements, and particularly the non-detection reported by Liu et al. (2004) with the MMT/BLINC, which requires a steep power law in order to reduce the amount of dust in the regions further than 1 AU. In addition, recent observations of Vega with the Palomar Fiber Nuller ($\sim 2.2\mu$m, Mennesson et al. 2011) suggest that any dust population contributing to at least 1% of the near-infrared flux can arise only within 0.2 AU, a conclusion in favour of $a_{\rm min}$ equal to 0.2 μm in order to sufficiently reduce the dust emission beyond 0.2 AU.

Finally, we used a Bayesian approach to compute the normalised probability density of the disk models based on the χ^2 grid. The results of this analysis shows that the dust mass has a probability density that peaks at about $10^{-9} M_{\oplus}$, equivalent to the mass of an asteroid about 20 km in diameter (assuming $2.5 g/cm^3$ density).

In summary, the most straightforward scenario consists in a compact debris disk with a steep density profile ($\alpha \leq -3$) producing a thermal emission that is largely dominated by small ($a_{\rm min} < 1.0$ μm) silicates and carbonaceous grains located between 0.1 and 0.3 AU from Vega. A representative SED is shown in Fig. 8, together with the SED of the stellar photosphere as seen pole-on (upper solid curve, $T_{\rm eff} = 10150$ K) and as seen by the exozodiacal dust (lower solid curve, $T_{\rm eff} = 8027$ K). This model assumes a size distribution exponent of -5 with limiting grain sizes of $a_{\rm min} = 0.2$ μm and $a_{\rm max} = 1000$ μm, a surface density power law of -3, and a disk composed of 50% silicates and 50% carbonaceous grains. By using this disk model to fit our interferometric data set, we derived a best-fit contrast of $1.23 \pm 0.45\%$. Finally, the flux ratio derived here is about 1.5σ above the value extrapolated from the K-band CHARA/FLUOR measurements (expected H-band excess of 0.6%, Absil et al. 2006). Although this model successfully reproduces the Vega SED, including both CHARA/FLUOR and IOTA/IONIC flux ratios, another possible scenario that could explain the small discrepancy (at least partially) is that the brightness of the exozodiacal disk around Vega is evolving on time scales as short as one year.

Considering the best-fit model, a dust mass of approximately equivalent to the mass of an asteroid about 20 km in diameter, would be necessary to explain the near-infrared excess emission. Given the short lifetime of the small dust grains our model identifies in the inner Vega system, a major dynamical event, similar to the solar system's late heavy bombardment, might be currently ongoing in the Vega system. This would support the idea that the debris disk around Vega is the only visible component of a more complex planetary system harbouring unknown planets.

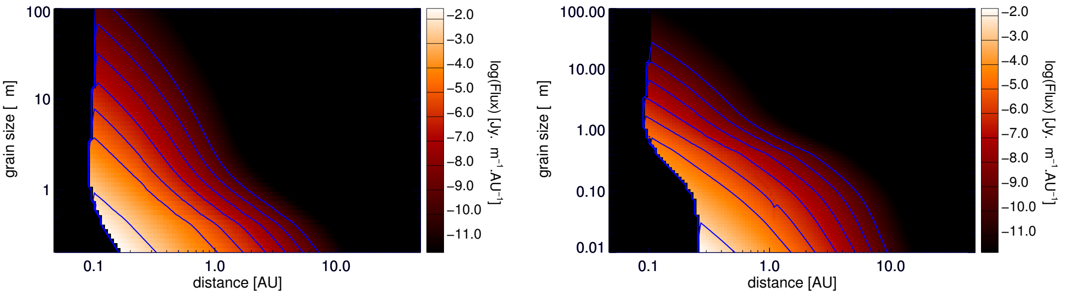

Figure 4.5: Flux density maps given as a function of grain size and distance to the star computed for $a_{\rm min} = 0.2\,\mu$m (best-fit model, left figure) and $_{\rm amin} = 0.01$ μm (right figure). A surface density power law of $\alpha = -3$ and a size distribution power-law exponent of $\kappa = -5$ have been assumed in these plots, with a maximum size of 1000 μm. In this simulation, the disk is composed of 50% silicates and 50% carbonaceous grains. The contours are plotted every power of 10 between 10^{-1} and 10^{-7} of the maximum flux density.

4.3 Warm and hot dust around Fomalhaut: nulling interferometry and modelling

The Fomalhaut debris disk was among the first ones discovered by IRAS and is also particularly emblematic. Various instruments have allowed to resolve a 140 AU-wide outer belt, inclined by 65.6° and shifted by 10 AU with respect to the central star, probably by the influence of the directly imaged planet Fomalhaut b. The innermost parts of the system are accessible to interferometers and have been detected with the VLTI/VINCI instrument.

In the mid-IR, single telescopes such as the MMT/BLINC (Hinz et al. 2001, Liu et al. 2004), the PFN (Palomar Fiber Nuller, e.g. Mennesson et al. 2011 and reference therein), or long baseline interferometers like KIN (Keck Interferometer Nuller, Colavita et al. 2009, Millan-Gabet et al. 2011) and soon the LBTI (Large Binocular Telescope Interferometer, Hinz 2009) provide high contrast ratio using a technique called ”nulling interferometry”. Light from multi-apertures is combined to eliminate the starlight with destructive interferences and highlight the ”excess null leackage” produced by resolved dust emission. The following section consists in an article from the Astrophysical Journal by Mennesson et al. 2012. First new nulls measurements obtained for Fomalhaut are presented and confronted to simple models. I was in charge of the preliminary modelling of the near- to mid-infrared interferometric observations. In the Chapter 5, I will investigate in more details the nature of the Fomalhaut exozodi and possible source mechanisms for its origin.

B. Mennesson, O. Absil, J. Lebreton, J.-C. Augereau, E. Serabyn, M. M. Colavita, R. Millan-Gabet, W. Liu, P. Hinz, and P. Thebault. **An interferometric study of the Fomalhaut inner debris disk II. Keck Nuller mid-infrared observations**. The Astrophysical Journal (accepted Nov. 2012).

An interferometric study of the Fomalhaut inner debris disk
II. Keck Nuller mid-infrared observations

B. Mennesson[1], O. Absil[2,3], J. Lebreton[4], J.-C. Augereau[4], E. Serabyn[1], M.M. Colavita[1], R. Millan-Gabet[5], W. Liu[6], P.Hinz[7], P. Thébault[8]

ABSTRACT

We report on high contrast mid-infrared observations of Fomalhaut obtained with the Keck Interferometer Nuller (KIN) showing a small resolved excess over the level expected from the stellar photosphere. The measured null excess increases from 8 to 13 microns, with a derived mean value of 0.35% ± 0.10% between 8 and 11 μm. Given the small field of view of the instrument, the source of this marginal excess must be contained within 2AU of Fomalhaut. This result is reminiscent of previous VLTI K-band ($\simeq 2\mu$m) observations by some of us, which implied the presence of a $\sim 0.88\%$ excess, and argued that thermal emission from hot dusty grains located within 6 AU from Fomalhaut was the most plausible explanation. Using a parametric 2D radiative transfer code and a Bayesian analysis, we examine different dust disk structures to reproduce both the near and mid-infrared data simultaneously. From this preliminary modeling, which should not be considered a definitive explanation to the hot excess of Fomalhaut, we conclude that the most likely inner few AU disk geometry consists of a two-component structure, with two different and spatially distinct grain populations. The first population is revealed by the VLTI near infrared data and contributes very little mid-infrared flux. It consists of a hot ring of very small ($\simeq$ 10 to 300 nm) carbon-rich grains concentrating around 0.1 AU. The second population - inferred from the KIN mid infrared data - is constituted of larger grains (size of a few microns to a few tens of microns) located further out in a colder region where regular astronomical silicates could survive, with an inner edge around 0.4 AU to 1 AU. From a dynamical point of view, the presence of the inner concentration

---

[1] Jet Propulsion Laboratory, California Institute of Technology, 4800 Oak Grove Drive, Pasadena CA 91109-8099, USA

[2] IAGL, Université de Liège, 17 Allée du Six Août, B-4000 Sart Tilman, Belgium

[3] FNRS Postdoctoral Researcher, Belgium

[4] IPAG, UMR 5274, CNRS and Université Joseph Fourier, BP 53, F-38041 Grenoble, France

[5] Michelson Science Center, California Institute of Technology, 770 South Wilson Avenue, Pasadena CA 91125, USA

[6] Infrared Processing and Analysis Center, California Institute of Technology, Mail Code 100-22, Pasadena, CA 91125, USA

[7] Steward Observatory, University of Arizona, 933 N Cherry Avenue, Tucson, AZ 85721, USA

[8] Observatoire de Paris, Section de Meudon, F-92195 Meudon Principal Cedex, France

of sub-micron sized grains is surprising, as such grains should be expelled from the inner planetary system by radiation pressure within only a few years. This could either point to some inordinate replenishment rates (e.g. many grazing comets coming from an outer reservoir) or to the existence of some braking mechanism preventing the grains from moving out.

Subject headings: instrumentation: interferometers—infrared: stars—stars: circumstellar matter—stars: individual (Fomalhaut)

1. Introduction

Fomalhaut is a bright ($V = 1.2$) relatively young (~ 200 Myr, Di Folco et al. (2004)) A4 main sequence star located 7.7 pc away featuring a large far infrared excess first detected by IRAS (Aumann 1985). The suspected surrounding debris disk was first resolved in the far-infrared by the Kuiper Airborne Observatory (Harvey et al. 1996), then in the sub-millimeter (Holland et al. 1998), and more recently in scattered light using HST/ACS (Kalas et al. 2005). The latter optical observations show a belt of cold dust concentrated around 140 AU from the star, with an asymmetric structure consistent with gravitational sculpting by an orbiting planet (Kalas et al. 2005; Quillen 2006). Recent ALMA 350 GHz observations of the Fomalhaut debris ring (Boley et al. 2012) demonstrate that the disk parent body population is 13 to 19 AU wide with a sharp inner and outer boundary, and also suggest that debris confined by shepherd planets is the most likely origin for the ring's observed morphology. Interestingly, the detection of a point source located at 118 AU from the star - just inside the inner edge of the ring, matching its predicted location - was reported in 2008 using HST's Advanced Camera for Surveys (ACS) (Kalas et al. 2008). It was interpreted as a direct image of the disk-perturbing planet, and named Fomalhaut b. However this detection was made at 600-800 nm, and no corresponding signatures were found so far in the near-infrared range (Kalas et al. 2008; Marengo et al. 2009) , where the bulk emission of such a planet should be expected, nor at 4.5 μm with Spitzer / IRAC (Janson et al. 2012). The true nature of this HST detected source hence remains unclear at this point.

Zooming further inside the ring, now looking within a few tens of AUs from the star, a warm dust component has also been detected by Spitzer (Stapelfeldt et al. 2004): the InfraRed Spectrograph (IRS) measured an excess continuously increasing with wavelength between 17.5 and 34 microns, while direct images obtained with the MIPS instrument (Multiband Imaging Photometer for Spitzer) resolved the circumstellar disk down to a wavelength of 24 microns. Both of these observations point to a region of compact residual excess emission extending inward of $\sim$ 20 AU, but whose spatial and physical structure can not be uniquely determined given the limited resolution of Spitzer. The presence of warm dust close to the star is independently confirmed by recent 70 μm images of Fomalhaut obtained with Herschel/ PACS (Photodetector Array camera and Spectrometer) (Acke et al. 2012). These spectacular images show both the cold outer ring and an unresolved excess source co-located with the central star (i.e within 5.7", given Herschel beam size) carrying 50% ± 10% of its flux.

High accuracy long baseline interferometric observations provide the resolution and contrast required to probe this central region in greater details. They focus on the very inner part of Fomalhaut's environment (within a few AU), probing very different astrophysical scales and conditions than those studied by single optical/ infrared telescopes. Near infrared interferometric observations obtained at the VLTI were already reported in a first paper (Absil et al. 2009, hereafter Paper I), concluding to the presence of a K-band excess of $0.88 \pm 0.12\%$, and arguing that thermal emission from hot dusty grains located within 6 AU from Fomalhaut is the most plausible explanation for the detected excess. We present here new data obtained at N band (8 to $13\,\mu$m) with the Keck Interferometer Nuller (KIN) in August 2007 as part of KIN's commissioning "shared risk" science operations, and in July 2008 as part of the KIN key science program (PI: Phil Hinz). These near infrared (VLTI) and mid-infrared (Keck) interferometric measurements are then used in conjunction with spectro-photometric data to constrain the physical parameters of inner few AU of Fomalhaut's debris disk. Finally, we discuss a few possible astrophysical scenarios which are compatible with the observed disk and dust characteristics.

2. Nulling Set-Up and Observable Quantities

The overall KIN system architecture and performance are presented in full detail in recent publications (Colavita et al. 2008, 2009; Serabyn et al. 2012). In brief, four beams are recombined by the KIN system. A split mirror located downstream of each Keck telescope adaptive optics system—close to a pupil plane—divides the light gathered by each telescope into "left" and "right" beams. Interferometric nulling occurs separately between the two Keck left beams, and between the two right beams. The resulting nulled output fields are then coherently recombined using a standard Michelson interferometer, called the "cross-combiner". As the optical delay is rapidly scanned inside the cross-combiner, one measures the cross combiner fringe amplitude at null in each of ten independent spectral channels covering the full N band (8 to $13\,\mu$m). The operation is then repeated with the two left beams and the two right beams interfering constructively, now measuring the cross-combiner fringe amplitude "at peak". The null depth is defined as the ratio of the cross-combiner fringe amplitudes obtained at null and at peak. The rationale for this complex 4-beam combination and modulation, is that the resulting measured null depth is free of slow drifts in the incoherent background, a source of strong potential bias for ground-based interferometric observations in the thermal infrared. Two different scales and baselines are then involved: the interferometric nulling baseline of length $B \simeq 85\,$m, separating the telescopes centers, and the short cross combiner baseline $b \simeq 4\,$m, characteristic of the interference between the "left" and "right" parts of a given Keck telescope.

For a perfect instrument, defined as providing a null depth of zero on a point source, one can relate the measured monochromatic astrophysical null $N_{\rm ast}$ to the source brightness distribution on the sky $I(\vec{\theta})$. The observed null can be expressed in the following way (Serabyn et al. 2012)

$$N_{\rm ast}(\lambda) = \frac{\int I(\vec{\theta}) \sin^2(\pi\vec{B}\cdot\vec{\theta}/\lambda)) \cos(2\pi\vec{b}\cdot\vec{\theta}/\lambda)\sqrt{T_L(\vec{\theta})T_R(\vec{\theta})}d\vec{\theta}}{\int I(\vec{\theta}) \cos^2(\pi\vec{B}\cdot\vec{\theta}/\lambda) \cos(2\pi\vec{b}\cdot\vec{\theta}/\lambda))\sqrt{T_L(\vec{\theta})T_R(\vec{\theta})}d\vec{\theta}}\,, \tag{1}$$

where $T_L(\vec{\theta})$ and $T_R(\vec{\theta})$ designate the sky transmission patterns of the left and right Keck beams, respectively. They are computed from the telescopes orientation and from the overall beam train propagation, which includes an intermediary focal plane pinhole. As a result, the field of view FWHM is at maximum 450 mas, along the direction perpendicular to the left-right split, corresponding to about ± 2AU at Fomalhaut's distance. As shown in Equation 1, in the case of an extended source, the measured null level is not only affected by the long baseline nulling pattern (fast oscillating squared sine term), but also by the cross fringe pattern (slowly oscillating cosine term) [1] and by the lobe antenna of each single beam. As representative examples of these 3 contributors to the effective KIN sky transmission, the left and right panels of Fig. 1 show the monochromatic (10 μm) KIN's transmission patterns corresponding to the 2007 and 2008 observations of Fomalhaut, respectively. Both are derived at the time of meridian transit and mostly differ in the orientation of the short baseline (see section 3). Also indicated in these figures is the orientation of Fomalhaut's outer debris disk major axis (156° East of North), as imaged by HST/ACS (Kalas et al. 2005). For both epochs, the projected Keck to Keck interferometric baseline orientation is $\simeq$ 73 degrees away from the outer dust disk main axis.

In the case where no extended emission is present (source angular size $\ll \lambda/b$), the astrophysical null expression (Equation 1) can be approximated by:

$$N_{\rm ast}(\lambda) = \frac{\int I(\vec{\theta}) \sin^2(\pi\vec{B}\cdot\vec{\theta}/\lambda)d\vec{\theta}}{\int I(\vec{\theta})d\vec{\theta}}\,. \tag{2}$$

In particular, for a naked star represented by a uniform disk (UD) of diameter θ_* ($\ll \lambda/B$), the observed astrophysical null is given by:

$$N_{\rm ast}(\lambda) = \left(\frac{\pi B\theta_*}{4\lambda}\right)^2\,. \tag{3}$$

For a more realistic model, in which a naked star is represented by a limb darkened disk of diameter $\theta_{\rm LD}$, with a linear limb darkening coefficient u_λ, the observed astrophysical null is (Absil et al. 2006, 2011):

$$N_{\rm ast}(\lambda) = \left(\frac{\pi B\theta_{\rm LD}}{4\lambda}\right)^2 \left(1-\frac{7u_\lambda}{15}\right)\left(1-\frac{u_\lambda}{3}\right)^{-1}\,. \tag{4}$$

In practice, the null depth measured on a point source is not zero but equal to the instrumental null, noted $N_{\rm ins}$. Consequently, the observed null depth $N_{\rm obs}$ is not strictly equal to the astrophysical null

---

[1] A curious effect of the KIN 4-beam combination is that for emission sources extending further out than λ/b in the direction of the cross-combiner baseline b (b $\simeq 4\,m$), some regions will contribute "negatively", i.e. effectively decrease the observed null depth. This is illustrated by the areas of negative transmission shown in Fig. 1

$N_{\rm ast}$ characteristic of the source, and one measures instead:

$$N_{\rm obs} = (N_{\rm ast} + N_{\rm ins})/(1 + N_{\rm ast}N_{\rm ins})\ . \tag{5}$$

Full details on the terms contributing to the instrumental null can be found in Colavita et al. (2009) and Serabyn et al. (2012). For all the observations considered here, both $N_{\rm ins}$ and $N_{\rm ast}$ are small ($< 2\%$), so that one can use the approximation:

$$N_{\rm obs} = N_{\rm ast} + N_{\rm ins}\ . \tag{6}$$

As in classical stellar interferometry, the instrumental null $N_{\rm ins}$ is derived from nulling observations of calibrator stars with known diameters and limb darkening properties, i.e., with predictable astrophysical nulls (Equation 4).

3. Observations and Data Analysis

The basic observing block of the KIN is a 400ms long ”null/ peak micro-sequence” (see Colavita et al. (2009), figure 3). Each micro-sequence yields an individual null depth estimate defined as the ratio of the cross-combiner fringe amplitudes measured at null and at peak. A null measurement sequence consists in 1000 consecutive micro-sequences, from which a mean null estimate is derived, together with its standard deviation.

Six such null measurement sequences were recorded on Fomalhaut in 2007: one on August 28 and five more on August 30 (shared risk science observations). Only the six spectral channels with wavelengths shorter than 11 μm provided adequate signal to noise and are discussed here. Eight more individual null measurement sequences were then obtained on July 17 and 18, 2008 (key science program observations, PI: Phil Hinz). This time, the full 8 to 13 μm range was covered using ten spectral channels.

3.1. Calibrators

Fomalhaut’s observations were interleaved with measurements of four nearby calibrator stars, whose characteristics are given in Table 1. Their limb darkened (LD) diameters are estimated from V and K magnitudes (corrected for interstellar reddening) and surface brightness relationships developed by Di Benedetto (2005), except for the redder source HD 214966. In this case, the V-K color falls outside of Di Benedetto’s relationships applicability range, and we use instead the surface brightness relationships derived by Bonneau et al. (2012).

At the central wavelength of each spectral channel, the expected calibrators astrophysical nulls are then derived using Equation 4, assuming a constant N-band linear limb darkening coefficient $u_N = 0.12$ (Tango & Davis 2002) for all four calibrators. Limb darkening corrections are expected to be small for such stars at 10 μm, and fairly constant over the range of $T_{\rm eff}$ and $\log(g)$ covered by our calibrators.

While Di Benedetto (2012) reports relative uncertainties as low as 2% in his LD diameter estimations, we use larger (1-σ) error bars to account for uncertainties in K band photometry or mid-infrared LD coefficients. For HD 222547 and HD215167, which have accurate K band photometry, we adopt a relative error of 6%. For HD 214966, we use the 7% relative error quoted by Bonneau et al. (2012). Finally, HD 210066 only has 2MASS (saturated) photometric measurements available at K-band, and we adopt a conservative LD diameter error of 10%.

3.2. Calibrated Astrophysical Nulls

The instrumental null at the time of a given Fomalhaut observation is computed by interpolation between the instrumental nulls derived on adjacent calibrators. At each wavelength and for each projected baseline length, one computes Fomalhaut's calibrated astrophysical null from the observed nulls using Equation 6. The resulting calibrated astrophysical nulls are summarized in Table 2.

Overall, the length of the long baseline $\vec{B}$ projected onto the sky plane (B_p) varied between 55.12 m and 77.81 m during the observations, while the projected baseline azimuth varied only slightly (between $47\overset{\circ}{.}4$ and $49\overset{\circ}{.}9$).

The projected length of the short baseline $\vec{b}$, on the other hand, does not change: by construction, it is always located in the (pupil) plane perpendicular to the line-of-sight (see Fig. 2). We note that the short baseline orientation was changed by 90° between the 2007 and 2008 observations. In 2007, it was located in the plane defined by the zenith and the line-of-sight, while in 2008, it was located in the local horizontal plane (see Fig. 2). These variations in the short baseline azimuth do not have a large influence on the measurements but were included in the null computations (Equation 1) and modeling.

3.3. Null excess leakage

The next step in the data analysis is to evaluate the fraction of Fomalhaut's calibrated astrophysical null that actually comes from the circumstellar environment. This requires the computation of the null depth expected from the photosphere alone (naked star scenario, Equation 4). We use Fomalhaut's limb darkened diameter $\theta_{\rm LD} = 2.223 \pm 0.022$ mas deduced from the latest VLTI K band measurements (Paper I) and a constant linear limb darkening coefficient $u_N = 0.06$ between 8 and 13 μm (Tango & Davis 2002). For the baselines considered here, the stellar contribution to the total null depth typically ranges from 0.5% and 0.2% for wavelengths from 8 to 13 μm. The difference between Fomalhaut's observed calibrated null and this purely photospheric leakage is noted "null excess" hereafter. It characterizes the contribution of any source of circumstellar emission located within the nuller field of view.

For each of the 14 independent calibrated observations reported in Table 2, we compute the resulting null excess as a function of wavelength. Since there is very little variation in azimuth over the full data set but some projected baseline length variations and some changes in the instrumental set-up between 2007 and 2008, we further regroup the measurements according to mean baseline length ('"short" or "long") and year of observation. This allows to generate 4 final data sets form the original 14, which reduces null measurements uncertainties and the modeling computation time (section 4). For instance the 2007 "short" baseline data summarize measurements from the three shortest baselines, ranging from 58 to 63 m. From that sub-ensemble of measured null excesses and associated error bars, we compute the weighted mean null excess and its 1-σ uncertainty (we use the weighted standard deviation). This provides an accurate estimate of the null excess at the 2007 short observing baseline, which has a mean length of 60.72 m and an equivalent azimuth of 49.77°. Fig. 3 (top left) shows Fomalhaut's measured null excess at this baseline, as a function of wavelength. Fig. 3 (bottom left) shows similar curves for the 2007 long baseline data (mean length of 71.88 m, for an equivalent azimuth of 48.66°). Analogous results are presented for the 2008 observations in Fig. 3 (right panels), grouping the four shortest baselines (55 to 62 m, mean length of 58.43 m, azimuth of 49.42°, top right inset), or the four longest ones (73 to 78 m, mean length of 75.79 m, azimuth of 47.40°, bottom right inset). These figures show that our 2007 and 2008 data sets are consistent with each other (generally to within 1σ), although the short wavelengths excess null looks slightly larger in 2007 than in 2008.

Based on the results presented on Fig. 3 and taking all 2007 and 2008 observations into account, the (weighted) average null excess measured between 8 and 11 μm is 0.35%. Small systematic errors have been previously identified in the KIN data (Colavita et al. 2009), potentially biasing the nulls measured at different wavelengths in a systematic way during a given night. As a consequence, we use for our measurements the 1-σ uncertainty level recommended in Colavita et al. (2009), which represents our best understanding of the instrument. For KIN measurements of stars as bright as Fomalhaut in the 8 to 11 μm range, this uncertainty corresponds to 0.2% rms *per night*, or 0.1% over the 4 nights of observations reported here. Our final estimate of Fomalhaut's averaged null excess in the 8 to 11 μm region is then $0.35\% \pm 0.10\%$. Finally, we note that for the 2008 data - covering the whole 8 to 13 μm atmospheric N band window-, the observed excess increases with wavelength, for both baseline ranges considered.

4. Modeling and Interpretation

Although each of our four data subsets is formally consistent with pure photospheric emission to within 2-3 σ, an excess null is measured at all wavelengths and for *all four* of the observing nights, covering years with slightly different KIN instrumental set-ups. This urges us to go beyond a simple photospheric model to explain our observations. Owing to the various observational evidences for warm emission in the Fomalhaut inner system (Paper I & Stapelfeldt et al. (2004); Acke et al. (2012)), we try hereafter to model the measured excess null using purely morphological debris disk models. In particular, we do not favor the assumption that either the observed KIN or the VLTI /VINCI emission is due to gaseous free-free emission from a stellar wind, and there are three main reasons for that:

- For A stars, the photospheric emission still goes as ν^2 in the near infrared (IR), while the

$\nu^{0.6}$ spectral slope for free-free emission starts to break down in the mid-IR, where free-free emission becomes optically thin, and the slope flattens for shorter wavelengths (e.g. Wright & Barlow (1975)). As a result, the free-free emission level relative to the star is expected to be smaller in the near-IR than in the mid-IR. Free-free emission would probably not be sufficient to reproduce the observed VINCI K-band excess (Paper I). And if it were, then it would be stronger in the mid-IR, which is not compatible with the low level of emission seen by the KIN.

- Second, the size of free-free emission regions decrease at shorter wavelengths. Actually, at the wavelength where free-free emission becomes optically thin, the size of the emitting region is of the order of the stellar size. Therefore, we would not expect the near-IR free-free emission to be significantly extended (while the previous VLTI observations show the K-band emitting region to be at least 10 times larger than the photosphere).
- Third, stellar models predict very small mass loss rates for A-stars (e.g., 1e-16 $M_\odot/yr$, Babel et al. (1995)), which are not compatible with strong free-free emission.

4.1. Modeling the Mid-Infrared Data with a Solar Zodiacal Disk Model

Since the observed null depth is a function of source brightness distribution and baseline orientation (see Equation 1), we first need to define a morphological model for any excess emission before computing its associated photometric flux. In other words, the true astrophysical excess can not be uniquely derived from the data, unless some assumptions are made on its spatial brightness distribution. As a first rough attempt to estimate the luminosity of the marginal excess detected, we have used a scaled model of the solar system's zodiacal disk around Fomalhaut. This model is based on the parametric description of the zodiacal cloud observations by the COBE/DIRBE instrument Kelsall et al. (1998) and is implemented in the ZODIPIC package[2]. The dust density and temperature profiles are assumed to follow the power laws derived in the solar system case: n(r) $\propto r^{-1.34}$, and T(r) $\propto L^{\delta/2}/r^{\delta}$, with δ=0.467 (Kelsall et al. 1998) and Fomalhaut's luminosity L= 17.7 L$\odot$ (Di Folco et al. 2004). The dust is assumed to extend from the sublimation radius corresponding to a temperature of $1500\,K$ (typical of silicate grains found in the solar system), all the way to 10 AU, i.e. much further out than the KIN field of view. The exo-zodi disk is modeled with the same inclination (65.6°) and position angle (156°) as Fomalhaut's outer dust disk (Kalas et al. 2005). The result of the best fit is a luminosity (and density) scaling factor of 350 with respect to the solar case, with 1-σ uncertainty of about 100. Such a disk would produce a total emission of 0.55 Jy across the KIN field-of-view at $10\,\mu$m, i.e., a flux ratio of $\simeq$ 3% with respect to the photosphere. This illustrates the fact that due to the nuller sky transmission pattern, the true 10 μm astrophysical excess around Fomalhaut could be significantly larger than our observed null excess of $\simeq$ 0.35%. This is especially true in the case of Fomalhaut, where the disk PA is almost perpendicular to the long Keck to Keck baseline (Fig. 1).

---

[2] ZODIPIC is an IDL program originally developed by M. Kuchner & E. Serabyn for synthesizing images of exozodiacal clouds. It can be downloaded at `http://asd.gsfc.nasa.gov/Marc.Kuchner/home.html`.

While such a simple zodiacal disk model can reproduce the full KIN data set reasonably well (Fig. 3), this result seems at odds with the significant K-band excess reported in Paper I, which would require an equivalent dust surface density 5000 times larger than the solar zodiacal cloud to be reproduced. This is an order of magnitude larger than the level derived to fit the KIN data. This inconsistency forces an examination of dust disk morphologies other than the standard zodiacal disk model, which fails to explain the near- and mid-IR observations simultaneously, and which has really no physical grounding in the case of Fomalhaut. Given the small excess null detected by the KIN (or even considering its 3-σ upper limit of just 0.65%), it is clear that the grains responsible for the near-IR emission are not contributing much at 10 μm. We will now look for models consistent with this observational result.

4.2. Combined Modeling of Near- and Mid-Infrared Data

We used the GRaTeR code (Augereau et al. 1999) to compute a grid of models that we compare with our full data set consisting of spectro-photometric and interferometric data gathered in the near and mid-infrared (see Table. 3 and Fig. 4). GRaTeR calculates models for optically thin disks. It is designed to simulate spectral energy distributions (SEDs), images and interferometric data with parametric grain size and radial distributions, or distributions from dynamical simulations. Both the scattered light and the continuum emission of dust grains in thermal equilibrium with a star are computed, using the Mie theory and the Bruggeman effective medium method, depending on the material optical constants (Bohren & Huffman 1983). Particular care is given to the removal of grains when their temperature exceeds the material sublimation temperature. When multi-material grains are used with various sublimation temperatures $T_{\rm sub}$, the first material to sublimate is replaced by porosity (affecting the optical properties with respect to compact grains of the same size). We compute a grid of models where we let 6 parameters vary: (1) the geometry of the exozodiacal disk (assuming azimuthal symmetry before sky-plane projection) defined through its surface density profile $\Sigma(r) = \Sigma_0 \sqrt{2} \left((\frac{r}{r_0})^{-2\alpha_{\rm in}} + (\frac{r}{r_0})^{-2\alpha_{\rm out}} \right)^{-1/2}$ where Σ_0 is the density at the peak position r_0, $\alpha_{\rm in}$ the inner slope (fixed to +10 to mimic a sharp inner edge), $\alpha_{\rm out}$ the outer slope, (2) the dust size distribution (parameters κ and $a_{\rm min}$ of the classical power-law $dn(a) \propto a^{\kappa} da$ valid for grains from $a_{\rm min}$ to $a_{\rm max} = 1$ mm), (3) the dust composition $v_{\rm C}/v_{\rm Si}$, that assumes mixtures of carbonaceous material (volume fraction $v_{\rm C}$) and astronomical silicates ($v_{\rm Si}$), (4) the total disk mass $M_{\rm dust}$ in grains up to 1 mm in radius. The range of values used for each parameter is summarized in Tab.4. This parameter space leads to a wide range of different models that we compare with the data using both a classical χ^2 minimization and the statistical Bayesian method described in Lebreton et al. (2012). All parameters are assumed to have uniform prior probabilities, at the exception of the treatment we use to account for the inner sublimation radius $r_{\rm sub}(a, \text{material})$. In that case, we define prior probabilities in order to eliminate all models for which $r_0 < \min(r_{\rm sub})$.

4.2.1. Fitting data obtained at all wavelengths

We first attempt to fit all the near and mid-infrared data simultaneously (34 data points, see Tab. 3). The shape of the exozodi spectrum requires very hot grains which is achieved when these are small and close to the star. Indeed, the probability curves derived from the fit Bayesian analysis and presented in Fig. 6 (red curves) shows that, *when considering each parameter independently*, the most probable models are found for very small grains ($a_{\rm min} \leq 0.08\ \mu m$ and $\kappa \leq -5.3$ with 1-σ confidence), confined very close to the sublimation distance ($0.07 \leq r_0 \leq 0.14$ AU, $\alpha_{\rm out} \leq -5.0$) [3]. The model requires that these high-temperature grains include a large fraction of carbonaceous material ($\frac{v_{\rm C}}{v_{\rm C}+v_{\rm Si}} \geq 91\%$), to reduce the 10 microns emission feature that submicron-sized silicate grains would produce, and to reach higher temperatures. Indeed, the sublimation temperature of carbon is higher than that of silicates ($T_{\rm sub}$(C) = 2000 K, $T_{\rm sub}$(Si) = 1200 K, Kobayashi et al. 2009) allowing carbon grains to survive closer to the star. The smallest sublimation distances are obtained for the largest grains, with min($d_{\rm sub}$(C)) = 0.07 AU, and min($d_{\rm sub}$(Si)) = 0.21 AU (see sublimation curves in Fig. 5 for details).

A clear secondary peak in the disk inner edge probability curve reveals that a second family of solutions is of statistical relevance, one that uses grains located further out from the star ($r_0 \sim 0.4$ AU). In fact the model with the smallest overall χ^2 (see Tab. 5) is found among this second family of solutions[4], where $\sim 0.2\ \mu m$ grains orbiting in the ∼0.4 AU region, dominate the emission, with a characteristic temperature of 1600 K. The disk is largely dominated by thermal emission over scattered light at the wavelengths considered here. The result of this fit to the null and spectrophotometric data is shown in Fig. 4 (red curves). The SED is well fitted for a total dust mass of $\sim 4 \times 10^{-10} M_{\oplus}$. The flux contributed by grains of different sizes depending on their distance to the star is illustrated in Fig. 5 (upper panels). From Fig. 4 (red curves), it is clear that this overall best fit model fails at reproducing the rising null depth observed toward the mid-IR ($\lambda \geq 11 \mu m$) with the KIN in 2008. The model predicts instead a monotonically decreasing contrast toward longer wavelengths and overpredicts the shortest wavelengths null depth from 2008, while staying compatible with the 2007 data. Overall, it appears impossible to fit *all* the data with a single-annulus / single grain population model, since the VLTI detection requires very hot dust close to the sublimation radius, while the apparent rise of the KIN nulls beyond 11 microns is reminiscent of colder dust. The binomial distribution of the best fit inner radius (r_0, Tab. 5) is also suggestive of a two component dust distribution.

In an attempt to explore this two dust component scenario with the GRaTeR code, which is currently limited to a *single* dust population (already exploring a large 6-parameter space, see Tab.4), we now fit

---

[3] Formally, these probabilities must read as the *probability of the models knowing the data*. It must be noted that for some parameters, the probability curves tend to peak towards the limits of the parameter space, in a physically unmeaningful manner. Thus the confidence intervals we provide must be taken cautiously. In particular, κ and $\alpha_{\rm out}$ should be considered as weakly constrained.

[4] The most probable solution for individual parameters can indeed be distinct from that found in the 6-dimensions parameter space.

separately the data shortward of $11\mu m$ (hereafter labelled "SHORT") and the data longward of $11\mu m$ (hereafter labelled "LONG"). An improved version of the GRaTeR code, including self consistent modeling and radiative transfer calculations through multiple dust components is currently under development (Lebreton in prep.) but behind the scope of this paper.

4.2.2. Fitting data subsets

The shortest wavelengths ($\lambda < 11$ μm, observations (26 data points, see Tab. 3) can be fitted by a family of models comparable to the one previously discussed: the probability curves (Fig. 6) reveal that very small grains located very close to the sublimation limit are favored. The solution now has r_0 in the range 0.08-0.11 AU, *i.e.* located as close as possible to the star, next to the size- and composition-dependent sublimation radius. The best fit model is presented in Tab. 5 and Fig. 4 (blue curves). Fig. 5 (middle panels) reveals that this solution also consists of sub-micron grains with $a_{\rm min}$ in the range 0.01-0.21 μm.

Now fitting only the longer wavelengths observations ($\lambda > 11\mu m$, 11 points including Spitzer/IRS upper limits, see Tab. 3), significantly different results are found. As can be seen in Fig. 4 (green curves) and Fig. 5 (lower panels), the KIN observations are well reproduced if grains are located in a ring located further out from the star, and two families of solutions emerge with $r_0 \sim 0.45$AU or $r_0 \sim 1.0$AU. With an unconstrained κ, and $a_{\rm min}$ close to the radiation pressure blowout size ($a_{\rm blow}({\rm C}) = 3.5\mu m$, $a_{\rm blow}({\rm Si}) = 2.3\mu m$), the size distribution appears compatible with the dynamical and collisional constraints. Any carbon to silicates ratio is equally probable. A wide range of disk masses is allowed, from 10^{-9} $M_\oplus$ for the first family of solutions, to 10^{-6} $M_\oplus$. The density profile does not necessarily need to be very steep, a -1.0 power-law index for instance yields a satisfactory fit with a mass of 4×10^{-7} $M_\oplus$. While it fails to reproduce the observed K-band excess satisfactorily (Fig. 4 SED green curve), this model clearly provides the best fit to the overall KIN data.

Simulating the emission of a fully self-consistent two-rings structure based on a combination of the "SHORT" and "LONG" models presented here is beyond the scope of this work. Yet, the rising slope of the nulls depths measurements produced by the LONG model gives us confidence that a two-peak model is the best solution to reconcile all of the data.

5. Summary

Our approach demonstrates that the near and mid-infrared interferometric data are consistent with a hot debris disk residing interior to the habitable zone of the Fomalhaut system (which extends from $\simeq 4$ AU to $\simeq 6$ AU given the star's luminosity). The description of this hot debris disk as a single population of grains is not sufficient to explain both the near-IR excess flux found by VLTI/VINCI, and the small mid-IR flux reported here. A possible explanation is that the exozodi has a more complex geometry, for instance a double-peak structure.

In order to be consistent with the KIN measurements, the VLTI near infrared excess requires a large population of small ($\simeq$ 10 to 300 nm) hot dust located very close to the rim defined by the sublimation distance of carbon. Such grains are however much smaller than the radiation pressure blowout size and they should be placed on hyperbolic orbits and ejected very fast from this region. A similar paradox was found by Defrère et al. (2011) for the disk of Vega, and unveiling the origin of this hot dust is still a challenge to debris disk science. The main difficulty is to explain how such high levels of sub-micron grains can be present, when these grains should be blown out by radiation pressure on very short timescales, typically of the order of a dynamical timescale, i.e., much less than a year in these inner regions. Is it because these grains are prevented from moving out by a braking mechanism, and if yes, which one? gas drag? collisions in a very dense and radially optically thick disc? Or is it because the production rate of these small particles is so high in these regions that, despite their fast removal, a significant amount is always present at a given time? These issues will be explored in a forthcoming paper (Lebreton et al., in preparation).

On the other hand, the KIN observations detected a small mid-IR excess which appears to increase with wavelength between 8 and 13 microns, which constrains the dust location to lie in a colder region where astronomical silicates could survive. While the VLTI excess only probes the inner hotter component, this second dust population is traced by the KIN data. With micrometer sizes compatible with a classical-collisional equilibrium, mid-IR emission at the level seen, would require an independent dust population, originating from a much more massive population of planetesimals, comparable to the Solar System Main Belt. The low statistics associated with this warm component do not allow firm conclusions on the parameters of this grain population, but it is a serious hint that a secondary zodiacal belt lies within the field of the interferometer, i.e. inside a few AU.

Finally, we underline that our approach suffers some limitations and should not be considered a definitive explanation to the hot excess of Fomalhaut. First, because each component contributes to both subsets of data, a proper parameterization of the double-population should be used to self-consistently describe the exozodi. Second, our treatment of dust sublimation is still very coarse as it eliminates instantaneously the grains when they exceed the sublimation temperature. Kama et al. (2009) show that a proper treatment of time-dependent sublimation physics allows grains hotter than the current $T_{\rm sub}$ to survive a certain time before vanishing, depending on their size. Allowing for these transient grains would likely results in putting some large grains inside the current sublimation rim, thus impacting the best-fit models. In a future study, we will improve these aspects of our model, hopefully reconciling the results with theoretical predictions. Of course, another possibility is that the disk has suffered important variability in the time interval between VLTI and Keck observing runs. Follow-up observations are needed to answer this open question, and more generally constrain hot dust transience around mature stars.

Acknowledgments

The Keck Interferometer was funded by the National Aeronautics and Space Administration (NASA). Part of this work was performed at the Jet Propulsion Laboratory, California Institute of Technology, and at the NASA Exoplanet Science Center (NExSci) , under contract with NASA. The Keck Observatory was made possible through the generous financial support of the W.M. Keck Foundation. O. Absil, J.-C. Augereau, J. Lebreton and P. Thébault thank the French National Research Agency (ANR, contract ANR-2010 BLAN-0505-01, EXOZODI) for financial support.

REFERENCES

Absil, O., den Hartog, R., Gondoin, P., et al. 2011, A&A, 527, C4+

Absil, O., Mennesson, B., Le Bouquin, J.-B., et al. 2009, ApJ, 704, 150 (Paper I)

Absil, O., den Hartog, R., Gondoin, P., et al. 2006, A&A,448, 787

Acke, B., et al 2012, A&A, 540, 125

Augereau, J. C., Lagrange, A. M., Mouillet, D., Papaloizou, J. C. B., & Grorod, P. A. 1999, Astronomy & Astrophysics, 348, 557

Aumann, H. H. 1985, PASP, 97, 885

Babel, J., 1995, A&A, 301, 823

Bohren, C. F. & Huffman, D. R. 1983, Absorption and scattering of light by small particles, ed. Bohren, C. F. & Huffman, D. R.

Boley, A.C., et al 2012, ApJ, 750, 21

Bonneau, D., et al 2006, A&A, 456, 789

Bouchet, P., Schmider, F. X., & Manfroid, J. 1991, Astronomy and Astrophysics Supplement Series, 91, 409

Colavita, M. M., Serabyn, E., Booth, A. J., et al. 2008, in Society of Photo-Optical Instrumentation Engineers (SPIE) Conference Series, Vol. 7013, Optical and Infrared Interferometry

Colavita, M. M., Serabyn, E., Millan-Gabet, R., et al. 2009, PASP, 121, 1120

Defrère, D., Absil, O., Augereau, J.-C., et al. 2011, Astronomy & Astrophysics, 534, A5

Di Benedetto, G. P. 1998, A&A, 339, 858

Di Benedetto, G. P. 2005, MNRAS, 357, 174

Di Folco, E., Thévenin, F., Kervella, P., Domiciano de Souza, A., Coudé du Foresto, V., Ségransan, D., & Morel, P. 2004, A&A, 426, 601

Harvey, P. M., Smith, B. J., Difrancesco, J., Colome, C., & Low, F. J. 1996, ApJ, 471, 973

Holland, W. S., Greaves, J. S., Zuckerman, B., et al. 1998, Nature, 392, 788

Janson, M., et al 2012, ApJ, 747, 116

Kalas, P., Graham, J. R., Chiang, E., et al. 2008, Science, 322, 1345

Kalas, P., Graham, J. R., & Clampin, M. 2005, Nature, 435, 1067

Kama, M., Min, M., & Dominik, C. 2009, Astronomy & Astrophysics, 506, 1199

Kelsall, T., Weiland, J. L., Franz, B. A., et al. 1998, ApJ, 508, 44

Kobayashi, H., Watanabe, S.-I., Kimura, H., & Yamamoto, T. 2009, Icarus, 201, 395

Lahuis, F., Kessler-Silacci, J. E., Evans, N. J., I., et al. 2006, c2d Spectroscopy Explanatory Supplement, Tech. rep., Pasadena: Spitzer Science Center

Lebreton, J., Augereau, J.-C., Thi, W.-F., et al. 2012, Astronomy & Astrophysics, 539, A17

Li, A. & Greenberg, J. M. 1997, Astronomy & Astrophysics, 323, 566

Marengo, M., et al 2009, ApJ, 700, 1647

Quillen, A. C. 2006, MNRAS, 372, L14

Serabyn, E., Mennesson, B., Colavita, M.M., Koresko, C., & Kuchner M. 2012, ApJ, 748, 55

Stapelfeldt, K. R., Holmes, E. K., Chen, C., Rieke, et al. 2004, ApJS, 154, 458

Tango, W. J., & Davis, J. 2002, MNRAS, 333, 642

Wright, A. E., & Barlow, M. J. 2002, MNRAS, 170, 41

Zubko, V. G., Mennella, V., Colangeli, L., & Bussoletti, E. 1996, Mon. Not. R. Astron. Soc., 282, 1321

This preprint was prepared with the AAS LaTeX macros v5.2.

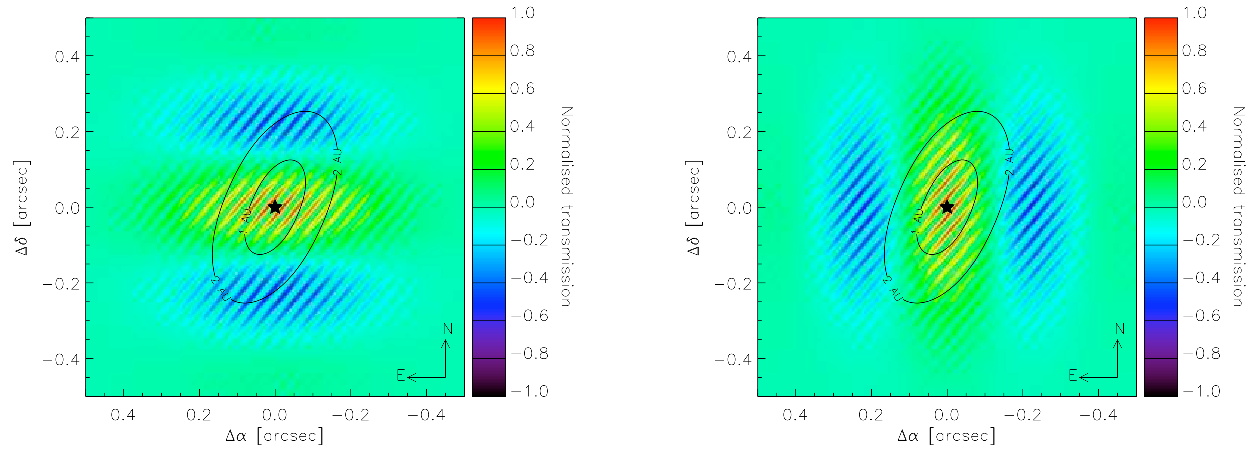

Fig. 1.— Left panel: Keck Nuller sky transmission at 10 μm, when observing Fomalhaut at meridian transit on August 30, 2007 (Julian date: 2454342.95, projected baseline length: 67.6 m, azimuth: 48.°7). North is up, East is to the left. High frequency fringes correspond to the long baseline separating the telescopes. The low frequency modulation is produced by interference between the sub-apertures of a single Keck telescope (”cross combiner” fringes); these fringes are aligned with the North-South direction when observing a star at transit. The contours indicate inner regions of the Fomalhaut system ($i = 66°$, PA $= 156°$), showing that the KIN is sensitive to dust emission in the 0.05 to 2 AU range. Right panel: Keck Nuller sky transmission at 10 μm, when observing Fomalhaut at meridian transit on July 17, 2008 (Julian date: 2454664.07, projected baseline: 67.8 m, azimuth: 49.°6). For the 2008 observations, the telescope pupil was rotated by 90° with respect to 2007. As a result, the low frequency (“cross combiner” fringes) are now aligned with the East-West direction when observing a star at transit.

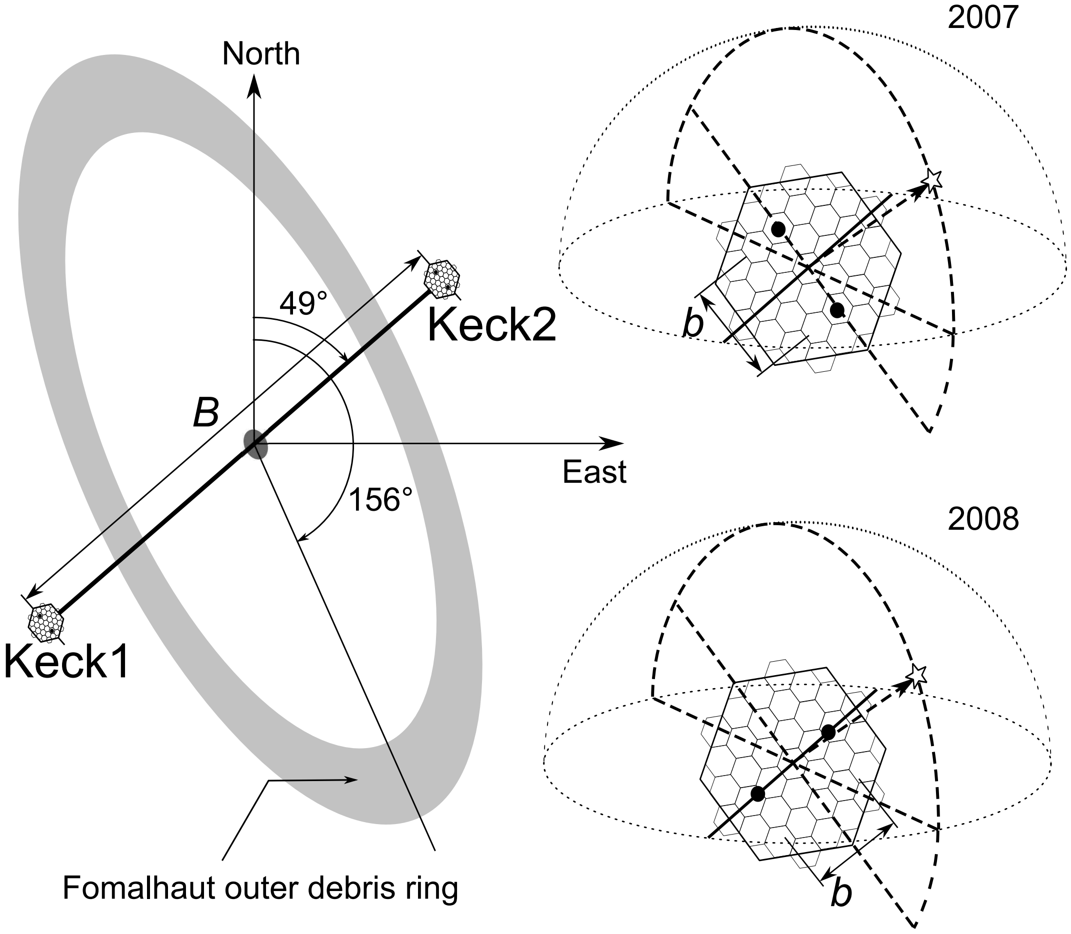

Fig. 2.— Configuration of the long baseline B (left) and of the short baseline b (right) of the Keck Interferoemter Nuller relative to the Fomalhaut planetary system (represented by its cold dust annulus, with a position angle of 156°). All the dashed lines and curves are located within the same plane, including the zenith and the line-of-sight. The two bold dots represent the centers of the two sub-pupils defined on a given Keck pupil.

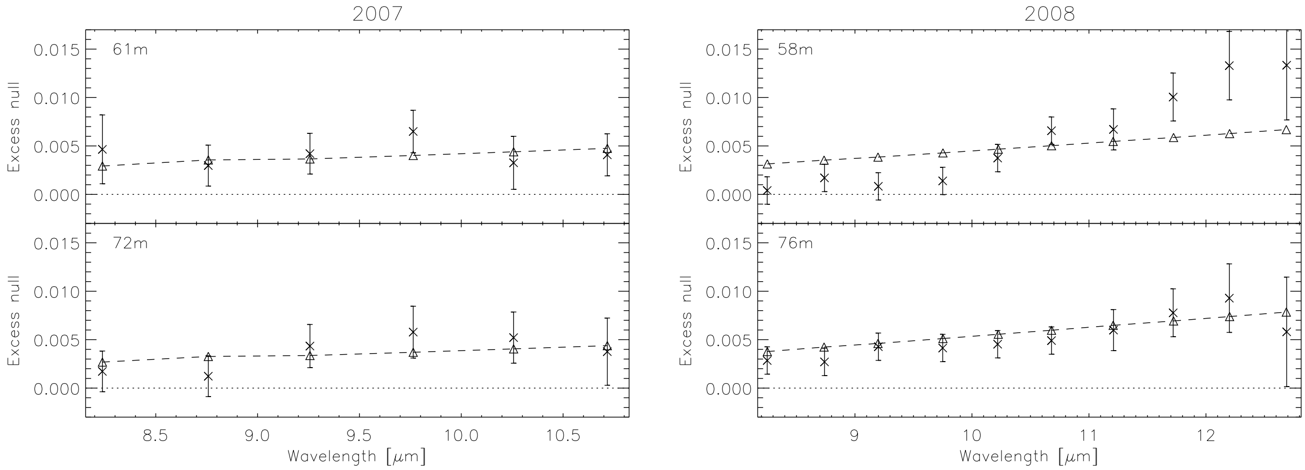

Fig. 3.— Left panel: 2007 calibrated excess null depth measurements of Fomalhaut plotted as a function of wavelength (crosses with error bars). Data were obtained at six different baselines and grouped into one short equivalent baseline ($\simeq$ 61 m) and one long ($\simeq$ 72 m, see text for details). Right panel: 2008 calibrated excess null depth measurements of Fomalhaut plotted as a function of wavelength (crosses with error bars). Data were obtained at eight different baselines and grouped into one short equivalent baseline ($\simeq$ 58 m) and one long ($\simeq$ 76 m, see text for details). In both panels, the expected photospheric null depth has been subtracted from the original KIN data to construct the "excess null", which reveals a possible circumstellar excess. The excess null created by a 350-zodi exozodiacal disk is shown with triangles and dashed lines for comparison.

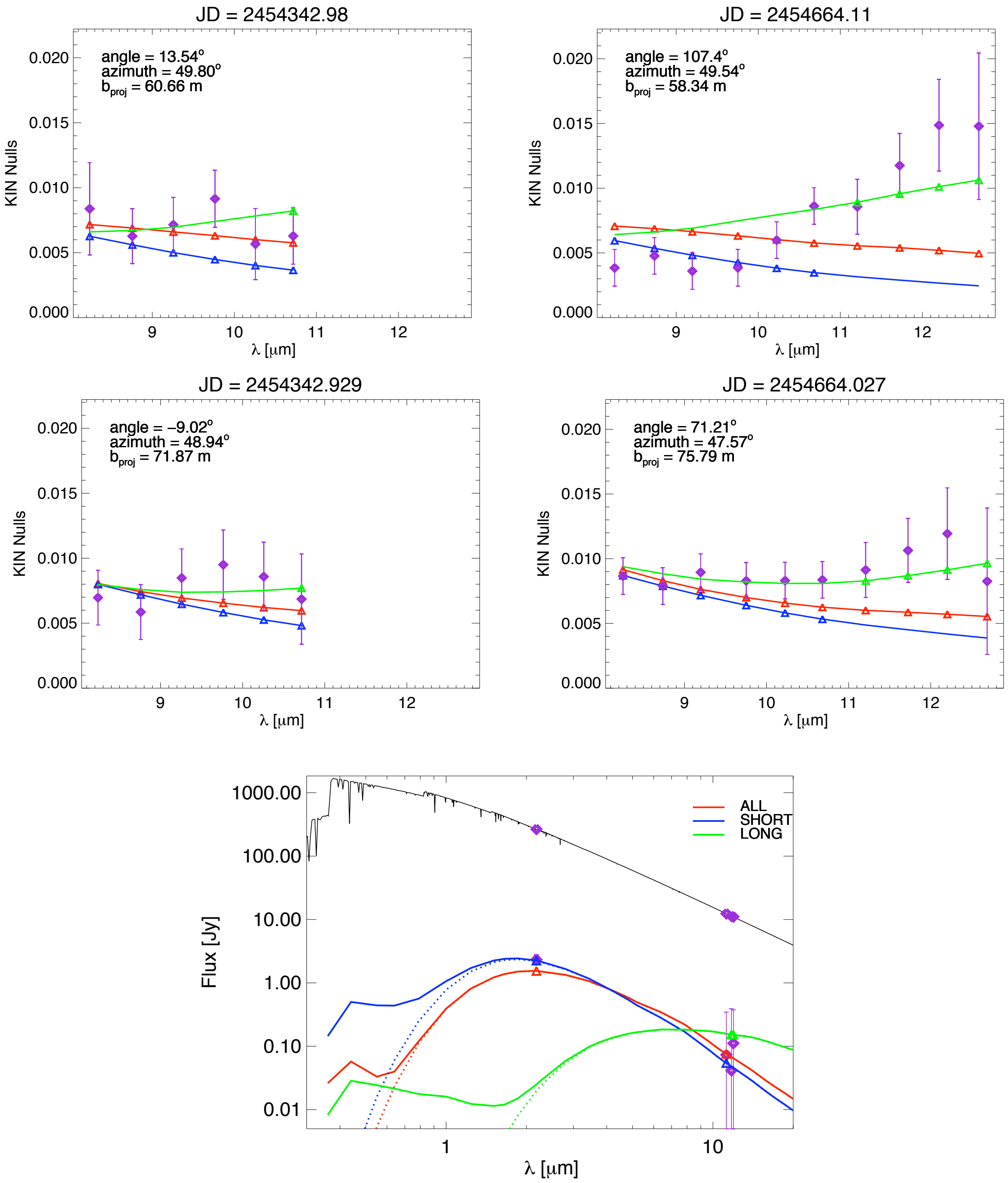

Fig. 4.— Upper 4 panels: KIN calibrated null measurements (purple diamonds) and results of best fit models (Tab. 5) using all interferometric and spectrophotometric data from 2 to 13 μm (red curve), 2 to 11 μm data only (blue curve), 11 to 13 μm data only (green curve). Bottom panel: solid black line: synthetic photosphere SED model. Purple diamonds: mid-infrared spectro-photometric measurements and K-band VLTI excess. Red, blue and green curves: resulting emission from the disk, for each of the 3 best fit models (same color codes as for upper panels). Solid thick lines: total (scattered + thermal light) emission. Dotted lines: thermal light only. A summary of data points used for each of the 3 models can be found in Tab. 3).

Fig. 5.— Flux density maps as a function of grain size and distance from the star. Left: $\lambda = 2$ μm, right: $\lambda = 13$ μm. Several solutions are presented, that correspond to the best-fit models of Tab. 5. Upper panel: all data (ALL); middle : short wavelengths ($\lambda \leq 11 \mu m$, SHORT); bottom : long wavelengths ($\lambda \geq 11 \mu m$, LONG). For each of these 3 models, the 2 and 13 μm flux densities essentially differ by a scaling factor, except that larger grains contribute sightly more relative emission at 13 μm than at 2 μm due to their lower temperature. The maps are weighted according to the real (fitted) size distributions and they corresponds to the total flux per unit grain size per elemental annulus of radius distance: the flux in janskys can thus be retrieved through direct integration over distance and grain size. Solid lines: sublimation distances of silicates (green), and carbon (when relevant, white). The contours are plotted every power of 10 between 10^{-1} and 10^{-7} of the maximum flux density.

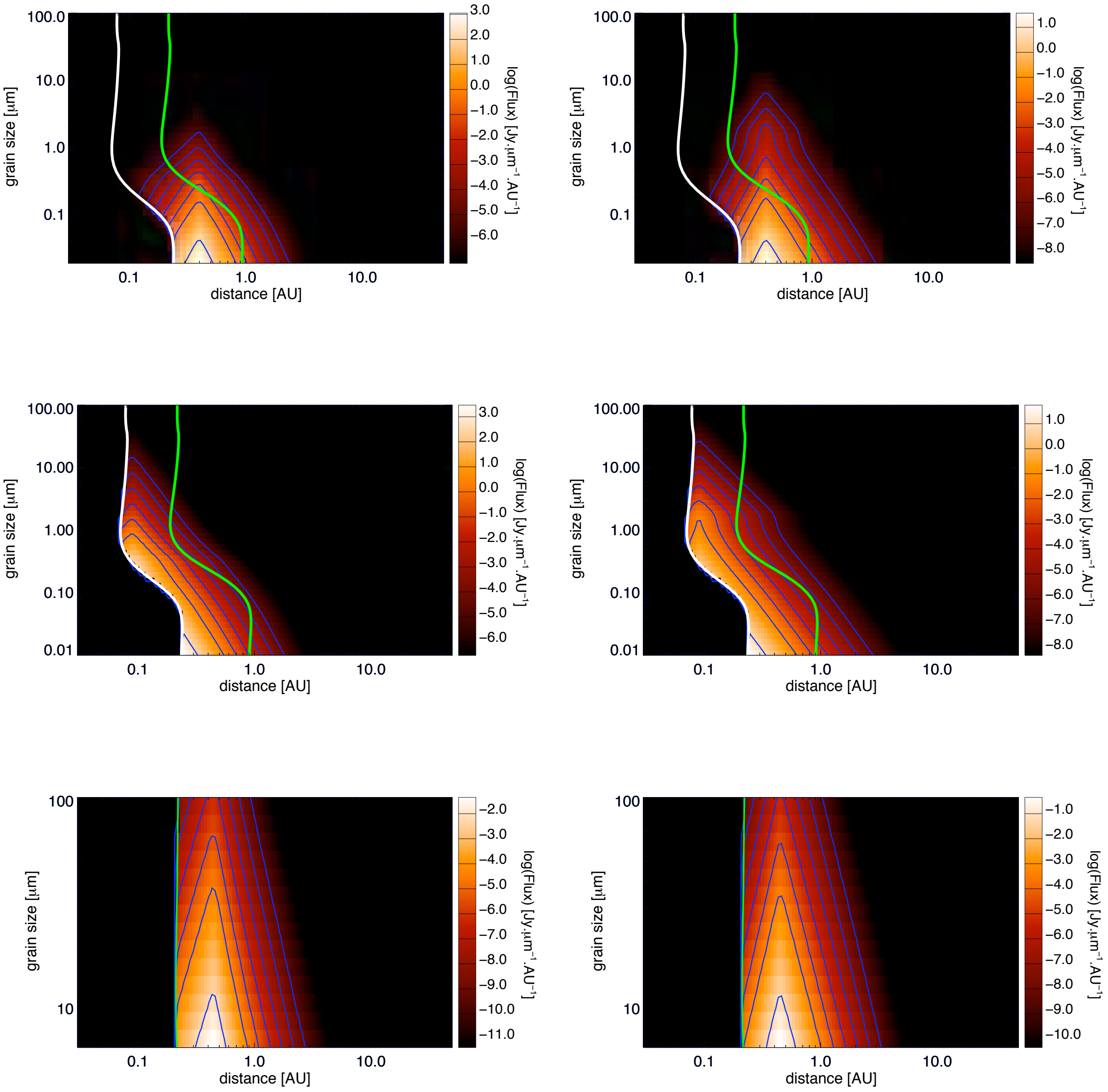

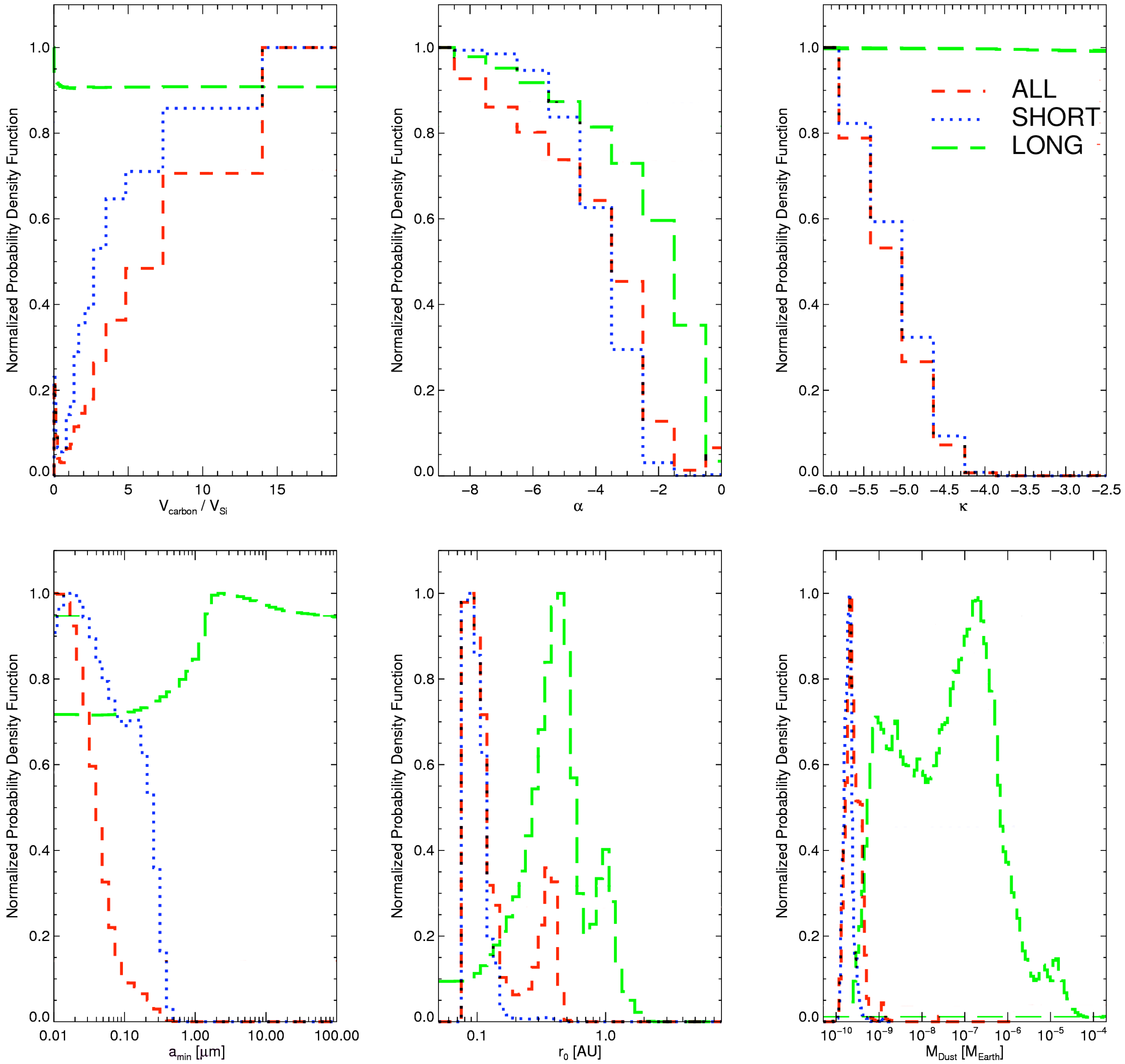

Fig. 6.— Probability of the models knowing the data calculated over a grid of $\sim 4,000,000$ solutions for the fit to all observations (ALL), the short wavelengths observations ($\lambda \leq 11\mu m$, SHORT), and the long wavelengths observations ($\lambda \geq 11\mu m$, LONG). Depending on the exact composition, the sublimation distances range from approximately 0.07 AU to 0.2 AU for carbon and from approximately 0.2 AU to 0.8 AU for silicates. It is remarkable that the probability curves for the parameter r_0 is encompassed within these intervals

Table 1. Calibrators Characteristics

Star	Type	Dec	R.A.	$\theta_{\rm LD}$ (mas)
HD 222547	K4/5III	23 41 34	–18 01 37	2.70±0.16
HD 210066	M1III	22 08 26	–34 02 38	2.58±0.26
HD 214966	M5III	22 42 22	–29 21 40	3.89±0.27
HD 215167	K3III	22 43 35	–18 49 49	2.67±0.16

Note. — Calibrators used for the Fomalhaut observations.

Table 2. Summary Of Fomalhaut KIN Observations

Date	MJD	B_p	Az	$N_{8.25}$	$N_{8.74}$	$N_{9.20}$	$N_{9.75}$	$N_{10.22}$	$N_{10.68}$	$N_{11.21}$	$N_{11.72}$	$N_{12.20}$	$N_{12.69}$
08/28/07	54340.47787	62.54	49.88	1452±207	710±132	842±140	1076±191	313±172	805±233				
08/30/07	54342.40356	76.14	47.41	666±148	540±143	1074±159	1341±189	1187±202	933±234				
08/30/07	54342.42594	72.46	48.78	699±144	717±135	874±98	879±176	898±134	1051±234				
08/30/07	54342.45259	67.10	49.75	758±164	623±156	621±145	649±178	505±201	88±264				
08/30/07	54342.47787	61.10	49.81	459±199	499±123	600±111	948±181	473±139	501±233				
08/30/07	54342.48829	58.59	49.54	631±129	689±158	718±123	733±133	915±198	601±204				
07/17/08	54663.51324	77.81	46.50	442±110	462±118	481±90	353±165	503±119	675±139	406±190	959±265	922±41	351±681
07/17/08	54663.53845	73.94	48.31	390±96	417±96	653±76	479±106	650±128	511±147	639±156	944±294	820±624	322±998
07/17/08	54663.59463	62.22	49.86	107±110	281±98	148±121	117±172	365±139	673±158	662±232	902±261	971±474	913±793
07/17/08	54663.62064	55.59	48.99	526±180	250±151	203±145	318±174	618±164	584±219	790±286	1630±309	1998±772	1771±892
07/18/08	54664.50661	78.33	46.17	498±150	502±126	683±120	680±164	756±152	739±181	946±266	565±383	1043±503	1502±723
07/18/08	54664.54028	73.14	48.57	750±176	633±160	626±157	670±143	494±170	575±172	846±212	1027±518	1245±591	1506±790
07/18/08	54664.59729	60.90	49.79	536±115	527±85	367±99	495±115	605±166	878±140	1049±171	1179±241	1788±447	994±681
07/18/08	54664.61968	55.12	48.88	188±123	285±109	230±116	146±139	505±125	867±143	390±212	810±272	1481±606	2388±898

Note. — Date format: month/day/year. MJD: Modified Julian Day = Julian Day - 2400000.5. B_p: projected baseline in m. Az: baseline azimuth East of North in degrees. N_λ: calibrated astrophysical null (x 10^3) at wavelength λ.

Table 3: Summary of the measurements fitted in this study. The last column indicates which data are used for each run of simulations (A: ALL wavelengths from 2 to 13 μm, S: SHORT wavelengths only, from 2 to 11 μm, L: LONG wavelengths only, from 11 to 13 μm). [1] Lahuis et al. (2006)

Wavelength (μm)	Flux[Jy]	Uncertainty (1σ)	Instrument	fit
11.2328	12.42	0.27	Spitzer/IRS (c2d) [1]	--L
11.7363	11.37	0.35	Spitzer/IRS (c2d) [1]	--L
11.9366	11.07	0.26	Spitzer/IRS (c2d) [1]	--L

Wavelength (μm)	Null	Uncertainty (1σ)	Instrument	fit
8.25	0.008381	0.003551	KIN 2007 SB	AS-
8.74	0.006274	0.002116	KIN 2007 SB	AS-
9.20	0.007156	0.002106	KIN 2007 SB	AS-
9.75	0.009150	0.002196	KIN 2007 SB	AS-
10.22	0.005664	0.002738	KIN 2007 SB	AS-
10.68	0.006289	0.002175	KIN 2007 SB	AS-
8.25	0.006966	0.002105	KIN 2007 LB	AS-
8.74	0.005859	0.002104	KIN 2007 LB	AS-
9.20	0.008484	0.002234	KIN 2007 LB	AS-
9.75	0.009504	0.002671	KIN 2007 LB	AS-
10.22	0.008586	0.002648	KIN 2007 LB	AS-
10.68	0.006852	0.003473	KIN 2007 LB	AS-
8.25	0.003848	0.001414	KIN 2008 SB	AS-
8.74	0.004776	0.001414	KIN 2008 SB	AS-
9.20	0.003602	0.001414	KIN 2008 SB	AS-
9.75	0.003854	0.001414	KIN 2008 SB	AS-
10.22	0.005990	0.001414	KIN 2008 SB	AS-
10.68	0.008624	0.001414	KIN 2008 SB	AS-
11.21	0.008571	0.002121	KIN 2008 SB	A-L
11.72	0.011752	0.002475	KIN 2008 SB	A-L
12.20	0.014865	0.003536	KIN 2008 SB	A-L
12.69	0.014790	0.005657	KIN 2008 SB	A-L
8.25	0.008658	0.001414	KIN 2008 LB	AS-
8.74	0.007888	0.001414	KIN 2008 LB	AS-
9.20	0.008950	0.001414	KIN 2008 LB	AS-
9.75	0.008292	0.001414	KIN 2008 LB	AS-
10.22	0.008310	0.001414	KIN 2008 LB	AS-
10.68	0.008367	0.001414	KIN 2008 LB	AS-
11.21	0.009132	0.002121	KIN 2008 LB	A-L
11.72	0.010642	0.002475	KIN 2008 LB	A-L
12.20	0.011935	0.003535	KIN 2008 LB	A-L
12.69	0.008260	0.005657	KIN 2008 LB	A-L

Wavelength (μm)	Fractional Excess	Uncertainty (1σ)	Instrument	fit
2.18	0.0088	0.0012	VLTI fractional excess	AS-

Table 4: Parameter space explored with GRaTer

Parameter	Explored range	Values	Distribution
r_0 [AU]	[0.05, …8.0]	45	log
α_{out}	[-9.0, …, 0.0]	10	linear
a_{min} [μm]	[0.01, …, 100]	45	log
κ	[-6.0, …, -2.5]	10	linear
a_{max} [mm]	1.00	fixed	–
M_{dust} [$M_\oplus$]	> 0	fitted	–
$\dfrac{v_{\mathrm{C}}}{v_{\mathrm{C}} + v_{\mathrm{Si}}}$	[0%,…, 95%]	20	linear

NOTES – We use the astronomical silicates from of Li & Greenberg (1997) and the ACAR sample of carbonaceous material from Zubko et al. (1996). M_{dust} is scaled independently when adjusting the surface density Σ_0 at the peak position to fit the SED.

Table 5: Best-fitting parameters for the three approaches. The bracketed values correspond to the 1-σ confidence intervals derived from our Bayesian analysis (possibly several families of solutions can co-exist), while the individual values are those corresponding to the smallest χ^2 on the grid. Some confidence intervals must be taken cautiously (semi-open intervals) because their margins correspond to the limits of the parameter space explored (see Fig. 6).

	ALL	SHORT	LONG
$v_{\mathrm{C}}/v_{\mathrm{Si}}$	[9.6,19[19	[8.3,19[19	[0,19[0
r_0 (AU)	$[0.07, 0.14]\bigcup[0.33, 0.41]$ 0.40	[0.08, 0.11] 0.09	$[0.21, 0.62]\bigcup[0.88, 1.08]$ 0.45
α_{out}	]-9.0,-5.0] -9.0	]-9.0,-5.2] -8.0	]-9.0,-4.0] -9.0
$a_{\mathrm{min}}(\mu\mathrm{m})$	]0.01,0.08] 0.02	]0.01, 0.21] 0.01	[1.5,69.0] 6.6
κ	]-6.0,-5.3] -6.0	]-6.0,-5.2] -6.0	]-6.0,-3.6] -6.0
$M_{\mathrm{dust}}(10^{-10}\mathrm{M}_{\oplus})$	[1.1,5.6] 2.2	[1.5,2.4] 2.2	$[2.3,6.1\times10^5]\bigcup[1.7\times10^6,5.6\times10^6]$ 75.5
χ^2 (dof)	42.53 (28)	29.04 (20)	1.87 (5)

4.4 The peculiar case of the edge-on star β Pictoris

4.4.1 Introduction

The star β Pictoris with its renowned debris disk, is one of the most widely explored planetary systems. The one that was referred to as the "Grenoble star" by an American lecturer at the "Atoms to Pebbles" 2012 conference has a strong history with IPAG. It has been imaged with various instruments and shows considerable structure. For instance, the scattered light image presented in Figure 4.6 — that covers spatial scales ranging from 30 to 300 AU — shows large scale asymmetries, as well as an inner "warped structure" consistent with an inner disk inclined by $\sim 5°$ with respect to the outer disk. The observed brightness profile and the warp were proposed to arise from perturbations of a then undiscovered planet on an inclined orbit (Mouillet et al. 97, Augereau et al. 2001). The planet was later imaged at the predicted location by Lagrange et al. (2010). However, we critically lack constrains on the innermost part of the system. During my thesis, I have taken part of two interferometric projects dedicated to β Pictoris.

First I performed visitor-mode observations at the VLTI with the AMBER instrument in January 2010 and February 2011. The initial objective of the observing proposal was to measure the orientation of the spin of the star and check whether its equatorial plane is aligned with the inner inclined disk or with the extended outer disk. The Sun for instance is known to be inclined by 7 ° with respect to the ecliptic plane. I obtained closure-phase measurement at high-spectral resolution in order to measure the spectro-astrometric shift (that is the differential-phase) across a photospheric line (Br-γ) enlarged by the stellar rotation. We found out that the required precision was not achievable to measure the rotation axis orientation better than a few degrees, not sufficient to determine its relationship with the disk. However the closure-phase measurements could serve to constrain the presence of a planet in the inner few AU from β Pictoris which is the subject of the article presented in Appendix. A.

In Sec. 4.4.2 (Defrère et al. 2012), I present a multi-spectral study of the β Pictoris debris disk in its first few AU (considering projected distances from the star). A large amount of data were collected with the VLTI/PIONIER instrument bringing new constraints on the origin of this excess. I took care of the modelling of the data discussed in the paper and presented in more details in Sec. 4.4.3.

- Sec. 4.4.2: *D. Defrère, J. Lebreton, J.-B. Le Bouquin, A.-M. Lagrange, O. Absil, J.-C. Augereau, J.-P. Berger, E. di Folco, S. Ertel, J. Kluska, G. Montagnier, R. Millan-Gabet, W. Traub, and G. Zins.* **Hot circumstellar material resolved around β Pictoris Pic with VLTI/PIONIER**. Astronomy & Astrophysics, 546:L9, Oct. 2012.

- Appendix A: *O. Absil, J. Le Bouquin, J. Lebreton, J. Augereau, M. Benisty, G. Chauvin, C. Hanot, A. M´erand, and G. Montagnier.* **Deep near-infrared interferometric search for low-mass companions around β Pictoris**. Astronomy & Astrophysics, 520:L2+, Oct. 2010.

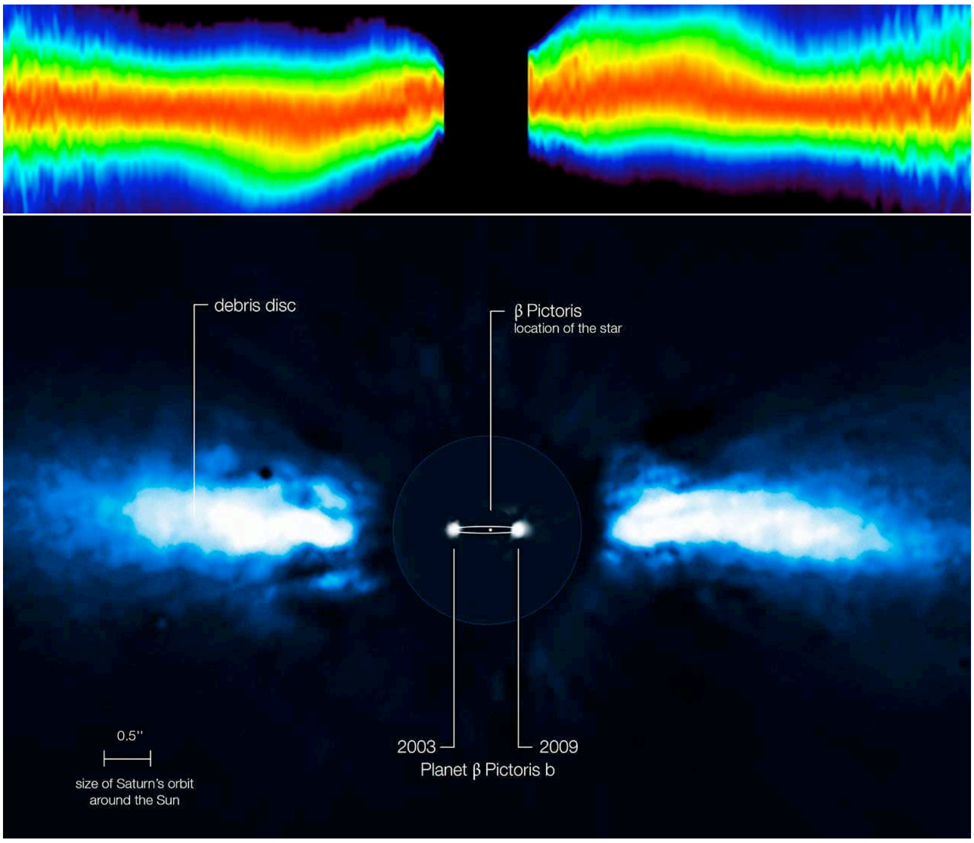

Figure 4.6: **Top panel**: Close-up view of the β Pictoris warped debris disk seen by HST/STIS down to 15 AU. The vertical scale is exaggerated to highlight the asymmetric structure. **Bottom panel**: composite ADONIS 3.6-metre telescope image showing the β Pictoris debris disk in scattered light and NaCo 8.2-metre Unit Telescope image of the planet β Pictoris b at two different epochs (ESO).

4.4.2 Hot circumstellar material resolved around β Pic with VLTI/PIONIER

Astronomy & Astrophysics manuscript no. defrere2012_submitted
October 9, 2012

LETTER TO THE EDITOR

Hot circumstellar material resolved around β Pic with VLTI/PIONIER[*]

D. Defrère[1], J. Lebreton[2], J.-B. Le Bouquin[2], A.-M. Lagrange[2], O. Absil[3,**], J.-C. Augereau[2], J.-P. Berger[4], E. di Folco[5], S. Ertel[2], J. Kluska[2], G. Montagnier[4], R. Millan-Gabet[6], W. Traub[7], and G. Zins[2]

[1] Max Planck Institut für Radioastronomie, Auf dem Hügel 69, 53121 Bonn, Germany
e-mail: `ddefrere@mpifr-bonn.mpg.de`
[2] UJF-Grenoble 1 / CNRS-INSU, Institut de Planétologie et d'Astrophysique de Grenoble (IPAG) UMR 5274, France
[3] Université de Liège, 17 Allée du Six Août, B-4000 Liège, Belgium
[4] European Southern Observatory, Alonso de Cordova, 3107, Vitacura, Chile
[5] Université de Bordeaux, Observatoire Aquitain des Sciences de l'Univers UMR 5804, Floirac, France
[6] NASA Exoplanet Science Institute (Caltech), MS 100-22, 770 South Wilson Avenue, Pasadena, CA 91125, USA
[7] Jet Propulsion Laboratory (NASA/JPL), MS 301-355, 4800 Oak Grove Drive, Pasadena, CA 91109, USA

Received; accepted

ABSTRACT

Aims. We aim at resolving the circumstellar environment around β Pic in the near-infrared in order to study the inner planetary system (<200 mas, i.e., $\sim$4 AU).
Methods. Precise interferometric fringe visibility measurements were obtained over seven spectral channels dispersed across the H band with the four-telescope VLTI/PIONIER interferometer. Thorough analysis of interferometric data was performed to measure the stellar angular diameter and to search for circumstellar material.
Results. We detected near-infrared circumstellar emission around β Pic that accounts for 1.37% ± 0.16% of the near-infrared stellar flux and that is located within the field-of-view of PIONIER (i.e., $\sim$200 mas in radius). The flux ratio between this excess and the photosphere emission is shown to be stable over a period of 1 year and to vary only weakly across the H band, suggesting that the source is either very hot ($\gtrsim 1500$ K) or dominated by the scattering of the stellar flux. In addition, we derive the limb-darkened angular diameter of β Pic with an unprecedented accuracy ($\theta_{\rm LD} = 0.736 \pm 0.019$ mas).
Conclusions. The presence of a small H-band excess originating in the vicinity of β Pic is revealed for the first time thanks to the high-precision visibilities enabled by VLTI/PIONIER. This excess emission is likely due to the scattering of stellar light by circumstellar dust and/or the thermal emission from a yet unknown population of hot dust, although hot gas emitting in the continuum cannot be firmly excluded.

Key words. Instrumentation: high angular resolution – techniques: interferometric – circumstellar matter

1. Introduction

The young ($\sim 12^{+8}_{-4}$ Myr, Zuckerman et al. 2001) A6V-type star β Pic (HD 39060, A6V, 19.3 pc) is surrounded by a famous planetary system, which is a prime target for understanding planetary system formation and evolution. Since its discovery (Smith & Terrile 1984), successive generations of telescopes have reported the detection of an edge-on debris disc with several distinctive features suggestive of a multiple-belt system (Telesco et al. 2005), star-grazing comets ("falling evaporating bodies", Beust et al. 1990), circumstellar gas (e.g., Hobbs et al. 1985; Roberge et al. 2006), and a 9-$M_{\rm Jup}$ planetary companion orbiting at a projected distance of approximately 4.3 AU (Lagrange et al. 2009). The existence of other planets seems likely (Freistetter et al. 2007) and might explain several asymmetries identified in the debris disc, including a warp at $\sim$50 AU (Augereau et al. 2001; Mouillet et al. 1997) inclined by $\sim 4°$ with respect to the outer disc (Lagrange et al. 2012a).

Over the past few years, the close environment ($\lesssim$ a few AU) of β Pic has been the focus of several studies trying to detect a putative sub-stellar companion (e.g., Absil et al. 2010; Lagrange et al. 2012b). In this paper, we present high-accuracy H-band interferometric observations of β Pic that were originally aimed at a deep search for faint companions in the inner disc but which revealed instead the presence of a more extended circumstellar emission. Using our spectrally dispersed measurements and revisiting archival K-band VLTI/VINCI measurements, we constrain the nature of this excess emission and discuss briefly its origin.

2. Observations and data reduction

Interferometric data were obtained with the PIONIER combiner (Le Bouquin et al. 2011) at the VLT interferometer on three different occasions (see Table 1). The fringe measurements were dispersed over seven spectral channels across

---

[*] Based on data collected at the ESO Paranal Observatory under commissioning time and programme 088.C-0266.
[**] FNRS Postdoctoral Researcher.

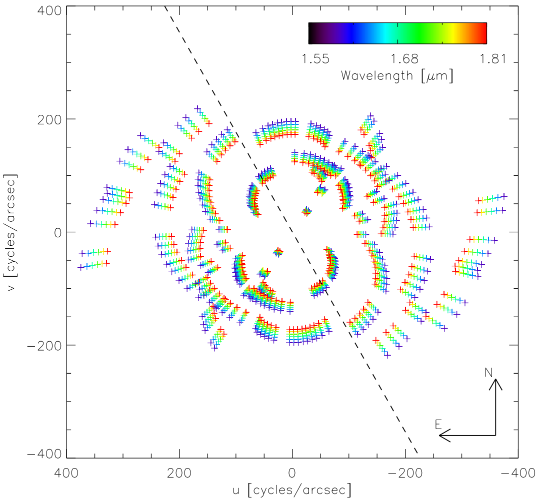

Fig. 1. Sampling of the Fourier (u,v) plane obtained for the complete data set (one colour per spectral channel). The orientation of the outer disc midplane (i.e., 29°.5 Boccaletti et al. 2009) is represented by the black dashed line.

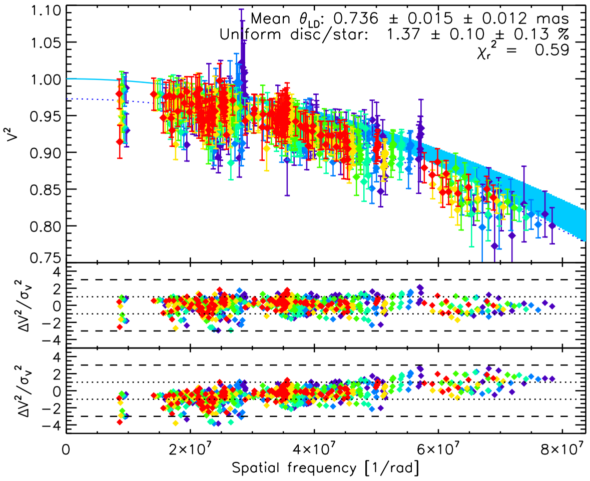

Fig. 2. Expected squared visibility of the limb darkened photosphere (blue solid line) as a function of the spatial frequency, along with the measured squared visibilities and related $1-\sigma$ error bars (one colour per wavelength). The thickness of the blue solid line corresponds to the 3-σ error related to the uncertainty on the stellar diameter. The best-fit model is represented by the dotted blue line with the residuals of the fit given in the middle panel. It corresponds to a limb-darkened photosphere of 0.736 ± 0.015 ± 0.012 mas in diameter surrounded by a uniform circumstellar emission of 1.37 ± 0.10 ± 0.13% in the H band. The bottom panel gives the residuals obtained by fitting only the stellar diameter (no circumstellar emission).

Table 1. Overview of the data obtained with VLTI/PIONIER on β Pic.

ID	Date	Config.	Seeing	OB[a]	Calib.[b]
A	2010/12/04	E0-G0-H0-I1	0.9”	2	3,4,5
B	2010/12/20	A0-G1-I1-K0	1.0”	5	1,2,3
C	2011/11/02	D0-G1-H0-I1	0.9”	14	2,3,4

[a] An observing block consists in a single observation (see more details in Le Bouquin et al. 2011).

[b] Calibrator stars correspond to (1) HD 34642 (K1IV), (2) HD 35765 (K1III), (3) HD 39640 (G8III), (4) HD 46365 (K3III), and (5) HD 223825 (G9III).

the H band (1.50 - 1.80 μm) but in the following we discard the first spectral channel (1.50 - 1.55 μm) that is systematically of lower quality and not suitable for the high-precision visibility measurements required by our programme. Observations of β Pic were interleaved with observations of reference stars to calibrate the instrumental contribution in the observed quantities. Calibrators were chosen close to β Pic, in terms of both position and magnitude, from the catalogue of Mérand et al. (2005). The total u-v plane covered by the observations is shown in Fig. 1.

Data were reduced and calibrated with the `pndrs` package (Le Bouquin et al. 2011). We focus here on the squared visibilities ($\mathcal{V}^2$) to measure both the stellar angular diameter and search for circumstellar material. The final calibrated data set ($\mathcal{V}^2$) is shown in Fig. 2. The search for faint companions by means of a closure-phase analysis will be presented elsewhere (Lagrange et al. in prep).

3. Data analysis

The calibrated $\mathcal{V}^2$ were fitted to a range of models consisting of an oblate limb-darkened photosphere surrounded by a uniform emission (“disc”) filling the entire field-of-view of PIONIER on the auxiliary telescopes. Under typical seeing conditions, this field-of-view can be approximated by a Gaussian profile with a full width at half maximum of 400 mas (Absil et al. 2011), equivalent to 4 AU in radius at the distance of β Pic. Our model is based on two free parameters, namely the limb-darkened angular diameter of the star and the disc/star contrast. The distortion of the photosphere produced by the rapid rotation ($v \sin i$ = 130 km/s, Royer et al. 2007) was considered to produce a realistic model of the star. Following the parametric approach of Absil et al. (2008), the distorted photosphere was modeled by an ellipse with an oblateness of 1.038 and a rotation axis perpendicular to the outer disc midplane (which has a position angle of 29°.5, Boccaletti et al. 2009). The $\mathcal{V}^2$ expected from the limb-darkened photosphere was then estimated according to Hanbury Brown et al. (1974) considering a linear limb-darkening H-band coefficient of 0.24 (Claret et al. 1995).

To search for circumstellar material, we compared the measurements to the expected $\mathcal{V}^2$ of the stellar photosphere. The circumstellar emission then appears as a $\mathcal{V}^2$ deficit at short baseline lengths as detailed in Absil et al. (2006). In this first approach, we assume that the disc/star contrast does not depend on the wavelength and fit all measurements simultaneously with this single parameter. We used the bootstrapping method to compute the statistical error bars on the stellar angular diameter and the disc/star contrast. Considering correlation between the baselines, the spectral channels, and the successive measurements of the same baseline, we found that correlations mostly occur between all spectral channels of the same measurement. Hence, we performed the bootstrapping by drawing all spectral channels together, which corresponds to 126 independent data sets out of our $6 \times 6 \times 21 = 726$ visibility mea-

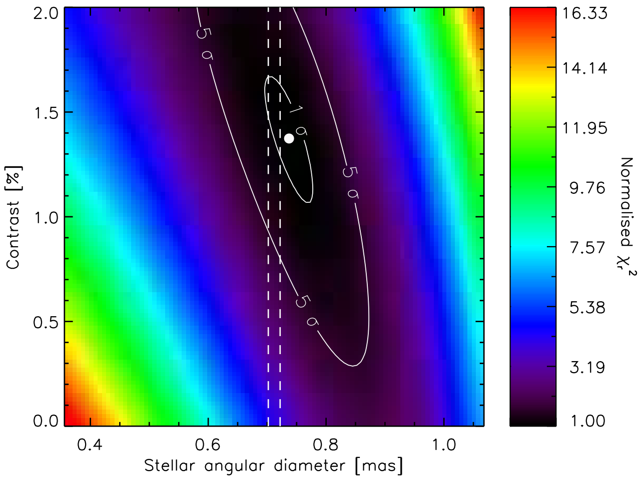

Fig. 3. Normalised χ^2 map for a model of an oblate photosphere (mean limb-darkened angular diameter in horizontal axis) surrounded by a uniform disc filling the whole field-of-view (in relative flux, vertical axis). The diameter predicted by the surface-brightness relations is represented by the vertical lines and the position of the best-fit model by a white filled circle.

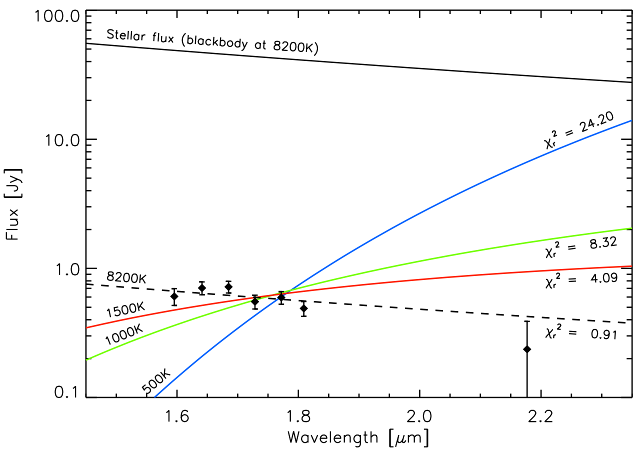

Fig. 4. Best-fit resolved fluxes given as a function of wavelength, assuming that β Pic emits as a blackbody of temperature 8200 K. The solid lines give the flux expected from blackbody sources of various equilibrium temperatures and the optimum emitting surface area (computed by χ^2 minimisation). The dashed line represents the flux from a blackbody source of 8200 K or, equivalently, from scattered stellar light (χ_r^2=0.91). The K-band flux obtained from archival VLTI/VINCI measurements is shown for comparison but is not included in the fit (see more information in the main text).

surements. We randomly produced 100 data sets from the original data and fitted them separately to our model. The standard deviation on the derived best-fit parameters then gave us reliable error bars. Finally, we considered an additional error to take the chromatic behaviour of the beam combiner and the different colours between β Pic (A6V) and its calibrators (G8III to K4III) into account. Based on the spectral shape of the transfer function across the H band (maximum variation of 40% over the entire band), we derived a maximum systematic error on the $\mathcal{V}^2$ of ±0.2% in a single spectral channel (see more details in Defrère et al. 2011). This value must be considered as very conservative since all other sources of systematic error are expected to be much smaller thanks to our optimised observing strategy, i.e. spectrally-dispersed observations obtained at various epochs on various configurations with different calibrators that are close to the science target in both magnitude and position. Using the approach described above, we produced the normalised χ^2 map shown in Fig. 3 as a function of the mean[1] angular diameter of the photosphere and of the H-band disc/star contrast. The two contours at 1 and 5-σ indicate the parameter space that falls within the respective confidence levels taking the number of degrees of freedom in the χ^2 distribution into account. In the present case, we assume that all spectral channels are fully correlated so that there are 21×6 independent measurements and two parameters to fit, hence 124 degrees of freedom. Using the surface brightness relations (SBR, Kervella et al. 2004) over various wavelength bands (B, V, J, H, K), we derived a stellar angular diameter of $\theta_{\rm LD} = 0.712 \pm 0.010$ mas. This value does not significantly depend on the chosen photometric bands, which is a good sign of robustness. For a purely photospheric model, the best-fit diameter is 0.875 ± 0.011 ± 0.012 mas, where the second and the third terms represent the statistical and the systematic errors, respectively. This value is at more than 10-σ from the one given by the SBR. Moreover, the $\mathcal{V}^2$ residuals show a systematic trend versus spatial frequencies (Fig. 2, bottom panel). Now accounting for a possible excess emission, the best-fit model is obtained for a stellar diameter of $0.736 \pm 0.015 \pm 0.012$ mas and a disc/star contrast of 1.37 ± 0.10 ± 0.13%. The best-fit diameter is fully compatible with the one given by the SBR, and no other trend is seen in the residuals (Fig. 2, middle panel). We conclude that our dataset unambiguously demonstrates the existence of an H-band circumstellar emission around β Pic and in the field-of-view of PIONIER. This excess emission is repeatedly detected in each run with at least a 5-σ confidence level and with compatible values within error bars. Using our best-fit angular diameter, we derived best-fit flux ratios of 1.48 ± 0.13 ± 0.17% and 1.32 ± 0.10 ± 0.13% by fitting the data of observing runs A&B and C separately. This suggests that the excess emission was present and did not vary during the time covered by our observations, i.e. approximately one year.

Finally, we revisited the K-band $\mathcal{V}^2$ measurement obtained in 2002 with the VLTI/VINCI instrument. These observations used a single and relatively long baseline length (~92 m), making it impossible to lift the degeneracy between the stellar diameter and a circumstellar emission (see Fig. 7 in di Folco et al. 2004). By using our best-fit stellar angular diameter (i.e., 0.736 ± 0.015 ± 0.012 mas), we derived a best-fit K-band flux ratio of 0.76% ± 0.49%, which will be used in the following discussion.

4. Constraining the resolved emission

To constrain the origin of the resolved near-infrared emission, we first tried to fit the data with disc models of various geometries (see similar analyses in Absil et al. 2009; Defrère et al. 2011). This analysis provided only a constraint on the minimum spatial extent of the near-infrared excess emission zone, which must be resolved by PIONIER

---

[1] The mean angular diameter corresponds to the geometric mean of the minor and major axes of the elliptical photosphere.

on all baseline lengths and orientations (i.e., further than ∼0.1 AU from the star). Then, we fitted the data corresponding to each spectral channel separately, considering the procedure described in the previous section and the stellar angular diameter derived with all data (i.e., $0.736 \pm 0.015 \pm 0.012$ mas). Given the low spectral resolution of PIONIER (R≈40), we assumed that β Pic emits as a blackbody of temperature 8200 K and converted the dispersed best-fit contrasts into fluxes. The best-fit fluxes were then fitted to pure blackbody models of various temperatures as represented in Fig. 4. This figure shows that a relatively high temperature ($\gtrsim$1500 K) is required to fit the data in a satisfactory way ($\chi^2_r < 5$). Including the K-band best-fit flux in the fit would reinforce this statement, although this must be considered with care given the eight to nine years separation and the greater uncertainty of the K-band measurements. Models corresponding to temperatures in the range of 1500-2000 K would suggest the presence of hot material in the field-of-view of PIONIER while higher temperature models would rather point towards the scattering of stellar light by circumstellar dust (∼8200 K, χ^2_r=0.91) or towards a binary companion ($\gtrsim$2000 K). The latter scenario can, however, be excluded with good confidence based on other studies (Absil et al. 2010; Lagrange et al. 2012b) so it is not addressed in the following discussion.

5. Discussion

The most attractive scenario for explaining the wavelength-independent flux ratio across the H band is the scattering of stellar light in the outer debris disc ($\chi^2_r = 0.91$, see Fig. 4). Since the disc is seen edge-on, a significant amount of stellar light could be forward- (or back-) scattered towards the interferometer field-of-view. To assess the validity of this scenario, we performed radiative transfer modelling with the *GraTer* software (Augereau et al. 1999). This software computes synthetic fluxes and images of dust discs in scattered light and thermal emission over various parameters for the dust composition and for the spatial and grain size distributions. It accounts for the spatial filtering of the interferometers and uses the Mie theory to self-consistently simulate anisotropic scattering depending on grain properties. Considering a wide range for the dust parameters, we produced disc models that fit well our dispersed H-band best-fit flux ratios, the K-band contrast computed from archival VLTI/VINCI measurements, and upper limits in the mid-infrared provided by single-dish telescopes (Telesco et al. 2005). The results show that light scattered in the known debris disc might account for a significant part (up to 70%) of the near-infrared excess flux, while producing a very good match to archival mid- to far-IR data through its thermal emission. This maximum value of 70% must be considered as very conservative since the Mie theory tends to overestimate forward- and back-scattering owing to the spherical grain hypothesis. The spectral slope in the near-IR is reproduced well by this scenario, but additional hot circumstellar material must be present in the vicinity of β Pic in order to account for the remainder of the measured H-band flux ratio.

The presence of hot material around β Pic would not be a surprise and might have various origins, such as stellar wind (free-free emission), mass-loss events, hot gas, or hot exozodiacal dust. Stellar winds and mass-loss events can, however, be excluded with very good confidence since they are expected to be very weak in the case of A-type stars (see discussion in Absil et al. 2008). Hot gas is likely to be present in the inner system ($\lesssim$ a few AU, Hobbs et al. 1988) and must emit in the continuum in order to account for our measurements. Assuming that the gas is produced by evaporating comets and braked by a ring of neutral hydrogen located at about 0.5 AU, Lagrange et al. (1998) derived temperature estimates of 1500-2000 K with a gas production rate of $\sim 10^{-16}$ $M_\odot$/yr. The question is thus whether hot gas could accumulate in sufficient quantities to contribute (at least partially) to the detected near-infrared emission. This is, however, beyond the scope of this paper and will not be addressed here. A more likely scenario is the presence of hot exozodiacal dust as proposed for older A-type stars (e.g., Absil et al. 2006; Defrère et al. 2011, Mennesson et al., submitted to ApJ). In the case of β Pic, the hot dust in the inner region of the disc could be produced by comets ("falling evaporating bodies") dynamically perturbed by one or several planets (Beust et al. 1990, Bonsor et al., submitted to A&A). More investigations are clearly needed to establish the most realistic scenario and, particularly, the balance between hot material and scattered light. This will be the subject of a forthcoming paper (Lebreton et al., in prep) that will include both near-infrared (H and K bands, this work) and mid-infrared (di Folco et al., in prep.) resolved observations.

Acknowledgements. DD, JBLB, JL, OA, JCA, and SE thank the French National Research Agency (ANR) for financial support through contract ANR-2010 BLAN-0505-01 (EXOZODI). DD acknowledges the support of EII (Fizeau programme). OA acknowledges the support from an F.R.S.-FNRS Postdoctoral Fellowship. PIONIER was originally funded by the Poles TUNES and SMING of Université Joseph Fourier (Grenoble) and subsequently supported by INSU-PNP and INSU-PNPS. The integrated optics beam combiner is the result of collaboration between IPAG and CEA-LETI based on CNES R&T funding. The authors thank all the people involved in the VLTI project. We used the Smithsonian/NASA Astrophysics Data System (ADS) and the "Centre de Données astronomiques de Strasbourg" (CDS).

References

Absil, O., di Folco, E., et al. 2006, A&A, 452, 237
Absil, O., di Folco, E., et al. 2008, A&A, 487, 1041
Absil, O., Le Bouquin, J.-B., et al. 2011, A&A, 535, A68
Absil, O., Le Bouquin, J.-B., et al. 2010, A&A, 520, L2
Absil, O., Mennesson, B., et al. 2009, ApJ, 704, 150
Augereau, J. C., Lagrange, A. M., et al. 1999, A&A, 348, 557
Augereau, J. C., Nelson, R. P., et al. 2001, A&A, 370, 447
Beust, H., Vidal-Madjar, A., et al. 1990, A&A, 236, 202
Boccaletti, A., Augereau, J.-C., et al. 2009, A&A, 495, 523
Claret, A., Diaz-Cordoves, J., & Gimenez, A. 1995, A&AS, 114, 247
Defrère, D., Absil, O., et al. 2011, A&A, 534, A5
di Folco, E., Thévenin, F., et al. 2004, A&A, 426, 601
Freistetter, F., Krivov, A. V., & Löhne, T. 2007, A&A, 466, 389
Hanbury Brown, R., Davis, J., & Allen, L. R. 1974, MNRAS, 167, 121
Hobbs, L. M., Vidal-Madjar, A., et al. 1985, ApJ, 293, L29
Hobbs, L. M., Welty, D. E., et al. 1988, ApJ, 334, L41
Kervella, P., Thévenin, F., et al. 2004, A&A, 426, 297
Lagrange, A.-M., Beust, H., et al. 1998, A&A, 330, 1091
Lagrange, A.-M., Boccaletti, A., et al. 2012a, A&A, 542, A40
Lagrange, A.-M., De Bondt, K., et al. 2012b, A&A, 542, A18
Lagrange, A.-M., Gratadour, D., et al. 2009, A&A, 493, L21
Le Bouquin, J.-B., Berger, J.-P., et al. 2011, A&A, 535, A67
Mérand, A., Bordé, P., & Coudé Du Foresto, V. 2005, A&A, 433, 1155
Mouillet, D., Larwood, J. D., et al. 1997, MNRAS, 292, 896
Roberge, A., Feldman, P. D., et al. 2006, Nature, 441, 724
Royer, F., Zorec, J., & Gómez, A. E. 2007, A&A, 463, 671
Smith, B. A. & Terrile, R. J. 1984, Science, 226, 1421
Telesco, C. M., Fisher, R. S., et al. 2005, Nature, 433, 133
Zuckerman, B., Song, I., et al. R. A. 2001, ApJ, 562, L87

4.4.3 Morphology of the excess emission

We now explore in more details the models of β Pictoris discussed in the letter. Defrère et al. demonstrate that the spectral slope of the excess emission measured with VLTI/PIONIER and VINCI is indicative of scattering dust particles, possibly located in the main debris disk. This is a very special situation in the framework of exozodis study because the near edge-on configuration of β Pic allows a significant fraction of the outer disk to fall in the small FOV of the interferometer. A large range of grain sizes and compositions were tested with GRaTer, and the disk geometry was parametrized as such: it has a 2D geometry; it is axisymmetric (as seen from face-on) and the surface density is parametrized with a 2-power law radial profile with a cut-off at 10 AU, *i.e.* close to the planet location (see Tab. 4.1). The vertical width of the disk is artificially obtained by inclining the disk by 88° instead of 90°. We then project the instrument PSF over that inclined disk to integrate the flux along the line of sight. The orientation of β Pic disk calls for an accurate treatment of anisotropic scattering. It is indeed possible to scatter a consequent fraction of the starlight toward the observer because of this property. We use the Mie theory to calculate self-consistently the anisotropy scattering factor g_{Mie}, averaged over the cross section (Augereau & Beust 2006), of a distribution of grains as a function of wavelength (Fig. 4.7). A Henyey-Greenstein phase function

$$\Phi(\cos\theta) = \frac{1 - g_{\mathrm{HG}}}{[1 + g_{\mathrm{HG}}^2 - 2g_{\mathrm{HG}}\cos(\theta)]^{3/2}} \tag{4.6}$$

with $g_{\mathrm{HG}} = g_{\mathrm{Mie}}$ is then used to weight the emission with viewing angle θ and calculate the total flux.

Here we want to determine whether scattering from the outer debris belt could suffice to explain the measured near-infrared excess. To better appreciate the effects of the disk geometrical properties, we present surface brightness images and profiles of the disk. A geometrical approach is used to simulate scattered light images using the Henyey-Greenstein phase function, either in an isotropic case ($g_{\mathrm{HG}} = 0$) or with the Mie theory ($g_{\mathrm{HG}} = g_{\mathrm{Mie}}$). We underline that the Mie theory produces very strong anisotropies that were sometimes found to be inconsistent with resolved disk images (see *e.g.* Lebreton et al. 2012 and reference therein). This is because the spherical grain assumption maximizes forward- and back-scattering with respect to more realistic randomly oriented aggregates, and therefore the approach must be seen as a best-case scenario for *β Pic*.

For the purpose of Fig 4.8, the 2D model is converted to 3D using the following equations with the parameters summarized in Tab. 4.1, that correspond to a nearly-flat disk. These parameters are meant to describe roughly the structure of the β Pictoris outer disk with its parent-body belt located t $\sim 100 - 120$ AU; although it does not reflect the fine structures probed by various observations, this working model with its free inner profile can be used at first order to determine how much light can be scattered toward the interferometer.

$$\rho(r, z) = \rho(r, 0)\, Z(r, z) \tag{4.7}$$

$$Z(r, z) = \exp\left(-\left(\frac{|z|}{H(r)}\right)^{\gamma}\right) \tag{4.8}$$

$$H = H_0 \left(\frac{r}{r_0}\right)^{\beta} \tag{4.9}$$

where $\rho(r,z)$ is the disk surface number density ($\rho(r,0)$ the disk midplane number density). The disk surface density then reads $\Sigma(r) = \int_{-\infty}^{+\infty} \rho(r,z)\, dz$.

Table 4.1: *β Pic* disk geometrical parameters

Parameter	Value	Comment
r_0	[100,120] AU	10 values
r_{min}	10 AU	No inner dust disk
r_{max}	400 AU	–
σ_{out}	-1.5	dynamical equilibrium
σ_{in}	[0.0, +10.0]	10 values from a flat disk to a steep ring
H_0/r_0	0.01	low dynamical excitation
γ	1.0	exponential vertical distribution
β	1.0	no flaring (linear)

We first present exemplary images to show the effect of disk inclination, inner slope and anisotropic scattering factor (Fig. 4.8). We then focus on the slope of the inner disk to bring more constraints on the radiative transfer models. The ultimate objective would be to estimate the amount of flux that can be scattered toward the observer from the outer disk, and see how the resulting radial profiles compares with other observational constrains. With our simple model though, we stick to quantitative arguments at this stage.

The radial brightness profiles and SEDs shown in Fig. 4.9 can be confronted to resolved images and spectra to estimate the residual emission that can be attributed to the inner regions of the disk and discuss whether its spectral shape is consistent with thermal emission from exozodiacal grains or reversely scattered light. A very good fit to the thermal SED is ensured by the outer disk model, except in the mid-IR range. The quality of the fit is further determined by the near-infrared excesses depending on the fraction of dust that falls within the interferometer FOV. Our double power-law model favors flat ($\sigma_{\text{in}} = 0$) or linear ($\sigma_{\text{in}} = 1$) density profiles down to β Pictoris b's orbit, in order to maximize this flux. The disk is in fact known to harbor more complex structure (See e.g. Figure 1.6 and, for the most recent publication, Li et al. 2012) that this simple approach is not expected to re-create faithfully. Besides, the dust harbors a complex mineralogy as evidenced for instance by the recent Herschel/PACS mineralogic study performed by de Vries et al. (2012), indicative of the presence of olivine crystals in the 15-45 AU region, that should be responsible for additional mid-infrared emission with respect to this study. Despite these limitations, the exploration of a variety of models I performed yields a firm conclusion: the contribution from the outer disk to the interferometric excesses cannot exceed 70% of that measured, and is at least $\geq 10\%$. A more detailed characterization of the disk will require further complementary observations such as high resolution imaging at high-contrast, as well as more detailed, 3D model better suited to a near-edge on disk such as β Pictoris.

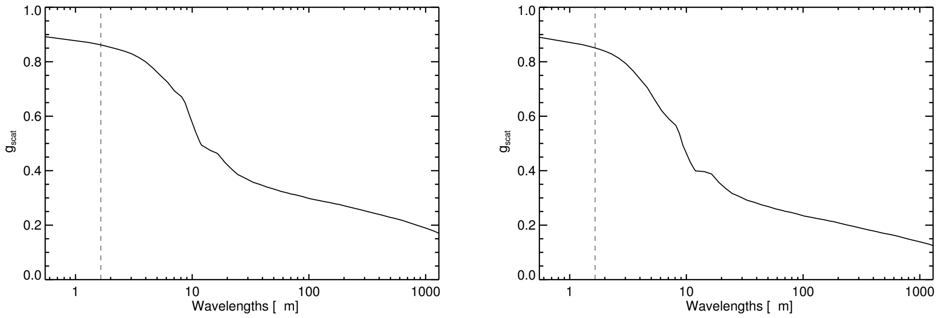

Figure 4.7: Anisotropic scattering factor g_{HG} averaged over cross-sections from the Mie theory for (left) a flat inner profile ($\sigma_{\mathrm{in}} = 0.0$) and (right) a very steep inner profile ($\sigma_{\mathrm{in}} = 9.0$). The best-fitting disk models were used in each case. The vertical dashed line marks the K-band.

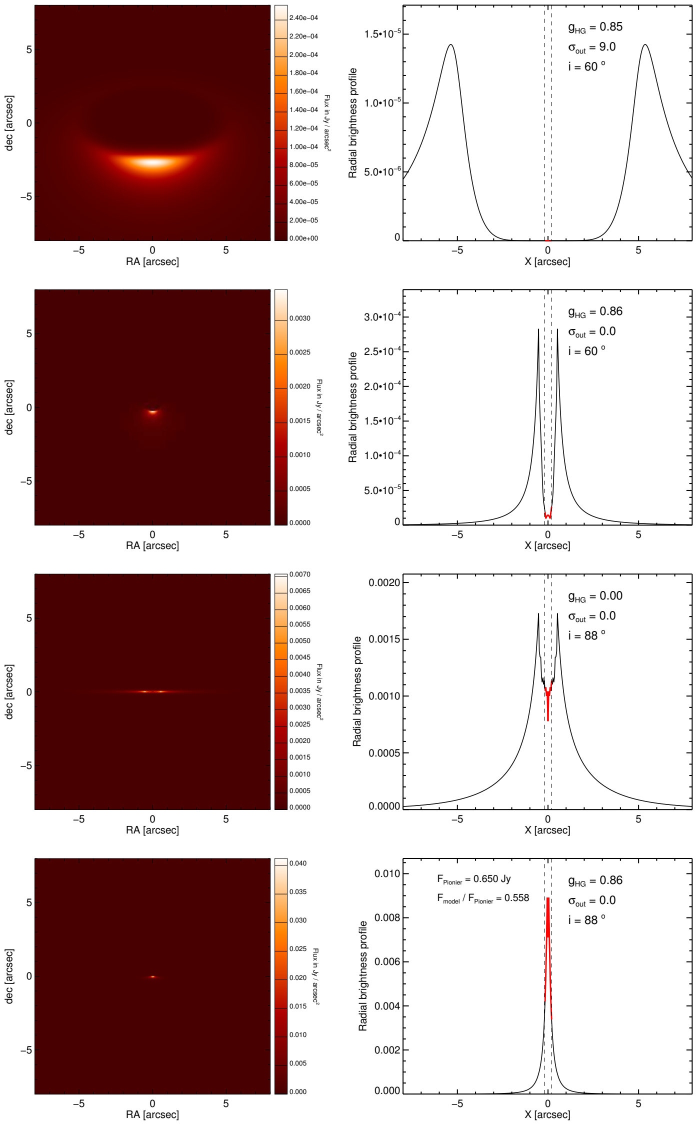

Figure 4.8: Models of the disk illustrating the effect of inclination, inner surface density slope $\sigma_{\rm in}$, and anisotropic scattering factor $g_{\rm HG}$. The two first lines show a disk inclined by 60deg in a steep anisotropic case ($g_{\rm HG} = g_{\rm Mie}, \sigma_{\rm in} = +9.0$) and a flat isotropic case $[g_{\rm HG} = 0.0, \sigma_{\rm in} = +0.0]$ respectively. The two last lines show a flat disk ($\sigma_{\rm in} = 0.0$) inclined by 88deg, *i.e.* close to edge-on, in the isotropic case ($g_{\rm HG} = 0.0$) and the anisotropic case ($g_{\rm HG} = g_{\rm Mie}$) respectively. Left: scattered light surface brightness images. Right: scattered light radial brightness profiles; the vertical dashed lines delimit the Gaussian field-of-view of VLTI/Pionier (UT, HWHM = 200 mas) to highlight the amount of flux that is seen by the instrument for the various models.

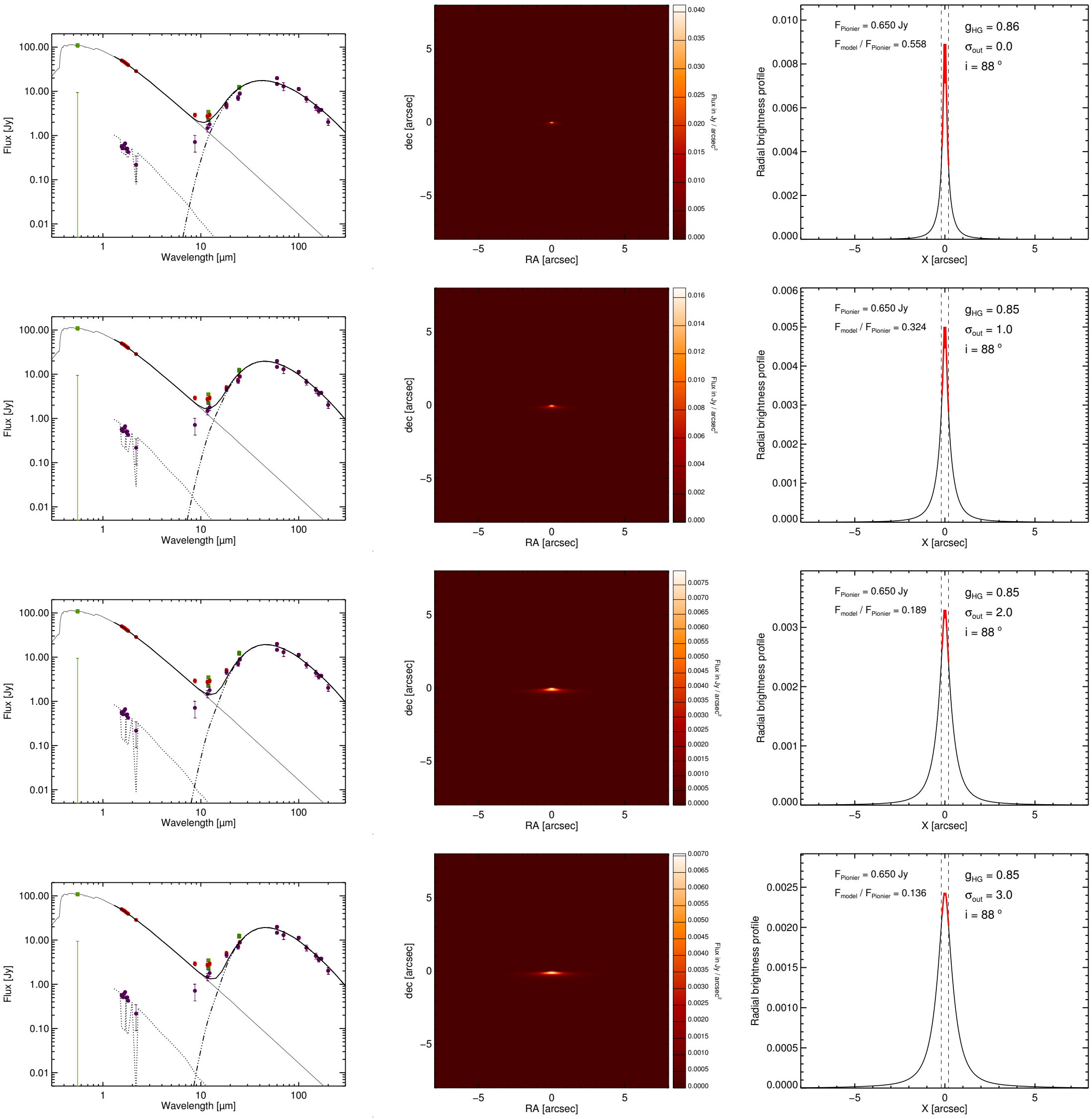

Figure 4.9: Spectral Energy Distribution, scattered light brightness images and radial profiles of a disk inclined by 88deg. $g_{\rm HG}$ was calculated with the Mie theory for $\sigma_{\rm in} = 0., 1., 2., 4.$ respectively (See Fig. 4.8 for details). The dip in the SED models is due to the interferometer transmission function.

Chapter 5

Toward a better understanding of inner debris disks

We have presented in the previous chapter our initial model of the exozodiacal dust around Fomalhaut. We find that two dust populations coexist inside of a few AUs: one ”classical” debris ring orbiting in the Habitable Zone (HZ), and a very hot ring of unbound grains close to the sublimation distance. Nevertheless, the dust masses, inferred parent-belt masses, and the high dust production rate needed to counterbalance the unbound grains depletion, are not understood from a theoretical point-of-view. In this chapter, adapted from an article recently published in A&A (Lebreton et al. 2013), I address the various processes that affect a grain in the Fomalhaut environment and propose a scenario that reconciles the presence of hot unbound grains with theoretical arguments on their dynamics and lifecycle. In this model, dust grains originating from a collisional cascade at ∼2AU are responsible for faint mid-IR excesses, as detected only around a handful of nearby stars. Subject to Poynting-Robertson drag, the grains spiral toward the star; they sublimate and disrupt in the form of numerous carbon monomers that produce strong thermal emission in the near-IR. This work was performed in collaboration with members of the Anton Pannekoek group in Amsterdam.

”Detailed models of the Fomalhaut exozodiacal disk and its origin”

J. Lebreton, R. van Lieshout, J.-C. Augereau,
O. Absil, B. Mennesson, M. Kama, C. Dominik, A. Bonsor, J. Vandeportal,
H. Beust, D. Defrère, S. Ertel, V. Faramaz, P. Hinz, Q. Kral,
A.-M. Lagrange, W. Liu, and P. Thébault

Published in A&A, Received March 5, 2013; accepted May 30, 2013

5.1 Introduction

During the past few years, the increasing number of smaller exoplanets and fainter debris disks have revealed that extrasolar analogs to our solar system may be common, and yet, little is known about the architecture of the very inner parts of planetary systems. A distinguishable feature of the inner solar system is the existence of the zodiacal cloud, composed of small (1 to 100 μm) dust grains (Grün 2007; Rowan-Robinson & May 2013), which are thought to come from the disruption and erosion of comets, asteroids, and

Kuiper belt objects (*e.g.* Nesvorný et al. 2010). Dusty debris disks orbiting other stars than the Sun were first detected by their excess emission in the mid- or far-infrared (IR), and could then be imaged at visible to submillimeter wavelengths. A few warm disks comparable to the zodiacal cloud have been found by space observatories around mature stars via their photometric excess emission at mid-IR wavelengths (Beichman et al. 2005a; Lawler et al. 2009; Lisse et al. 2012); but their characterization suffers from insufficient spatial resolution and large photometric uncertainties.

Recent developments in high-angular resolution interferometry have offered powerful tools to characterizing exozodiacal disks (exozodis), which reside in the close environment (typically less than 3 AU) of a large fraction of nearby stars. Large efforts have indeed been made to detect exozodis with near- and mid-IR interferometers worldwide, notably at the VLTI (Absil et al. 2009), the Keck Interferometer (Millan-Gabet et al. 2011) or the CHARA array at Mount-Wilson (Absil et al. 2006; Defrère et al. 2011b). Ongoing surveys in the near-infrared ($K < 5$) with the CHARA/FLUOR (Coudé du Foresto et al. 2003) and VLTI/PIONIER (Le Bouquin et al. 2011) interferometers indicate that as much as $\sim$ 30% of nearby AFGK mainsequence stars may harbor hot (typically 1000-2000K) circumstellar dust within a few AU at the 1% level with respect to photospheric emission (Ertel et al., in prep. Absil et al. 2013). Conversely, only $\sim$ 12% of the surveyed main sequence stars have been found to harbor mid-infrared excesses (i.e., warm dust) with nulling interferometry (Millan-Gabet et al. 2011).

From a theoretical point of view, the prevalence of these hot excesses around main sequence stars is not understood. Radiative transfer analysis identifies very hot and small refractory grains close to the sublimation limit that should be radiatively blown out over timescales of weeks. Yet they represent typical masses of 10^{-8} to 10^{-10} $M_\oplus$ that need to be delivered by equivalent masses of dust-producing planetesimals (*e.g.* Defrère et al. 2011a). Being much more massive than the zodiacal cloud, these hot exozodis are difficult to reconcile with the steady-state collisional evolution of parent body belts (Wyatt 2007).

One famous example of a dusty planetary system is the one surrounding the nearby (7.7 pc) A3V star Fomalhaut (α PsA, HD 216956). This young main sequence star (440 ± 40 Myr, Mamajek 2012) is well known for its prominent, $\sim$ 140 AU-wide, debris belt that was first resolved in scattered light with HST/ACS revealing a sharp inner edge and side-to-side brightness asymmetry suggestive of gravitational sculpting by a massive planet (Kalas et al. 2005; Quillen 2006). A point source attributed to the suspected planet was later detected in the optical at the predicted location, moving along its orbit over multiple epochs (Kalas et al. 2008). The absence of detection in the near- and mid- (thermal) infrared range (Janson et al. 2012) resulted in a controversial status for Fomalhaut b. More recent studies confirm the detections of a companion at 118 AU and interpret the various constraints as a large circumplanetary dust disk orbiting a hidden subjovian planet, but do not exclude an isolated dust cloud originating from a recent collision between planetesimals (Currie et al. 2012; Galicher et al. 2013) [1]. The cold planetesimal belt is indeed collisionally very active as shown by the recent analysis of resolved images and photometry at far-infrared to submillimeter wavelengths from ALMA (Boley et al. 2012) and *Herschel*/PACS and SPIRE (Acke et al. 2012). Using radiative transfer modeling, Acke et al. (2012) argue that a dust production rate of $\sim$ $3 \times 10^{-5}\, M_\oplus$/year is needed to justify the measured amount of blow-out grains, and estimate that the region interior to the cold belt at

---

[1] Kalas et al. (2013) recently announced a fourth epoch detection of Fomalhaut b. They argue in favor of an object larger than a dwarf planet evolving on a very eccentric orbit (see Section 6).

140 AU are not devoid of material.

The *Herschel*/PACS 70 μm, as well as the ALMA image, identify an unresolved excess in the vicinity of the star that was previously reported in the mid-infrared by Stapelfeldt et al. (2004) based on *Spitzer*/MIPS imaging and IRS spectroscopy. Su et al. (2013) recently analyzed the IRS and PACS data and concluded on the presence of a warm debris belt with a blackbody temperature of $\sim$ 170 K. However, these facilities lack the spatial resolution and accuracy needed to characterize this warm component.

Near- and mid-infrared long baseline interferometers offer the appropriate tools to study the Fomalhaut exozodi with enough contrast and resolution, free of any modeling assumptions on the stellar spectrum.

The present paper carries out a thorough analysis of the Fomalhaut inner debris disk. It is the last one of a series initiated by Absil et al. (2009) (henceforth Paper I) - who presented the VLTI/VINCI detection of hot excess in the close environment of the star - followed by a mid-infrared characterization using the Keck Interferometer Nuller (KIN) by Mennesson et al. (2013) (henceforth Paper II). In Paper I, we presented the clear K-band (2.18μm) detection of a short-baseline visibility deficit. It is best explained by circumstellar emission emanating from within 6 AU of the star with a relative flux level of $0.88 \pm 0.12\%$. In Paper II, we presented multiwavelength measurements performed across the N-band (8 to 13 μm) using the technique of nulling interferometry. A small excess is resolved within $\sim$ 2AU from the star, with a mean null depth value of $0.35\% \pm 0.10\%$ [2]. Preliminary modeling shows that the near- to mid-infrared excesses can only be explained by two distinct populations of dust emitting thermally; small ($\sim$20 nm) refractory grains residing at the sublimation distance of carbon are responsible for the near-infrared emission, while $> 1\,\mu$m grains located further than the silicate sublimation limit produce most of the mid-infrared excesses.

The paper is organized as follows. In Sec. 5.2 and 5.3, we present our radiative transfer model of optically thin disks, and introduce a new prescription for calculating the sublimation distance of dust grains in an exozodi. Results of the modeling of the inner Fomalhaut debris disk, based on multiwavelengths observations, are detailed in Sec.5.4. The mechanisms that produce and preserve the hot grains, as well as the connection with the warm and the cold belt are discussed in Sec. 5.5.6. We discuss further our results and attempt to place the Fomalhaut exozodi in the context of its planetary system in Sec. 5.6. We finally summarize our main findings in Sec.5.7.

5.2 A schematic exozodiacal disk model

In this section, we elaborate a schematic model of an optically thin exozodiacal dust disk. The model is implemented in the GRaTeR code originally developped by Augereau et al. (1999). It makes hardly any *a priori* assumptions regarding the nature of the grains and their production. Because of the limited constraints on detected exozodiacal disks, we restrain the model to a 2D geometry. The disk surface density and grain size distribution are parametrized with simple laws to limit the number of free parameters. This allows us to explore a broad range of disk properties using a Bayesian inference method.

---

[2] We note that the true astrophysical excess could be larger because some dust emission may be removed by the destructive fringes of the interferometer. The nuller transmission pattern is accounted for in the models discussed afterwards.

5.2.1 Scattered light and thermal emission

We consider a population of dust grains at a distance r from the star and with a differential size distribution $\mathrm{d}n(r, a)$, where a is the grain radius. In a self-consistent description of a collisional evolution of debris disks, the spatial and size distribution cannot be formally separated (Augereau et al. 2001; Krivov et al. 2006; Thébault & Augereau 2007). Since we know little about the properties and origin of observed exozodiacal disks, we assume here for simplicity that the dependence of the size distribution on the distance r essentially reflects the size-dependent sublimation distance of the grains. Since exozodiacal grains may reach very high temperatures, sublimation can prevent the smallest grains from surviving in regions where larger ones can remain, thereby truncating the size distribution at its lower end. We therefore write the differential size distribution $\mathrm{d}n(r, a)$ as follows:

$$\begin{array}{c} \mathrm{d}n(r,a) = H(a - a_{\mathrm{sub}}(r))\ \mathrm{d}n(a) \\ \text{with } \int_{a_{\min}}^{a_{\max}} \mathrm{d}n(a) = 1 \end{array} \tag{5.1}$$

where $a_{\min}$ and $a_{\max}$ are the minimum and maximum grain sizes respectively, $H(a - a_{\mathrm{sub}}(r))$ is the Heaviside function (assuming $H(0) = 1$) and $a_{\mathrm{sub}}(r)$ is the sublimation size limit at distance r from the star. Details of the calculation for sublimation will be given in Sec. 5.3.

At wavelength λ, the dust population thermally emits a flux

$$\Phi_{\mathrm{th}}(\lambda, r) = \int_{a_{\min}}^{a_{\max}} B_\lambda\left(T_{\mathrm{d}}(a, r)\right) \frac{\sigma_{\mathrm{abs}}(\lambda, r, a)}{4 d_\star^2} \mathrm{d}n(r, a) \tag{5.2}$$

where $d_\star$ is the distance of the observer to the star, $T_{\mathrm{d}}(a, r)$ is the grain temperature and B_λ is the Planck function. In the above equation, we implicitly assumed that grains thermally emit isotropically. The absorption cross-section $\sigma_{\mathrm{abs}}(\lambda, r, a)$ reads

$$\sigma_{\mathrm{abs}}(\lambda, r, a) = 4\pi a^2 Q_{\mathrm{abs}}\left(\frac{2\pi a}{\lambda}, \lambda, r\right) \tag{5.3}$$

where Q_{abs} is dimensionless absorption/emission coefficient that depends on the size parameter $2\pi a/\lambda$, on λ through the wavelength-dependent optical constants, and on the distance to the star as the grain composition may depend on r. The grain temperature $T_{\mathrm{d}}(a, r)$ is obtained by solving in two steps the thermal equilibrium equation of a grain with the star. For any grain size a, we first calculate the equilibrium distance r for a broad range of grain temperatures T_{d} knowing the Q_{abs} value

$$r(a, T_{\mathrm{d}}) = \frac{d_\star}{2} \sqrt{\frac{\int_\lambda Q_{\mathrm{abs}} F_\star(\lambda) \mathrm{d}\lambda}{\int_\lambda Q_{\mathrm{abs}} \pi B_\lambda\left(T_{\mathrm{d}}\right) \mathrm{d}\lambda}} \tag{5.4}$$

where $F_\star(\lambda)$ is the stellar flux at Earth. The $r(a, T_{\mathrm{d}})$ function is then numerically reversed to get $T_{\mathrm{d}}(a, r)$.

Assuming isotropic scattering for simplicity, a dust population at distance r from the star scatters a fraction of the stellar flux at wavelength λ is given by

$$\Phi_{\mathrm{sc}}(\lambda, r) = F_\star(\lambda) \frac{\sigma_{\mathrm{sca}}(\lambda, r)}{4\pi r^2} \tag{5.5}$$

with $\sigma_{\rm sca}$ the mean scattering cross section

$$\sigma_{\rm sca}(\lambda, r) \;=\; \int_{a_{\rm min}}^{a_{\rm max}} \pi a^2 Q_{\rm sca}\left(\frac{2\pi a}{\lambda}, \lambda, r\right) {\rm d}n(r, a) \tag{5.6}$$

and $Q_{\rm sca}$ the dimensionless scattering coefficient.

The total flux emitted at wavelength λ by the dust population finally reads

$$\Phi(\lambda, r) \;=\; \Phi_{\rm sc}(\lambda, r) + \Phi_{\rm th}(\lambda, r). \tag{5.7}$$

5.2.2 Synthetic observations

We synthesize single aperture photometric observations of non edge-on exozodiacal dust disks at wavelength λ by calculating the integral

$$\Phi(\lambda) \;=\; \int_{r=0}^{\infty} \Phi(\lambda, r)\Sigma(r) \times 2\pi\langle FOV\rangle_\theta(r) r{\rm d}r \tag{5.8}$$

$$\text{with} \qquad \langle FOV\rangle_\theta(r) = \int_{\theta=0}^{2\pi} FOV(\rho(r,\theta))\frac{{\rm d}\theta}{2\pi} \tag{5.9}$$

$$\text{and} \qquad \rho(r,\theta) = r\sqrt{1-\cos^2\theta\sin^2 i} \tag{5.10}$$

where r and θ are cylindrical coordinates in the disk plane and $\rho(r,\theta)$ the projected distance to the star in the sky plane, $\Sigma(r)$ is the dust surface number density of the exozodiacal disk, assumed to be axisymmetrical and i is the disk inclination with respect to the sky plane ($i = 0$ for pole-on geometry). In the above equations, we implicitly assumed that the instrument beam profile FOV only depends upon ρ, the projected distance to the star in the sky plane. The $\langle FOV\rangle_\theta(r)$ function gives the azimuthally averaged telescope transmission along circles of radius r in the exozodiacal disk frame.

Most single aperture telescopes such as *Spitzer* or *Herschel*, have sufficiently large beams (or slits in case of spectroscopy), which intercept the entire exozodiacal dust emission. In such a case, the exozodiacal flux emission can be obtained by taking $\langle FOV\rangle_\theta(r) = 1$ in Eq. 5.8. On the other hand, coherent near- and mid-IR interferometric observations, such as those obtained with the VLTI/VINCI and CHARA/FLUOR instruments, have much smaller fields of view (FOV) and the actual transmission profiles of the interferometric instruments on the sky plane is important[3].

5.2.3 Grain properties

In the solar system, the zodiacal dust particles are thought to originate from tails and disruption of comets, or to be produced when asteroids collide. Both interplanetary and cometary dust particles are composed of silicates and carbonaceous material, and zodiacal cloud dust particles are expected to be made of similar material. In this model, we consider mixtures of silicates and carbonaceous material, and calculate their optical properties with the Mie theory valid for hard spheres. The optical index of the mixture is calculated using the Bruggeman mixing rule, given a relative volume fraction $v_{\rm C}/v_{\rm Si}$ of carbonaceous grains. In the disk regions where the grain temperature is between the

---

[3] See Fig. 1 of Paper II for the KIN transmission map

sublimation temperature of silicates and carbon, the volume of silicates is replaced by vacuum, mimicking porous carbonaceous grains. The optical constants and grain bulk densities used in this study are summarized in Tab. 5.1.

We adopt a power-law differential size distribution

$$\mathrm{d}n(a) = \left(\frac{1-\kappa}{a_{\mathrm{max}}^{1-\kappa} - a_{\mathrm{min}}^{1-\kappa}}\right) a^{-\kappa}\mathrm{d}a \tag{5.11}$$

for grain radii a between a_{min} and a_{max}. The maximum grain size has no impact at the wavelengths considered and cannot be constrained with the adopted modeling approach. It is thus fixed to $a_{\mathrm{max}} = 1\,\mathrm{mm}$ in the rest of this study.

5.2.4 Fitting strategy

The adopted fitting stategy is based on a Bayesian inference method described in Lebreton et al. (2012). For that purpose, a grid of models is created. For each set of parameters, the goodness of the fit is evalutated with a reduced χ_{r}^2 that is transformed into probabilities assuming a Gaussian likelihood function ($\propto e^{-\chi_{\mathrm{r}}^2/2}$) for Bayesian analysis. Marginalized probability distributions for each free parameter are then obtained by projection of these probabilities onto each dimension of the parameter space.

In order to limit the number of free parameters, we adopt a two power-law radial profile for the surface density

$$\Sigma(r) = \Sigma_0\sqrt{2}\left[\left(\frac{r}{r_0}\right)^{-2\alpha_{\mathrm{in}}} + \left(\frac{r}{r_0}\right)^{-2\alpha_{\mathrm{out}}}\right]^{-1/2}. \tag{5.12}$$

This corresponds to a smooth profile, with an inner slope $r^{\alpha_{\mathrm{in}}}$ ($\alpha_{\mathrm{in}} > 0$) that peaks at about r_0, and that falls off as $r^{\alpha_{\mathrm{out}}}$ ($\alpha_{\mathrm{out}} < 0$) further to r_0.

The parameter space explored here is listed in Tab. 4 of Paper II and recalled in Sec. 5.4.2. Each set of parameters defines an emission spectrum, 2D emission, and scattered light maps that are flux-scaled by searching the optimal Σ_0 value (surface density at $r = r_0$) that gives the best fit to the panchromatic observations. The range of a_{min} values includes sizes that are far below the blow-out size limit for grains about Fomalhaut.

5.3 Dust sublimation model

5.3.1 Sublimation temperatures

We implement a new method of calculating the sublimation temperature T_{sub} of a dust grain as a function of its size and not only of its composition, based on the method introduced by Kama et al. (2009) to study the inner rim of protoplanetary disks. We first model a grain as an homogeneous sphere of radius a composed of a single material of density ρ_{d}. To ensure the stability of a grain (*i.e.* no net change of its size), the flux of particles (carbon / silicates monomeres) escaping from its surface must equal the flux of particles coming in from the ambient medium. From the kinetic theory of gases, the number of particles accreted onto and evaporated from the grain surface per unit time and unit surface reads respectively (Lamy 1974)

$$F_{\mathrm{accre}} = \frac{P_{\mathrm{gas}}}{\sqrt{2\pi\mu\, m_{\mathrm{u}}\, k_{\mathrm{B}}\, T_{\mathrm{gas}}}} \tag{5.13}$$

$$F_{\mathrm{evap}} = -\frac{P_{\mathrm{eq}}}{\sqrt{2\pi\mu\, m_{\mathrm{u}}\, k_{\mathrm{B}}\, T_{\mathrm{gas}}}} \tag{5.14}$$

where P_{eq} is the gas saturation partial pressure, P_{gas} the partial pressure of the ambient gas medium, T_{gas} the gas temperature assumed equal to the dust temperature T_{d} here, μm_{u} the mean molecular weight and k_{B} the Boltzmann constant. Introducing an efficiency factor α (constrained by laboratory experiments), the mass of a grains of radius a then evolves as

$$\frac{\mathrm{d}m}{\mathrm{d}t} = \alpha\,(F_{\mathrm{accre}} - F_{\mathrm{evap}}) \times \mu\, m_{\mathrm{u}}\, 4\,\pi a^2 \tag{5.15}$$

Injecting the ideal gas law $P = \rho k_{\mathrm{B}} T / \mu m_{\mathrm{u}}$ yields:

$$\frac{\mathrm{d}m}{\mathrm{d}t} = \alpha\, a^2 \sqrt{\frac{8\pi\, k_{\mathrm{B}}\, T_{\mathrm{d}}}{\mu\, m_{\mathrm{u}}}}\,(\rho_{\mathrm{gas}} - \rho_{\mathrm{eq}}) \tag{5.16}$$

$$\frac{\mathrm{d}a}{\mathrm{d}t} = \frac{\alpha}{\rho_{\mathrm{d}}} \sqrt{\frac{k_{\mathrm{B}}\, T_{\mathrm{d}}}{2\pi\, \mu\, m_{\mathrm{u}}}}\,(\rho_{\mathrm{gas}} - \rho_{\mathrm{eq}}). \tag{5.17}$$

For the purpose of this study, the grains are assumed to lie in empty space ($\rho_{\mathrm{gas}} = 0$) and their temperature equals by definition the sublimation temperature T_{sub}. The gas density at saturation pressure ρ_{eq} is given by the Clausius-Clapeyron equation

$$\log_{10} \rho_{\mathrm{eq}} = B - \frac{A}{T_{\mathrm{sub}}} - \log_{10} T_{\mathrm{sub}}^{-\mathrm{C}} \tag{5.18}$$

where the thermodynamical quantities A and B are determined from laboratory measurements and $C = -1$, as discussed by Kama et al. (2009). Integrating equation 5.17 from the initial grain size a to 0, under the assumption that the grain temperature $T_{\mathrm{d}} = T_{\mathrm{sub}}$ does not vary significantly during the sublimation process, yields

$$\frac{a}{t_{\mathrm{sub}}} = \frac{\alpha}{\rho_{\mathrm{d}}} \sqrt{\frac{k_{\mathrm{B}}\, T_{\mathrm{sub}}}{2\pi\, \mu m_{\mathrm{u}}}}\, 10^{\mathrm{B} - \frac{\mathrm{A}}{\mathrm{T_{sub}}} - \log_{10} \mathrm{T_{sub}}} \tag{5.19}$$

where we define t_{sub} as the time needed to sublimate an entire grain.

This equation relates the sublimation temperature of a grain to its size and to a sublimation timescale. Although determining this timescale without a time-dependent approach is tricky, we will see in Sec. 5.3.2 that our parametric approach allows to tackle the issue based on simple assumptions. Beforehand we need to extend the sublimation model to the case of multi-material grains.

We recall that our objective is to interpret real observations of individual debris disks. Fitting the spectral and spatial observables of these disks requires to solve accurately a radiative transfer problem and to model the optical properties of the materials at stake. To achieve this, the GRaTeR code handles grains made of multiple (in particular carbonaceous and silicate) materials by considering homogeneous spheres with optical constants obtained by means of an effective medium theory. Porous grains are represented by a compact sphere in which one of the "materials" is vacuum. When one of the material reaches its sublimation temperature, it is automatically replaced by vacuum. This is in particular the case for the grains that lie very close to the star: then a silicate-carbon mixture becomes a porous carbon grain. This approach proved efficient at reproducing the optical behavior of astronomical dust grains in various situations.

We consider homogeneously distributed mixtures of silicate and carbon characterized by a volume fraction $v_{\mathrm{C}}/v_{\mathrm{Si}}$. We anticipate that silicate will sublimate at lower temperatures than carbon whatever the grain size: silicates will have vanished entirely before the carbon starts its sublimation. As a first step the sublimation occurs as if the grains were entirely made of silicates. In a second step, the grains take the form of a carbon matrix filled with cavities. For spheroids, the porosity can be defined as the filling factor of vacuum $\mathcal{P} = \frac{V_{\mathrm{vacuum}}}{V_{\mathrm{grain}}}$. We introduce the porosity by correcting the grain density: $\rho_{\mathrm{d}}(\mathcal{P}) \rightarrow (1-\mathcal{P})\,\rho_{\mathrm{d}}$ in Eq. 5.19 which is then solved using the density of the porous carbonaceous leftover.

Eq. 5.19 is solved using the material properties summarized in Tab. 5.1, and the solution is inversed numerically to determine T_{sub} as a function of grain size for different timescales. The sublimation curves for pure silicate and carbon-rich grains ($\mathcal{P} \simeq 0$) is displayed in Fig. 5.1, together with that of porous carbonaceous grains mimicking mixtures of Si and C for which Si has sublimated. We observe that porosity tends to increase T_{sub}, as do smaller sublimation timescales. These are interpreted respectively as a loss of efficiency in the sublimation process for lower grain densities, and as a consequence of the exposure time. Compared with the usual constant T_{sub} approximation, large and small grains have their sublimation temperatures re-evaluated by as much as plus or minus ∼20%.

5.3.2 Timescales

From what precedes, we are able to define a size- and composition-dependent estimate for the sublimation temperature of a dust grain. Fig. 5.1 reveals an important deviation from the constant sublimation temperature. However, we first need to know on which timescale the sublimation has to be considered. One can notice that an order of magnitude error on the timescale estimate will result only in a modest shift in the sublimation curve. Sublimation can be expected to alter the steady-state grain size distribution because it introduces an additional (size-dependent) destruction mechanism; nonetheless we take advantage of the fact that we are using a parametric model and we address only the question: how big must a grain be to survive a temperature T_{sub} for some time t.

A grain lifetime is limited by its removal processes. In a debris disk, the main removal process for bound grains is generally destructive collisions, but when the optical depths and/or the dust stellocentric distance is sufficiently small, Poynting-Robertson (PR) drag can become the dominant effect (Wyatt 2005b). Unbound grains are placed on hyperbolic orbits and ejected from the system before they are destroyed: their survival timescale can be equaled to a "blowout timescale". Assuming near-circular orbits for the parent-bodies, the limit between bound and unbound grains is set by $a_{\mathrm{blow}} = a(\beta = 1/2)$ (Fig. 5.2), where β is the size-dependent ratio of radiation pressure to gravitational forces.

Here we want to determine the *survival timescale* of a grain, in the *sublimation zone* so depending on its size a. The *sublimation zone* is defined, for each of the materials that the grains are made of, as the interval $[d_1, d_2]$ between the minimum and maximum subli-

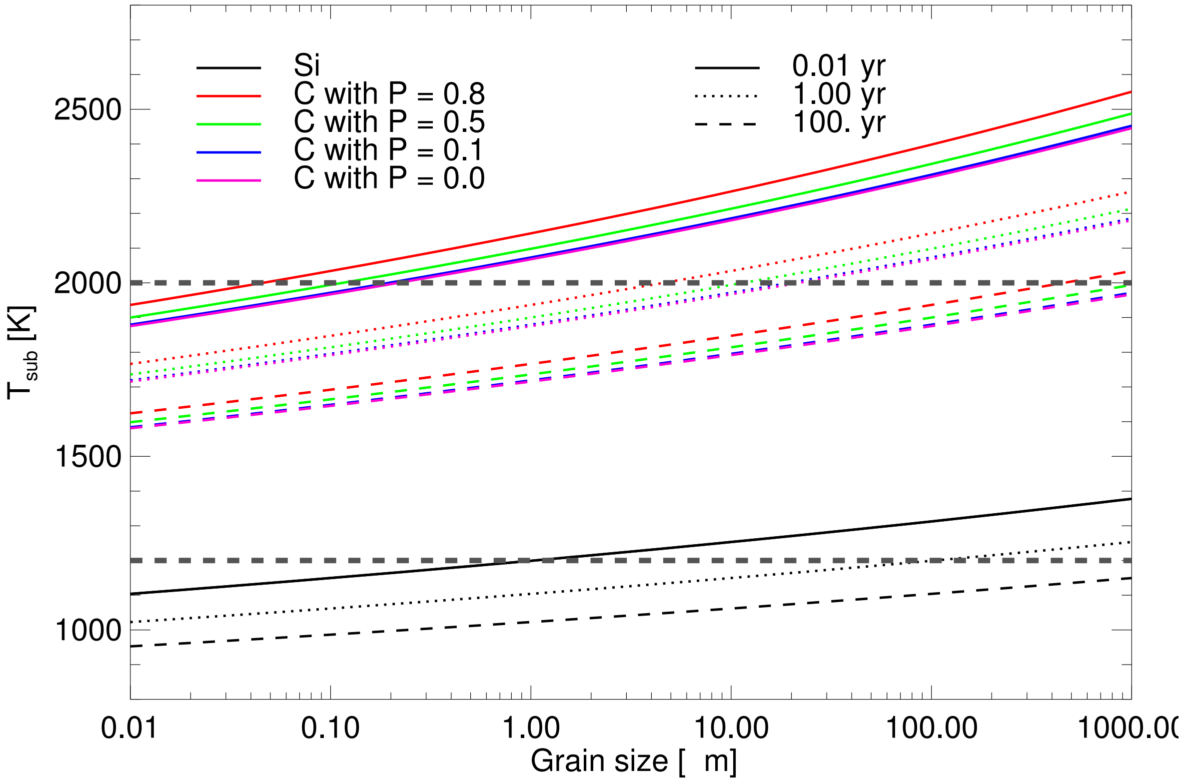

Figure 5.1: Sublimation temperatures of carbon and silicate as a function of grain size with several possible survival timescales, and assuming different porosities for carbonaceous grains or equivalently different volume fractions of silicate. The horizontal dashed lines show the constant $T_{\rm sub}$ values often used in past studies.

mation distances (all grain sizes considered) assuming constant sublimation temperature. d_1 is essentially independent of the maximum grain size $a_{\rm max}$ because the sublimation distance does not vary with size for grains larger than a few μm (Fig. 5.4).

We calculate a preliminary grid of models for each grain composition (with no fine computation of the sublimation temperature), and we identify the grain properties and disk surface density that best fit the observations. This provides an estimate of the vertical optical depths required to calculate the collisional timescale: the mean timescale a barely bound grain ($\beta \simeq 1/2$) can survive in a collision-dominated disk:

$$t^0_{\rm col}(a_{\rm blow}) = \frac{t_{\rm orbit}}{2\pi\tau_\perp^{\rm geo}} \tag{5.20}$$

with $t_{\rm orbit}$ the orbital period and $\tau_\perp^{\rm geo}$ the vertical geometrical optical depth at distance d_1, a distance representative of the sublimation distance of bound grains.

For larger grains, the collision timescale is scaled with size as (Thébault & Augereau 2007)

$$t_{\rm col}(a) = t^0_{\rm col}\left(\frac{a}{a_{\rm blow}}\right)^{0.3} \tag{5.21}$$

where $t_{\rm col}$ depends on the sublimation zone of a given material and on the assumed surface

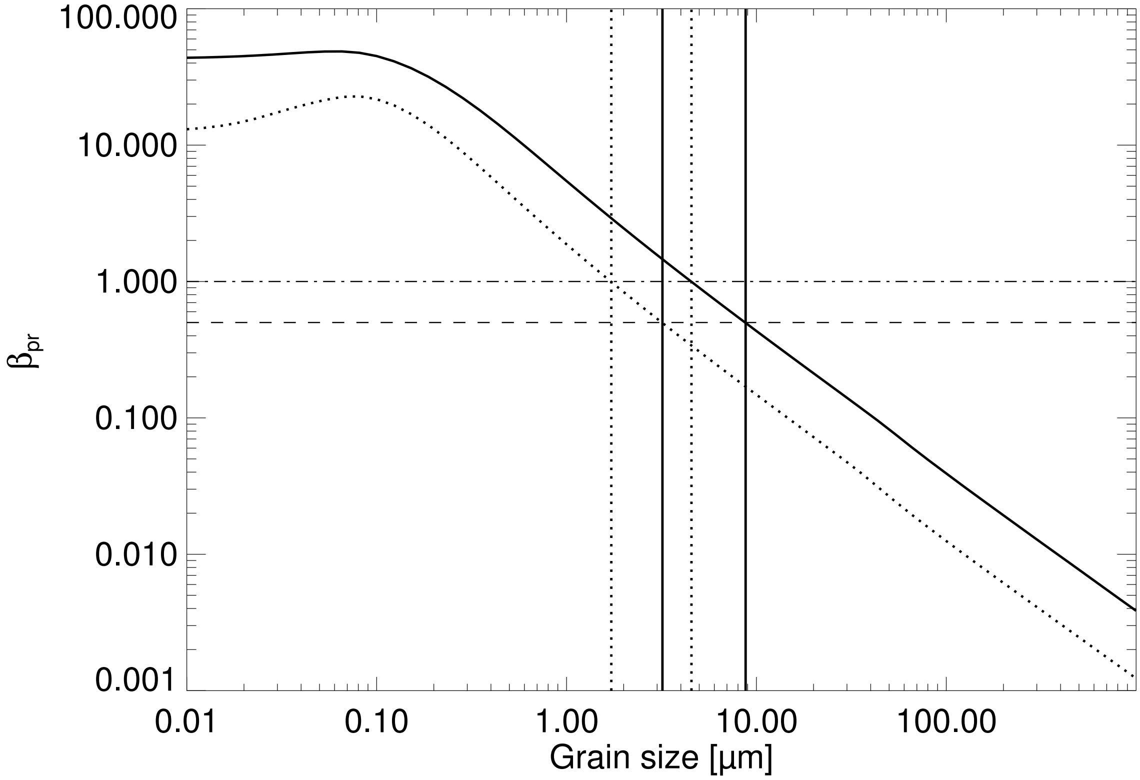

Figure 5.2: β ratio of a dust grain as a function of its size in the Fomalhaut environment. A 50-50 carbon-silicate mixture is assumed and depicted by the lower curve while the upper curve considers half porous carbon grains. The vertical and horizontal lines marks the $\beta =$ 0.5 (blowout size for grains released by parent-bodies on initially circular orbits) and $\beta = 1.0$ (blowout size for any initial orbit) limits, before and after the sublimation of silicates.

density profile.

We define the PR drag timescale as the time needed for bound grains to spiral from the outer edge of the sublimation zone, to the inner edge of the sublimation zone (Wyatt 2005b)

$$t_{\mathrm{PR}}(a) = 400\,\beta(a)\frac{(d_2-d_1)^2}{M_*}. \tag{5.22}$$

As soon as they are produced, unbound grains ($\beta > 1/2$) are placed onto hyperbolic orbits, they are ejected from the sublimation zone and eventually from the field of view. In the sublimation zone, the hyperbolic orbit is approximated by rectilinear uniform motion; we assume the grains are produced at the inner edge of the sublimation zone d_1 with initial velocity $v_{\mathrm{Kep}}(d_1)$. A grain will travel typically a distance between $\sqrt{d_2^2-d_1^2}$ ($\beta(a) = 1$) and $d_2 - d_1$ ($\beta \gg 1/2$). An estimate of the blowout timescale is given by the average between these two extremes (see Eq.5.31 and Appendix B.2 for a more general estimate)

$$t_{\mathrm{blow}} = \frac{1}{2}\left[\frac{(d_2^2-d_1^2)^{0.5}}{v_{\mathrm{Kep}}} + \frac{d_2-d_1}{v_{\mathrm{Kep}}}\right]. \tag{5.23}$$

Eventually, the sublimation timescale is equaled to the survival timescale, namely the longest time a grain can be exposed to sublimation, according to

$$t_{\rm sub}(a) = \begin{cases} \min(t_{\rm col}(a), t_{\rm PR}(a)) & ,\text{for } a > a_{\rm blow} \\ t_{\rm blow} & ,\text{for } a \leq a_{\rm blow} \end{cases} \tag{5.24}$$

A representative example for Fomalhaut is shown in Fig. 5.3. The properties of the silicate population and of the carbon population described in details in Sec. 5.4 have been assumed. $t_{\rm sub}$(C) is always smaller than $t_{\rm sub}$(Si) because of the respective locations of the two grain populations. The sharp discontinuity between the survival timescale of bound and unbound grains translates into a big jump in the sublimation temperatures and then the distances at the blowout limit. We stress that Fig. 5.3 only illustrates the survival time in the sublimation zone, it should not be used to find the dominant mechanism in the entire dust disk.

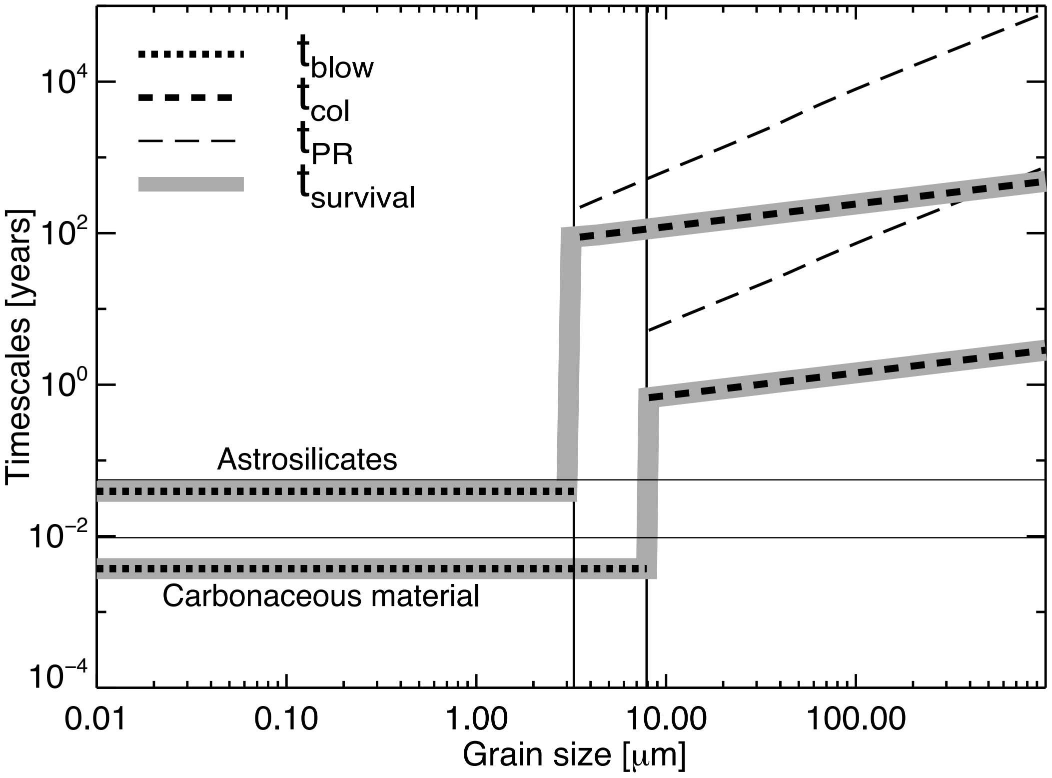

Figure 5.3: Examples of survival timescales against collisions, PR drag and radiation pressure blowout calculated for an exemplary grain composition ($v_{\rm C} = v_{\rm Si}$ for silicate, $\mathcal{P} = 50\%$ for carbonaceous material). For each effect, the upper curve corresponds to silicate and the lower curve to carbon, each in its sublimation zone and for the disk properties derived from preliminary modeling. The horizontal black lines give the orbital periods for reference. The vertical lines mark the blowout size before (left) and after (right) silicate sublimates.

Table 5.1: Material properties. The thermodynamical constants A and B are tabulated values from Kama et al. (2009) and Zavitsanos & Carlson (1973)

	Carbonaceous material	Silicates
Nickname	C	Si
Thermodynamical properties		
Material type	Graphite	Olivine
A [cgs]	37215	28030
B [cgs]	1.3028	12.471
$\mu\,[m_{\mathrm{p}}]$	12.0107	172.2331
$\rho\,[\mathrm{g.cm}^{-3}]$	1.95	3.5
Optical properties		
Material type	aC ACAR	Astrosilicates
Reference	Zubko et al. (1996)	Draine (2003)

5.3.3 Sublimation distances

The GRaTeR code handles the optical properties of various materials. Broad-band spectra and excesses attributed to warm circumstellar dust disks are well matched using materials of the silicate family or carbonaceous materials. For each of them, we use respectively the thermodynamical quantities associated to amorphous olivine ($MgFeSiO_4$) and graphite (C). They are indicated in Tab. 5.1.

After equaling the sublimation timescale to a timescale relevant for each grain (Sec. 5.3.2), we calculate the thermal equilibrium using the usual formula (Eq. 5.4). This provides the size dependent-sublimation distance presented in Fig. 5.4 for a few representative material mixtures. The overall shape of the curves is dictated by the thermal equilibrium distances. The net effect of the new model is generally an alteration of the sublimation distances of the small ($< 10\mu m$) grains, depending on the timescales used for each model. The inner edge of the sublimation is close to 0.2 AU for silicate, 0.05 AU for carbon, while their outer edge lies respectively at 0.7 - 1.2 AU, 0.18 - 0.25 AU respectively.

5.3.4 Sublimation model: summary

We presented an innovative model that is used to calculate size-dependent sublimation distances of dust grains depending on their compositions, porosities and survival timescales. The method can be summarized as follows

1. A preliminary grid of models is adjusted to the data assuming fixed sublimation temperatures and solving the size-dependent equilibrium temperatures. This provides estimates of the dust disk location and density (Paper II).
2. Size-dependent survival timescales are estimated by searching for the most efficient effect between destructive collisions, PR drag and photo-gravitational blowout (Fig. 5.3).
3. Size-dependent sublimation temperatures are calculated from the kinetic theory of gases and thermodynamics as a function of the timescale for when a grain is exposed to sublimation (Fig. 5.1).
4. This sublimation timescale is equaled to the survival timescale for each grain yielding a size-dependent sublimation temperature that accounts for each grain specific

dynamical regime. In particular, this causes a discontinuity at the blowout limit (Fig. 5.2).

5. Finally, size-dependent sublimation distances are re-evaluated by solving the equilibrium distance of each grain knowing its specific sublimation temperature (Eq. 5.4).

5.4 Application and results

5.4.1 Observational constraints and star properties

The model presented above is now confronted with the observations of Fomalhaut already presented in Table 3 of Paper II. Preliminary analysis of the near-infrared VLTI/VINCI excess, of mid-infrared KIN null excesses, complemented by (low accuracy) spectrophotometric data, suggested the coexistence of two populations of dust in the Fomalhaut environment located within the field of view of the interferometers (~ 4 AU and ~ 2 AU HWHM for FLUOR and KIN respectively). This architecture is imposed by the high level of the K-band excess with respect to N-band, and the inversion of the null excess slopes upon $\sim 10\mu$m, with a rising profile toward the longer wavelengths. Stark et al. (2009) observed a similar break around $10\,\mu m$ in the Keck null depths of 51 Ophiuchus. They were only able to reproduce it with a double-population of dust grains, however with much larger spatial scales due to the distance of the star. In Paper II, the two dust populations of Fomalhaut were adjusted separately and the model suffered from an inaccurate prescription for the sublimation distances. In the present study we propose a self-consistent modeling of the exozodi and we characterize precisely the properties of the emitting grains and their location. We assume the disk position angle and inclination to equal those of the cold ring (i = 65.6Σ, PA = 156Σ). A NextGen photosphere (Hauschildt et al. 1999a) is scaled to the V magnitude of Fomalhaut ($m_{\rm V} = 1.2\,$mag) in order to model the total flux received by the grains. It also serves to estimate the excesses attributable to the disk in the photometric data. The interferometric observables on the other hand are independent from the chosen star spectrum.

5.4.2 Data and modeling strategy

We adopt a strategy in which we fit (1) the "hot dust ring" ($\lesssim 0.4$ AU) probed by the shortest wavelengths data, using the same data subset as Paper II (most importantly the VINCI 2.18 μm excess), and then (2) the "warm dust belt" probed by the KIN nulls from 8 to 13 μm and mid- to far-infrared photometric measurements of the warm "on-star" excess (Fig. 5.5 and 5.6).

These photometric measurements are derived from unresolved observations of the inner Fomalhaut debris disk, well differentiated from the contribution of the cold belt by *Spitzer*/MIPS at $23.68\mu m$ ($F_{24} = 3.90 \pm 0.40\,$Jy, Stapelfeldt et al. 2004), *Herschel*/PACS at $70\mu m$ ($F_{70} = 0.51 \pm 0.05\,$Jy, Acke et al. 2012) and ALMA at 870 μm (taken as a $3\,\sigma$ upper limit: $F_{850} < 4.8\,$mJy, Boley et al. 2012); their spatial location is constrained by the instruments point spread functions / beam to be smaller than ~ 20AU. Additional *Spitzer*-IRS spectroscopic data is available: a small excess emission ($\lesssim 1\,$Jy) shortward of 30 μm is reported by Su et al. (2013). Due to large calibration uncertainties in the ab-

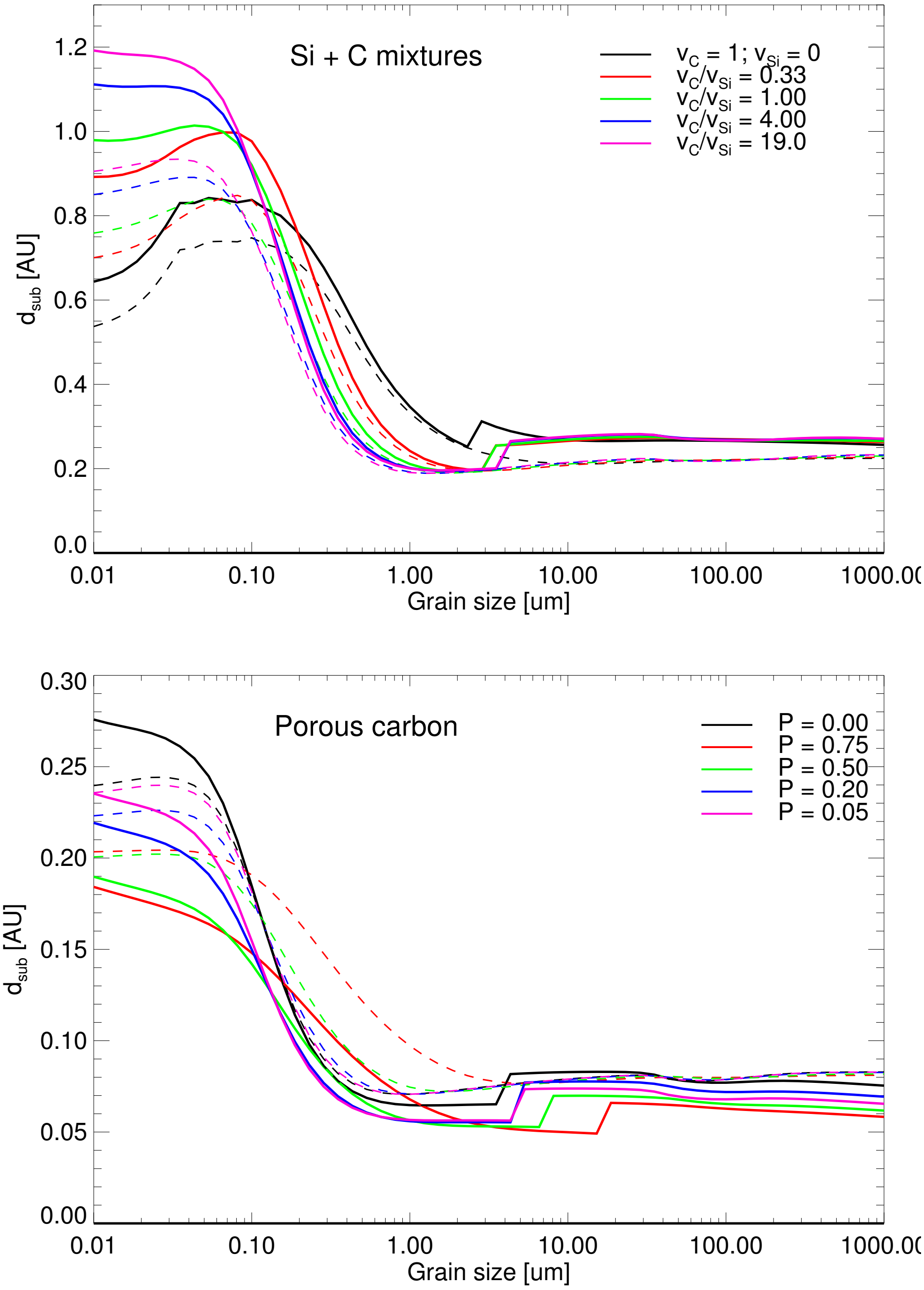

Figure 5.4: Sublimation distances of silicate (**top panel**) and carbonaceous material (**bottom panel**) in composite grains (C+Si or C+vacuum respectively) as a function of grain size in the Fomalhaut environment, with either a constant (dashed line) or a size-dependent (solid line) sublimation temperature. Relevant disk properties obtained from preliminary modeling are used (Sec. 5.4). Size-dependent sublimation temperatures are a function of the size-dependent survival timescales shown in Fig. 5.3 causing jumps at the material-dependent blowout limit.

solute photometry ($\sim 10\%$) compared with the interferometric measurements, we do not attempt to fit this spectrum. The IRS spectrophotometry is represented with 3σ upper limits in Figure 5.5 to verify the compatibility of the model at these wavelengths.

The GRaTeR code is used to adjust the dataset in several steps. We point out that all the results presented below correspond to thermal emission by the dust and that the scattering of the stellar spectra by the grains is always negligible (although systematically calculated).

As a first step, we assess the hot population, assumed to be composed of compact carbonaceous grains, because they are very small and lie within the silicate sublimation zone (Paper II). We adopt the same grid of models as the one presented in Table 4 of Paper II, yielding ~200,000 models for 5 free parameters: the minimum grain size $a_{\rm min}$, the slope of the size distribution κ, the surface density peak r_0, outer slope $\alpha_{\rm out}$ and the total disk mass $M_{\rm dust}$ (with the maximum grain size fixed to 1 mm). The inner density slope is assumed to be steep ($\alpha_{\rm in} = +10$) - but this has no impact as this region is within the sublimation radii of carbons as we will see.

As a second step we focus on the disk's warm component and take advantage of the linearity of the data that allows us to sum the contributions from the two components. Using the same parameter space, we adjust simultaneously 6 free parameters: the mass, geometry and disk properties of the warm component and the mass of the hot component (modeled in step 1) to the 36 measurements composing the full dataset (VINCI, KIN, MIPS, PACS, ALMA). The warm ring is made of a 50-50 mixture of astronomical silicates and carbonaceous material characteristic of the material properties commonly inferred from debris disks and solar system asteroids studies. We do not vary this parameter as it is found to be essentially unconstrained by the observations in the previous study.

Two approaches are used. In the first approach, the outer slope of the density profile is taken as a free parameter, and the inner slope is assumed to be very steep (fixed to +10). In the second approach, the outer slope is fixed to −1.5 - close to the best-fit for the first approach and consistent with the profile expected for a collisional equilibrium under the effect of size-dependent radiation pressure (Thébault & Wu 2008) - and we vary the inner slope $\alpha_{\rm in}$.

A χ^2 minimization is performed as well as a Bayesian statistical analysis to measure the likelihood of the model parameters. The best-fitting parameters and Bayesian estimates discussed in this section are summarized in Tab. 5.2 and the resulting models are shown in Fig. 5.5 and 5.6. Probability curves are shown in Appendix B.

5.4.3 The hot population

As expected, the hot component is mostly constrained by the near-infrared data and best explained by a very narrow ring of $\gtrsim 10$ nm refractive grains, with a density profile peak matching the sublimation distance of carbons ($r_0 = 0.09$ AU), where only the largest grains survive. The best model ($\chi^2_r = 1.4$ with 20 degrees of freedom, *d.o.f.*) is found for a minimum grain size matching the smallest values of the parameter space ($a_{\rm min} = 10$nm, $\kappa = -6$), although the Bayesian analysis favors $a_{\rm min} = 20$ nm. In fact, the exact properties of this ring have little impact on the resulting SED, as long as the grain size-dependent

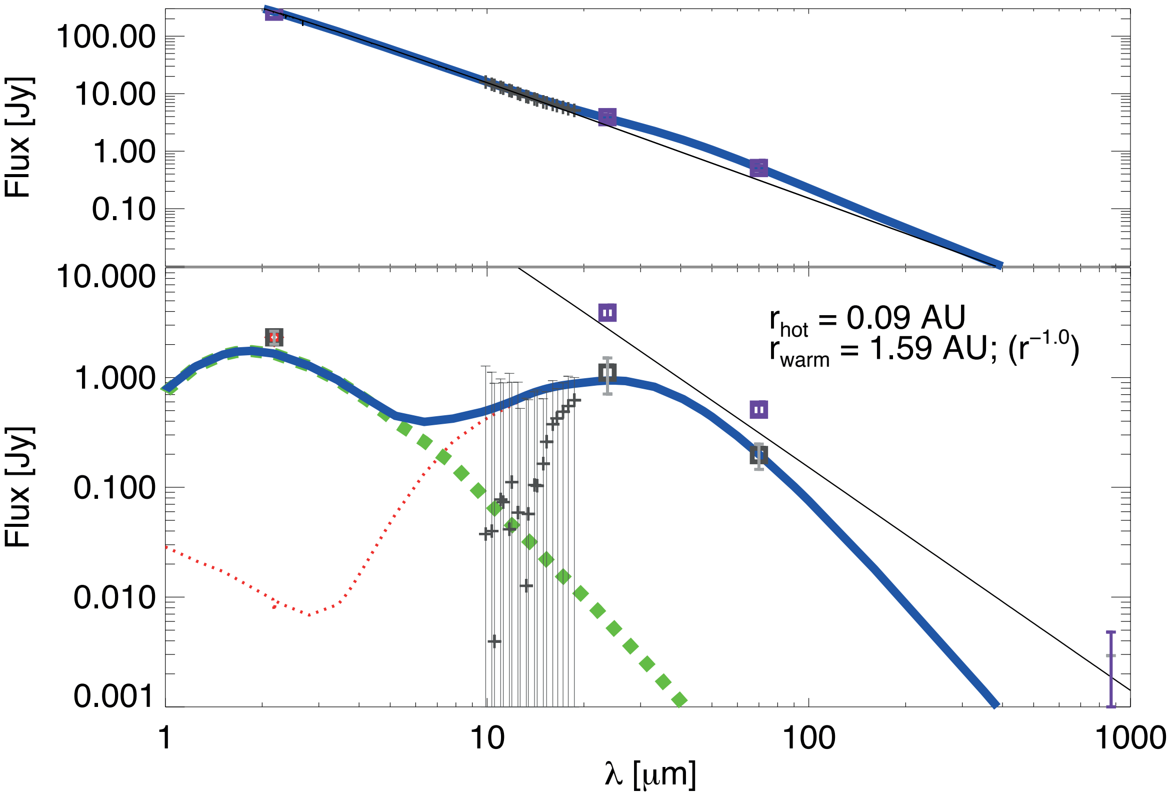

Figure 5.5: Measured spectral energy distribution, and SED of the best-fitting double-dust belt model (green: hot ring, red: warm belt, blue: total). **Top panel**: global SED including a NextGen photosphere model (solid black line), **bottom panel**: circumstellar excess emission. From left to right, thick squares denote the VLTI/VINCI 2.18μm excess, MIPS 24 μm and *Herschel*/PACS 70 μm photometry with 1σ error bars. *Spitzer*/IRS spectrum (grey crosses, not fitted) and ALMA 870 μm photometry (purple cross) are shown as 3σ upper limits.

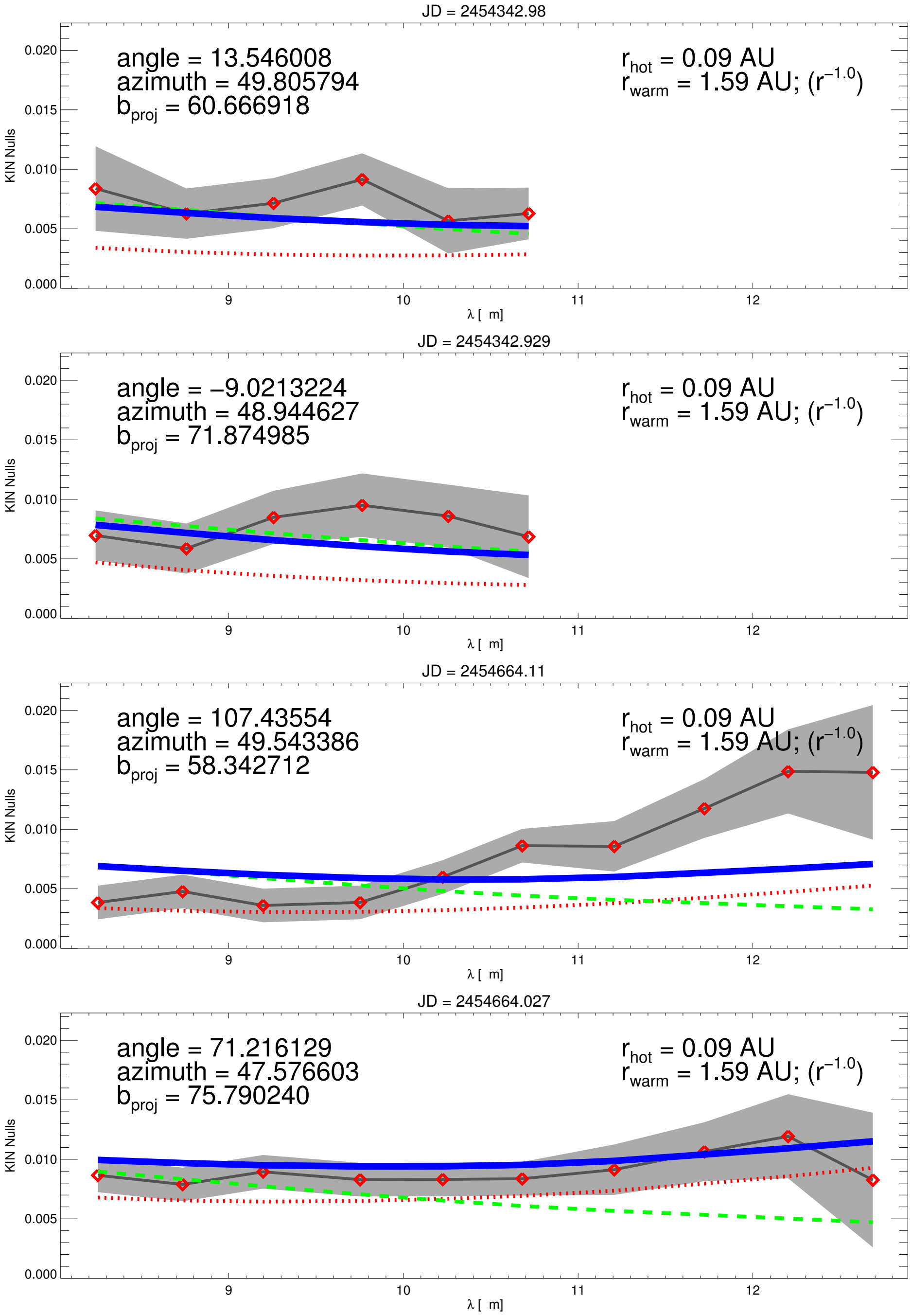

Figure 5.6: Measured KIN excess null depths and nulls of the best-fitting double-dust belt model (green: hot ring, red: warm belt, blue: total) for the four data subsets. The grey regions denote the 1σ confidence intervals on the data.

temperatures and total mass are consistent with the K-band excess. The slopes of the density profile and of the size distribution are qualitatively very steep but their exact values are not well identified due to the strong dependence of temperature with distance and grain size. However, the data also carries *spatial* information. In particular the dust must be confined within the (Gaussian) field-of-view of the VLTI *and* it must not let too much emission through the complex KIN transmission map in the mid-infrared. Grains larger than $\sim \lambda/2\pi \simeq 0.3\mu$m are also inefficient emitters in the K-band, and due to the single power law used, very small grains can become dominant. For these reasons and despite the modeling degeneracy between grain size and disk location, the minimum grain size cannot exceed a few ∼10 nm. For instance, the best model found with $a_{\rm min} = 1\mu$m has a $\chi^2_{\rm r}$ of 2.9. This result is reminiscent of what was found by Defrère et al. (2011a) who show that the exozodi of Vega must be composed of grain much smaller than 1 μm based on multiwavelengths constraints in the near-IR. We use $a_{\rm min} = 10$ nm as a working assumption for the rest of the study although what really matters is to determine which of the grains are the emitters.

In the inner solar system, the dust probed by the NASA's deep Impact mission likely consists of $\sim 20\mu$m-sized highly porous dust aggregates (*e.g.* Kobayashi et al. 2013). The hot exozodi of Fomalhaut rather consists of nanometer to submicrometer grains that we interpret as the elemental monomers produced after the break-up of larger dust particles. As demonstrated in Paper II (Fig. 6 and Tab. 5), models with higher porosity provide less good fit to the data. For instance, setting the porosity to 85 % yields a smallest $\chi^2_{\rm r}$ of 1.8 for $a_{\rm min} = 1.5\mu$m. A large amount of sensitive measurements would be needed to go beyond this solid carbon grain model (see *e.g.* Lebreton et al. 2012).

The new sublimation prescription provides a more reliable estimate of the dust location with respect to the constant sublimation temperature assumption (Fig. 5.7). With $\alpha_{\rm out} = -6$ (*i.e.* a very narrow ring), the sublimation distance of 0.01 μm grains is 0.235 AU ($\simeq d_2$); for these grains the emission falls down to 10% of the peak flux at 0.34 AU. Grains larger than $a_{\rm min}$, in particular those in the range 0.1-0.5 μm that lie close to d_1 contribute to thermal emission in similar proportions compared with 10 nm grains. Thus, independent from our choices for the parameter space limits, the emission is by far dominated by unbound grains and a robust result is that this hot exozodi is composed of grains smaller than ∼0.5 μm. The dust mass is dominated by the smallest grains, due to $\kappa < -4$. We would like to stress that forcing the material sublimation temperatures to higher values would not yield better fit to the data as it would only move the peak emission toward even shorter wavelengths (Tab. 5.2, Fig. 5.5). In the following, we adopt the above parameters for the hot ring and keep the total dust mass as the single free parameter for this component (Tab. 5.2).

5.4.4 The warm population

With the first approach (variable outer slope, fixed inner slope), the analysis indicates that the mid- to far-infrared data is best fitted by a dust belt peaking at $r_0 = 1.6$ AU and declining slowly as r^{-1}. The minimum size is close to the blowout limit ($a_{\rm blow} = 8.8\mu$m), in a rather steep distribution ($\kappa < -3.8$), yielding a reduced χ^2 of 1.56 (with 30 *d.o.f.*). These properties are consistent with the theoretical expectations that the warm population is produced through a collisional cascade in a parent-body belt, although the steep distribution might be more indicative of a recent catastrophic collision than a steady-state debris disk.

Interestingly, the second approach (fixed outer slope, variable inner slope) yields similar results to those of the first one, except that a second family of solutions arises, with very small grains located at the outer edge of the range of explored peak radii. Nonetheless this solution can be excluded based on the absence of silicate features in the *Spitzer*/IRS spectrum that would be created by such tiny silicate grains. We add prior information in the Bayesian analysis to reject solutions with $a_{\rm min} < a_{\rm blow}/10$ (Appendix B.2) and find a best reduced χ^2 of 1.60. Due to the different geometrical profile assumed, the peak radius is found to lie further out, at ~ 2.5 AU. The inner ring is not as steep as previously assumed ($\alpha_{\rm in} = +3$), which is suggestive of an inward transport of material by Poynting-Robertson drag mitigated by destructive collisions (See for example Löhne et al. 2012).

5.4.5 modeling summary

Fig. 5.5 shows an excellent fit to the spectral energy distribution. The near-infrared excess is almost solely produced by the hot ring at the sublimation distance. The warm belt at 2 AU is sufficient to explain the measured SED from mid- to far-infrared wavelengths and it is compatible with the *Spitzer*/IRS excesses. Furthermore the null excesses are mostly produced by the hot component below $\sim 10\,\mu$m in the 2007 configuration, but their rising profiles at longer wavelengths requires the contribution from the warm component. All the model excesses are compatible with the measurements within $\sim 1\sigma$ except for the short equivalent baseline in the 2008 sample that is underpredicted by $\sim 2\sigma$ upon 11μm. A possible interpretation would be the existence of an azimuthal asymmetry in the disk. Overall the warm ring is much more massive than the hot ring with respective values of $\sim 2\times 10^{-6}\,M_{\oplus}$ and $\sim 2.5\times 10^{-10}\,M_{\oplus}$ in grains smaller than 1 mm, but the hot ring is significantly brighter (Fig. 5.7) due not only to its high temperature, but also to the nature of its constituent grains. The tiny grains that the hot ring is made of constitute a much larger effective cross-section than an equivalent mass of material concentrated in large grains. The resulting profiles are illustrated in Figure 5.8 that shows the geometrical vertical optical depth and effective vertical optical depths at two representative wavelengths.

In summary, the hot ring at a fraction of AU consists essentially in grains that seem to contradict the dynamical/collisional theoretical constraints ($a \ll a_{\rm blow}$, $\kappa \leq -5.0$, steep density profile). The “warm belt” at about 2 AU seems compatible with the “classical” debris disk picture ($a_{\rm min}$, κ and $\alpha_{\rm out}$ are compatible with blowout of small grains and a collisional size distribution).

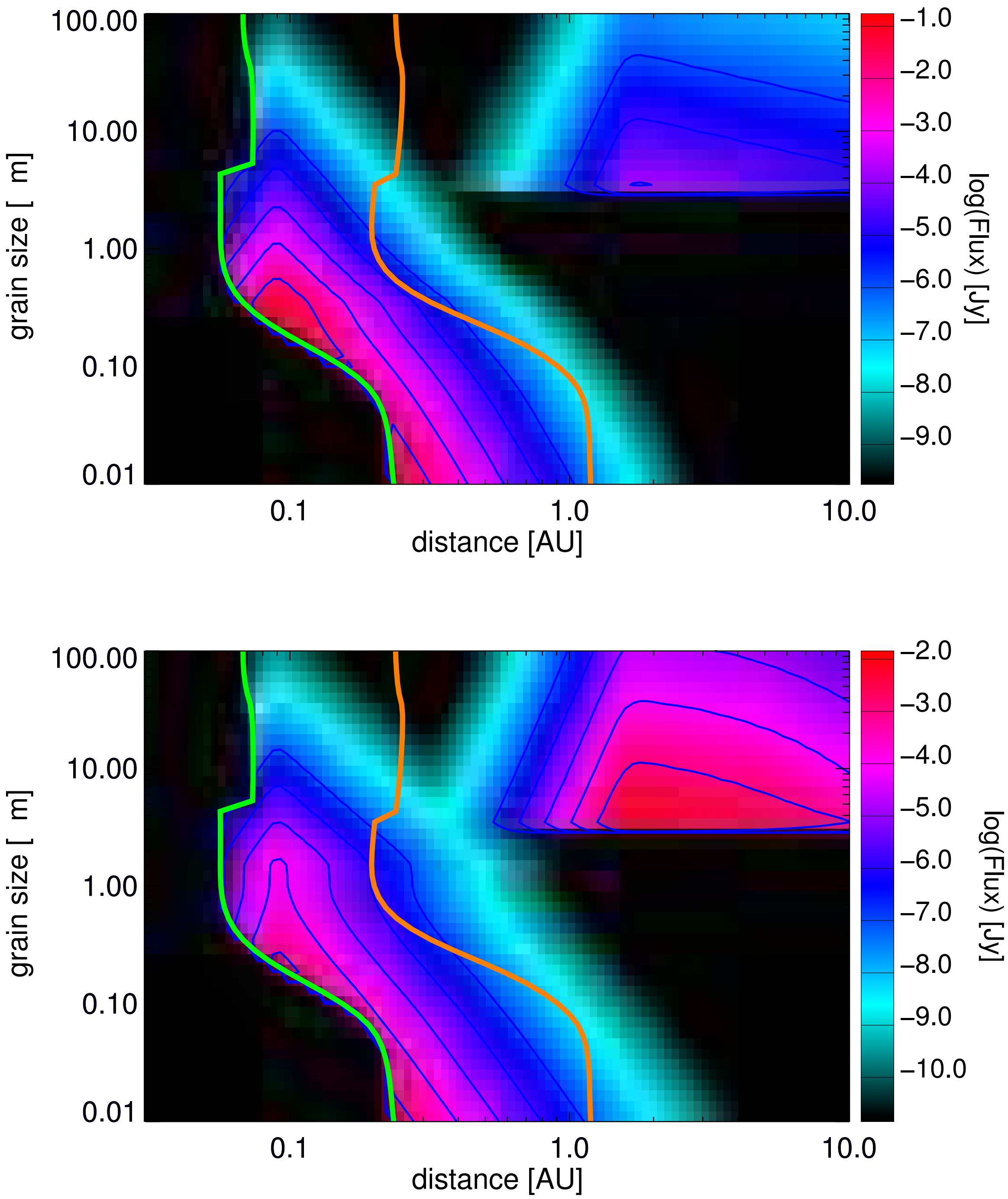

Figure 5.7: Maps showing the absolute distribution of flux as a function of distance from the star and grain size. **Top panel**: $\lambda = 2.18$ μm, **bottom panel**: $\lambda = 12.0$ μm. The orange and green lines mark the sublimation distances of silicate and carbon grains respectively.

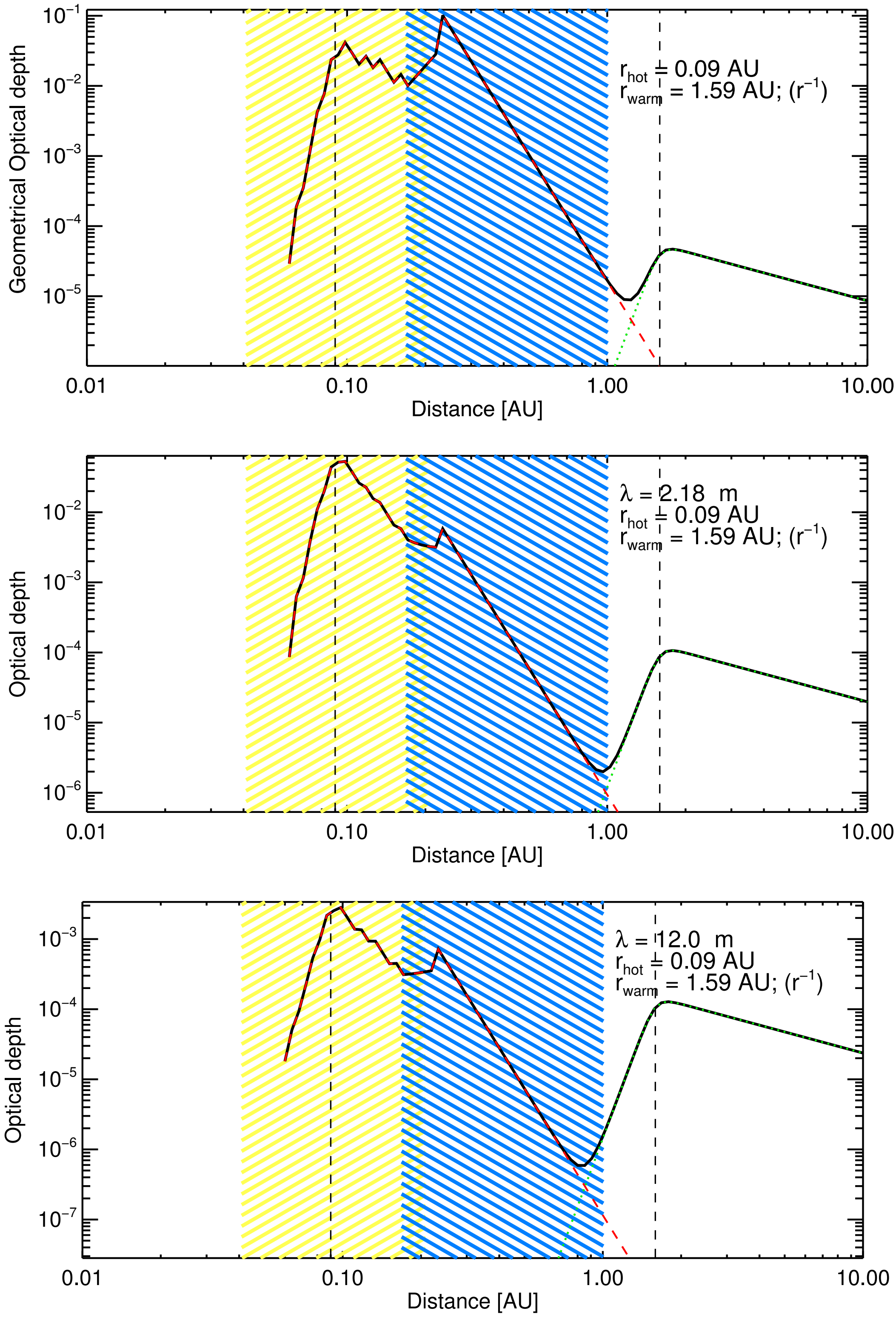

Figure 5.8: Radial profiles for the best-fitting double-ring model (approach 1. Red: hot ring; green: warm belt): geometrical vertical depth profiles (**top panel**), optical depth profiles at $\lambda = 2.18\mu$m (**middle panel**) and $\lambda = 12\mu$m (**bottom panel**). The dashed regions represent the sublimation zones of silicates (blue region) and carbons (yellow). The effect of size-dependent sublimation is evidenced by the ragged profile of the hot ring optical depth. A logarithmic sampling is used with 56 sizes ranging from 0.01 to 1000 μm.

Table 5.2: Properties of the Fomalhaut exozodiacal disk derived from the fit to the data. *Approach 1* labels the model with free outer slope, *approach 2* that with free inner slope. Numbers in bold are the parameters of the smallest χ^2 fits, while the intervals give the 1σ confidence intervals from the Bayesian analysis. The * exponent marks the fixed parameters.

Properties	Hot ring		Warm belt	
	Approach 1	*Approach 2*	*Approach 1*	*Approach 2*
Density peak r_0 [AU]	0.09^* (0.23[1])	0.09^* (0.23[1])	**1.59** [1.62, 2.43]	**2.52** [1.54, 2.15]
Inner density slope $\alpha_{\rm in}$	$+10^*$	$+10^*$	$+10^*$	**+3** [+2.99, +7.52]
Outer density slope $\alpha_{\rm out}$	-6^*	-6^*	**-1.0** [-3.62, -0.60]	-1.5^*
Mass up to 1 mm [$M_\oplus$]	**2.5 . 10^{-10}**	**2.6 . 10^{-10}**	**2.86 . 10^{-6}** $[6.12\,.\,10^{-7}, 9.53\,.\,10^{-5}]$	**1.87 . 10^{-6}** $[1.14\,.\,10^{-6}, 7.81\,.\,10^{-5}]$
Maximum surface density [cm^{-2}]	$7.24\,.\,10^{11}$	$7.46\,.\,10^{11}$	110	66.6
Maximum V-band optical depth $\tau_\perp$ [3]	**2.2 . 10^{-3}**	**2.3 . 10^{-3}**	**9.8 . 10^{-5}**	**1.2 . 10^{-4}**
Fractional luminosity $L_{\rm D}/L_\star$	$5.89\,.\,10^{-3}$	$5.71\,.\,10^{-3}$	$5.04\,.\,10^{-4}$	$6.09\,.\,10^{-4}$
Composition	C	C	Si+C	Si+C
Minimum grain size [μm]	0.01	0.01	**3.51** [1.37, 56.1]	**2.31** [0.99, 57.2]
Grain size slope	-6	-6	**-4.8** [-6.0, -3.8]	**-4.06** [-6.0, -3.7]
Typical temperatures [K][2]	[2000, 2200]	[2000, 2200]	[403,464]	[326,364]
χ^2 (dof = 30)	–	–	46.9	47.9

Notes – [1] Approximate density peak position of the *smallest* grains (they vanish below that distance).
[2] Give range of temperatures at r_0 from the smallest to 1 mm grains. For the hot ring, the temperature of the smallest grains is given at their sublimation distance. [3] The optical depth is directly proportional to the dust mass and therefore constitute another definition to this free parameter (given in V-band by convention).

5.5 Origin of the dust

In this section, we test several mechanisms as possible explanations for the peculiar morphology suggested by the modeling results. First, we discuss the viability of parent belts at the locations of the hot ring and the warm belt (Sec. 5.5.1). Subsequently, we review possible replenishing mechanisms for the warm belt (Sec. 5.5.2), and test whether the pile-up of dust in the sublimation zone can explain the hot ring (Sec. 5.5.3). In Sec. 5.5.4, we examine whether the observed population of unbound grains can be produced by the disruption of larger bodies due to sublimation. Finally, we investigate the role of gas in retaining the small grains in the hot ring by slowing down both their blowout and sublimation (Sec. 5.5.5). A short summary of our findings is presented in Sec. 5.5.6.

To compare theory with observation, we approximate the fractional luminosity of dust at radial distance r as the fraction of the star covered by dust at that location:

$$\frac{L_\mathrm{D}}{L_\star}(r) \approx \frac{\sigma_\mathrm{D}(r)}{4\pi r^2}. \tag{5.25}$$

Here, $\sigma_\mathrm{D}(r)$ is the collective cross section of the dust at radial distance r. When the excess flux can be assumed to be entirely due to spherical grains of a single size a (and hence with a mass of $m = 4\pi\rho_\mathrm{d}a^3/3$), the fractional luminosity is related to the total dust mass according to

$$\frac{L_\mathrm{D}}{L_\star}(r) \approx \frac{3M_\mathrm{D}}{16\pi\rho_\mathrm{d}ar^2}. \tag{5.26}$$

5.5.1 In-situ dust production through a collisional cascade?

Excess infrared emission from debris disks is normally interpreted as thermal emission from dust produced through mutual collisions between larger bodies in a planetesimal belt. Therefore, we first test whether the observed NIR excess can be explained by the production of small dust grains by asteroid belts at the locations of the hot ring and the warm belt.

In steady-state collisional evolution, a planetesimal belt at a given radial distance from the star can only contain a maximum amount of mass at any given time, because more massive belts process their material faster (Dominik & Decin 2003; Wyatt et al. 2007a). Assuming that the size distribution follows the classical Dohnanyi (1969) power law ($\kappa = -3.5$, valid if the critical specific energy for dispersal $Q_D^\star$ is independent of particle size) at all sizes, and extends down to the blowout size, the mass corresponds to a maximum fractional luminosity of (Wyatt et al. 2007a)

$$\begin{aligned}\max\left[\frac{L_\mathrm{D}}{L_\star}\right] = 7.0\times10^{-9}\left(\frac{r}{1\ \mathrm{AU}}\right)^{7/3} \\ \times\left(\frac{dr/r}{0.5}\right)\left(\frac{a_\mathrm{c}}{30\ \mathrm{km}}\right)^{0.5}\left(\frac{Q_D^\star}{150\ \mathrm{J\ kg^{-1}}}\right)^{5/6}\left(\frac{e}{0.05}\right)^{-5/3} \\ \times\left(\frac{M_\star}{1.92\ \mathrm{M_\odot}}\right)^{-5/6}\left(\frac{L_\star}{16.63\ \mathrm{L_\odot}}\right)^{-5/6}\left(\frac{t_\mathrm{age}}{440\ \mathrm{Myr}}\right)^{-1}.\end{aligned} \tag{5.27}$$

Here, we inserted fiducial values for the relative width of the planetesimal belt dr/r, the radius of the largest bodies a_c, the critical specific energy for dispersal $Q_D^\star$, and the mean planetesimal eccentricity e.[4] For the stellar mass $M_\star$, the stellar luminosity $L_\star$, and the age of the system t_{age}, we used the parameters of Fomalhaut found by Mamajek (2012). Cratering collisions, which have a specific energy lower than $Q_D^\star$, lead to an increased erosion of large bodies, and therefore a faster processing of the available material, and a lower maximum fractional luminosity at any given age. However, they are not accounted for in the model of Wyatt et al. (2007a). Including cratering collisions would lower the numerical factor in Eq. 5.27 by about a factor 4 to 5 (Kobayashi & Tanaka 2010). Our choice of $Q_D^\star = 150\ \mathrm{J\ kg^{-1}}$ can be seen as a conservative estimate.

Evaluating Eq. 5.27 at the radial locations of the hot ring ($r \approx 0.25$ AU) and the warm belt ($r \approx 2$ AU), gives maximum fractional luminosities of 2.7×10^{-10} and 3.5×10^{-8}, respectively. We note that the modeling results indicate steeper size distributions ($\kappa < -4.0$) for both components, which would yield much higher maximum fractional luminosities (using Eq. 16 of Wyatt et al. 2007a). However, the observations only probe the lower end of the size distribution, and it is unlikely that the steep power law extends all the way to parent body sizes. In contrast, the size distribution is expected to be shallower at large sizes, where the strengthening of bodies due to self-gravity becomes important. Furthermore, the theoretical $\kappa = -3.5$ is confirmed observationally for km-sized objects in the solar system's asteroid belt (Dohnanyi 1969). In a more thorough discussion of the stringentness of the maximum fractional luminosity, Wyatt et al. (2007a) find that by pushing the parameters, the fractional luminosity can be made to exceed the maximum given by Eq. 5.27 by a factor 100 at most. Since the fractional luminosities derived from modeling the interferometric data (Tab. 5.2) are more than two orders of magnitude higher than the maximum ones, we conclude that neither of the two components can be explained by in-situ asteroid belts that have been in collisional equilibrium for the age of the system.

5.5.2 Replenishing the warm belt

If the warm belt is in steady state (and not a transient phenomenon), some mechanism must operate to replenish the observed dust, other than an in-situ collisional cascade. A possible source of the material is the outer cold belt at about 140 AU. We now proceed to estimate the rate at which the dust needs to be replenished, and then examine whether PR drag from the cold belt is capable of providing this mass flux.

The warm belt is found to have a relatively steep size distribution ($\kappa < -4.0$), and therefore its total dust mass is dominated by the smallest grains present. In the warm belt these are particles close to the blowout size, which are destroyed by collisions on a timescale of several thousands of years (Eq. 5.21). With a dust mass of a few times $10^{-6}\ \mathrm{M_\oplus}$, the mass flux through the warm belt must be of the order of $10^{-9}\ \mathrm{M_\oplus\ yr^{-1}}$.

PR drag can only supply a limited amount of material, since grains undergo mutual collisions as they migrate inwards, and the fragments produced in these collisions can be blown out. This was demonstrated by Wyatt (2005b), using a model that assumes a single particle size, fully destructive collisions, and circular orbits.[5] Based on this model, we

---

[4] These values were found to give a good fit to debris disks around a sample of A stars (Wyatt et al. 2007b), and can be used as first order estimates for these poorly constrained parameters in the case of exozodiacal dust.

[5] The model of Wyatt (2005b) ignores stellar wind drag, but this process is not expected to be important for Fomalhaut and other A stars, because their mass loss rates are predicted to be very low.

can estimate the collision-limited PR drag mass flux from a dust source located at $r_{\rm source}$ inward to a radial distance r, which is

$$\max\left[\dot{M}_{\rm PR}(r)\right] = \frac{L_\star\sqrt{GM_\star}\beta Q_{\rm pr}}{2c^3\left(\sqrt{r_{\rm source}}-\sqrt{r}\right)}. \tag{5.28}$$

Here, $L_\star$ is the stellar luminosity, G is the gravitational constant, $M_\star$ is the stellar mass, $Q_{\rm pr}$ is the wavelength-averaged radiation pressure coefficient, c is the speed of light. A detailed derivation of this equation will be presented by R. van Lieshout et al. (in prep.). This maximum is independent of the amount of material at the dust source. Also, its dependence on grain properties is through $Q_{\rm pr}$ and β, for which we know $0 < Q_{\rm pr} < 2$, and $\beta < 0.5$ for dust released from large ($\beta \approx 0$) parent bodies on circular orbits.

We evaluate Eq. B.10 at the location of the warm belt ($r \approx 2$ AU), using $r_{\rm source} =$ 140 AU, the stellar parameters of Fomalhaut, $Q_{\rm pr} = 1.0$, and $\beta = 0.5$. The β ratio is that of the smallest bound grains, which are dragged in the most efficiently, and can therefore provide the highest mass flux. The resulting maximum mass flux is about 1.2×10^{-12} $\mathrm{M}_\oplus$ yr^{-1}, which is several orders of magnitude smaller than the mass flux required to maintain the warm belt. This indicates that PR drag is not the main replenishing mechanism for the warm belt.

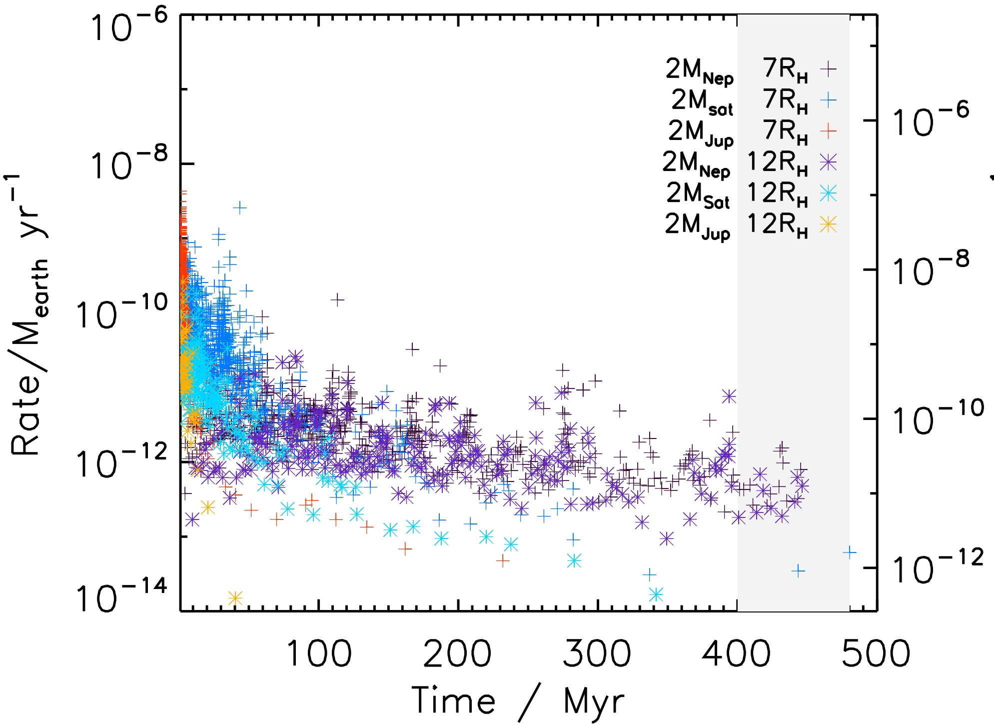

Figure 5.9: Steady-state time evolution of the rate at which material is scattered inward of 2 AU through planet scattering, in Earth masses per year; left axis: $M_{\rm outer} = 4M_\oplus$, right axis: $M_{\rm outer} = 105M_\oplus$. Several compact planetary configurations are tested with with 7 or 12 equal mass (2 Jupiter, 2 Neptune or 2 Saturn planets), equally spaced by 7 or 12 Hill-radii. The grey area represents the estimated age of Fomalhaut.

Another possible mechanism for transporting material from the outer cold belt to the warm belt is the inward scattering of small bodies by planets (Bonsor & Wyatt 2012;

Bonsor et al. 2012). The outer belt mass is constrained to be between 4 $M_\oplus$ (Boley et al. 2012) and 110 $M_\oplus$ (Acke et al. 2012) and the star age is 440±40Myr (Mamajek 2012). If a chain of planets were to orbit between the cold and warm belts, these planets could scatter small bodies inwards, in essence resupplying the warm and hot belt with material. Bonsor et al. (2012) used N-body simulations to investigate this scattering process and determined a maximum flux of scattered particles as a function of time. This maximum occurs if a chain of tightly packed, low mass planets, were to orbit between the belts. Here, we apply these models to the case of Fomalhaut, scaling the simulations to account for the stellar mass of $2.1 M_\odot$ and the inner edge of the outer belt at 133AU. The results are shown in Fig. 5.9. The important information given by this plot is the maximum possible rate at which material can be scattered inwards, given by the upper envelope of the scattered points. By assuming that the material is efficiently converted to small dust, this also gives us the maximum rate at which the observed small dust in the hot and warm belts could be resupplied. This process could potentially provide a mass flux of up to 5×10^{-11} $\mathrm{M}_\oplus$ yr^{-1} continuously for the age of the system, which is still not sufficient to compensate the collision rate (4×10^{-10} $\mathrm{M}_\oplus$ yr^{-1}). This value is very much a maximum mass flux, as it was calculated using the planet configuration that is the most efficient at scattering material inwards and it assumes that the scattered objects are entirely disrupted upon entering the inner regions of the Fomalhaut planetary system.

5.5.3 Accumulation of sublimating dust grains?

For the hot ring, the radial distribution of dust exhibits a strong peak in surface density in the carbon sublimation zone, with much lower levels of dust further out (see Fig. 5.8). This spatial profile suggests the existence of a mechanism to confine the carbonaceous dust in the sublimation zone.

Kobayashi et al. (2009) predicted that the dual effect of PR drag and radiation pressure blowout can result in an accumulation of grains around the sublimation radius. In the following we briefly explain the pile-up mechanism in terms of the three stages identified by Kobayashi et al. (2009). (1) Initially, the grains are far away from the star, and sublimation is negligible. The grains spiral inward due to PR drag and gradually heat up as they come closer to the star. (2) As the dust temperature approaches the sublimation temperature, the grains start to lose mass due to sublimation. As a consequence of the increasing cross-section-to-mass ratio of the dust grains, radiation pressure gains in relative importance compared to gravity (i.e. the β ratio of the dust grains becomes higher). This increases the eccentricity of the dust orbits, and therefore their orbital size. Hence, the inward radial migration is slowed down. Eventually, the decrease in semi-major axis due to PR drag is compensated by the increase due to sublimation. This happens roughly at the radial distance where the PR drag timescale equals the sublimation timescale (Kobayashi et al. 2008). (3) Finally, the size of the dust grains drops below the blowout radius, and their orbits become unbound. At this point the grains either leave the system, or they fully sublimate before they exit the sublimation zone. The net outcome of this process is an accumulation of dust in the sublimation zone, and this result is very robust against various grain properties (composition, porosity, fractal structure).

The pile-up mechanism is a result of the interplay between PR drag and sublimation, and was investigated for drag dominated disks (i.e. disks in which collisions are unimportant). If collisions are significant, they may inhibit the process of dust pile-up. Furthermore, a significant pile-up requires very low orbital eccentricities $e \lesssim 10^{-2}$ (Kobayashi et al. 2008, 2011). PR drag can circularize the orbits of dust particles, but only if the source region is distant enough. These caveats will be examined in further detail by R. van Lieshout et al. (in prep.).

The material in the pile-up needs to be replenished from further out by PR drag. Assuming that a dust source is located at the radius of the warm component ($r_{\mathrm{source}} = 2$ AU), without specifying how this source can be maintained, we now use Eq. B.10 to estimate how much material can be transported inward to the hot ring at $r = 0.23$ AU.[6] Inserting the parameters of Fomalhaut, together with $Q_{\mathrm{pr}} = 1.0$ and $\beta = 0.5$, yields a maximum mass flux of 1.4×10^{-11} $\mathrm{M}_{\oplus}$ yr^{-1}.

If the orbital eccentricities of the dust grains are sufficiently low, a pile-up of dust will occur at roughly the radial distance where the PR drag timescale equals the sublimation timescale. The dust stays in the pile-up until it is completely sublimated, or sublimated to below the blowout size, which approximately takes a sublimation timescale.[7] Therefore, the dust stays in the pile-up for a PR drag timescale.

A rough estimate of the maximum total mass of piled up dust can be found by multiplying the maximum mass flux rate found earlier with the PR drag timescale at the pile-up location. For $r = 0.23$ AU, the PR drag timescale is 22 yr, resulting in a maximum dust mass of 3.1×10^{-10} $\mathrm{M}_{\oplus}$, which is compatible with the modeled hot component mass. However, the maximum fractional luminosity due to this amount of mass in bound grains at this location (Eq. 5.26), is only 9.2×10^{-6}, which is several orders of magnitude lower than the value of the best fit model. This estimate is independent of the amount of material at the dust source, and only depends on grain properties through β, which should not be higher than $\beta = 0.5$. The reason for the discrepancy is that the dust grains found by the model are much smaller than the $\beta = 0.5$ particles considered for the pile-up mechanism, and therefore constitute a much larger cross section for the same amount of mass. Since these small grains are below the blowout size, they are removed from the system on timescales much shorter than the PR drag timescale. Hence, the pile-up of dust alone cannot explain the observed excess emission of the hot component.

5.5.4 The release of small dust grains in the sublimation zone

The observation of dust grains with sizes far below the blowout size presents a problem.[8] These particles have very short survival timescales, and therefore have to be replenished quickly. Their detection in the sublimation zone indicates that they could be released from unseen larger bodies that fall apart as they sublimate. The increase in the number of particles, with conservation of total mass, would lead to an increase in collective cross section, and the steep dependence of sublimation on temperature could explain the sharp peak in emission in the sublimation zone.

---

[6] In the best fit model, two populations of dust contribute equally to the hot component emission, one at $r = 0.1$ AU, and one at $r = 0.23$ AU. The latter is most optimistic choice for the PR drag scenario, resulting in the highest mass flux.

[7] Individual dust grains survive for longer than a sublimation timescale, since they end up on eccentric orbits that take them out of the sublimation zone. However, the time they spend in the pile-up, where they are observed, corresponds to the sublimation timescale.

[8] Very small grains sometimes have β ratios below unity, due to their low optical efficiencies. However, for the material types tested here, and Fomalhaut as the host star, β stays well above unity, and the smallest grains are unbound (see Fig. 5.2).

Larger bodies could be transported into the sublimation zone by various processes, such as P-R drag, or inward scattering by planets. Alternatively, the small particles could be released by an evaporating planet that is present in the sublimation zone for an extended period and gradually loses material. For now, we ignore what is the exact mechanism that provides the material, but rather focus on the mass source term $\dot{M}$ required to explain the observed fractional luminosity.

The fractional luminosity of the hot ring can be approximated by Eq. 5.26. This is possible because its size distribution is very steep, so the cross section is dominated by the smallest grains, and because its radial distribution is a sharp spike, so all grains are roughly located at the same radius. Furthermore, because of the steep size distribution ($\kappa < -4.0$), the total dust mass in the hot ring is dominated by the smallest grains. Hence, the modeling results provide a rough constraint on the product of the mass source term $\dot{M}$ and the survival timescale of the small grains $t_{\rm surv}$, according to

$$\frac{L_{\rm D}}{L_\star} = \frac{3\dot{M}t_{\rm surv}}{16\pi\rho_{\rm d}ar^2}. \tag{5.29}$$

A closer inspection of the modeling results reveals that the flux of the hot ring is mainly due to two populations of dust, which have similar contributions (see Fig. 5.7). The reason for this complication is that the radial distribution is truncated at the size dependent sublimation radius. One population consists of very small grains ($a = 0.01\,\mu$m) located at $r = 0.23\,$AU, the other of slightly larger grain ($a = 0.2\,\mu$m) at $r = 0.10\,$AU. These slightly larger grains are still well below the blowout size. In the following we will test both sets of parameters when evaluating the survival timescale. For the material density we assume that of carbon with a porosity of 5% ($\rho_{\rm d} = 1.85$ g cm^{-3}).

We now make an estimation of the survival timescale of the relevant dust grains, in order to find the required mass production or influx to explain the observed fractional luminosity. The mechanisms that are critical to the survival of small grains close to a star are sublimation and blowout. Sublimation destroys the grains on a timescale of

$$t_{\rm subl} = \frac{a}{|\dot{a}|}, \tag{5.30}$$

where $\dot{a}$ is given by Eq. 5.17. This is the time it takes for a grain to sublimate, assuming the sublimation rate remains constant. $t_{\rm subl}$ is highly dependent on r (through dust temperature), and therefore uncertain. For the blowout timescale, we take

$$t_{\rm dyn} = \sqrt{\frac{5r^3}{2GM_\star(\beta-1)}}, \tag{5.31}$$

which is the time it takes a particle to move outward from its release point to twice that radial distance, valid for $\beta \gg 1$ (a derivation is presented in App. B.2.1).

Figures 5.10a and 5.11a show the constraints that the observations put on the product of $\dot{M}$ and $t_{\rm surv}$ for the $a = 0.01\,\mu$m grains at $r = 0.23\,$AU and the $a = 0.2\,\mu$m grains at $r = 0.10\,$AU, respectively. Also shown are the typical survival timescales of these dust grains, and the maximum mass influx due to PR drag from a source region at 2 AU. The figures reveal that a mass source term of at least $\sim 10^{-7}$ M$_\oplus$ yr^{-1} is required to explain the observations, if the grains survive for $t_{\rm dyn}$. Comparing this with the maximum mass influx due to PR drag indicates that this mechanism cannot provide enough material.

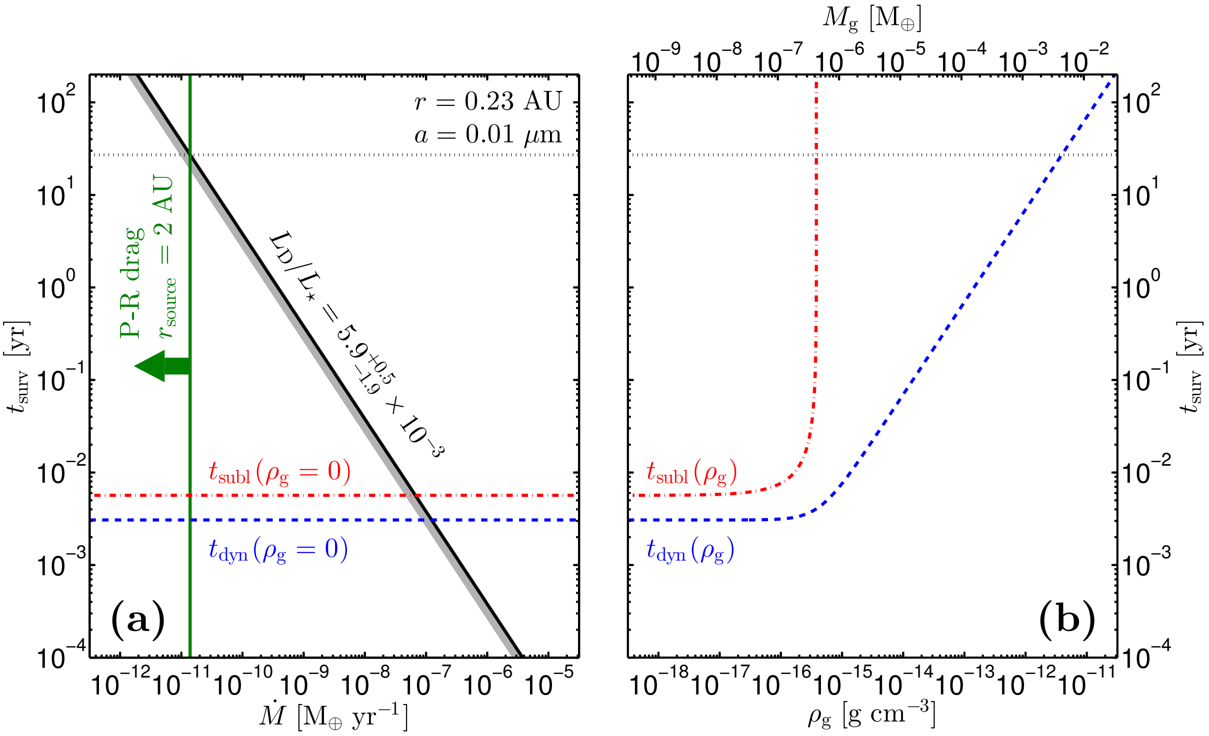

Figure 5.10: A summary of the constraints on the hot ring, assuming it consists of 0.01 μm carbon grains located at 0.23 AU. Panel **(a)**: The diagonal line shows the relation between the mass flux and the dust grain survival timescale, as constrained by the observed fractional luminosity (black, with error margins in grey, Eq. 5.29). The horizontal lines indicate the typical timescales (in a gas free environment) for destruction by sublimation (red, dash-dotted, Eq. 5.30), and removal by blowout (blue, dashed, Eq. 5.31). The vertical line with the arrow indicates the maximum mass flux due to P-R drag from a very dense source region located at 2 AU (green, Eq. B.10). Panel **(b)**: The dependence on gas density of the sublimation timescale (red, dash-dotted, Eq. 5.30), and the blowout timescale (blue, dashed, the sum in quadrature of Eq. 5.31 and Eq. 5.32) The top axis gives the total gas mass corresponding to the midplane gas densities on the bottom axis, assuming the gas is located in a vertically isothermal ring of width $\Delta r = r$ (Eq. 5.34). The horizontal, black, dotted line marks the minimum survival time required if the observed material is to be provided by PR drag. It extends across both panels to show the gas density and total gas mass this would imply.

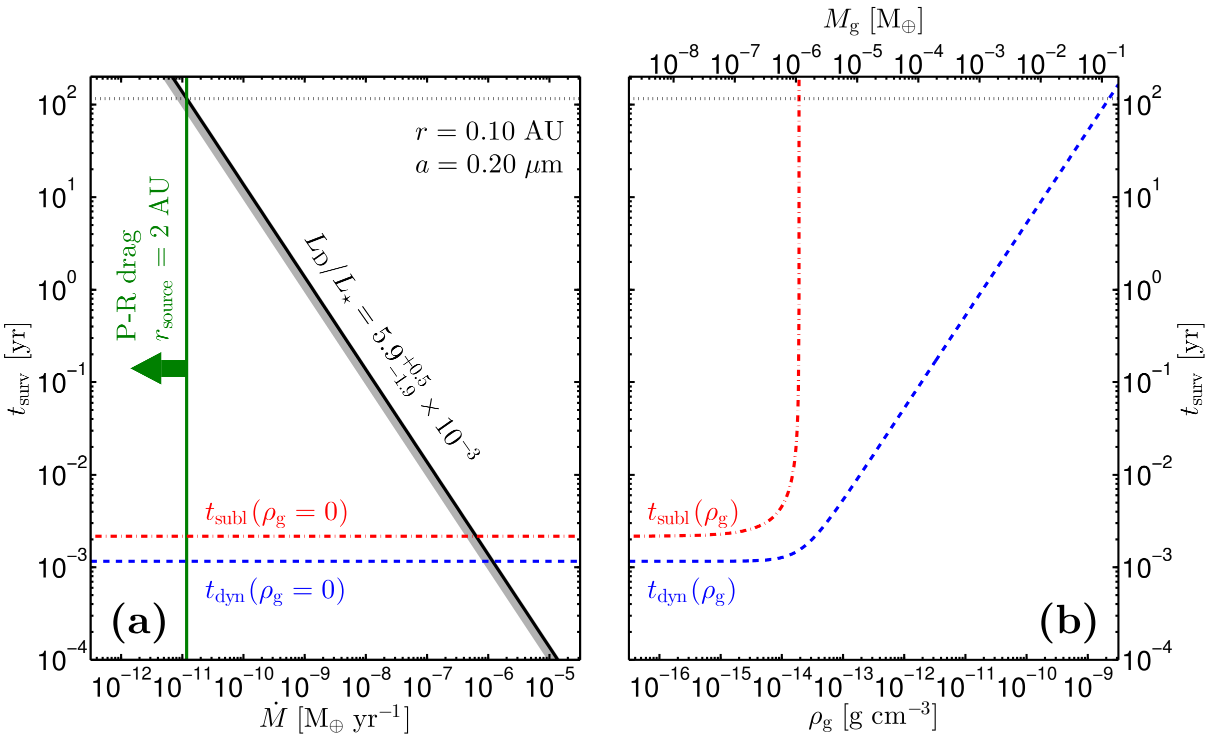

Figure 5.11: Same as Fig. 5.10, but assuming the hot ring consists of 0.2 μm carbon grains at 0.1 AU. Different scales are used on the horizontal axes in panel **(b)**.

Other processes that release small dust particles in the sublimation zone may yield higher mass source terms. For instance, Rappaport et al. (2012) report a mass loss rate from the possible evaporating planet KIC 12557548 b of $\sim 10^{-9}$ M$_\oplus$ yr^{-1}, sustainable for ~ 0.2 Gyr. This rate would still be insufficient to explain Fomalhaut's hot ring, and the dust morphology inferred for KIC 12557548 b is very different from a ring. However, the actual mass loss rate of an evaporating planet is highly dependent on variables such as its mass, size, temperature, and composition.

Alternatively, the estimates of the dust survival timescale could be too low. If the small dust grains would somehow be retained in the sublimation zone, their survival timescale could be larger. One possibility is that the assumption that the disk is completely gas free is not valid in the sublimation zone. In the next subsection, we explore the influence of gas on the dust survival timescales.

5.5.5 The influence of gas on dust survival timescales

Because dust sublimation converts solid dust to gas, some gas is expected to be present in the sublimation zone. The presence of gas increases the blowout timescale, because particles on their way out are slowed down by gas drag. Assuming that the subsonic Epstein drag law can be used for the gas drag force on the small dust grains, we find that the blowout timescale at high gas densities is given by

$$t_{\rm dyn}(\Delta r, \rho_{\rm g}) = \frac{\rho_{\rm g} v_{\rm th} \Delta r\, r^2}{G M_\star (\beta - 1) \rho_{\rm d} s}. \qquad (5.32)$$

Here, ρ_g is the mass density of the gas, v_th is the mean thermal speed of the gas, and Δr is the distance to be travelled by the blowout grain (this equation is derived in App. B.2.2). This timescale is shown for $\Delta r = r$ in Figs. 5.10b and 5.11b, using the gas densities on the lower axes.

By assuming that the gas is confined to a ring around the star with a radial width of Δr, and that it is vertically isothermal, we can express t_dyn in terms of the total gas mass, and eliminate the dependence on Δr and v_th. The gas surface density of a vertically isothermal disk with midplane density ρ_g is given by

$$\Sigma_\mathrm{g} = \frac{\pi\sqrt{\gamma}}{2}\rho_\mathrm{g} v_\mathrm{th}\sqrt{\frac{r^3}{GM_\star}}, \tag{5.33}$$

where γ is the adiabatic index, for which we assume $\gamma = 1.5$. Then, the total gas mass is given by

$$\begin{aligned} M_\mathrm{g} &= 2\pi r \times \Delta r \times \Sigma_\mathrm{g} && (5.34) \\ &= \pi^2\sqrt{\gamma}\rho_\mathrm{g} v_\mathrm{th}\Delta r\sqrt{\frac{r^5}{GM_\star}}, && (5.35) \end{aligned}$$

and the blowout timescale becomes

$$t_\mathrm{dyn}(M_\mathrm{g}) = \frac{M_\mathrm{g}}{\pi^2\sqrt{\gamma GM_\star r}(\beta-1)\rho_\mathrm{d}s}. \tag{5.36}$$

This is shown in Figs. 5.10b and 5.11b with the gas masses on the upper axes.

In the optimistic case that the hot ring is due to $a = 0.01\,\mu$m grains at $r = 0.23\,$AU, the hypothesis that the dust is supplied by PR drag from the warm belt requires a survival timescale of about 30 yr (the dotted black line in Fig. 5.10). This timescale is reached at a gas density of approximately 4×10^{-12} g cm^{-3}, which corresponds to a total gas mass of about 5×10^{-3} M$_\oplus$. Assuming that all this gas is provided by sublimating dust at the maximum PR drag rate, this mechanism needs to have operated for approximately M_g / $\max[\dot{M}_\mathrm{PR}] \approx 5 \times 10^{-3}$ M$_\oplus$ / 1.4×10^{-11} M$_\oplus$ yr^{-1} ≈ 0.4 Gyr, which equals the age of the system, to explain the total gas mass.

The gas will also affect the sublimation of dust grains, since the presence of gas raises the sublimation temperature (see Sec. 5.3). Figs. 5.10b and 5.11b also show the dependence of the sublimation timescale on gas density. This assumes that the ambient gas only consists of carbon, so the gas densities on the lower axes correspond to the partial densities used to compute the sublimation rate in Sec. 5.3. For high gas densities, the dust particles will not sublimate, but grow. This would stabilize the dust grains, possibly explaining their very high temperatures.

5.5.6 Summary of theoretical findings

The distribution of dust in the inner few AU of the Fomalhaut system that was found by modeling the observations, is difficult to reconcile with a steady-state model. Both the hot and warm components contain more dust than can be explained by in-situ production via a collisional cascade that has operated for the age of the system. If these two components are in steady state (as opposed to being transient phenomena), other processes must be operating to maintain the observed dust populations. We considered several mechanisms as potential sources of the dust. Table 5.3 gives an overview of the mass fluxes that can be attained by these mechanisms.

Table 5.3: Mass fluxes of several potential supply or production mechanisms, and of the main destruction mechanisms (destructive collisions and radiative transfer blowout).

Mechanism	Mass flux ($\mathrm{M}_\oplus\ \mathrm{yr}^{-1}$)
Warm belt	
PR drag from 140 AU	$< 1.2 \times 10^{-12}$
Planetesimal scattering	$\lesssim 5 \times 10^{-11}$
Collisions	$\sim -4 \times 10^{-10}$
Hot ring	
PR drag from 2 AU	$< 1.4 \times 10^{-11}$
Evaporating planet[1]	$\sim 10^{-9}$
Blowout	$\sim -8 \times 10^{-8}$

Notes – [1] This is the value found by Rappaport et al. (2012) for KIC 12557548 b. It is given here for comparison.

The warm belt is dominated by barely bound grains that are primarily destroyed by mutual collisions. It needs a mass flux of the order of 10^{-9} $\mathrm{M}_\oplus$ yr^{-1} in order to be sustained. This rate cannot be maintained through PR drag of material from the outer cold belt at about 140 AU, but the inward scattering of small bodies by a chain of planets can marginally provide the required mass flux.

The hot ring seems to require an even higher replenishment rate ($\sim 10^{-7}$ $\mathrm{M}_\oplus$ yr^{-1}). It consists of small particles that are removed from the system by blowout. A lower mass flux is possible if these grains are somehow retained near their production site, lengthening their survival timescale. The pile-up of dust due to the interplay of PR drag and sublimation is insufficient to explain the observations. PR drag of dust grains from the warm belt could provide the required mass flux, if a large amount of gas is present in the sublimation zone, which slows down the blowout of unbound grains. The viability of such a substantial gas ring and its consistency with existing observations remain to be tested. Both oxygen and carbon will remain unaffected by radiation pressure around Fomalhaut. In the case of the β Pictoris debris disk, Fernández et al. (2006) show that several species can potentially act as self-braking agents on the gas disk, and that more than 0.03 $M_\oplus$ of gas could be retained consistent with observed upper limits on the column densities.

5.6 Discussion

In the last section, we showed that the hot exozodi of Fomalhaut could be the result of an accumulation of small unbound grains at the carbon sublimation distance brought there by the PR drag effect. For this mechanism to work, a trapping mechanism such as braking by a gaseous component needs to be invoked. Alternative sources of continuum emission, such as free-free emission from a stellar wind, mass-loss events or hot gas, have been discussed *e.g.* in Paper II, Absil et al. (2008) and Defrère et al. (2012) and can be considered unsatisfying explanations: emission by very hot dust is the most convincing explanation to date. In the solar system, nanometer-sized particles are detected with the STEREO and Ulysse spacecrafts (Meyer-Vernet et al. 2009; Krüger et al. 2010, respectively), with an increase in the particle flux in the inner solar system. These very small grains, which are affected by the Lorentz force (Czechowski & Mann 2010), could thus be expected in exozodiacal disks. In fact, magnetic trapping of nanograins could be a valuable alternative to the gas-braking mechanisms we have investigated in this study as discussed by Su et al. (2013). We note that it cannot be excluded that these nanograins might produce non-thermal emission, such as a PAH continuum.

The bright hot component can be seen as the "tip of the iceberg" in the sense that it may be a bright counterpart to the warm belt. Our model of the warm belt confirms previous attempts to constrain its properties based on unresolved observations, although our detailed treatment of grain optics and the addition of spatial constraints point towards a closer in location than previously suspected. In particular using a blackbody model, Su et al. (2013) estimated the belt location to be around 11 AU. While preserving the consistency with their dataset, the small FOV of the nulling interferometer impose the warm dust peak distance to be in the [1.5, 2.5] AU range after an appropriate subtraction of the hot dust contribution.

Furthermore, future detection of a polarization signal could provide a confirmation of the model, and additional constraints on the grain properties and the disk geometry (in particular its inclination, assumed to match that of the cold belt in this study). We use the MCFOST radiative transfer code (Pinte et al. 2006, 2009) with identical model parameters and assumptions as those discussed above[9] in order to predict polarimetric signals for the exozodi. We find that the linear polarization integrated over the disk range from 3×10^{-7} to 5×10^{-7} for the warm belt, and reaches 2×10^{-5} to 3×10^{-6} for the hot ring in bands U to I. These values are compatible with the upper limits of 9×10^{-3} to 3×10^{-3} given by Chavero et al. (2006). For the hot ring, such signals would potentially be detectable by future sensitive polarimeters.

The warm belt has a distribution of temperatures that ranges from ~320 to 470 K. The suspected parent-body belt location is thus consistent with the prediction that such belts form preferentially before the snowline, $R_{\rm snow} = 2.7\,(L/L_{\odot})^{1/2}\,\mathrm{AU} = 11\,\mathrm{AU}$, because giant planet accretion is triggered beyond that limit. At such distance, the parent-body population should have eroded in a short timescale compared to the age of the star. Given the properties of the cold dust belt, Poynting-Robertson drag is not a valuable mechanism to transport sufficient amount of material from ~140 AU down to the warm belt. Even in a very favorable planetary system configuration, scattering of small bodies (comets, asteroids, planetesimals) from the cold belt by a chain of planets could not sustain the required mass production rate in the warm disk for the age of the star.

Another explanation to the unexpectedly large mass in the warm component could be that the dust originates in stochastic and / or isolated catastrophic events, such as planetesimal collisions or break-up, or major dynamical perturbations. In the solar system, the Late Heavy Bombardment (LHB) was responsible for the depletion of the Kuiper-Belt, the release of large numbers of icy objects into its inner regions and probably a durable increase of the inner Zodiacal cloud infrared luminosity (Nesvorný et al. 2010; Booth et al.

---

[9] MCFOST uses a 3D geometry: we assume linear flaring, and we test scale heights of 0.001, 0.01 or 0.1 (unitless) at the reference distance of 1 AU, with little impact on the results. $r_{\rm max}$ is fixed to 1 AU and 20 AU for the hot ring and the warm belt respectively. Here the grain temperatures are independent of their sizes.

2009). The orbital parameters of Fomalhaut b have recently been reevaluated based on an fourth epoch detection with the HST. The planet orbit is found to be very eccentric (≥ 0.8) such that it likely approaches the innermost parts of the system at periastron, where additional planetary perturbers might be present (Kalas et al. 2013, Beust et al., in prep.). Thus an LHB-like event may be occurring around Fomalhaut as a result of a planet-planet scattering event causing delayed stirring in both the cold and the warm belt. In summary, a valuable scenario to understand the global debris disk is that a high collisional activity has been triggered by the presence of perturbing planets, reminiscent of the solar system history.

Finally, it is attractive to place our study in the context of the long-term objective of finding and characterizing an Earth-like planet in the habitable zone of a star. Scaling the Mars and Venus criteria for Fomalhaut (Selsis et al. 2007), the habitable zone ranges between 2.5 and 5.5 AU. Under favorable 100% cloud-cover conditions, it would extend from 1.4 to 8.1 AU. At these distances, the level of warm dust emission around Fomalhaut is high and represent therefore a threat for future spectroscopic and direct imaging missions (e.g., Defrère et al. 2010; Roberge et al. 2012). In turn, the existence of a massive asteroid belt may be an indication that there is no planet in these region as it would have cleared its neighborhood around its orbit. A noticeable feature that we have not discussed yet is that the gap between the two exozodi components could be sculpted by the gravitational influence of a hidden planet at around 1 AU. Constraints from radial velocities, astrometric measurements, and high-contrast imaging have been summarized in Paper I and are currently compatible with an hypothetical small mass companion in these regions.

5.7 Conclusion

In a series of three papers, we have performed an interferometric study of the Fomalhaut inner debris disk. Paper I presented the detection of a circumstellar excess in K-band, attributed to very hot dust, confined well inside the 3AU-HWHM FOV of the VINCI instrument. Despite the limited spatial constraints, the brightness temperature required calls for extremely hot, refractory grains lying very close to the star, at the sublimation limit. Conversely, KIN null depth measurements presented in paper II are indicative of a warmer dust component at a few AU (2AU-HWHM FOV) that produces a rising excess upward of 10μm. In the present study, we have presented the detailed results of self-consistent modeling of these two components by means of a parametric radiative transfer code and accurate treatment of debris disk physics. To account for the expected size-dependent sublimation temperature of dust, we introduced a new prescription for the treatment of grain sublimation accounting for their specific dynamics and lifecycle. This enabled us to assess realistically the spatial and size distribution of the emitting grains. We find that the Fomalhaut exozodiacal disk consists of two dust populations, one “classical”, though massive, disk of warm ($\sim$ 400K) dust peaking at $\sim$ 2AU and declining slowly with distance, responsible for most of the mid-infrared emission, and a hotter ($\sim$2000 K) and brighter counterpart dominated by small (0.01 - 0.5 μm), unbound dust particles at the limit of sublimation. The stellar radius is approximately 9×10^{-3} AU and the hot grains are actually located at typically 10 to 35 stellar radii. The degeneracy inherent to SED fitting is partially broken by the spatial information contained in the interferometric data. We find that the model also fits the photometric mid/far-infrared measurements from Spitzer/MIPS and Herschel/PACS, and is consistent with the flux level measured in the Spitzer/IRS mid-infrared spectrum. If the warm dust, or an additional colder (but unresolved) component, were present further out in the system - as suggested by the suspected on-star excess from ALMA - it should produce moderate emission in the mid/far-infrared to preserve the compatibility between the KIN and Herschel / Spitzer data.

We analytically explored the various processes that can affect a dust grain: photo-gravitational and Poynting-Robertson drag forces, collisions, sublimation and disruption of big aggregates. We propose a framework for interpreting self-consistently the simultaneous prevalence of both hot and warm dust in the inner regions of Fomalhaut, similar to that also reported for samples of nearby main sequence stars by near- and mid- infrared exozodi surveys. Firstly we find that neither of the two inner belts can be explained by a steady-state collisional cascade in a parent-body reservoir. Ignoring the production mechanism for the warm dust, we estimate that PR drag, from this component down to the sublimation radius, could transport enough mass into the hot component, provided that it can accumulate there. We showed that small carbon monomeres released by the disruption of larger aggregates that originate from the warm component can explain the observed flux level in the near-infrared, because this process considerably enhances the effective cross section of the dust population. Finally braking by a gaseous component could preserve these unbound grains from radiative transfer blowout for a sufficient time providing enough gas mass is available. If sublimation is the main source for this gas, it must have accumulated for a timescale comparable to the age of the star.

In summary, the intriguing hot dust phenomenon reported by various interferometric surveys could be understood in the light of the cumulation of multiple effects that eventually yield an accumulation of very small grains at a fraction of an AU. These hot rings are likely the counterparts of warm debris disks orbiting at a few AU that have their dust production triggered by intense collisional activity. In the near future, this scenario will need to be tested against statistical samples of objects, including later type stars.

Chapitre 6

Conclusions et perspectives futures

"Ils consacraient une nouvelle nuit de leur vie à ce travail lent et obsessionnel consistant à attendre qu'un rocher perdu dans l'espace passe entre une étoile et la Terre. Le dévouement et la sincérité qui permettaient d'extraire des données d'occasions aussi brèves et à peine visibles avaient quelque chose d'effrayant qui forçait le respect."

Stephen Baxter, *Temps - Les Univers multiples I*, 2007

Ce manuscrit relate trois années de recherches sur les systèmes planétaires extrasolaires que j'ai menées à l'Institut de Planétologie et d'Astrophysique de Grenoble. Au cours de ma thèse, initialement ciblée sur les programmes-clés Herschel voués à l'étude des disques circumstellaires, je me suis d'abord intéressé à l'analyse d'observations de disques froids, analogues massifs de la Ceinture de Kuiper, tels que HD 181327. J'ai démontré l'importance de ces réservoirs glacés pour le devenir des systèmes planétaires internes. Les contraintes spatiales manquent pour caractériser les échelles de distance où résident les poussières les plus chaudes, au voisinage de la zone habitable. L'interférométrie optique offre une solution adéquate pour scruter les disques de débris chauds, que j'ai appréhendée dans le deuxième volet principal de ma thèse. A travers l'étude de quelques étoiles à la résonance toute particulière : Vega, β Pictoris et Fomalhaut, j'ai exploré la physique à l'oeuvre dans les disques exo-zodiacaux. Je propose ici une synthèse de mes travaux, et des perspectives de recherches sur les systèmes planétaires, à court puis à plus long terme.

6.1 De la nature de la matière planétaire extrasolaire

6.1.1 Des aggrégats de poussière glacée et poreuse

HD 181327 est un disque de débris *jeune*. Massif et brillant, il est bien contraint spatialement par des images en lumière diffusée. En combinant ces informations spatiales aux informations spectrales fournies par de multiples instruments, en premier lieu Herschel, j'ai confirmé que le disque se concentre en un anneau étroit de poussières micrométriques. Il s'agit essentiellement de silicates et de matériaux carbonés, orbitant à 89 UA de l'étoile. En sondant les longueurs d'ondes cruciales correspondant au pic d'émission, dont l'allure est fortement impactée par la taille et la composition chimique des poussières, j'ai pu modéliser en détails les propriétés du matériau entourant la jeune étoile. Face à des données abondantes et traitées avec la plus grande précision, les modèles bénéficient fortement de l'apport de l'*analyse Bayésienne*, qui permet de mesurer les différents paramètres du disque avec un niveau de fiabilité bien déterminé par la statistique.

Les poussières sont composées en grande partie de glace d'eau. Elles revêtent la forme d'aggrégats poreux, qui diffusent la lumière à la manière de petits grains, mais rayonnent comme des gros grains. Ces propriétés, démontrées avec rigueur par l'analyse Bayésienne, constituent une des premières preuves formelles de la nature glacée des corps-parents dans les disques de débris. A l'inverse du disque exozodiacal de Fomalhaut, pour lequel des fragments compacts de grains rocheux semblent favorisés, HD 181327 nous révèle des poussières dont la nature aggrégée et la couverture de glace semblent tracer un lent processus de collisions/fragmentations. L'extrême richesse en eau et les tailles des grains en jeu distinguent clairement ces disques de poussières de seconde génération des nuages moléculaires ou des coeurs préstellaires, d'où le matériau tire son origine.

On peut aujourd'hui considérer que les propriétés des poussières froides sont bien comprises : les modèles de grains du type de celui que j'ai proposé peuvent devenir un "standard", afin de mieux se concentrer sur la structure des disques de poussières. L'identification des matériaux en présence permet de déduire leurs processus de production, la nature des impacts et les processus dynamiques à l'œuvre au sein des corps parents.

6.1.2 L'héritage d'Herschel

Après environ 1400 jours d'opération, le télescope spatial Herschel arrivera bientôt en fin de mission alors qu'il épuisera ses réserves de fluide cryogénique. L'ESA considère à l'heure actuelle plusieurs possibilités pour le devenir du télescope : la possibilité d'une mission en phase tiède, celle de l'extraire de son orbite de Lissajous au point L2 pour l'envoyer suivre sa propre orbite solaire, voire même celle de l'amener percuter la Lune pour y déceler des traces d'eau. L'équipe DUNES, en collaboration avec l'équipe DEBRIS qui poursuivait des objectifs similaires, a mis en évidence qu'avec la sensibilité d'Herschel, environ 29% des étoiles proches de type solaire (FGK) harborent un excès attribué à un disque de débris [1]. Une grande variabilité est mesurée dans leurs propriétés. La fréquence et la luminosité des disques apparaissent plus grandes pour les étoiles âgées de moins de 400 à 500 millions d'années, et on constate un déclin jusqu'à quelques milliards d'années. Le niveau de flux de la Ceinture de Kuiper ($\sim 10^{-7}$) a été atteint, bien que pour des disques plus froids à des longueurs d'ondes situées au delà du pic d'émission de celle-ci. Les modèles tels que celui mis en œuvre par le code GRaTer s'avèrent performants pour analyser les observations, aussi bien les SED que les multiples nouvelles images résolues, ce de manière systématique. L'interprétation de l'observation de certains objets représente encore un défi : c'est le cas des disques froids (Section 3.2.3) qui semblent affectés d'une dynamique encore mal comprise. Les observations des programmes DUNES et GASPS sont aujourd'hui complétées et laissent aux modélisateurs un héritage considérable qu'il faudra encore des années pour exploiter.

6.1.3 Des poussières aux corps parents : ALMA et HD 181327

Tandis que les poussières microscopiques vues dans le proche-infrarouge sont susceptibles de peupler l'extérieur des disques sous l'effet de la pression de radiation, des corps de l'ordre du millimètre sont déjà assez grands pour être largement dominés par la dynamique Képlerienne, à l'instar des planétésimaux qui les ont produits. Si les planètes suspectées de sculpter les sculptures annulaires observées résident sur des orbites excentriques, leur empreinte séculaire sur les orbites des corps parents pourrait créer des "grumeaux" ou une assymétrie de température potentiellement détectables en imagerie à haute dynamique.

Pour notre exemple de référence, HD 181327, j'ai estimé détectables des détails fins du disque dans le sub-millimétrique, moyennant une résolution spatiale et une sensibilité que seul l'Atacama Large Millimeter Antenna (ALMA) peuvent aujourd'hui offrir. La figure 6.1 montre une simulation que j'ai réalisée avec le simulateur CASA de l'anneau de HD 181327, tel qu'il serait vu par ALMA. L'anneau serait résolu avec un rapport signal-à-bruit de 20 après seulement 2h d'observations, pour une résolution de $0.22''$ inférieure à son épaisseur et suffisante pour mesurer l'extension spatiale de l'anneau parent.

---

[1] Eiroa et al. 2013, en préparation. Voir Section 3.2.3 / Lebreton et al. (2011) pour les derniers résultats publiés.

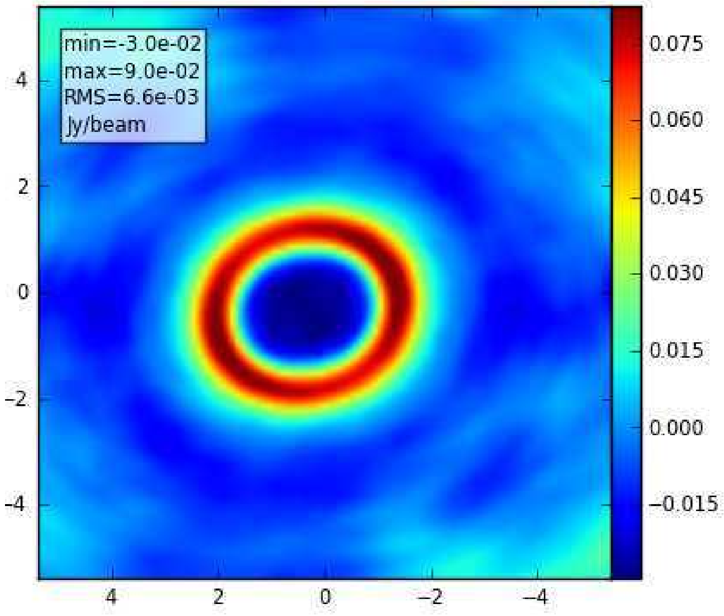

FIGURE 6.1: Simulation CASA de HD 181327 tel que vu par ALMA en bande 7 (870 μm) en configuration étendue. Le temps a été calculé avec l'ALMA Sensitivity Calculator pour atteindre 0.26 μJy/beam. Le modèle est basé sur le profil radial HST/NICMOS et les propriétés optiques issues du fit de la SED.

6.1.4 "Dissecting The Moth" : mieux comprendre la dynamique des grains

J'ai par ailleurs été le premier co-investigateur d'un *proposal* d'observations VLT/NaCo (PI : Buenzli, observations conduites en période P88), visant à imager le disque de l'étoile HD 61005, surnommé *The Moth* pour sa structure asymmétrique à grande échelle. Ce disque est composé d'un anneau fin à 61 AU, incliné et décentré de 3 AU, prolongé par une composante externe incurvée supposément à cause de l'interaction avec le milieu interstellaire (Buenzli et al. 2010). Les petits grains sont placés par la pression de radiation sur de larges orbites excentriques, de telle sorte qu'ils peuplent seuls les régions externes du disque, tandis que les plus gros grains demeurent liés à l'anneau-parent. Le déficit de petits grains dans le disque externe est bien décrit par une loi de puissance révisée avec une pente $\kappa < -3.5$. Ainsi, κ peut-être utilisé comme un traceur de la distance à l'étoile, $d = d(\kappa)$. La Figure 6.2 représente pour plusieurs cas les rapports théoriques σ_{sca} des sections efficaces de diffusion en bandes J et Ks — directement proportionnels à l'indice de couleur J - Ks — en fonction de $\kappa = \kappa(d)$. Le flux diffusé par une distribution de grains pour une composition donnée est en effet proportionnel à la section efficace de diffusion moyenne $\sigma_{\text{sca}}(\lambda)$, qui dépend de la distribution de taille. On constate que la variation de couleur entre le disque interne et le disque externe mesurés dans les images multi-chromatiques peut fournir des contraintes fortes sur les propriétés des grains et leurs distributions spatiales. Dans le cas présent, l'interaction avec le milieu interstellaire pourrait également affecter la couleur du disque externe.

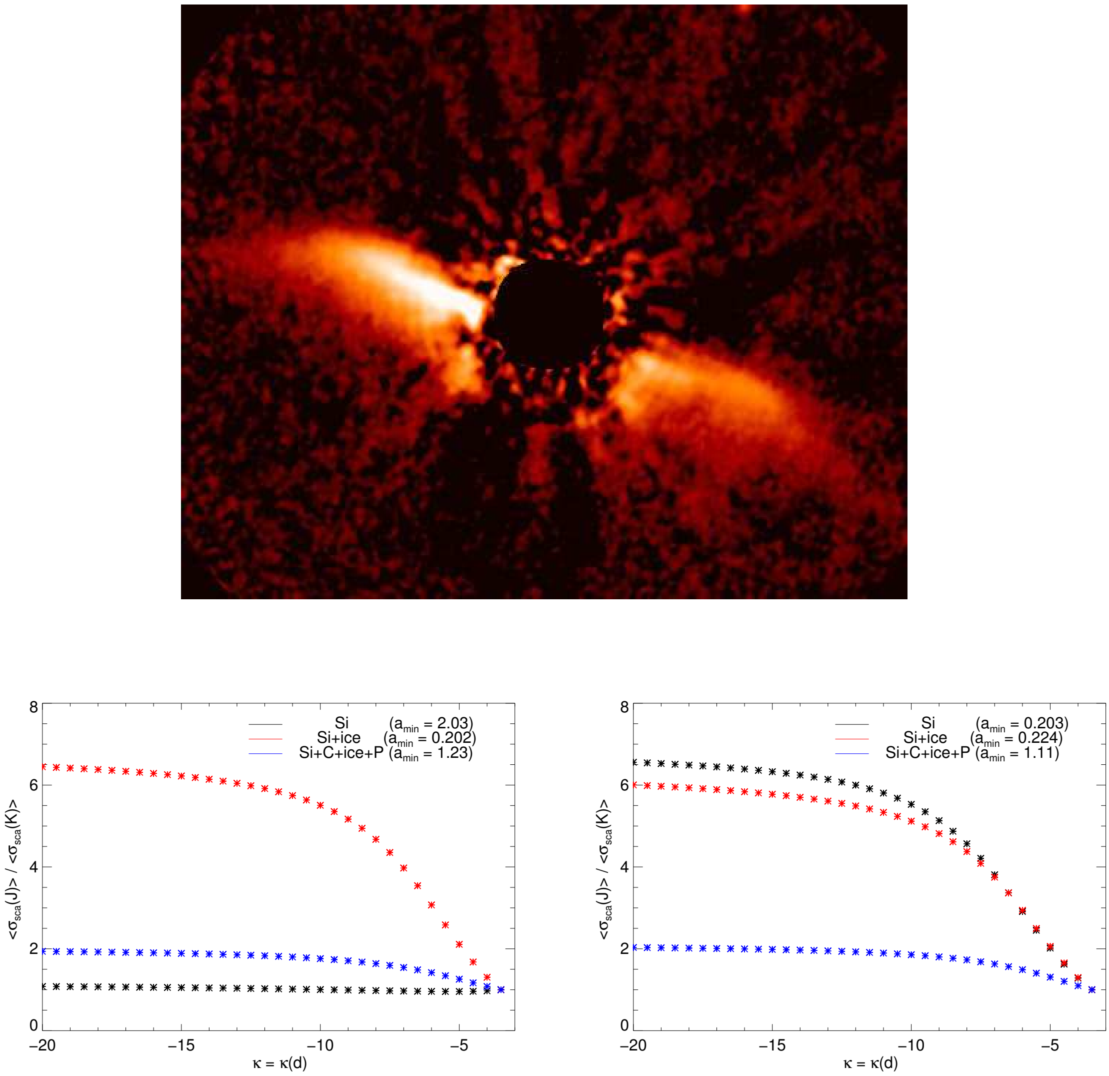

FIGURE 6.2: **En haut** : Le disque de HD 61005 imagé en bande K par le VLT/NaCo et traité avec l'algorithme LOCI corrigé des effets de l'auto-soustraction (E. Buenzli).
En bas : Modèles préliminaires du disque de poussière obtenus avec GRaTer : rapports de sections efficaces théoriques $\sigma_{\rm sca}$ en bandes J et Ks, en fonction de l'indice κ de la loi de puissance de la distribution de taille, prise comme un traceur de la distance à l'étoile (et normalisés de sorte que $\sigma_{\rm sca}(\kappa = -3.5) = 1$). Un plus grand rapport indique des couleurs plus bleues (dans l'anneau parent). J'ai considéré plusieurs compositions (silicates astronomiques purs, 50% silicates + 50% glaces, mélange matériaux carbonés (12%), silicates (23%), glaces (65%) et porosité ($\mathcal{P} = 0.65$)), et une valeur de $a_{\rm min}$ égale soit à la valeur issue du meilleur ajustement de la SED en infrarouge thermique (**à gauche**), soit à la taille d'éjection (**à droite**).

6.2 Vers des études dynamiques et collisionnelles

6.2.1 Les régions internes de β Pictoris et sa dynamique

La dynamique des disques de débris peut être abordée en première instance à l'aide de simulateurs N-corps. Pendant ma dernière année de thèse, j'ai acquis de l'expérience avec l'intégrateur symplectique SWIFT/RMVS (Wisdom & Holman 1991; Levison & Duncan 1994) adapté aux systèmes hiérarchiques par Beust (2003). Appliquée au disque de β Pictoris une telle approche promet de mieux déterminer la structure du disque de corps-parents à partir d'observations de la distribution de poussière (voir Annexe C). Cette dernière est contrainte par de multiples observations, depuis des échelles de plusieurs centaines d'UA jusqu'aux régions internes du disque, à l'intérieur de l'orbite de la planète. Les paramètres orbitaux de la planète sont de mieux en mieux connus grace à l'ajustement de modèle orbitaux aux images directes fournies par NaCo ($e \leq 0.17$, $A = 8 - 9$ AU – 17-21 ans, $i = 88.5 \pm 1.7°$, Chauvin et al. 2012; Lagrange et al. 2012a) et aux données de vitesses radiales ($M < 10 - 12 M_{\oplus}$, Lagrange et al. 2012b). β Pictoris b se révèle alignée avec le disque interne déformé plutôt qu'avec le disque externe, suggérant que c'est bien la planète qui perturbe les planétésimaux.

J'ai supposé pour β pic b une masse de $9\,M_{\text{jupiter}}$, un demi-grand axe de 9 AU, une inclinaison de 3° (pour tenir compte de l'inclinaison du système par rapport à la ligne de visée) et une excentricité nulle (pour cette étape préliminaire — l'ajustement indiquant une solution possible pour une excentricité de 0.17). J'ai réalisé des simulations préliminaires de l'interaction disque-planète avec pour objectif d'étudier l'impact de la déformation (gauchissement) due à la planète sur les régions les plus internes du Système, jusqu'à sa zone habitable, et son impact sur les observables. La Figure 6.3 donne le résultat de l'évolution d'un disque de corps-parents après 12 million d'années. Les coupes verticales du disque montrent que la planète produit une déformation bien au-delà de son orbite, sur des échelles de temps séculaires, et permettent de confirmer que le "warp" se propage avec un taux dépendant uniquement du produit de la masse de la planète par le carré de sa distance orbitale (Annexe C).

Le mécanisme est bien illustré par les diagrammes demi-grand axe - excentricité, et demi-grand axe - nœud ascendant : ils montrent que l'effet est dû à la précession des orbites des particules et est limité en demi-grand axe par les temps dynamiques. En vue de face, le phénomène se traduit par une structure spirale, qui se préserve pendant au moins 20 millions d'années. Par ailleurs, on peut simuler artificiellement la dynamique instantanée de grains de poussières affectés par la pression de radiation en corrigeant la masse de l'étoile avec le rapport β dépendant de la taille, comme illustré en Figure 6.3 pour $\beta = 0.1$ et $\beta = 0.5$. On voit que, bien que ces grains ne suivent pas exactement les corps-parents, ils portent également la structure imposée par β Pic b. Cette approche permet par suite de simuler des disques de poussières incluant des distributions de tailles et des propriétés optiques, en ignorant les collisions.

De nouveaux outils sont à présent disponibles pour coupler les résultats de simulation N-corps à GRaTer afin d'y injecter des lois d'émissivités. Je prévois ainsi de générer de véritables images synthétiques que je comparerai aux données observationnelles, notamment les données interférométriques PIONIER (Section 4.4.2), complétées par des observations proche-infrarouge MIDI (Di Folco et al., en préparation). Il sera ainsi possible de démêler le rôle de la diffusion par le disque froid de celui du disque chaud, dans la continuité de l'étude présentée en Section 4.4.2, et notamment de réexplorer l'hypothèse des FEB dans le contexte des exozodis. L'étude de la structure à de multiples échelles permettra aussi de considérer l'existence de planètes supplémentaires, susceptible de sculpter le disque et d'expliquer l'assymétrie à grande échelle observée.

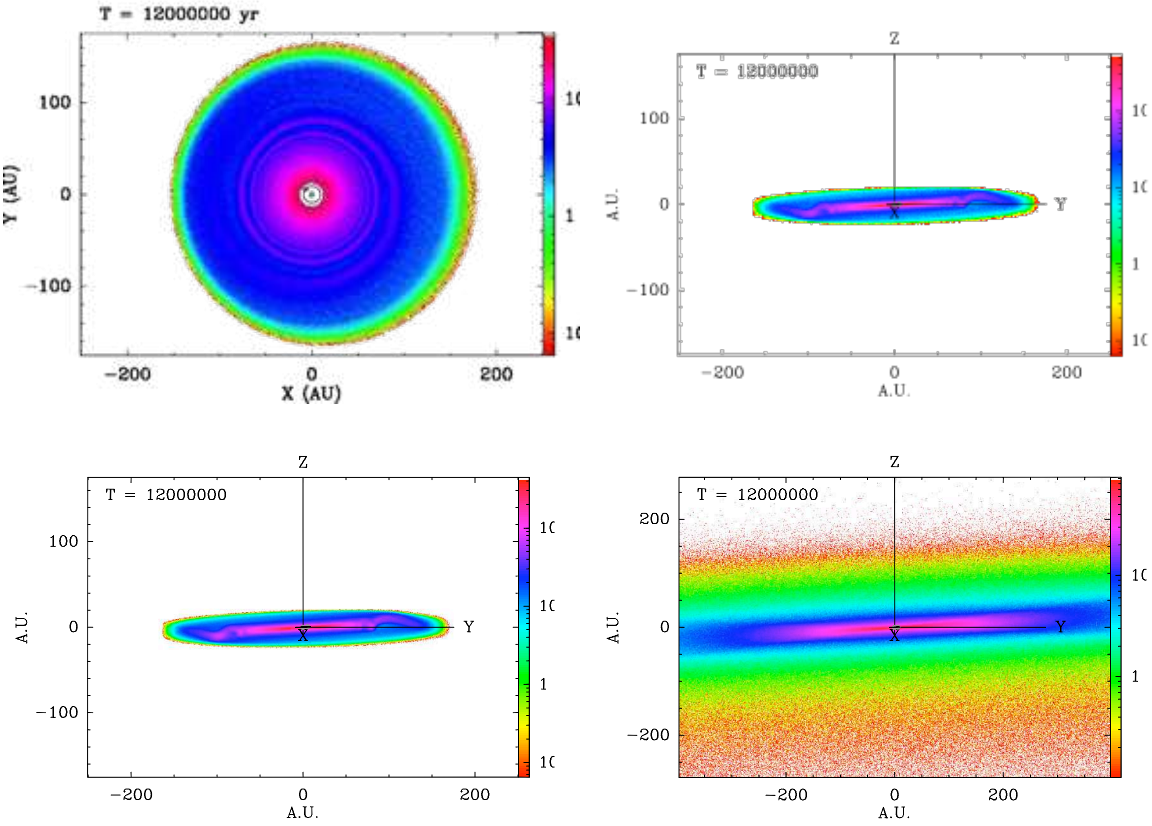

FIGURE 6.3: Simulation dynamique du système disque-planète de β Pictoris réalisée avec l'intégrateur symplectique SWIFT/RMVS : résultat de l'évolution d'un disque de 150,000 particules-test après 12 millions d'années sous l'influence d'une planète de $9M_{\mathrm{Jup}}$ à 9 AU inclinée de 3°. **En haut** : Le disque de planétésimaux et sa déformation interne (warp) vus de face (**à gauche**) et par la tranche (**à droite**). **En bas** : Vu par la tranche, le disque de poussières (liées) affectées par la pression de radiation, à gauche : $\beta = 0.1$, à droite : $\beta = 0.5$ (unités arbitraires).

6.2.2 Le potentiel d'ALMA : exemple de HD 141569A

La transition entre les étoiles pré-séquence principale et la Séquence Principale étant rapide, très peu de disques optiquement minces contenant du gaz ont été découverts. Lorsque c'est le cas, on considère préférentiellement le gaz comme de seconde génération, c'est-à-dire qu'il est produit lors de collisions ou par la sublimation, comme nous l'avons vu à plusieurs reprises au cours de cette thèse. Les *disques de transition* sont des objets particulièrement intéressants puisqu'ils sont susceptibles de présenter des structures dynamiques considérables. Celui qui entoure HD 141569A en représente un prototype rare. Ainsi que je l'explique dans le paragraphe suivant, il représente une cible de choix pour ALMA qui permettra d'étudier la dynamique disque(s)-compagnon(s), en présence de gaz. La structure du disque de poussières et la détection de gaz font de HD 141569A un cas tout à fait unique pour l'étude de la formation des planètes et des processus de dissipation.

Situé à 99 ± 10 pc, HD 141569A est un jeune (5 ± 3 Ma) système triple, composé d'une primaire B9.5 et de deux naines M. Classée comme une étoile Herbig Be, HD 141569A est entourée d'un disque circumprimaire optiquement fin, l'un des rares à avoi été résolu en lumière visible et dans l'infrarouge-proche (Mouillet et al. 2001; Augereau et al. 1999, Figure 6.4). Il harbore d'importantes structures : le disque est dominé par deux anneaux principaux piquant à 200 et 325 UA, séparés par une région vide, et leurs centres est décalé par rapport à l'étoile de 20 et 50 UA respectivement. L'anneau extérieur montre une structure en spirale qui est également détectée sous la forme d'un bras sur plus de 600 UA dans le Nord-Est du disque, tandis qu'un autre bras est suggéré, dans la direction des compagnons. En dépit de sa classification en tant que disque de débris, il contient encore d'importantes quantités de gaz comme en témoignent les détections de raies de CO dans le proche infrarouge et le sub-millimétrique (Ardila et al. 2005; Dent et al. 2005) et de raies de [OI] et [CII] par Herschel/PACS (Meeus et al. 2012). Le double-pic mesuré en ^{12}CO 3-2 suggère un systèmes de 2 anneaux à 90 et 250 UA, et possiblement une asymétrie intrinsèque dans la distribution de la densité de gaz en surface.

Les structures radiales, azimuthales et en forme d'arcs indiquent que le disque est gravitationnellement perturbé. La structure spirale serrée est compatible avec l'idée que le disque est déformé par les deux compagnons, moyennant qu'ils soient sur des orbites de forte excentricité (Augereau & Papaloizou 2004), bien que d'autres études par Ardila et al. (2005) et Reche et al. (2009) suggèrent plutôt un "flyby" récent. Plusieurs structures demeurent inexpliquées et sont soupçonnées être causées par un ou plusieurs compagnons planétaires. Reche et al. (2009) constatent que la morphologie du disque est bien expliquée par un "flyby" stellaire combiné à l'effet gravitationnel à long terme d'une planète d'une masse de Jupiter en orbite excentrique. Wyatt (2005a) propose un scénario alternatif dans lequel une planète de 3 masses de Jupiter en orbite à 235 UA avec une excentricité modérée produirait deux spirales. La forme particulière du disque de HD 141569A et plus généralement la forme uni- ou multi-annulaire souvent inférée pour les disques de débris proches pourrait trouver une explication dans des processus hydrodynamiques régissant l'interaction entre le gaz et la poussière. Takeuchi & Artymowicz (2001) et Klahr & Lin (2005) par exemple proposent que le couplage dynamique gaz-poussières en présence de pression de radiation peut générer un anneau ou une distribution bimodale de la poussière semblable à celle produite par une planète. En raison de son jeune âge et de la grande quantité de gaz, HD 141569A représente un banc d'essai idéal pour ce scénario. Il est pour cela crucial de mieux contraindre la composante gazeuse du disque.

Des résultats prometteurs ont été obtenus en 2001 avec l'interféromètre du Plateau de Bure dans la raie CO 2-1 par J.C. Augereau et al. La Figure 6.4 montre la superposition d'une image moyen-infrarouge du disque de poussières avec des cartes du champ de vitesses du gaz moléculaire. Ces dernières s'avèrent en accord avec la géométrie du disque de poussières, mais une assymétrie entre la composante décalée vers le bleu et la composante décalée vers le rouge est suggérée, à l'instar de celle détectée dans le spectre en CO 3-2 — il nous foudra la confirmer avec des données de plus grande sensibilité.

J'ai estimé les spécifications requises par ALMA pour cartographier la raie de ^{12}CO 2-1 (bande 6 d'ALMA, *i.e.* 230.538 GHz ou 1300 μm) en imagerie Doppler, de mesurer son champ de vitesses dans les bras spiraux et dans les régions internes permettant ainsi d'étudier l'interaction entre le gaz et la poussière dans un disque susceptible de former des planètes, et de contraindre l'évolution chimique du système. ALMA permet de mesurer simultanément le continuum émis par les poussières pour obtenir une image profonde des deux anneaux et de leur possible contrepartie interne, tout en détectant les bras spiraux jusqu'à $\sim$ 600 AU afin de contraindre la dynamique des corps-parents et d'identifier les traces de compagnons.

L'étendue spatiale de la poussière, moins de $\sim 4''$ de rayon, est tout à fait appropriée pour les observations ALMA et ne nécessite qu'un seul pointage avec une base maximale de 558.2 mètres. ALMA offre la possibilité d'observer plusieurs lignes et un continuum simultanément. J'ai utilisé l'*Observing Tool Sensitivity Calculator* pour estimer les sensibilités discutées ci-après. Une résolution spectrale de 0.079 km/s (61 kHz) est suffisante pour résoudre les motifs de rotation des deux anneaux dans la bande correspondante au CO 2-1, et il est possible d'ajuster la résolution des autres bandes pour assurer la détection d'isotopologues (C^{18}O et ^{13}CO) tout en maximisant le continuum. À partir des données PdBI, une détection à 15-σ du principal motif de rotation est prédite après un temps d'observation total de 3,85 heures (2,4 heures sur la source). La profondeur du pic secondaire (vitesse Képlerienne inférieure) devrait être détectée au moins à 4 σ et résolue spectralement. Il sera ainsi possible de produire des cartes assez détaillées pour détecter les sous-structures dans le champ de vitesses du gaz, semblable à la figure 6.4, mais avec une résolution spatiale $\sim$ 3 fois meilleure et $\sim$ 12 fois plus de sensibilité. Dans le continuum, l'image sera suffisamment contrastées pour distinguer entre les régions de forte et de faible densité, ainsi que l'espacement de $\sim$ 80 UA séparant les deux anneaux, et le décalage du disque par rapport à l'étoile centrale (détectée à $\sim 2\sigma$).

À partir de ces données, il sera possible d'étudier la dynamique de HD 141569 via des simulations N-corps — avec une connaissance précise de la structure des corps parents. Alternativement, on pourra utiliser un code hydrodynamique pour étudier l'interaction poussière-gaz. Grace à ProDiMo (voir Sec. 3.1) et à partir de la mesure des raies de CO, de OI et de CII, il sera possible d'étudier le contenu du disque de gaz, un problème en grande partie dégénéré qui nécessite des connaissances sur les propriétés de la poussière. Ainsi, les performances sans précédents d'ALMA permettront bientôt de combler l'écart entre les simulations de systèmes planétaires et leur observation.

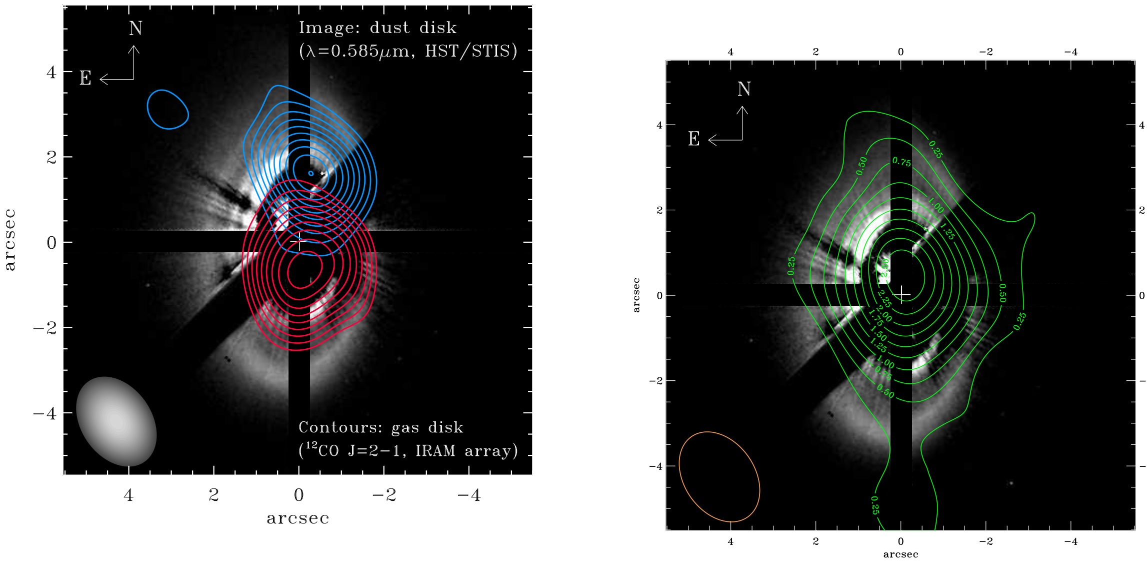

FIGURE 6.4: **Gauche :** Carte de l'émission en ^{12}CO 2-1 de HD 141569 obtenue avec l'interféromètre du Plateau de Bure superposée à une image coronagraphique HST/STIS. Les contours bleus et rouges représentent V_{helio} = -5.27 et -10.10 km/s, respectivement. **Droite :** Carte de contour de l'intensité intégrée en CO 2-1 superposée à l'image STIS. 1$''$ correspond à 100 UA.

6.2.3 La nécessité de codes dynamiques collisionnels

Au delà de ces projets de recherche à court terme, l'étude et en particulier la modélisation des disques de débris devra faire appel à des perspectives plus vastes. Les intégrateurs N-corps tels que SWIFT permettent aujourd'hui d'étudier l'évolution de systèmes planétaires sur des échelles de temps suffisamment longues moyennant des temp de calculs abordables. Ils sont très précis et performants lorsqu'il s'agit de simuler la dynamique de planètes et de planétésimaux, par exemple dans le cas du Système Solaire, mais trouvent leur limite lorsqu'ils doivent être comparés aux observations de disques de poussières. En effet ceux-ci sont non seulement soumis à leur dynamique spécifique, mais leur profil est aussi fortement dépendant des processus collisionnels à l'œuvre. Ces derniers peuvent être abordés séparément par des approches de type *particle-in-a-box* pour résoudre leur évolution collisionnelle, en particulier les tailles de grains. A moyen terme, on peut escompter que de nouveaux codes prenant en compte à la fois la dynamique et les collisions pourront être utilisés de manière courante. Différentes approches complémentaires sont actuellement en développement.

Je citerai tout d'abord le nouveau code statistique de R. van Lieshout et al., qui utilise l'approche cinétique du groupe de Jena (A. Krivov, T. Löhne) et permet de suivre la distribution de particules dans l'espace des orbites et des masses sous l'effet simultané des collisions, de la dynamique et de la sublimation. Il se limite cependant à de la symmétrie sphérique et ne permet pas d'étudier l'impact de planètes. Des approches comme celle mise en œuvre par le code CGA de Stark & Kuchner (2008) et le code DyCoSS de Thebault et al. (2012) permettent de simuler des disques de poussière et les structures engendrées par un perturbateur, mais elles se limitent à un régime d'équilibre et traitent grossièrement les collisions.

Des codes de nouvelle génération permettront bientôt d'aborder le problème dans toute sa complexité, ce qui nécessite des solutions pour suivre dynamiquement les innombrables fragments produits à l'issue de chaque collision. Le code LIDT-3D (Charnoz & Taillifet 2012), hérité de modèles de disques circumplanétaires, résout astucieusement cette difficulté pour gérer à la fois la dynamique et les collisions. Son adaptation à la physique des disques de débris promet d'adresser dans un futur proche des problèmes physiques complexes, comme la diffusion dynamique par des planètes, les instabilités ou encore les impacts à haute vitesse (code LIDT-DD, Q. Kral et al., en préparation). Ces nouveaux modèles seront nécessaires pour interpréter les futures observations de disques et d'exoplanètes et révêler leur connexion.

6.3 Vers des systèmes planétaires semblables au Système Solaire

6.3.1 L'impact des disques de débris sur la compréhension du Système Solaire et de son histoire

En remontant plus loin vers le sommet de la cascade collisionnelle, nous devenons capables d'observer l'activité dynamique et collisionnelle des systèmes planétaires à sa source. Comme nous l'avons vu dans le cas de HD 181327, les systèmes planétaires jeunes sont potentiellement sujets à un intense bombardement cométaire dans leurs régions internes. Ce peut être l'indication que la formation des planètes rocheuses est toujours en cours, ce qui est possible pendant les 100 premiers millions d'années. Ainsi il faut garder à l'esprit que la formation de la Lune des suites de la collision d'une planète de la taille de Mars avec la proto-Terre, n'a eu lieu que 42 millions d'années après l'effondrement initial du nuage de gaz qui a donné naissance au Soleil (Canup & Asphaug 2001; Stevenson 1987). Au delà de quelques 20 à 100 millions d'années comme dans le cas de Fomalhaut, il faut voir les disques massifs que nous observons comme la preuve d'une intense activité dynamique, éventuellement comparable au Grand Bombardement Tardif du Système Solaire.

En sus, les disques de débris doivent être considérés du point de vue de l'Exobiologie. L'émergence de la vie probablement survenue aux débuts du Précambrien (-3.8 Ga) n'a été rendue possible qu'à la suite du Grand Bombardement Tardif. Antérieurement à cet épisode d'intense bombardement astéroidal vers les planètes internes, la croute terrestre ne pouvait définitivement se solidifier du fait des impacts destructeurs, ceux-la même qui ont en retour permis la formation de l'atmosphère et des océans par leur apport en composés volatils. Les suites de cette évênement marquent le début de l'Archéen, ère géologique qui est aussi celle de l'apparition de la vie sur Terre. On pense que l'assemblage de molécules organiques complexes, peut-être issues de molécules prébiotiques apportées par les comètes (*e.g.* Taquet et al. 2011), a débouché sur les premiers systèmes vivants dans les profondeurs des océans. Au cours des temps géologiques, la biosphère a subi plusieurs crises majeures : la plus récente est la crise d'extinction Crétacé-Paléocène pour laquelle on met en cause principalement l'effet d'une collision destructrice avec un astéroide. Le

LHB a dépeuplé les réservoirs d'astéroides et de comètes, avec pour conséquence de limiter de tels impacts destructeurs pour le restant de l'histoire de la Terre. Paradoxalement, ces catastrophes ont d'un point de vue évolutionniste l'effet de faire exploser la biodiversité en encourageant la course vers la complexité. Il conviendrait donc de considérer les disques de débris comme un critère d'habitabilité, encore insuffisamment délimité à l'heure actuelle.

6.3.2 Futurs progrès observationnels

Nous l'avons vu au cours des deux derniers chapitres, l'interférométrie optique permet d'accéder aux régions les plus internes des systèmes planétaires. Les programmes d'observations menés actuellement avec PIONIER et FLUOR permettront à terme de recenser la présence de poussières chaudes dans l'environnement des étoiles proches jusqu'à une sensibilité de 0.5%. Néanmoins ces exozodis, souvent situés proches de la limite de sublimation des grains, demeurent bien différents du Nuage Zodiacal ou encore de la Ceinture d'Astéroïdes. Le seul instrument prévu à court terme qui permettra d'explorer les exozodis dans la zone habitable des étoiles proches est le LBTI, un imageur en infrarouge thermique (bandes L, M, N) et interféromètre annulant composé de deux miroirs de 8.4 mètres. Il permettra d'atteindre un niveau de 10 fois le disque Zodiacal pour des poussières à 300 K.

Du côté de l'imagerie, c'est bientôt vers les nouveaux intruments SPHERE et GPI, exploitant des optiques adaptatives extrêmes dans le proche-infrarouge, qu'il faudra compter. Ils permettront tous deux l'imagerie différentielle de disques et de planètes, mais aussi des observations spectroscopiques et de la polarimétrie (qui apportent des contraintes supplémentaires fortes sur les grains) à haute dynamique. A plus long terme, le JWST et l'E-ELT devriendront les successeurs respectifs du HST et du VLT. Avec son miroir segmenté de 6.5 mètres de diamètre, le JWST sera équipé de plusieurs instruments : un imageur proche-infrarouge (NIRCam), un spectrographe proche infrarouge multi-objet (NIRSpec), un spectro-imageur fonctionnant dans l'infrarouge moyen (5-27 μm, MIRI). L'E-ELT et ses 39 mètres de diamètre, bénéficiant d'une optique adaptative qui représente encore un défi, pourra presque rivaliser en résolution avec les interféromètres actuels. Les deux télescopes permettront d'imager l'environnement des étoiles proches, notamment leur zone habitable, avec un constraste inégalé.

Finalement, en quelques décennie la science des systèmes planétaires sera passée du stade de la découverte à celui de l'exploration détaillée. Le fossé qui sépare encore l'astrophysique observationnelle de la théorie commence à se combler et les progrès techniques nous rapprochent sans cesse de l'objectif ultime de découvrir un système jumeau du Système Solaire. On remarque d'ailleurs que, d'une part les simulations théoriques peuvent de plus en plus être confrontées directement à des observations — notamment les structures des disques, ou les planètes prédites — d'autre part les nouvelles techniques observationnelles doivent maintenant s'appuyer sur des modèles — par exemple pour éliminer les artefacts des images de disques ou tester la viabilité des planètes détectées. Face à l'immense diversité relevée pour les systèmes planétaires proches, le Système Solaire semble revêtir des charactéristiques assez exceptionnelles, mais seul le futur proche nous permettra d'établir sa place au sein de la multitude de réalisations de la formation planétaire qui nous est donnée à étudier.

Annexe A

Deep near-infrared interferometric search for low-mass companions around β Pictoris

Astronomy & Astrophysics manuscript no. betPic˙closure˙v5
August 31, 2010

Letter to the Editor

Deep near-infrared interferometric search for low-mass companions around β Pictoris[⋆]

O. Absil[1,⋆⋆], J.-B. Le Bouquin[2], J. Lebreton[2], J.-C. Augereau[2], M. Benisty[3], G. Chauvin[2], C. Hanot[1], A. Mérand[4], and G. Montagnier[4]

[1] Institut d'Astrophysique et de Géophysique, Université de Liège, 17 Allée du Six Août, B-4000 Liège, Belgium
[2] LAOG–UMR 5571, CNRS and Université Joseph Fourier, BP 53, F-38041 Grenoble, France
[3] INAF - Osservatorio Astrofisico di Arcetri, Largo E. Fermi 5, 50125 Firenze, Italy
[4] European Southern Observatory, Casilla 19001, Santiago 19, Chile

Received 4 June 2010; accepted XXX

ABSTRACT

Aims. We aim at searching for low-mass companions in the innermost region (< 300 mas, i.e., 6 AU) of the β Pic planetary system.
Methods. We obtained interferometric closure phase measurements in the K band with the VLTI/AMBER instrument used in its medium spectral resolution mode. Fringe stabilization was provided by the FINITO fringe tracker.
Results. In a search region between 2 and 60 mas, our observations rule out at 3σ the presence of companions with K-band contrasts larger than 5×10^{-3} for 90% of the possible positions in the search zone (i.e., 90% completeness). The median 1σ error bar on the contrast of potential companions within our search region actually amounts to 1.2×10^{-3}. The best fit to our data set using a binary model is found for a faint companion located at about 14.4 mas from β Pic, with a contrast of $1.8\times10^{-3} \pm 1.1\times10^{-3}$ (a result consistent with the absence of companions). For angular separations larger than 60 mas, the effect of time smearing and field-of-view limitations reduce the sensitivity.
Conclusions. We can exclude the presence of brown dwarfs with masses larger than 29 $M_{\rm Jup}$ (resp. 47 $M_{\rm Jup}$) at a 50% (resp. 90%) completeness level within the first few AUs around β Pic. Interferometric closure phases offer a promising way to directly image low-mass companions in the close environment of nearby young stars.

Key words. Stars: individual: β Pic – Planetary systems – Planets and satellites: detection – Techniques: interferometric

1. Introduction

The young (~ 12 Myr, Zuckerman et al. 2001), nearby (19.3 pc) and bright ($K = 3.5$) A5V-type star β Pictoris (HD 39060) is surrounded by one of the most famous extrasolar planetary systems, consisting of a recently detected planetary companion (Lagrange et al. 2009a, 2010) inside an optically thin debris disk seen edge-on (Smith & Terrile 1984), which has been resolved at various wavelengths. Several asymmetries have been identified in the debris disk, including a warp at ~ 50 AU (Heap et al. 2000) that is now understood to be the result of the dynamical influence of a massive body (a few Jupiter masses) on an eccentric orbit around the central star (Freistetter et al. 2007). The 9-$M_{\rm Jup}$ companion discovered by Lagrange et al. (2009a) could be at the origin of this warp. It must be noted that the planetary nature of this companion was not easy to ascertain (Lagrange et al. 2009b), due to the companion being at a projected distance smaller than the inner working angle of VLT/NACO (335 mas for 9 $M_{\rm Jup}$) between the discovery observations in 2003 and the confirmation observations in late 2009.

Long-baseline optical interferometry is a promising technique to search for faint companions at angular separations smaller than the diffraction limit of a single aperture. In particular, closure phase measurements on a closed triangle of baselines are very sensitive to asymmetries in the brightness distribution of the source, and can be used to detect faint companions. Closure phases have the further advantage to be insensitive to telescope-specific phase errors (unlike visibilities and phases), including atmospheric turbulence effects (for a review of closure phases, see Monnier 2003).

The interferometric detection of extrasolar planets (hot Jupiters in particular) has already been attempted by a few groups, in particular using precision closure phase measurements. Despite the exquisite accuracy that has already been reached (e.g., $0.^{\circ}1$ stability on the CHARA/MIRC closure phases, Zhao et al. 2008), no extrasolar planet has been detected so far. Differential phase techniques have not been more successful, due to atmospheric and instrumental limitations (e.g., Millour et al. 2008; Matter et al. 2010). Higher sensitivities to faint companions can be reached when closure phases are obtained on fully resolved stellar photospheres (e.g. Lacour et al. 2008; Duvert et al. 2010), but this is unfortunately not the case for most main sequence stars with currently available interferometric baselines. In this Letter, we perform a deep interferometric search for faint companions at short angular distances from the unresolved young main sequence star β Pic ($\theta_{\rm LD} = 0.85 \pm 0.12$ mas, Di Folco et al. 2004), based on closure phase measurements with VLTI/AMBER.

2. Observations and data reduction

Observations of β Pic have been obtained on four different nights from January 24th to 28th 2010 with the AMBER instrument,

---

[⋆] Based on observations collected at the ESO La Silla Paranal Observatory under program IDs 084.C-0566 and 384.C-0806.

[⋆⋆] FNRS Postdoctoral Researcher, email: `absil@astro.ulg.ac.be` used in its medium resolution mode ($R \simeq 1500$ from 1.93 to 2.27 μm) with three 1.8-m Auxiliary Telescopes of the VLTI arranged on the A0-G1-K0 triangle (ground baselines from 90 m to 128 m). Fringe tracking was provided by the FINITO facility during all our observations. A total of 12 Observing Blocks (OBs) have been obtained on β Pic, with Detector Integration Times (DIT) ranging from 0.5 to 1 sec depending on the atmospheric conditions. To reduce time smearing in our data set, long OBs have been split into shorter sequence of 15 min or less, giving a total of 26 OBs. Our observations of β Pic were interleaved with observations of HD 39640, a G8III calibration star of magnitude $K = 3.0$ and angular diameter $\theta_{\rm LD} = 1.235 \pm 0.015$ mas (Mérand et al. 2005), located at only 1°.2 from β Pic on sky.

Raw data have been reduced using the amdlib v3.0 package (Tatulli et al. 2007; Chelli et al. 2009), using all recorded detector frames (no fringe selection). The β Pic closure phases have been calibrated by a simple subtraction of the average closure phase of all calibrator measurements obtained during the same night with the same instrumental set-up. This implicitly assumes that the closure phase transfer function does not significantly vary on several hours of observations, an hypothesis that we have checked on our four observing nights. The error bar related to the calibration process is generally estimated by measuring the standard deviation of the calibrator closure phases during the night. In our case, too few calibrator measurements are available to provide a reliable error bar, so that we have decided to use the standard deviation of all measurements (science and calibrator) instead. It must be noted that, in case the scientific target had a companion producing a significant closure phase signal, this would lead to an overestimated calibration error bar and could possibly hide the presence of the companion (this issue is addressed in the last paragraph of Section 3.1). The evaluation of the calibration error bar is illustrated in Fig. 1 for the night of January 24th, which is actually the poorest night in our data set in terms of transfer function stability. In this plot, the data have been binned into 6 spectral channels to reduce their statistical errors and isolate the effect of transfer function instabilities. The short end of the K band (top panel of Fig. 1) shows significant instabilities in its closure phases, most probably due to strong and variable spectral lines in the Earth atmosphere. These instabilities disappear beyond about 2.0 μm, so that we restrict our spectral range to the 2.00–2.26 μm region. In this spectral range, we evaluate that the RMS calibration errors range between 0°.20 and 0°.37 depending on the night. These error bars will be added quadratically on our whole data set, night by night (after binning individual spectral channels, where required).

3. Searching for faint off-axis companions

3.1. Data analysis

The field-of-view (FOV) of the AMBER instrument is limited by the use of single-mode fibers. We have estimated the off-axis transmission of a point-like object in presence of atmospheric turbulence corrected for tip-tilt fluctuations by the STRAP system on the ATs. Our simulations result in a Gaussian transmission with a full width at half maximum of 420 mas for the median seeing of our observations ($\sim$ 0″.8). For angular distances larger than 210 mas, the transmission quickly drops to low values and we limit our analysis to separations smaller than about 300 mas, where the transmission drops by a factor 4. This corresponds to a linear distance of $\sim$ 6 AU from β Pic. Let us note however that, due to the Earth rotation, closure phases are variable in time. In order not to smear the closure phase signal too much during our $\sim$15 min OBs, we actually need to restrict our search region to a FOV radius of about 50 mas. A better time sampling would be needed to explore the full 300 mas FOV at the highest sensitivity.

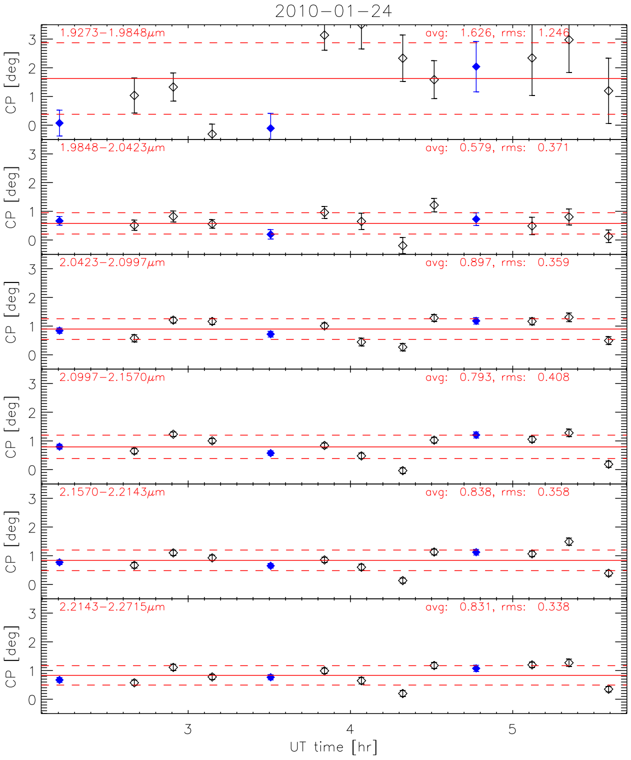

Fig. 1. Fluctuation of the closure phase as a function of time for β Pic (black empty diamonds) and its calibrator (blue filled diamonds) during the night of January 24th. Data have been binned into 6 spectral channels to reduce statistical errors. The solid lines represent the mean of the CP transfer functions and the dashed lines their standard deviations.

The first step in our data analysis is to adapt the spectral resolution to the explored FOV, by making sure that the variations of the closure phase as a function of wavelength, created by a potential companion, are sampled with at least four data points per period. The periodicity in the closure phase signal as a function of wavelength is roughly given by $P_\lambda = \lambda^2/(B\theta - \lambda)$, with B the mean interferometric baseline length. With $B \simeq 100$ m in our case, and for a maximum angular separation of 50 mas, this gives $P_\lambda \simeq 0.2$ μm. The appropriate spectral bin size to cover a 50 mas FOV is thus $\Delta\lambda = P_\lambda/4 = 50$ nm, so that a total of 5 spectral channels are needed across the 2.00 – 2.26 μm spectral range. We use a 5-sigma clipping method to remove outliers when binning our data into the synthetic spectral channels, and statistical error bars are estimated through the standard deviation of individual data points in each bin.

The next step is to search the entire FOV for the possible presence of companions. To do this, we use the photospheric model of β Pic proposed by Di Folco et al. (2004), to which we add a secondary point-like companion at various locations within the FOV. The χ^2 distance between the data and all our binary models is then computed, and for each position we select the companion contrast that produces the lowest χ^2. The resulting χ^2 map can then be converted into a probability map (Fig. 2) using the χ^2 probability distribution function, taking into account the number of degrees of freedom in our χ^2 distribution. In the present case, there are 26×5 independent data points and 1 parameter to fit (the companion contrast for each bi-

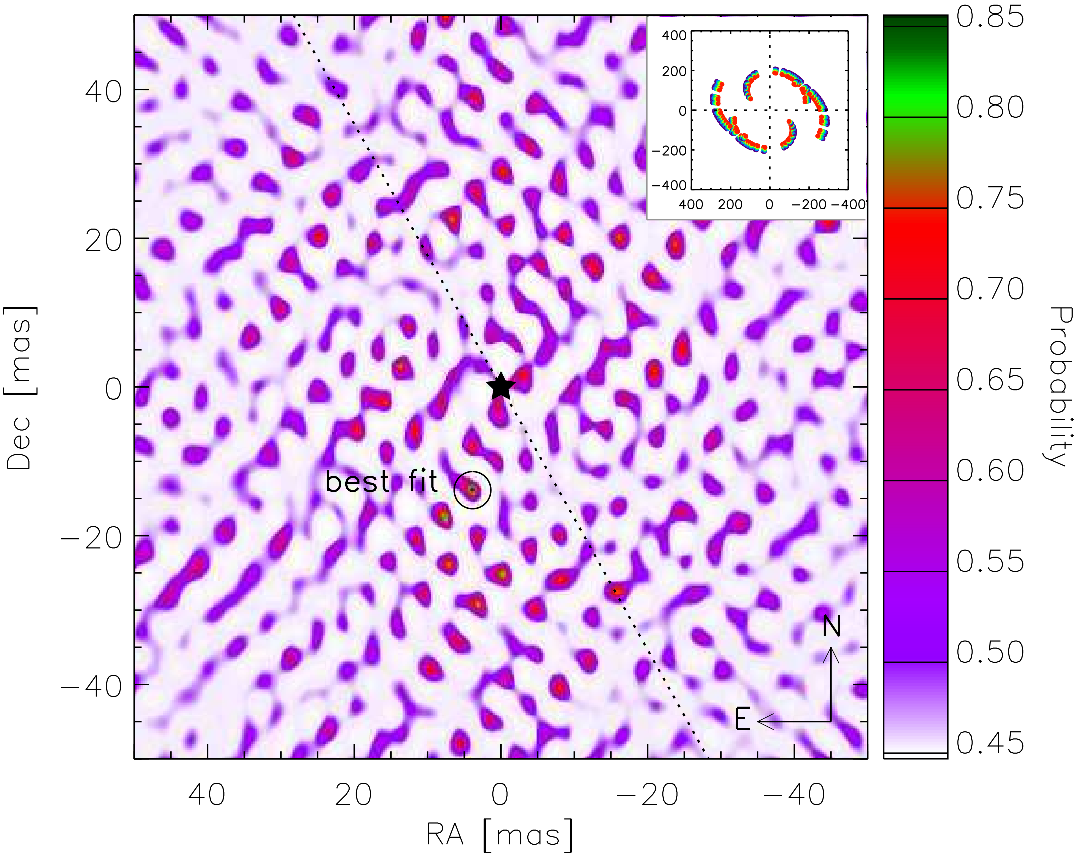

Fig. 2. Probability for a binary model to reproduce our data set, for various positions of the secondary companion on a FOV 50 mas in radius. At all places of the FOV, the flux of the companion has been tuned to minimize the χ_r^2. The zones in white have their minimum χ_r^2 for a companion of zero flux. The position of β Pic is represented by a star, and the orientation of the circumstellar disk midplane (PA = 29$.\!\!^\circ$5, Boccaletti et al. 2009) by a black dotted line. The u, v coverage of our data set is represented in the upper right inset, including wavelength dependence (using colors from blue to red), with the axes graduated in cycles per arcsec.

nary position), hence 129 degrees of freedom. In the absence of companion, the reduced chi square (χ_r^2) amounts to 1.01, which corresponds to a probability of 45% for our photospheric model alone to reproduce the data set.

Our probability map shows a local maximum of 86% (i.e., $\chi_r^2 = 0.87$) at a position (ΔRA, ΔDec) = (3.9, −13.9) mas, with a best-fit contrast of 1.8×10^{-3}. The quality of our best-fit model, illustrated in Fig. 3, confirms that this model reproduces nicely our data set. Several other companion positions within our FOV would provide (almost) equally good fits. We note however that the pure photospheric model also reproduces the data quite well, so that there is no real evidence for the presence of a companion. Let us check whether this could not be due to an overestimation of the calibration error bars, as discussed in Section 2. For that, we artificially decrease our estimated calibration error bars until $\chi_r^2 = 1$ for our best fit model (which is reached when calibration error bars are multiplied by 0.92). The significance of this possible detection can then be estimated by converting the probability of the null hypothesis (i.e., no companion), which is now of only 9%, into an equivalent number of sigmas on the possible detection of a companion, using standard relationships for normal distributions. We infer a 1.7σ significance for our detection, giving a companion contrast of $1.8 \times 10^{-3} \pm 1.1 \times 10^{-3}$. This low significance confirms that it cannot be considered as a real detection.

3.2. Sensitivity limits

Sensitivity limits can be derived from our χ_r^2 map (or equivalently, probability map), by looking on each point of the FOV for the companion contrast that would produce a χ_r^2 larger than a pre-defined threshold. We choose a 3σ criterion to define our sensitivity limit (i.e., probability of less than 0.27% for the model to reproduce the data). With 129 degrees of freedom, this corresponds to a threshold $\chi^2_{r,\mathrm{lim}} = 1.38$. Once the 3σ upper limit on the detectable companion contrast is computed on each point of the FOV, one can define global sensitivity limits by building and inspecting the histogram of the 3σ detection levels on the considered FOV. For instance, for the 50 mas FOV used in Fig. 2, the contrast upper limit is $< 3.6 \times 10^{-3}$ for 50% of all positions in the FOV (*50% completeness*) and $< 4.8 \times 10^{-3}$ for 90% completeness. This confirms that the typical 1σ error bar on the contrast of a detected companion would be about 1.2×10^{-3}, as estimated in the previous paragraph.

These sensitivity limits have been confirmed by a double-blind test, where synthetic companions of various contrasts have been introduced into our raw data set. In these blind tests, we have been able to retrieve the companions with a contrast of 3.0×10^{-3} in about 50% of the cases (although with a formal significance generally between 2 and 3σ), and the companions with a contrast of 5.0×10^{-3} in all cases. These tests confirm the validity of our contrast upper limits based on the χ_r^2 analysis.

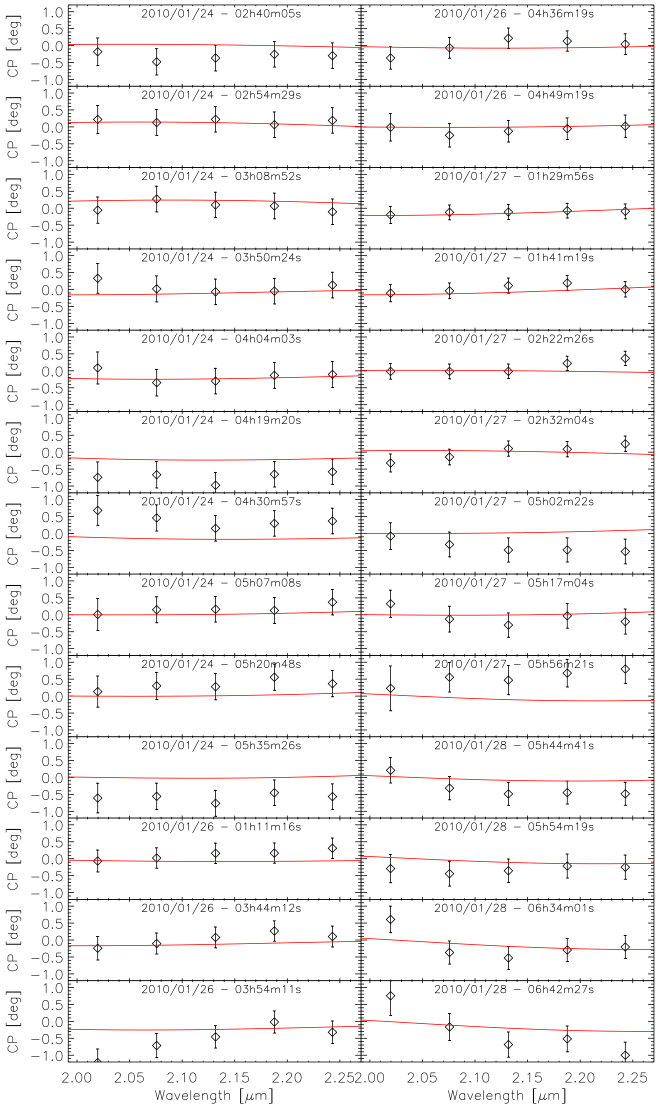

Fig. 3. Representation of the whole data set (diamonds with error bars, binned into 5 spectral channels) and of the best-fit model (red curves) found on the 50 mas radius FOV. This model corresponds to a companion with a contrast of 1.8×10^{-3} located at cartesian coordinates ΔRA = 3.9 mas and ΔDec = −13.9 mas relative to the central star.

Sensitivity limits can also be computed as a function of angular separation, by building χ_r^2 maps on annular fields-of-view of increasing size. This is what we have done in Fig. 4, where annuli 10% in relative width have been used. This figure shows that VLTI/AMBER reaches its optimum sensitivity in the 2–60 mas region, where a median contrast of 3.5×10^{-3} (resp. 5.0×10^{-3}) can be reached at 50% (resp. 90%) completeness level using the ATs. Beyond 60 mas, the effect of time smearing on the closure phase signal of potential companions becomes significant, which reduces the sensitivity. For larger separations (> 200 mas), the sensitivity degrades more rapidly due to the decreasing off-axis transmission of the single-mode fibers. The inner working angle of our interferometric study is about 1 mas, where the sensitivity drops to a few percent in contrast (e.g., 5×10^{-2} at 90% completeness) due to the limited angular resolution provided by our baselines.

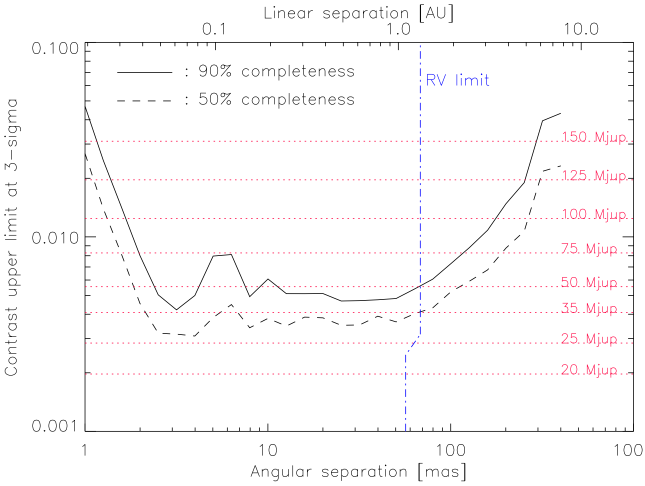

Fig. 4. Sensitivity curves showing the 3-sigma upper limit on the contrast of off-axis companions as a function of the angular separation for 50% and 90% completeness, computed on annular fields-of-view with 10% relative width. Equivalent masses have been computed using the COND model of Baraffe et al. (2003), for an age of 12 Myr. The upper limits on possible companion masses from radial velocity measurements (Galland et al. 2006) are shown for comparison.

4. Discussion

In order to compare our sensitivity limits with other studies, it is useful to express them in terms of companion masses. The first step is to convert contrasts into absolute magnitudes, taking into account the K magnitude and distance of β Pic. Absolute magnitudes are then converted into masses using the COND evolutionary models of Baraffe et al. (2003), assuming an age of 12 Myr. The result is illustrated in Fig. 4, where mass upper limits are represented by dotted lines. In the 2–60 mas region, the median upper limit on companions masses amounts to 29 $M_{\rm Jup}$ (resp. 47 $M_{\rm Jup}$) for 50% (resp. 90%) completeness.

These upper limits should be compared with two other types of studies, which have been used to survey nearby main sequence stars: radial velocity (RV) monitoring and direct (single-pupil) imaging. State-of-the-art RV measurements obtained with HARPS on β Pic (Galland et al. 2006) have reached an accuracy of 180 m s^{-1} (after correction for its pulsations), which provides a typical sensitivity of 10 $M_{\rm Jup}$ for a semi-major axis $a = 1$ AU. The sensitivity then scales as a^{-2}. The largest semi-major axis that can be reached depends on the time scale of the RV monitoring: in order to cover most of our interferometric search region (up to 6 AU in semi-major axis), β Pic should be surveyed for about 5 years. With such a time coverage, the only companions that could be detected by our interferometric search and not by the RV monitoring would be those located at orbital distances larger than 6 AU, which would by chance be at projected angular separations smaller than 300 mas at the time of our observations. Regarding direct imaging, K-band observations using a Four Quadrant Phase Mask (FQPM) coronagraph on VLT/NACO have yielded an upper limit $< 2.5 \times 10^{-4}$ for the contrast off-axis companions at projected distances > 335 mas (Lagrange et al. 2009b), and can reach a contrast of 1.3×10^{-2} at the FQPM inner working angle of 70 mas (Boccaletti et al. 2009). In practice, the NACO-FQPM sensitivity becomes better than that of AMBER for angular distances larger than ∼ 100 mas, so that the two techniques can be considered as very complementary.

Although our detection limits are promising, and would allow brown dwarfs to be detected around bright young stars such as β Pic, they are not yet sufficient to detect the planetary companion discovered by Lagrange et al. (2009a), which has an estimated K-band contrast of 2.5×10^{-4}. The accuracy of our measurements needs to be improved by at least a factor 10 to reach this level of performance. The same improvement in measurement accuracy would be required to bring our sensitivity down to the realm of hot-Jupiter type planets. It is expected that the next generation of interferometric instruments at the VLTI (PIONIER, GRAVITY and eventually VSI) could bring the needed improvements in instrumental stability and sensitivity to reach such performance.

Acknowledgements. The authors thank the anonymous referee for a thoughtful report that improved the data analysis. O.A. and C.H. acknowledge support from the "Communauté Française de Belgique – Actions de Recherche Concertées – Académie universitaire Wallonie-Europe". This research has made use of the AMBER data reduction package of the Jean-Marie Mariotti Center (`amdlib v3.0`, available at http://www.jmmc.fr/amberdrs).

References

Baraffe, I., Chabrier, G., Barman, T. S., Allard, F., & Hauschildt, P. H. 2003, A&A, 402, 701
Boccaletti, A., Augereau, J.-C., Baudoz, P., Pantin, E., & Lagrange, A.-M. 2009, A&A, 495, 523
Chelli, A., Utrera, O. H., & Duvert, G. 2009, A&A, 502, 705
Di Folco, E., Thévenin, F., Kervella, P., et al. 2004, A&A, 426, 601
Duvert, G., Chelli, A., Malbet, F., & Kern, P. 2010, A&A, 509, A66
Freistetter, F., Krivov, A. V., & Löhne, T. 2007, A&A, 466, 389
Galland, F., Lagrange, A., Udry, S., et al. 2006, A&A, 447, 355
Heap, S. R., Lindler, D. J., Lanz, T. M., et al. 2000, ApJ, 539, 435
Lacour, S., Meimon, S., Thiébaut, E., et al. 2008, A&A, 485, 561
Lagrange, A., Bonnefoy, M., Chauvin, G., et al. 2010, Science, 329, 57
Lagrange, A.-M., Gratadour, D., Chauvin, G., et al. 2009a, A&A, 493, L21
Lagrange, A.-M., Kasper, M., Boccaletti, A., et al. 2009b, A&A, 506, 927
Matter, A., Vannier, M., Morel, S., et al. 2010, A&A, 515, A69
Mérand, A., Bordé, P., & Coudé du Foresto, V. 2005, A&A, 433, 1155
Millour, F., Petrov, R. G., Vannier, M., & Kraus, S. 2008, in Proc. SPIE, Vol. 7013, Optical and Infrared Interferometry
Monnier, J. D. 2003, Reports on Progress in Physics, 66, 789
Smith, B. A. & Terrile, R. J. 1984, Science, 226, 1421
Tatulli, E., Millour, F., Chelli, A., et al. 2007, A&A, 464, 29
Zhao, M., Monnier, J. D., ten Brummelaar, T., Pedretti, E., & Thureau, N. D. 2008, in Proc. SPIE, Vol. 7013, Optical and Infrared Interferometry, 1K
Zuckerman, B., Song, I., Bessell, M. S., & Webb, R. A. 2001, ApJ, 562, L87

Annexe B

Complements to Chapter 5

B.1 Maximum mass flux under PR drag and collisions

Here I provide a proof to equation Eq. 5.28 that will appear in R. van Lieshout et al. 2013. The inward mass flux due to P-R drag, for a single particle size, as function of radial distance r, is given by

$$\dot{M}_{\mathrm{PR}}(r) = mn(r)|\dot{r}_{\mathrm{PR}}|, \tag{B.1}$$

where m is the mass of an individual dust grain, $n(r)$ is the one dimensional particle number density ($\mathrm{d}n/\mathrm{d}r$), and $\dot{r}_{\mathrm{PR}}$ is the P-R drag velocity, defined as the rate of semimajor axis change of a circular orbit.

Convert $n(r)$ to effective optical depth $\tau_{\mathrm{eff}}(r)$, using the approximation (e.g., Wyatt 1999)

$$\tau_{\mathrm{eff}}(r) = \frac{\sigma n(r)}{2\pi r}, \tag{B.2}$$

with $\sigma = \pi a^2$ is the cross-section of a single particle (a is the particle radius).

Fill in (Burns et al. 1979)

$$\dot{r}_{\mathrm{PR}} = -\frac{2GM_\star\beta}{cr}, \tag{B.3}$$

with

$$\beta = \frac{3L_\star}{16\pi GM_\star c}\frac{Q_{\mathrm{pr}}}{\rho_{\mathrm{d}}a}. \tag{B.4}$$

Here, G is the gravitational constant, $M_\star$ is the stellar mass, $L_\star$ is the stellar luminosity, Q_{pr} is the wavelength-averaged radiation pressure efficiency ($0 \leq Q_{\mathrm{pr}} \leq 2$), and ρ_{d} is the bulk density of the dust.

This gives

$$\dot{M}_{\mathrm{PR}}(r) = \frac{L_\star}{c^2}Q_{\mathrm{pr}}\tau_{\mathrm{eff}}(r). \tag{B.5}$$

Wyatt (2005) finds that the balance of P-R drag and collisional destruction leads to a radial dust distribution

$$\tau_{\mathrm{eff}}(r) = \frac{\tau_{\mathrm{eff}}(r_0)}{1 + 4\eta(r_0)(1-\sqrt{r/r_0})}, \tag{B.6}$$

where r_0 is the radial location of the dust producing parent belt, and η is the ratio between the P-R drag and collisional timescales

$$\eta(r) = \frac{t_{\rm PR}}{t_{\rm coll}} = \frac{c\tau_{\rm eff}(r)}{2\beta}\sqrt{\frac{r}{GM_\star}}. \tag{B.7}$$

In the limit of $\eta(r_0) \gg 1$ (i.e. a very dense parent belt), this leads to a maximum value for $\tau_{\rm eff}(r)$

$$\max[\tau_{\rm eff}(r)] = \frac{\beta}{2c}\frac{\sqrt{GM_\star}}{\sqrt{r_0}-\sqrt{r}}. \tag{B.8}$$

This can be plugged into equation B.5 to get a maximum mass flux.

Usually, when considering sublimation, radial distances are relatively small ($r_0 \gg r$). In such cases, it is convenient to use the approximation $r = 0$, which leads to

$$\max[\tau_{\rm eff}(r=0)] \approx 2.5\times10^{-5}\left(\frac{M_\star}{1\ \rm M_\odot}\right)^{1/2}\left(\frac{r_0}{1\ \rm AU}\right)^{-1/2}\left(\frac{\beta}{0.5}\right), \tag{B.9}$$

typically accurate to within a few tens of percents when compared to equation B.8. This gives a maximum mass flux in Earth masses per year of

$$\begin{aligned}\max[\dot{M}_{\rm PR}(r=0)] \ &\approx\ 5.6\times10^{-13}\left(\frac{L_\star}{1\ \rm L_\odot}\right)\left(\frac{M_\star}{1\ \rm M_\odot}\right)^{1/2}\\ &\times\left(\frac{r_0}{1\ \rm AU}\right)^{-1/2}\left(\frac{Q_{\rm pr}}{1}\right)\left(\frac{\beta}{0.5}\right)\ \rm M_\oplus\ yr^{-1}.\end{aligned} \tag{B.10}$$

B.2 The blowout timescale

Particles with high β ratios are removed from the system by radiation pressure. Here, we derive the typical timescale for this process, for the case of $\beta \gg 1$. In this limit, the transverse movement of the particles is small compared to the radial movement, and only the radial acceleration of the particle needs to be considered.

B.2.1 The gas free case

We need to consider the forces of gravity and direct radiation pressure (the PR drag force is negligibly small, and we do not consider gas drag at this stage). These forces are given by

$$F_{\rm rad} + F_{\rm grav} = \frac{(\beta-1)GM_\star m}{r^2}. \tag{B.11}$$

For small radial displacements Δr, the acceleration $\ddot{r} = (F_{\rm rad} + F_{\rm grav})/m$ can be assumed to be independent of r, and the displacement as a function of time is given by $\Delta r = \frac{1}{2}\ddot{r}t^2$. The resulting timescale is

$$t_{\rm dyn,\,\Delta r\to0}(\Delta r) = \sqrt{\frac{2\Delta r r_{\rm release}^2}{GM_\star(\beta-1)}}. \tag{B.12}$$

At large distances from the release point, the acceleration tends to zero, and the velocity of the particle approaches a constant : $\dot{r}(r \to \infty) = \sqrt{2GM_\star\beta/r_{\rm release}}$ (Lecavelier des Etangs et al. 1998). Hence, for large displacements, the removal happens on a timescale of

$$t_{\rm dyn,\,\Delta r\to\infty}(\Delta r) = \frac{\Delta r}{\dot{r}(r\to\infty)} = \sqrt{\frac{(\Delta r)^2 r_{\rm release}}{2GM_\star(\beta-1)}}. \tag{B.13}$$

Adding Eqs. B.12 and B.13 in quadrature leads to the removal timescale

$$t_{\rm dyn}(\Delta r) = \sqrt{\frac{\Delta r\, r_{\rm release}}{GM_\star(\beta-1)}\left(2r_{\rm release} + \frac{\Delta r}{2}\right)}. \tag{B.14}$$

Comparing this equation with a numerical evaluation of the equation of motion shows that its relative errors are less than 5% for the values of β and $r_{\rm release}$ considered here.

We define $t_{\rm dyn}$ as the time it takes for a particle to fly from its release point ($r_{\rm release}$) to a point twice that radial distance from the star ($2r_{\rm release}$). This is motivated by the fact that the small grains are seen in a very narrow radial range, so only the time they spend close to the release point is relevant. Setting $\Delta r = r_{\rm release} = r$ gives the blowout timescale given by Eq. 5.31.

B.2.2 The high gas density case

For high gas densities, the gas drag force cannot be ignored. Since the particles considered here are small (compared to the mean free path of the gas molecules), and their velocities are low (compared to the sound speed of the gas), the gas drag force is given by the subsonic Epstein drag law. It is given by

$$F_{\rm drag} = -\frac{4\pi a^2 \rho_{\rm g} v_{\rm th} \Delta v}{3}, \tag{B.15}$$

where $\rho_{\rm g}$ is the mass density of the gas, Δv is the relative speed between the dust grain and the gas, and $v_{\rm th}$ is the mean thermal speed of the gas. The latter is given by $v_{\rm th} = \sqrt{8k_{\rm B}T_{\rm g}/(\pi\mu_{\rm g}m_{\rm u})}$, where $\mu_{\rm g}$ is the molecular weight of gas molecules, $m_{\rm u}$ is the atomic mass unit, $k_{\rm B}$ is the Boltzmann constant, and $T_{\rm g}$ is the temperature of the gas. To calculate $v_{\rm th}$, we assume that the gas temperature equals the dust temperature ($T_{\rm g} = T_{\rm d}$), and that the gas consists of the same molecules as the dust grains ($\mu_{\rm g} = \mu_{\rm d}$).

For high gas densities, the particles quickly reach the terminal velocity $v_{\rm term}$, which is found by solving $F_{\rm rad} + F_{\rm grav} + F_{\rm drag} = 0$ for Δv. This gives

$$v_{\rm term} = \frac{GM_\star(\beta-1)\rho_{\rm d} s}{\rho_{\rm g} v_{\rm th} r^2}. \tag{B.16}$$

In the high gas density case, the average velocity over the radial range Δr can be approximated by the terminal velocity. The blowout timescale for high gas densities is then found from $t_{{\rm dyn},\,\rho_{\rm g}\to\infty}(\rho_{\rm g}, \Delta r) = \Delta r/v_{\rm term}$, which leads to Eq. 5.32.

B.3 Bayesian probability curves

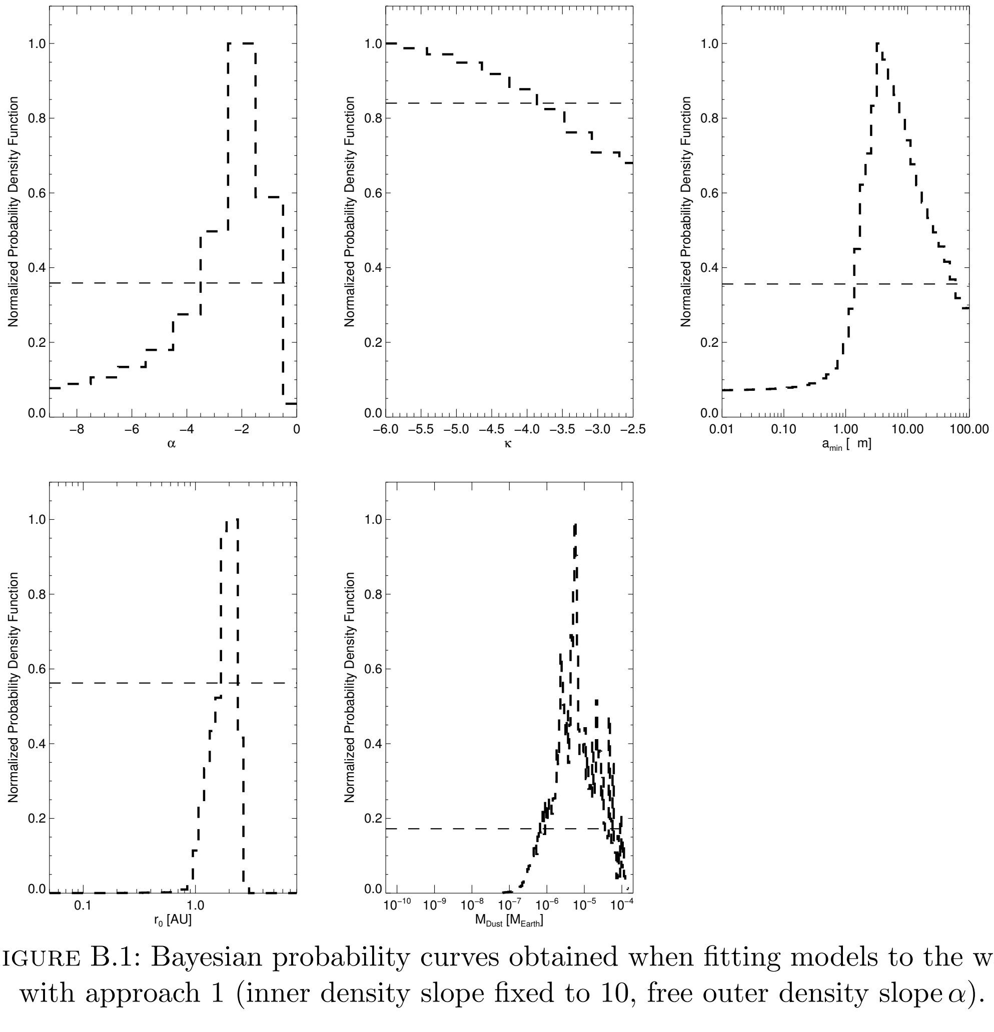

FIGURE B.1: Bayesian probability curves obtained when fitting models to the warm component with approach 1 (inner density slope fixed to 10, free outer density slope α).

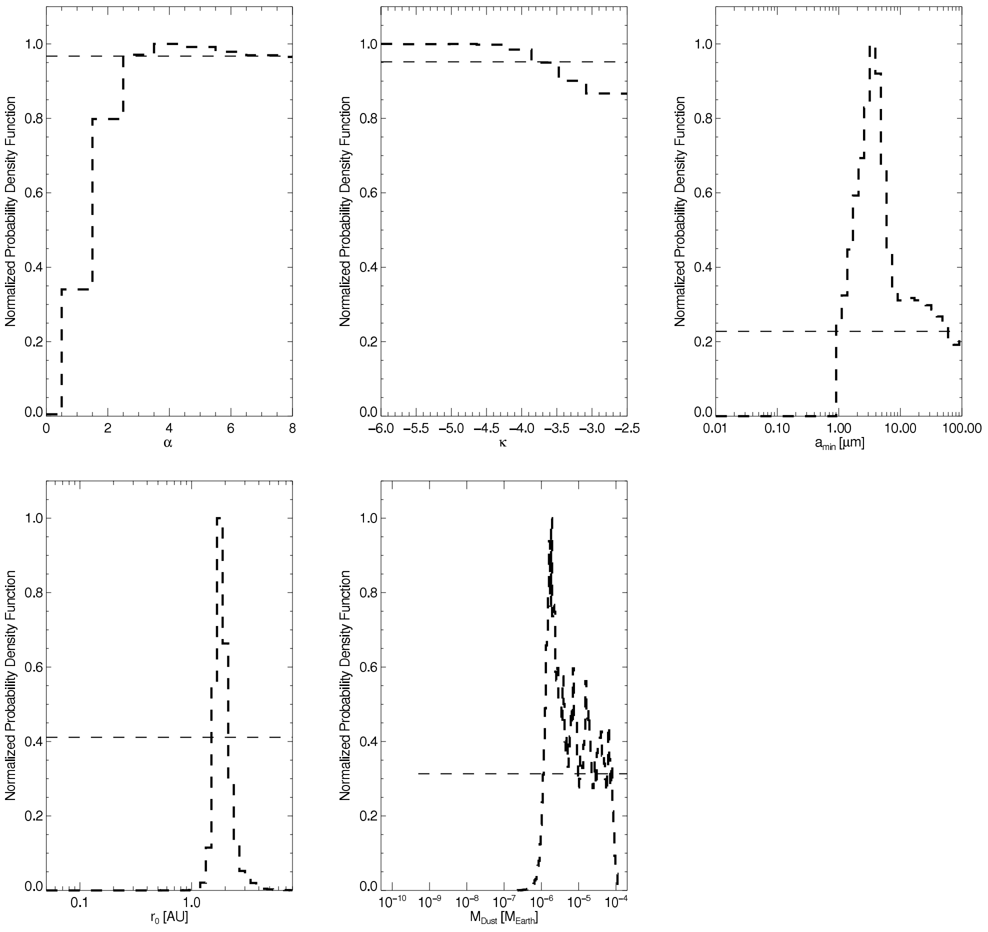

FIGURE B.2: Bayesian probability curves obtained when fitting models to the warm component with approach 2 (outer density slope fixed to 1.5, free inner density slope α). The analysis uses some prior information regarding the grain sizes $P(a < a_{\mathrm{blow}}/10 = 0)$

.

Annexe C

Dynamical simulations of β Pictoris

This appendix comes in complement to Section 6.2.1 and presents some preliminary dynamical simulations of the β Pictoris system obtained with the RMVS3 symplectic integrator. The motion of test-particle in orbit around a central star under the influence of a planetary companion can be integrated precisely for times up to billions of years — here the system age is only 12 Myr allowing 150,000 test-particles to be considered. The planetesimal disk is divided into concentric rings, each with its own time scale ($t_{\mathrm{orb}}/20$), which allows an efficient parallel computing. Each parent-body is subsequently converted into 100 β-particles to produce the images shown in Figure 6.3. The simulations initial conditions are the following :

Planet :
- Mass : M = 9 $\mathrm{M_{jup}}$
- Semi-major axis : a = 9 AU
- Inclination : i = 3°
- Eccentricity : e = 0
- Longitude of the ascending node $\Omega = 0$, Argument of periapsis $\omega = 0$

Disk :
- 150,000 test particles
- Eccentricity : uniformly distributed from e = 0 to 0.05
- Inclination : cosine uniformly distributed from -3° to+3°
- Semi-major axis : logarithmically distributed from a = 12 to 150 AU.

We observe that the warp propagates following the formula obtained by Mouillet et al. (1997) and confirmed by Augereau et al. (2001) :

$$\log \frac{R_{\mathrm{w}}}{10\mathrm{AU}} = 0.29 \log \left(\frac{M}{M_\star} \left(\frac{D}{10\mathrm{AU}} \right)^2 \frac{t}{t_{\mathrm{unit}}} \right) - 0.2 \tag{C.1}$$

where R_{w} is the warp position, M the mass of the planet and D its orbital distance.

Figure C.1: Beta Pictoris at t = 0 Myr. **Top** : The disk of planetesimals as seen edge-on (left) and face-on (right) ; **bottom :** diagrams $\Omega - A$ (ascending node - semi-major axis, **left**) and $e - A$ (eccentricity - semi-major axis, **right**) of the test-particles.

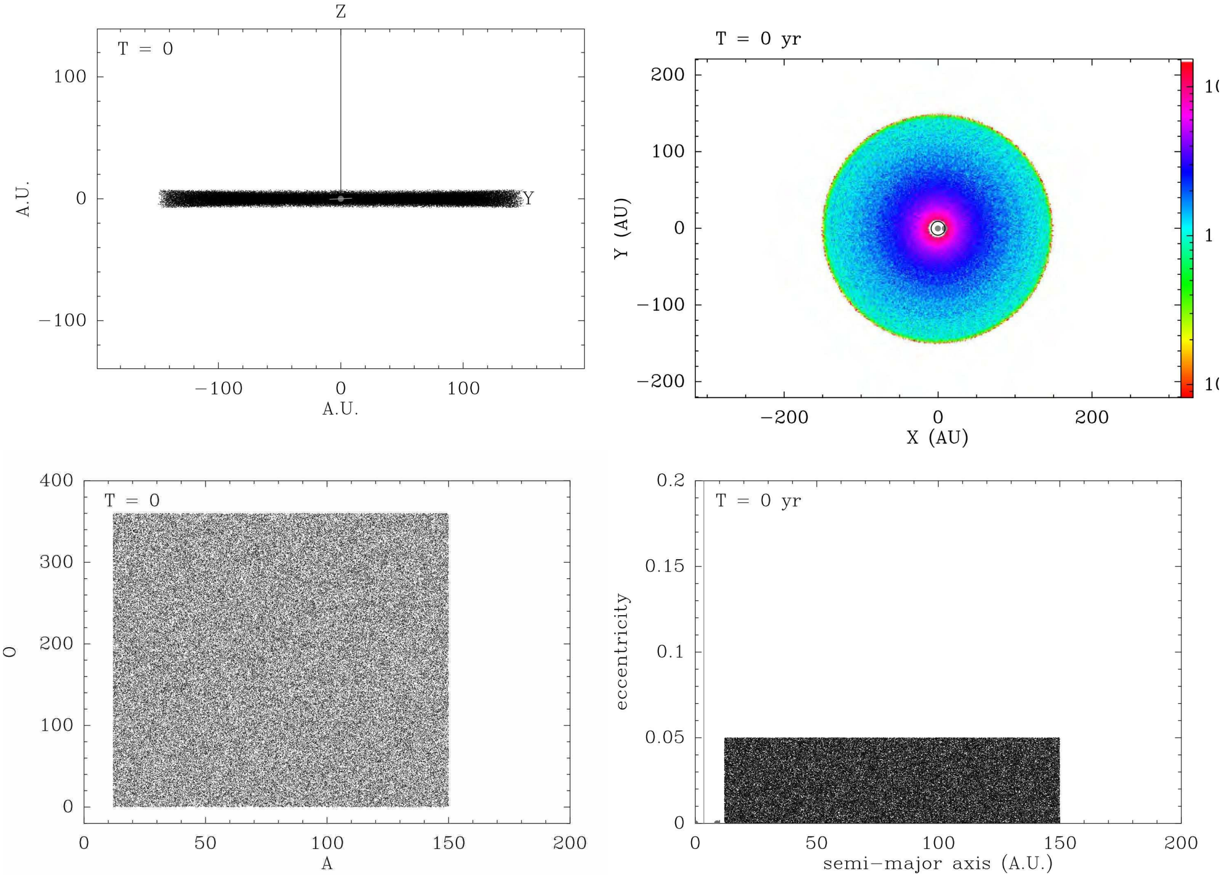

Figure C.2: Same as Fig. C.1 at t = 6 Myr

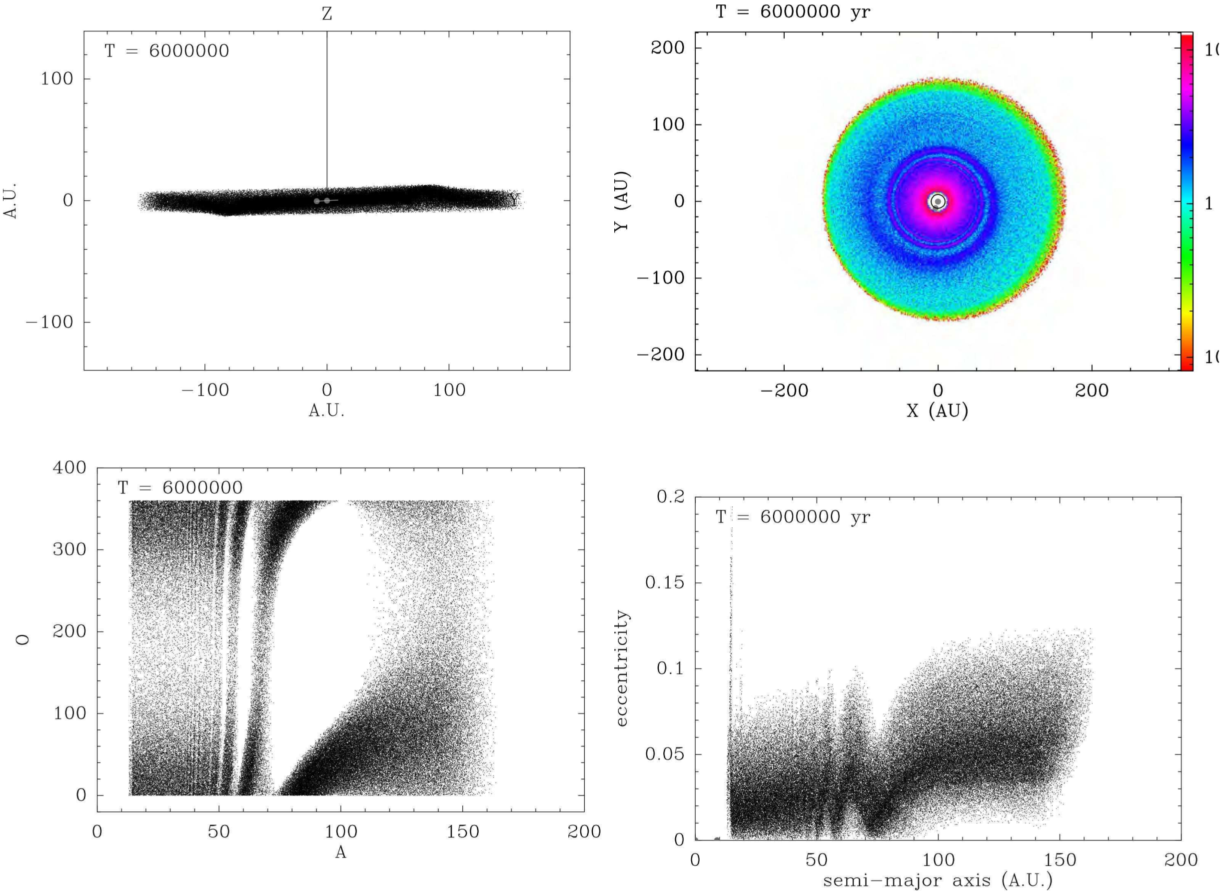

FIGURE C.3: Same as Fig. C.1 at t = 12 Myr

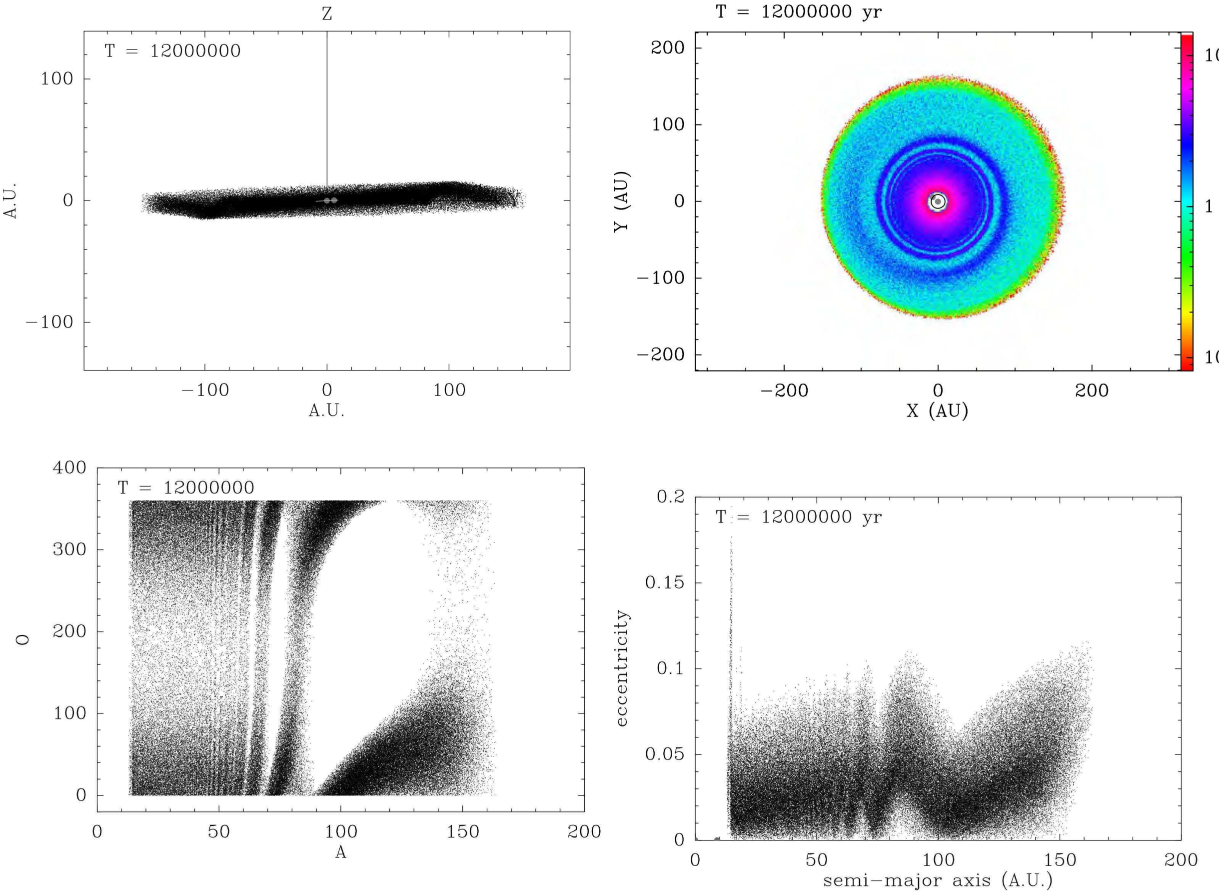

Bibliographie

Absil, O., Defrère, D., Coudé du Foresto, V., et al. 2013, Astronomy & Astrophysics, 555, A104

Absil, O., di Folco, E., Mérand, A., et al. 2006, Astronomy & Astrophysics, 452, 237

Absil, O., di Folco, E., Mérand, A., et al. 2008, Astronomy & Astrophysics, 487, 1041

Absil, O., Le Bouquin, J., Lebreton, J., et al. 2010, Astronomy & Astrophysics, 520, L2+

Absil, O., Mennesson, B., Le Bouquin, J.-B., et al. 2009, The Astrophysical Journal, 704, 150

Acke, B., Min, M., Dominik, C., et al. 2012, Astronomy & Astrophysics, 540, A125

Ardila, D. R., Lubow, S. H., Golimowski, D. A., et al. 2005, The Astrophysical Journal, 627, 986

Armitage, P. J. 2009, in American Institute of Physics Conference Series, Vol. 1192, American Institute of Physics Conference Series, ed. F. Roig, D. Lopes, R. de La Reza, & V. Ortega, 3–42

Augereau, J. & Beust, H. 2006, Astronomy & Astrophysics, 455, 987

Augereau, J. C., Lagrange, A. M., Mouillet, D., Papaloizou, J. C. B., & Grorod, P. A. 1999, Astronomy & Astrophysics, 348, 557

Augereau, J. C., Nelson, R. P., Lagrange, A. M., Papaloizou, J. C. B., & Mouillet, D. 2001, Astronomy & Astrophysics, 370, 447

Augereau, J. C. & Papaloizou, J. C. B. 2004, Astronomy & Astrophysics, 414, 1153

Aumann, H. H., Beichman, C. A., Gillett, F. C., et al. 1984, The Astrophysical Journal Letters, 278, L23

Backman, D. E., Caroff, L. J., Sandford, S. A., & Wooden, D. H., eds. 1998, Exozodiacal Dust Workshop

Backman, D. E. & Paresce, F. 1993, in Protostars and Planets III, ed. E. H. Levy & J. I. Lunine, 1253–1304

Batalha, N. M. & Kepler Team. 2012, in American Astronomical Society Meeting Abstracts, Vol. 220, American Astronomical Society Meeting Abstracts 220, 306.01

Beichman, C., Bryden, G., Lisse, C., & Wyatt, M. 2007, Spitzer Proposal, 40109

Beichman, C. A., Bryden, G., Gautier, T. N., et al. 2005a, The Astrophysical Journal, 626, 1061

Beichman, C. A., Bryden, G., Rieke, G. H., et al. 2005b, The Astrophysical Journal, 622, 1160

Bessell, M. S. 2000, Publications of the Astronomical Society of the Pacific, 112, 961

Beust, H. 2003, Astronomy & Astrophysics, 400, 1129

Beust, H., Bonfils, X., Delfosse, X., & Udry, S. 2008, Astronomy & Astrophysics, 479, 277

Beust, H. & Morbidelli, A. 2000, Icarus, 143, 170

Boccaletti, A., Augereau, J.-C., Lagrange, A.-M., et al. 2012, the Astrophysical Journal, 544, A85

Bohren, C. F. & Huffman, D. R. 1983, Absorption and scattering of light by small particles, ed. Bohren, C. F. & Huffman, D. R.

Boley, A. C., Payne, M. J., Corder, S., et al. 2012, The Astrophysical Journal Letters, 750, L21

Bonfils, X., Delfosse, X., Udry, S., et al. 2011, ArXiv e-prints

Bonsor, A., Augereau, J.-C., & Thébault, P. 2012, Astronomy & Astrophysics, 548, A104

Bonsor, A. & Wyatt, M. C. 2012, Mon. Not. R. Astron. Soc., 420, 2990

Booth, M., Wyatt, M. C., Morbidelli, A., Moro-Martín, A., & Levison, H. F. 2009, Monthly Notices of the Royal Astronomical Society, 399, 385

Buenzli, E., Thalmann, C., Vigan, A., et al. 2010, Astronomy & Astrophysics, 524, L1+

Busemann, H., Nguyen, A. N., Cody, G. D., et al. 2009, Earth and Planetary Science Letters, 288, 44

Canup, R. M. & Asphaug, E. 2001, Nature, 412, 708

Carpenter, J. M., Wolf, S., Schreyer, K., Launhardt, R., & Henning, T. 2005, Astronomical Journal, 129, 1049

Catanzarite, J. & Shao, M. 2011, The Astrophysical Journal, 738, 151

Charnoz, S. & Taillifet, E. 2012, The Astrophysical Journal, 753, 119

Chauvin, G., Lagrange, A.-M., Beust, H., et al. 2012, Astronomy & Astrophysics, 542, A41

Chavero, C., Gómez, M., Whitney, B. A., & Saffe, C. 2006, Astronomy & Astrophysics, 452, 921

Chen, C. H., Fitzgerald, M. P., & Smith, P. S. 2008, The Astrophysical Journal, 689, 539

Chen, C. H., Sargent, B. A., Bohac, C., et al. 2006, The Astrophysical Journals, 166, 351

Ciardi, D. R., Fabrycky, D. C., Ford, E. B., et al. 2012, ArXiv e-prints

Cieza, L., Padgett, D. L., Stapelfeldt, K. R., et al. 2007, The Astrophysical Journal, 667, 308

Coudé du Foresto, V., Borde, P. J., Merand, A., et al. 2003, in Society of Photo-Optical Instrumentation Engineers (SPIE) Conference Series, Vol. 4838, Society of Photo-Optical Instrumentation Engineers (SPIE) Conference Series, ed. W. A. Traub, 280–285

Currie, T., Debes, J., Rodigas, T. J., et al. 2012, The Astrophysical Journal Letters, 760, L32

Currie, T. & Sicilia-Aguilar, A. 2011, ArXiv e-prints

Czechowski, A. & Mann, I. 2010, The Astrophysical Journal, 714, 89

Dalgarno, A. 2006, Proceedings of the National Academy of Science, 103, 12269

de Muizon, M. J. 2005, Space and Science Review, 119, 201

de Vries, B. L., Acke, B., Blommaert, J. A. D. L., et al. 2012, Nature, 490, 74

Defrère, D., Absil, O., Augereau, J.-C., et al. 2011a, Astronomy & Astrophysics, 534, A5

Defrère, D., Absil, O., Augereau, J. C., et al. 2011b, in EPSC-DPS Joint Meeting 2011, 1084

Defrère, D., Absil, O., den Hartog, R., Hanot, C., & Stark, C. 2010, Astronomy & Astrophysics, 509, A9

Defrère, D., Lebreton, J., Le Bouquin, J.-B., et al. 2012, Astronomy & Astrophysics, 546, L9

Delsanti, A., Merlin, F., Guilbert, A., et al. 2010, Astronomy & Astrophysics

DeMeo, F. E., Binzel, R. P., Slivan, S. M., & Bus, S. J. 2009, Icarus, 202, 160

Dent, W. R. F., Greaves, J. S., & Coulson, I. M. 2005, Monthly Notices of the Royal Astronomical Society, 359, 663

Dermott, S. F., Kehoe, T. J. J., Durda, D. D., Grogan, K., & Nesvorný, D. 2002, in ESA Special Publication, Vol. 500, Asteroids, Comets, and Meteors : ACM 2002, ed. B. Warmbein, 319–322

Dohnanyi, J. S. 1969, Journal of Geophysical Research, 74, 2531

Dominik, C. & Decin, G. 2003, The Astrophysical Journal, 598, 626

Donaldson, J. K., Lebreton, J., Roberge, A., Augereau, J.-C., & Krivov, A. V. 2013, The Astrophysical Journal, 772, 17

Draine, B. T. 2003, Annu. Rev. Astron. Astrophys., 41, 241

Draine, B. T. 2006, The Astrophysical Journal, 636, 1114

Drake, M. J. 2005, Meteoritics and Planetary Science, 40, 519

Dumas, C., Carry, B., Hestroffer, D., & Merlin, F. 2011, Astronomy & Astrophysics, 528, A105+

Durda, D. D. & Dermott, S. F. 1997, Icarus, 130, 140

Eiroa, C., Fedele, D., Maldonado, J., et al. 2010, Astronomy & Astrophysics, 518, L131

Eiroa, C., Marshall, J. P., Mora, A., et al. 2011, Astronomy & Astrophysics, 536, L4

Eiroa, C., Marshall, J. P., Mora, A., et al. 2013, Astronomy & Astrophysics, 555, A11

Ertel, S., Wolf, S., Marshall, J. P., et al. 2012, Astronomy & Astrophysics, 541, A148

Fernández, R., Brandeker, A., & Wu, Y. 2006, The Astrophysical Journal, 643, 509

Fitzgerald, M. P., Kalas, P. G., Duchêne, G., Pinte, C., & Graham, J. R. 2007, The Astrophysical Journal, 670, 536

Fujiwara, A., Kawaguchi, J., Yeomans, D. K., et al. 2006, Science, 312, 1330

Galicher, R., Marois, C., Zuckerman, B., & Macintosh, B. 2013, The Astrophysical Journal, 769, 42

Gaspar, A., Rieke, G. H., & Balog, Z. 2012, ArXiv e-prints

Golimowski, D. A., Krist, J. E., Stapelfeldt, K. R., et al. 2011, ArXiv e-prints

Gomes, R., Levison, H. F., Tsiganis, K., & Morbidelli, A. 2005, Nature, 435, 466

Graham, J. R., Kalas, P. G., & Matthews, B. C. 2007, The Astrophysical Journal, 654, 595

Greaves, J. S., Holland, W. S., Moriarty-Schieven, G., et al. 1998, The Astrophysical Journal Letters, 506, L133

Greaves, J. S., Holland, W. S., Wyatt, M. C., et al. 2005, The Astrophysical Journal Letters, 619, L187

Greaves, J. S. & Wyatt, M. C. 2010, Monthly Notices of the Royal Astronomical Society, 404, 1944

Greenberg, J. M. 1998, Astronomy & Astrophysics, 330, 375

Grün, E. 2007, Encyclopedia of the Solar System, second edition edn., ed. L.-A. McFadden, P. R. Weissman, & T. V. Johnson No. 621 - 636 (San Diego : Academic Press)

Gustafson, B. A. S. 1994, Annual Review of Earth and Planetary Sciences, 22, 553

Hartogh, P., Lis, D. C., Bockelée-Morvan, D., et al. 2011, Nature, 478, 218

Hauschildt, P. H., Allard, F., & Baron, E. 1999a, the Astrophysical Journal, 512, 377

Hauschildt, P. H., Allard, F., Ferguson, J., Baron, E., & Alexander, D. R. 1999b, The Astrophysical Journal, 525, 871

Holland, W. S., Greaves, J. S., Zuckerman, B., et al. 1998, Nature, 392, 788

Holmberg, J., Nordström, B., & Andersen, J. 2009, Astronomy & Astrophysics, 501, 941

Janson, M., Carson, J. C., Lafrenière, D., et al. 2012, the Astrophysical Journal, 747, 116

Jewitt, D. 2010, in IAU Symposium, Vol. 263, IAU Symposium, ed. J. A. Fernández, D. Lazzaro, D. Prialnik, & R. Schulz , 3–16

Jewitt, D. C. & Luu, J. X. 2000, Protostars and Planets IV, 1201

Kalas, P., Graham, J. R., Chiang, E., et al. 2008, Science, 322, 1345

Kalas, P., Graham, J. R., & Clampin, M. 2005, Nature, 435, 1067

Kalas, P., Graham, J. R., Fitzgerald, M. P., & Clampin, M. 2013, ArXiv e-prints

Kama, M., Min, M., & Dominik, C. 2009, Astronomy & Astrophysics, 506, 1199

Kamp, I., Tilling, I., Woitke, P., Thi, W., & Hogerheijde, M. 2010, Astronomy & Astrophysics, 510, A18+

Kelsall, T., Weiland, J. L., Franz, B. A., et al. 1998, The Astrophysical Journal, 508, 44

Klahr, H. & Lin, D. N. C. 2005, The Astrophysical Journal, 632, 1113

Kobayashi, H., Kimura, H., Watanabe, S.-i., Yamamoto, T., & Müller, S. 2011, Earth, Planets, and Space, 63, 1067

Kobayashi, H., Kimura, H., & Yamamoto, S. 2013, Astronomy & Astrophysics, 550, A72

Kobayashi, H. & Tanaka, H. 2010, Icarus, 206, 735

Kobayashi, H., Watanabe, S.-I., Kimura, H., & Yamamoto, T. 2008, Icarus, 195, 871

Kobayashi, H., Watanabe, S.-I., Kimura, H., & Yamamoto, T. 2009, Icarus, 201, 395

Köhler, M., Mann, I., & Li, A. 2008, The Astrophysical Journal Letters, 686, L95

Krist, J. E., Stapelfeldt, K. R., Bryden, G., et al. 2010, The Astronomical Journal, 140, 1051

Krivov, A. V. 2010, Research in Astronomy and Astrophysics, 10, 383

Krivov, A. V., Eiroa, C., Löhne, T., et al. 2013, The Astrophysical Journal, 772, 32

Krivov, A. V., Herrmann, F., Brandeker, A., & Thébault, P. 2009, Astronomy & Astrophysics, 507, 1503

Krivov, A. V., Löhne, T., & Sremčević, M. 2006, Astronomy & Astrophysics, 455, 509

Krüger, H., Dikarev, V., Anweiler, B., et al. 2010, Planetary and Space Science, 58, 951

Lagrange, A.-M., Boccaletti, A., Milli, J., et al. 2012a, Astronomy & Astrophysics, 542, A40

Lagrange, A.-M., Bonnefoy, M., Chauvin, G., et al. 2010, Science, 329, 57

Lagrange, A.-M., De Bondt, K., Meunier, N., et al. 2012b, Astronomy & Astrophysics, 542, A18

Lagrange, A.-M., Milli, J., Boccaletti, A., et al. 2012c, Astronomy & Astrophysics, 546, A38

Lahuis, F., Kessler-Silacci, J. E., Evans, N. J., I., et al. 2006, c2d Spectroscopy Explanatory Supplement, Tech. rep., Pasadena : Spitzer Science Center

Lamy, P. L. 1974, Astronomy & Astrophysics, 35, 197

Lawler, S. M., Beichman, C. A., Bryden, G., et al. 2009, The Astrophysical Journal, 705, 89

Le Bouquin, J.-B., Berger, J.-P., Lazareff, B., et al. 2011, Astronomy & Astrophysics, 535, A67

Lebreton, J., Augereau, J.-C., Thi, W.-F., et al. 2012, Astronomy & Astrophysics, 539, A17

Lebreton, J., Marshall, J. P., Augereau, J. C., & Eiroa, C. 2011, in EPSC-DPS Joint Meeting 2011, 1287

Lebreton, J., van Lieshout, R., Augereau, J.-C., et al. 2013, A&A, 555, A146

Lestrade, J.-F., Matthews, B. C., Sibthorpe, B., et al. 2012, Astronomy & Astrophysics, 548, A86

Levison, H. F. & Duncan, M. J. 1994, Icarus, 108, 18

Li, A. & Greenberg, J. M. 1997, Astronomy & Astrophysics, 323, 566

Li, A. & Greenberg, J. M. 1998, Astronomy & Astrophysics, 331, 291

Li, A. & Lunine, J. I. 2003a, The Astrophysical Journal, 594, 987

Li, A. & Lunine, J. I. 2003b, The Astrophysical Journal, 590, 368

Li, D., Telesco, C. M., & Wright, C. M. 2012, ArXiv e-prints

Liseau, R., Eiroa, C., Fedele, D., et al. 2010, the Astrophysical Journal, 518, L132

Lissauer, J. J., Fabrycky, D. C., Ford, E. B., et al. 2011a, Nature, 470, 53

Lissauer, J. J., Ragozzine, D., Fabrycky, D. C., et al. 2011b, The Astrophysical Journal Supplement Series, 197, 8

Lisse, C. M., Wyatt, M. C., Chen, C. H., et al. 2012, the Astrophysical Journal, 747, 93

Liu, M. C. 2004, Science, 305, 1442

Löhne, T., Augereau, J.-C., Ertel, S., et al. 2012, Astronomy & Astrophysics, 537, A110

Löhne, T., Krivov, A. V., & Rodmann, J. 2008, The Astrophysical Journal, 673, 1123

Lovis, C., Mayor, M., Pepe, F., et al. 2006, Nature, 441, 305

Lyra, W. & Kuchner, M. 2013, Nature, 499, 184

Lyra, W. & Kuchner, M. J. 2012, ArXiv e-prints

Mamajek, E. E. 2012, The Astrophysical Journal Letters, 754, L20

Mamajek, E. E., Meyer, M. R., Hinz, P. M., et al. 2004, The Astrophysical journal, 612, 496

Mannings, V. & Barlow, M. J. 1998, The Astrophysical Journal, 497, 330

Marshall, J. P., Löhne, T., Montesinos, B., et al. 2011, Astronomy & Astrophysics, 529, A117

Mathews, G. S., Dent, W. R. F., Williams, J. P., et al. 2010, Astronomy & Astrophysics, 518, L127+

May, B. 2008, A Survey of Radial Velocities in the Zodiacal Dust Cloud

Mayor, M., Marmier, M., Lovis, C., et al. 2011, ArXiv e-prints

Mayor, M. & Queloz, D. 1995, Nature, 378, 355

Meeus, G., Montesinos, B., Mendigutia, I., et al. 2012, ArXiv e-prints

Meeus, G., Pinte, C., Woitke, P., et al. 2010, Astronomy & Astrophysics, 518, L124+

Mennesson, B., Absil, O., Lebreton, J., et al. 2013, The Astrophysical Journal, 763, 119

Meyer-Vernet, N., Maksimovic, M., Czechowski, A., et al. 2009, Solar Physics, 256, 463

Mie, G. 1908, Annalen der Physik, 330, 377

Millan-Gabet, R., Serabyn, E., Mennesson, B., et al. 2011, The Astrophysical Journal, 734, 67

Moór, A., Ábrahám, P., Derekas, A., et al. 2006, The Astrophysical Journal, 644, 525

Morbidelli, A., Chambers, J., Lunine, J. I., et al. 2000, Meteoritics and Planetary Science, 35, 1309

Moro-Martin, A. 2012, ArXiv e-prints

Mouillet, D., Lagrange, A. M., Augereau, J. C., & Ménard, F. 2001, Astronomy & Astrophysics, 372, L61

Mouillet, D., Larwood, J. D., Papaloizou, J. C. B., & Lagrange, A. M. 1997, Mon. Not. R. Astron. Soc., 292, 896

Nesvorný, D., Jenniskens, P., Levison, H. F., et al. 2010, the Astrophysical Journal, 713, 816

Nilsson, R., Liseau, R., Brandeker, A., et al. 2009, Astronomy & Astrophysics, 508, 1057

Nordström, B., Mayor, M., Andersen, J., et al. 2004, The Astronomical Journal, 418, 989

Ott, S. 2010, in Astronomical Society of the Pacific Conference Series, Vol. 434, Astronomical Data Analysis Software and Systems XIX, ed. Y. Mizumoto, K.-I. Morita, & M. Ohishi, 139–+

Pilbratt, G. L., Riedinger, J. R., Passvogel, T., et al. 2010, A&A, 518, L1

Pinte, C., Harries, T. J., Min, M., et al. 2009, Astronomy & Astrophysics, 498, 967

Pinte, C., Ménard, F., Duchêne, G., & Bastien, P. 2006, Astronomy & Astrophysics, 459, 797

Poglitsch, A., Waelkens, C., Geis, N., et al. 2010, Astronomy & Astrophysics, 518, L2+

Poppe, A., James, D., Jacobsmeyer, B., & Horányi, M. 2010, Geophysical Research Letters, 37, 11101

Quillen, A. C. 2006, Monthly Notices of the Royal Astronomical Society, 372, L14

Rappaport, S., Levine, A., Chiang, E., et al. 2012, The Astrophysical Journal, 752, 1

Reche, R., Beust, H., & Augereau, J.-C. 2009, Astronomy & Astrophysics, 493, 661

Richardson, J. E., Melosh, H. J., Lisse, C. M., & Carcich, B. 2007, Icarus, 190, 357

Rieke, G. H., Su, K. Y. L., Stansberry, J. A., et al. 2005, The Astrophysical Journal, 620, 1010

Riviere-Marichalar, P., Barrado, D., Augereau, J.-C., et al. 2012, Astronomy & Astrophysics, 546, L8

Roberge, A., Chen, C. H., Millan-Gabet, R., et al. 2012, Publications of the Astronomical Society of the Pacific, 124, 799

Rowan-Robinson, M. & May, B. 2013, Mon. Not. R. Astron. Soc., 533

Saija, R., Iatì, M. A., Giusto, A., et al. 2003, Monthly Notices of the Royal Astronomical Society, 341, 1239

Sault, R. J., Teuben, P. J., & Wright, M. C. H. 1995, in Astronomical Society of the Pacific Conference Series, Vol. 77, Astronomical Data Analysis Software and Systems IV, ed. R. A. Shaw, H. E. Payne, & J. J. E. Hayes, 433–+

Schneider, G., Carson, J., Debes, J., et al. 2012, in American Astronomical Society Meeting Abstracts, Vol. 220, American Astronomical Society Meeting Abstracts n220, 331.02

Schneider, G., Silverstone, M. D., Hines, D. C., et al. 2006, The Astrophysical Journal, 650, 414

Schneider, G., Smith, B. A., Becklin, E. E., et al. 1999, The Astrophysical Journal Letters, 513, L127

Selsis, F., Kasting, J. F., Levrard, B., et al. 2007, Astronomy & Astrophysics, 476, 1373

Shankman, C., Gladman, B., Kaib, N., Kavelaars, J. J., & Petit, J.-M. 2012, ArXiv e-prints

Shen, Y., Draine, B. T., & Johnson, E. T. 2009, The Astrophysical Journal, 696, 2126

Stapelfeldt, K. R., Holmes, E. K., Chen, C., et al. 2004, The Astrophysical Journal Supplement Series, 154, 458

Stark, C. C. & Kuchner, M. J. 2008, The Astrophysical Journal, 686, 637

Stark, C. C., Kuchner, M. J., Traub, W. A., et al. 2009, the Astrophysical Journal, 703, 1188

Stern, S. A. 2003, Nature, 424, 639

Stevenson, D. J. 1987, Annual Review of Earth and Planetary Sciences, 15, 271

Strubbe, L. E. & Chiang, E. I. 2006, The Astrophysical Journal, 648, 652

Su, K. Y. L., Rieke, G. H., Malhotra, R., et al. 2013, The Astrophysical Journal, 763, 118

Takeuchi, T. & Artymowicz, P. 2001, The Astrophysical Journal, 557, 990

Tanner, A., Beichman, C., Bryden, G., Lisse, C., & Lawler, S. 2009, The Astrophysical Journal, 704, 109

Taquet, V., Ceccarelli, C., & Kahane, C. 2011, ArXiv e-prints

Tedesco, E. F. & Desert, F.-X. 2002, Astronomical Journal, 123, 2070

Thébault, P. 2009, Astronomy & Astrophysics, 505, 1269

Thébault, P. & Augereau, J. 2007, Astronomy & Astrophysics, 472, 169

Thébault, P. & Augereau, J.-C. 2005, Astronomy & Astrophysics, 437, 141

Thébault, P. & Beust, H. 2001, Astronomy & Astrophysics, 376, 621

Thebault, P., Kral, Q., & Ertel, S. 2012, Astronomy & Astrophysics, 547, A92

Thébault, P. & Wu, Y. 2008, Astronomy & Astrophysics, 481, 713

Thi, W., Woitke, P., & Kamp, I. 2011, Monthly Notices of the Royal Astronomical Society, 412, 711

Traub, W. A. 2012, The Astrophysical Journal, 745, 20

Vitense, C., Krivov, A. V., Kobayashi, H., & Löhne, T. 2012, Astronomy & Astrophysics, 540, A30

Voshchinnikov, N. V., Videen, G., & Henning, T. 2007, Applied Optics, 46, 4065

Warren, S. G. 1984, Applied Optics, 23, 1206

Wisdom, J. 1980, Astronomical Journal, 85, 1122

Wisdom, J. & Holman, M. 1991, The Astronomical Journal, 102, 1528

Woitke, P., Kamp, I., & Thi, W. 2009, Astronomy & Astrophysics, 501, 383

Woitke, P., Riaz, B., Duchene, G., et al. 2011, ArXiv e-prints

Wyatt, M. C. 2005a, Astronomy & Astrophysics, 440, 937

Wyatt, M. C. 2005b, Astronomy & Astrophysics, 433, 1007

Wyatt, M. C. 2008, Annu. Rev. Astron. Astrophys., 46, 339

Wyatt, M. C., Dermott, S. F., Telesco, C. M., et al. 1999, The Astrophysical Journal, 527, 918

Wyatt, M. C., Smith, R., Greaves, J. S., et al. 2007a, the Astrophysical Journal, 658, 569

Wyatt, M. C., Smith, R., Su, K. Y. L., et al. 2007b, The Astrophysical Journal, 663, 365

Zavitsanos, P. D. & Carlson, G. A. 1973, Journal of Chemical Physics, 59, 2966

Zubko, V. G., Mennella, V., Colangeli, L., & Bussoletti, E. 1996, Mon. Not. R. Astron. Soc., 282, 1321

Zuckerman, B. & Song, I. 2004, The Astrophysical Journal, 603, 738

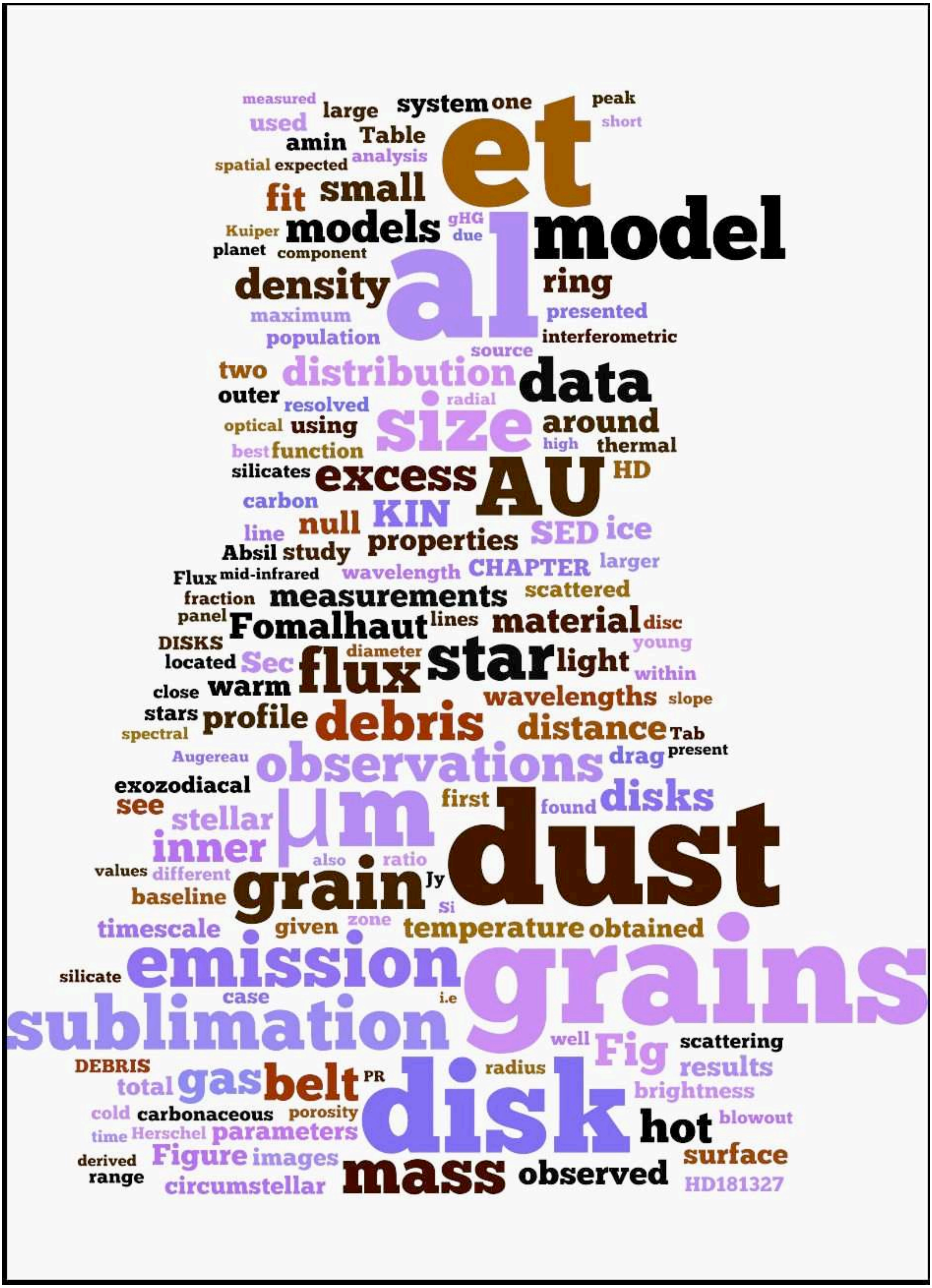
measured
large
system
one
peak
used
short
amin
Table
et
spatial
expected
analysis
fit
small
Kuiper
models
gHG
due
model
planet
component
density
al
ring
maximum
presented
population
interferometric
source
two
distribution
data
outer
resolved
radial
optical
using
size
around
best
function
high
thermal
silicates
excess
AU
HD
carbon
KIN
line
null
SED
ice
Absil
study
properties
Flux
mid-infrared
wavelength
CHAPTER
larger
fraction
measurements
scattered
panel
Fomalhaut
lines
material
disc
DISKS
diameter
young
located
Sec
flux
star
light
within
close
warm
wavelengths
slope
stars
profile
debris
distance
Tab
spectral
Augereau
observations
drag
present
exozodiacal
first
found
disks
see
stellar
μm
dust
inner
also
ratio
values
different
Jy
baseline
grain
Si
timescale
given
zone
temperature
obtained
silicate
emission
grains
case
i.e
sublimation
well
scattering
DEBRIS
Fig
radius
results
total
gas
belt
PR
brightness
cold
carbonaceous
porosity
disk
blowout
time
Herschel
parameters
hot
derived
Figure
images
surface
range
mass
observed
circumstellar
HD181327